Exploring the secreted proteome and metabolome of iron-starved *Aspergillus fumigatus* for tools to combat fungal infection

Nicola Moloney BSc

This thesis is submitted to Maynooth

University for the degree of

Doctor of Philosophy

October 2017

Supervisor:

Professor Sean Doyle,

Department of Biology,

Maynooth University,

Maynooth,

Co. Kildare, Ireland

Head of Department:

Professor Paul Moynagh

Table of contents

Declaration of authorship

This thesis has not previously been submitted, in whole or in part, to this, or any other University, for another degree. This thesis is the sole work of the author with the exception of: (i) glucanase activity assay of secreted proteins, which was carried out by Ms Rose Waldron (Maynooth University), (ii) murine immunisations, which were carried out by staff at Biomedical Research Facility, Beaumont Hospital, Dublin, (iii) fusion procedure for the FSC-KLH immunised mouse, which was carried out by Dr Andrew McCann (NICB), and (iv) design of sequencing primers for the anti-TAFC IgG Fab region, which was carried out by Dr Linan Xu (Maynooth University).

_____

Nicola Moloney, BSc

Acknowledgments

First and foremost, I wish to thank my PhD supervisor, Professor Sean Doyle. Thank you for giving me the opportunity to undertake this research project and most of all, for your unrelenting support and guidance. I have greatly appreciated your encouragement, discussions and patience during the PhD. I would also like to thank Dr Annemarie Larkin and Professor Martin Clynes for kindly hosting me in the NICB. I am very grateful to Dr Annemarie Larkin for her guidance and expertise on the monoclonal antibody development. Thank you to SFI for funding this PhD *via* a Principal Investigator award to Professor Sean Doyle (12/IP/1695) and to SFI (12/RI/2346(3)) and the HEA for funding LC-MS facilities in Maynooth University. I am grateful to the Microbiology Society and Wellcome Trust for funding my attendance at conferences and courses during the PhD. I would also like to thank Professor Hubertus Haas for kindly providing the *A. fumigatus* Δ*sidG* and Δ*sidD* strains, which were utilised during this work.

I am sincerely grateful to all those who have trained me, collaborated with me and made this work possible. I must thank Dr Rebecca Owens and Dr Gráinne O'Keeffe for their training and patient answering of my many questions, as well as Dr Lara Manzanares and Dr Stephen Dolan, all of whom have helped and encouraged me since I first came to this lab as an undergraduate. I would like to thank Dr Eoin Mulvihill who also worked on this grant, for all of his help and teamwork. I am very thankful to Caroline Batchelor for her very extensive LC-MS support and to Nicholas Irani for support with various instruments, especially the HPLC. I am grateful to Dr Ica Dix for her help and training with the fluorescence microscope. I would also like to thank members of the NICB, in particular Dr Andrew McCann for training me on hybridoma generation and for his help, along with Charles O'Doherty and Dr Edel McAuley, on cell culture. I am also very grateful to Dr Linan Xu for his work on the antibody-sequencing project and to Rose Waldron for her work with the glucanase assay.

I would like to say a special thank you to past and present members of the Biotechnology, Yeast Genetics, Genome Evolution, and Fungal Genetics and Secondary Metabolism labs. Betim, Daragh, Elizabeth, Eoin M, Eoin O'C, Gráinne, Kevin, Lara, Linan, Mevlüt, Niall, Niamh, Özlem, Rebecca, Rose, Stephen B, and Stephen D. Thank you for your help and friendship. For coffee breaks, lab safety

listening, lifts, ducklings, doggos, dinners, drinks, practical help, and practical jokes. I am grateful to Linan, Rose and Eoin O'C for their support in the final stages of this project. I would also like to particularly thank Lara, Stephen, and Niamh for their friendship, support, and motivation. For all the times they made me leave the lab and all the times they made me go back in.

Thank you to friends outside the lab, David, Jenny, Alan, Andrea, Benny, and Elina for being there and reminding me that there is a world outside the PhD.

Finally, thank you to my mother, Helen, and my father, Aidan for their continuous support and belief in my ability. Thank you to my brother, David and to Marie-Louise for always being there to listen, deliberate with, and for inspiring me. David, I'm extremely grateful to have had you at my back throughout this process. Thank you to Warner, for your support and for understanding everything, including siderophores. I dedicate this thesis to all of you.

Publications

Moloney, N. M.[*], Owens, R. A.[*], Meleady, P., Henry, M., Dolan, S. K., Mulvihill, E., Clynes, M., Doyle, S. (2016). The iron-responsive microsomal proteome of *Aspergillus fumigatus*. *Journal of Proteomics*, 135, 99-111. DOI: 10.1016/j.jprot.2015.12.025

Moloney, N. M., Owens, R. A., Doyle, S. (2016). Proteomic analysis of *Aspergillus fumigatus* - clinical implications. *Expert Review of Proteomics*, 13 (7), 635-649. DOI: dx.doi.org/10.1080/14789450.2016.1203783

Mulvihill, E. D., **Moloney, N. M**., Owens, R. A., Dolan, S. K., Russell, L., and Doyle, S. (2017). Functional investigation of iron-responsive microsomal proteins, including MirC, in *Aspergillus fumigatus*. *Front. Microbiol*. 8, 418. DOI:10.3389/FMICB.2017.00418.

Sipos, G., Prasanna, A. N., Walther, M. C., O'Connor, E., Balint, B., Krizsan, K., Kiss, B., Hess, J., Slot, J., Riley, R., Boka, B., Rigling, D., Barry, K., Lee, J., Mihaltseva, S., Labutti, K., Lipzen, A., Waldron, R., **Moloney, N. M.**, Sperisen, C., Kredics, L., Vagvolgyi, C., Patrigniani, A., Fitzpatrick, D., Nagy, I., Doyle, S., Anderson, J. B., Grigoriev, I. V, Guldener, U., Munsterkotter, M., Varga, T. and Nagy, L. G. (2017). Genome expansion and lineage-specific genetic innovations in the forest pathogenic fungi Armillaria. *Nature Ecology and Evolution*. DOI: doi.org/10.1101/166231 [in press].

Moloney, N. M., Doyle, S. *et al.* (2017). Iron starvation induces a host-relevant secretomic remodelling of the cell surface in *Aspergillus fumigatus.* [in preparation].

* Equal contribution

Oral Presentations

Moloney, N. M. (2016) Exploiting the secretory struggle for iron in fungal infection. 5th Annual Biology Research Day. National University of Ireland Maynooth, Kildare, Ireland; 13 June. Awarded best postgraduate oral presentation.

Moloney, N. M. (2016) Dissecting and exploiting adaptations to iron starvation in *Aspergillus fumigatus*. 6th Annual Meeting of the Irish Fungal Society. The Grand Hotel, Malahide, Dublin, Ireland; 20-22 March. Awarded best postgraduate oral presentation.

Moloney, N. M. (2015) The iron starved proteome of *Aspergillus fumigatus*: Exposing core adaptations for high affinity iron acquisition. Industrial Applications of Metal Microbe Interactions. Charles Darwin House, London, United Kingdom; 9-10 November.

Moloney, N. M. (2015) *Aspergillus fumigatus* and iron: Exposing tactics in the battlefield for an essential resource. 4th Annual Biology Research Day. National University of Ireland Maynooth 12 June.

Poster Presentations

Moloney, N. M., Mulvihill, E., Dix, S., Manzanares, L., O'Keeffe, G., Doyle, S. (2017) Exploring adaptations to iron starvation in the *Aspergillus fumigatus* secretome. Microbiology Society Annual Conference 2017. Edinburgh, United Kingdom; 3-6 April.

Moloney, N. M., Owens, R. A., Mulvihill, E., Dolan, S. K., Clynes, M., Henry, M., Meleady, P., Doyle, S. (2016) The iron-starved microsomal proteome of *Aspergillus fumigatus*. Proteomics Bioinformatics Course. Wellcome Genome Campus, Hinxton, Cambridge, United Kingdom; 5 December.

Moloney, N. M., Owens, R. A., Mulvihill, E., Dolan, S. K., McHugh, A., Clynes, M., Henry, M., Meleady, P., Doyle, S. (2015) Iron limitation significantly alters the microsomal and secreted proteome of *Aspergillus fumigatus*. ASM GM 2015. New Orleans, United States of America; 30 May–2 June.

Moloney, N. M., Mulvihill, E., Manzanares, L., O'Keeffe, G., Doyle, S. (2015) Characterising the extracellular armoury of *Aspergillus fumigatus* in a battle for iron. 5th Annual Meeting of the Irish Fungal Society. Trinity College Dublin, Ireland; 11-12 June.

Moloney, N. M., Gordon, N., Manzanares, L., Billen, F., Hayes, N., Doyle, S. (2014) Immunological detection of Aspergillosis using gliotoxin biosynthetic enzyme, GliT. Applications of Proteomics in Human Clinical and Infectious Disease. Dublin City University, Ireland; 16 September.

Moloney, N. M., Gordon, N., Manzanares, L., Billen, F., Hayes, N., Doyle, S. (2014) Immunological detection of Aspergillosis using gliotoxin biosynthetic enzyme, GliT. 3rd Biology Research Day. Maynooth University; 12 September.

Moloney, N. M., Gordon, N., Manzanares, L., Billen, F., Hayes, N., Doyle, S. (2014) Using gliotoxin biosynthetic enzyme, GliT for the detection of Aspergillosis. 4th Annual Meeting of the Irish Fungal Society, National University of Ireland Galway, Ireland; 19-20 June.

Moloney, N. M., Gordon, N., Manzanares, L., Billen, F., Hayes, N., Doyle, S. (2014) Detection of Aspergillosis by GliT-specific IgG ELISA. 12th European Conference on Fungal Genetics (ECFG12). Seville, Spain, 23-27 March.

Moloney, N. M., Gordon, N., Manzanares, L., Billen, F., Hayes, N., Doyle, S. (2014) Detection of Aspergillosis by GliT-specific IgG ELISA. The 11th International Aspergillus Meeting (Asperfest11). Seville, Spain, 22 March.

Abbreviations

1-DE	1-dimensional gel electrophoresis
2-DE	2-dimensional gel electrophoresis
ABPA	Allergic bronchopulmonary aspergillosis
AIDS	Acquired immune deficiency syndrome
ALC	Average local confidence
AMB	Amphotericin B
APS	Ammonium persulphate
ART	Artemisinin
ATP	Adenosine triphosphate
BAL	Bronchoalveolar lavage
BmGT	Bis(methylthio)gliotoxin
BPS	Bathophenanthrolinedisulfonic acid disodium salt hydrate
BSA	Bovine serum albumin
CF	Cystic fibrosis
CGD	Chronic granulomatous disease
COPD	Chronic obstructive pulmonary disease
CSF	Caspofungin
DAD	Diode Array Detector
DAFC	Diacetylfusarinine C (ferri-diacetylfusarinine C unless otherwise stated)
$DAFC^{+Fe}$	Ferri-diacetylfusarinine C
$DAFC^{-Fe}$	Desferri-diacetylfusarinine C
DAUDA	11-([5-(dimethylamino)-1-naphthalenyl]sulfonylamino) undecanoic acid
DIGE	Difference gel electrophoresis
DMSO	Dimethyl sulfoxide
DTT	Dithiothreitol
EDC	1-ethyl- 3-(3-dimethylaminopropyl) carbodiimide
EDTA	Ethylenediaminetetraacetic acid
EIC	Extracted ion chromatogram
ELISA	Enzyme-linked immunosorbant assay

EORTC	European Organisation for the Research and Treatment of Cancer
Fab	Fragment antibody binding
FAD	Flavin adenine dinucleotide
FC	Ferricrocin
Fc	Fragment crystallisable
FDA	US Food and Drug Administration
FLD	Fluorescence Detector
FSC	Fusarinine C (ferri-fusarinine C unless otherwise stated)
FSC^{+Fe}	Ferri-fusarinine C
FSC^{-Fe}	Desferri-fusarinine C
FSC BD	Fusarinine C breakdown product
GAPDH	Glyceraldehyde 3-phosphate dehydrogenase
GM	Galactomannan
GO	Gene Ontology
GPI	Glycosylphosphatidylinositol
GST	Glutathione-S-transferase
GT	Gliotoxin
HAT	Hypoxanthine aminopterin thymidine
HEPES	4-(2-Hydroxyethyl) piperazine-1-ethanesulfonic acid, N-(2-Hydroxyethyl) piperazine -N′-(2-ethanesulfonic acid)
HFC	Hydroxyferricrocin
HG Buffer	HEPES-glucose buffer
HPLC	High performance liquid chromatography
HRCT	High resolution computerised tomography
HRP	Horse radish peroxidase
HSPs	Heat shock proteins
HT	Hypoxanthine thymidine
IA	Invasive Aspergillosis
IAA	Iodoacetamide
ITC	Itraconazole
iTRAQ	Isobaric tag for relative and absolute quantification
KLH	Keyhole limpet hemocyanin

LAL	Limulus ameboecyte lysates
LC	Light chain
LC-MS	Liquid chromatography mass spectrometry
LFQ	Label-free quantitative
m/z	Mass to charge
mAb	Monoclonal antibody
MAFC	Monoacetylfusarinine C (ferri-monoacetylfusarinine unless otherwise stated)
MALDI-ToF/ToF	Matrix assisted laser desorption/ ionisation-time of flight
MAPK	Mitogen-activated protein kinase
MEA	Malt extract agar
MFS	Major facilitator superfamily
MM	Minimal media
MS	Mass spectrometry
msa	Multiple sequence alignment
NAD+	Nicotinamide adenine dinucleotide
NADPH	Nicotinamide adenine dinucleotide phosphate
NBD	7-nitrobenz-2-oxa-1,3-diazole
NBD-X-SE	Succinimidyl 6-(N-(7-Nitrobenz-2-Oxa-1,3-Diazol-5-yl)Amino) Hexanoate
NCBI	National Center for Biotechnology Information
NHS	N-Hydroxysuccinimide
NRPS	Non-ribosomal peptide synthetase
OD	Optical density
ORF	Open reading frame
PAMPs	Pattern-associated molecular patterns
PBMCs	Peripheral blood mononuclear cells
PBS	Phosphate buffered saline
PBST	Phosphate buffered saline - Tween 20
PCR	Polymerase chain reaction
PEG	Polyethylene glycol
PET	Positron-emission tomography
qRT-PCR	Real-time polymerase chain reaction

RGD	Arginine-glutamic acid-aspartic acid
ROS	Reactive oxygen species
RP-HPLC	Reverse phase high performance liquid chromatography
RT	Retention time
SATA	*N*-succinimidyl-*S*-acetylthioacetate
SDS	Sodium dodecyl sulphate
SDS-PAGE	Sodium dodecyl sulphate-polyacrylamide gel electrophoresis
SITs	Siderophore iron transporters
SMCC	Succinimidyl-4-(*N*-maleimidomethyl)cyclohexane-1-carboxylate
SNA	Sulfo-NHS-Acetate
Sulfo-SMCC	Sulfosuccinimidyl-4-(*N*-maleimidomethyl)cyclohexane-1-carboxylate
TAFC	Triacetylfusarinine C (ferri-triacetylfusarinine C unless otherwise stated)
$TAFC^{+Fe}$	Ferri-triacetylfusarinine C
$TAFC^{-Fe}$	Desferri-triacetylfusarinine C
TBST	Tris buffered saline - Tween 20
TCA	Trichloroacetic acid
TFA	Trifluoroacetic acid
TfR1	Transferrin receptor 1
TIC	Total ion chromatogram
TMB	3,3', 5,5'-tetramethylbenzidine

Summary

Aspergillus fumigatus is a prevalent airborne fungal pathogen with the potential to cause Invasive Aspergillosis (IA) in susceptible hosts. Limited treatment and diagnostic options largely underlie the high mortality associated with IA. Like many human pathogens, *A. fumigatus* possesses sophisticated mechanisms for iron acquisition that are crucial to its virulence. Comparative proteomics revealed that iron starvation induced significant ($p < 0.05$) remodelling of the *A. fumigatus* secretome. A cell wall remodelling response was induced with significantly ($p < 0.0001$) decreased glucanase activity during iron starvation. The secretomic remodelling was relevant to host recognition, evident in the increased abundance of many immunogenic proteins. ELISA analysis also indicated significantly ($p < 0.0001$) increased immunoreactivity against proteins isolated from iron-starved growth using sera from the general population. This highlights the importance of iron-starved *A. fumigatus* in host interactions. During iron starvation *A. fumigatus* utilises extracellular siderophores, fusarinine C (FSC) and triacetylfusarinine C (TAFC), for iron uptake. Fluorescently derivatised siderophores were taken up by *A. fumigatus* during iron-starved growth, evidenced by the vacuolar fluorescence observed exclusively therein. In addition to informing on the fate of siderophores following uptake, this demonstrated an amine-based derivatisation strategy for *A. fumigatus* siderophores with other applications. Using this strategy, FSC and TAFC immunogens were synthesized for murine immunisations. These mice were then used to generate hybridomas producing anti-siderophore antibodies. Antibody production was verified using a novel competitive FSC or TAFC ELISA. An anti-FSC IgM was isolated and characterised. This IgM demonstrated the proteinaceous inhibition of siderophore-mediated iron uptake in *A. fumigatus in vitro*. An anti-TAFC IgG was also isolated and characterised. This IgG could detect low concentrations of TAFC within clinically relevant ranges in a competitive ELISA, indicative of its potential for implementation in a diagnostic assay. Using a proteogenomic strategy, putative N- and C-terminal sequences associated with this IgG were identified by MS to permit cDNA sequencing for further expression. Overall this work has comprised an application-driven exploration of iron-starved *A. fumigatus* and successfully yielded output for future diagnostic and therapeutic strategies against *A. fumigatus* infection.

Chapter 1

Introduction

Chapter 1 Introduction

1.1 *Aspergillus fumigatus* – saprophyte and pathogen

1.1.1 General characteristics of *A. fumigatus*

Aspergillus fumigatus is one of the most prevalent airborne fungal pathogens (Dagenais and Keller, 2009; Latgé, 1999; Owens *et al.*, 2014). Infection with *Aspergillus* species is termed Aspergillosis and worldwide there are estimated to be over 200,000 cases of life-threatening Aspergillosis in humans per year. Aspergillosis predominantly affects immunocompromised hosts and carries mortality rates from 30 – 95% (Brown *et al.*, 2012; Pianalto and Alspaugh, 2016). The most devastating manifestation of Aspergillosis is Invasive Aspergillosis (IA) and this is largely attributed to opportunistic infection with *A. fumigatus* (Abad *et al.*, 2010).

A. fumigatus is a saprophytic mould found in soil and decaying vegetation across wide pH (3.7 – 7.6) and temperature (12 – 65 °C) ranges. An ability to tolerate a range of environmental conditions and effectively produce robust airborne spores have contributed to the global distribution of *A. fumigatus* (Kwon-Chung and Sugui, 2013). The virulence factors that allow *A. fumigatus* to cause disease in susceptible hosts can be attributed to the same traits that allow it to thrive in its natural environment. These include: spore production, thermotolerance, secondary metabolite production, nutrient acquisition, stress tolerance and adaptability, and cell wall composition and maintenance (Abad *et al.*, 2010; Owens *et al.*, 2014). In particular, *A. fumigatus* employs sophisticated nutrient acquisition mechanisms to facilitate its survival in iron-starved environments (Haas, 2014). It can produce a plethora of bioactive secondary metabolites including compounds that function in iron acquisition, termed siderophores (Abad *et al.*, 2010; Owens *et al.*, 2014).

This Chapter will discuss recent studies that have advanced our understanding of *A. fumigatus* as a pathogen. In particular, it will focus on how studying the proteins expressed by *A. fumigatus* have informed on traits pertinent to its pathogenesis (Moloney *et al.*, 2016). Environmental cues within the host can carry significant phenotypic consequences for microbial pathogens. Following this, the adaptations of *A. fumigatus* to iron starvation, which is encountered within the host, will be discussed in light of their impact on virulence, as well as on diagnostic and therapeutic strategies.

1.1.2 *A. fumigatus* pathogenesis

A. fumigatus predominantly reproduces asexually; however, it has also been demonstrated to reproduce sexually (O'Gorman *et al.*, 2009). The asexual life cycle is comprised of several stages utilising different growth forms for development and dispersion. Firstly, condiophores developed during vegetative growth support the production of small (2 – 3 μm) haploid spores, termed conidia. These conidia are quite robust and can become easily airborne. Germination of conidia commences vegetative growth, whereby the fungus extends through hyphae forming a growing mass of mycelium. Ultimately, conidiophores again develop during vegetative growth for the release of conidia (Kwon-Chung and Sugui, 2013; Latgé, 1999; Ward *et al.*, 2005). Conidia produced by *A. fumigatus* are so small that they can penetrate the alveoli of the lungs. It is estimated that humans inhale several hundred conidia per day; however manifestation of disease is restricted to certain risk groups (Dagenais and Keller, 2009; Latgé, 1999). Host status represents the main factor in determining the pathogenicity of *A. fumigatus* (Abad *et al.*, 2010; Kwon-Chung and Sugui, 2013). In healthy individuals, inhaled conidia are rapidly cleared by the mucociliary escalator. Any conidia that escape this initial defence are subsequently cleared by

alveolar macrophages, neutrophils and a T cell-mediated response (Dagenais and Keller, 2009; Margalit and Kavanagh, 2015). However, when lung function or the immune system are compromised in some way, *A. fumigatus* can effect various forms of disease within the host (Latgé, 1999; Owens *et al.*, 2014).

In individuals with impaired lung function, including cystic fibrosis (CF) and asthma, *A. fumigatus* can invoke a hypersensitive allergic response and cause allergic bronchopulmonary aspergillosis (ABPA). Development of ABPA is associated with conidial germination and *A. fumigatus* colonisation. It is characterised by reduced lung function, *Aspergillus* skin reactivity, high IgE levels, and fungal infiltrates (Knutsen *et al.*, 2012). *A. fumigatus* can also cause hypersensitivity reactions in chronic obstructive pulmonary disease (COPD) patients. Non-invasive colonisation of the lung with aspergilloma, also termed "fungus-ball", can occur in pre-existing lung cavities, for example those resulting from tuberculosis infection. The aspergilloma comprises a mass of hyphae embedded in an extracellular matrix with proteins and host constituents. Surgical removal is often necessary (Latgé, 1999; Owens *et al.*, 2014). The most notorious manifestation of *A. fumigatus* disease is IA, carrying mortality rate of up to 95% in high-risk patient groups. Risk factors for IA include: chronic granulomatous disease (CGD), neutropenia, COPD, organ or haematopoietic stem-cell transplantation, corticosteroid therapy, haematological malignancy, and acquired immune deficiency syndrome (AIDS) (Baddley, 2011; Kousha *et al.*, 2011). In such cases, inhaled *A. fumigatus* conidia germinate, forming hyphae, which can invade the blood vessels and disseminate throughout the host. Lack of early diagnostic methods and limited treatment options are major factors underlying the morbidity of *A. fumigatus* related diseases.

1.1.3 Current diagnostic and therapeutic strategies for the treatment of Aspergillosis

1.1.3.1 Diagnosis of IA

The European Organisation for the Research and Treatment of Cancer (EORTC) has developed criteria for the diagnosis of invasive fungal infections, including Aspergillosis (De Pauw *et al.*, 2008). This outlined three subsets of IA including proven, probable, and possible. Proven IA classification requires positive culture from a normally sterile site and positive histopathological study. Probable IA classification requires patients with defined host factors that predispose individuals to Aspergillosis (e.g. neutropenia) to display clinical symptoms of the disease and show microbiological evidence of disease. In the absence of microbiological evidence, non-culture based diagnostic methods are also accepted for the diagnosis of probable IA (Walsh *et al.*, 2008). High resolution computerised tomography (HRCT) imaging of infection has also proven an extremely helpful investigational tool in the diagnosis of IA (Barton, 2013).

Histopathological confirmation of *A. fumigatus* infection can prove difficult, as *A. fumigatus* cannot be easily differentiated from other species, such as *Fusarium,* through tissue examination alone (Barton, 2013). Positive culture from the same tissue sample used for histopathology can provide a robust diagnosis of proven Aspergillosis. Culturing a patient-isolated specimen also permits further study, such as antifungal susceptibility testing. However, this method can take time, therefore, delaying diagnosis or treatment. In cases where tissue excision is contraindicated, non-culture based *in vitro* diagnostics can be particularly advantageous by providing a non-invasive method (Johnson *et al.*, 2014).

Two non-invasive diagnostic assays have been approved by the US Food and Drug Administration (FDA) utilising cell wall components (galactomannan (GM) and 1,3-β-D-glucan) as biomarkers of *A. fumigatus* infection (De Pauw *et al.*, 2008). The fungal cell wall is composed of a matrix of polysaccharides arranged above the cell membrane (Figure 1.1) (Gow *et al.*, 2017; Latgé, 2010). It is widely employed in current diagnostic and antifungal strategies for IA (Barton, 2013; Valiante *et al.*, 2015). Along with 1,3-β-glucan, 1,4-β-glucan and chitin, GM is found in the fungal cell wall and released from actively growing *A. fumigatus in vivo.* A monoclonal antibody (mAb) recognising the side residues of GM is implemented in the Platelia™ assay for the detection of GM in serum or bronchoalveolar lavage (BAL) samples (Barton, 2013). Though the assay is reported to be quite specific and sensitive, GM is also present in the cell walls of other fungi as well as some drug preparations which can lead to false positives (Barton, 2013). 1,3-β-D-glucan represents a major component of the fungal cell wall and, like GM, is released from growing *A. fumigatus*, but also found in the cell walls of many other fungal species (Barton, 2013; Free, 2013; Gow *et al.*, 2017). The principle of the 1,3-β-D-glucan assay is based on the activation of a serine protease coagulation cascade in *Limulus* amebocyte lysates (LAL). 1,3-β-D-glucan interacts with factor G in LAL to activate an enzyme that can cleave a chromogenic substrate to generate a coloured product detectable by spectrophotometry (Barton, 2013; Johnson *et al.*, 2014). Given that 1,3-β-D-glucan is present in the cell walls of many fungal species, this bioassay serves moreso as a pan-fungal biomarker of invasive infection and not a specific biomarker for Aspergillosis. In addition, PCR represents a potential non-invasive *in vitro* diagnostic strategy allowing the amplification of *A. fumigatus* specific DNA from patient samples; however lack of standardisation has excluded this method from the EORTC

diagnostic guidelines (Johnson *et al.*, 2014).

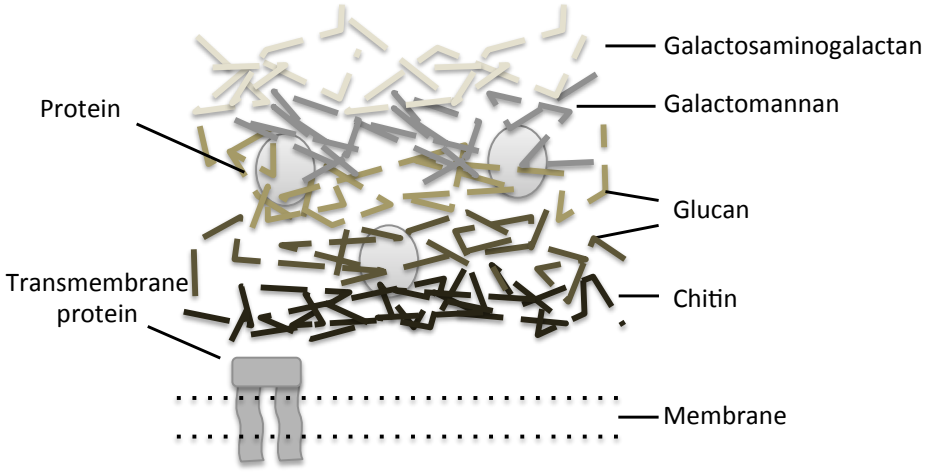

Figure 1.1 Schematic of the *A. fumigatus* cell wall. The cell wall is composed of a matrix of polysaccharides (chitin, glucan (1,3-α, 1,4-α, 1,3-β, and 1,4-β) galactomannan, and galactosaminogalactan) with embedded proteins atop a cell membrane composed largely of ergosterol. Components of the cell wall and membrane serve as common targets for currently implemented diagnostic therapeutic strategies against *A. fumigatus* infection (Gow *et al.*, 2017; Latgé, 2010; Valiante *et al.*, 2015).

1.1.3.2 Treatment of IA

There are currently three classes of antifungal drugs approved for treatment of Aspergillosis: polyenes, echinocandins, and azoles. These compounds all target components of the fungal cell wall or membrane *via* either ergosterol or β-1,3-glucan (Valiante *et al.*, 2015). Approved polyenes include amphotericin B (AMB) and its lipid formulations. AMB acts by binding ergosterol and forming pores in the cell membrane leading to cell death. AMB can have severe side effects in nephrotoxicity for the host (Pianalto and Alspaugh, 2016; Walsh *et al.*, 2008). Caspofungin (CSF) is the only approved echinocandin and targets cell wall integrity by inhibiting β-1,3-

glucan synthesis through the enzyme β-1,3-glucan synthase. This drug has limited host toxicity but is implemented as an alternative treatment for Aspergillosis in patients intolerant to other treatment methods (Pianalto and Alspaugh, 2016; Walsh *et al.*, 2008). Approved azoles include itraconazole, voriconazole, posaconazole, and isavuconazole. Azoles act by inhibiting the biosynthesis of ergosterol by blocking the final enzymatic step in ergosterol biosynthesis (Pianalto and Alspaugh, 2016; Valiante *et al.*, 2015). Voriconaozle is the primary antifungal recommended for treating infections in most patient groups (Walsh *et al.*, 2008). Isavuconazole is the most recent to be approved by the FDA for the treatment of Aspergillosis (Pianalto and Alspaugh, 2016). Resistance in *A. fumigatus* against azoles has been increasingly reported in recent years and there is evidence that the use of azoles in agriculture for the fungicidal treatment of crops has contributed to the spread of resistance (Warris, 2015).

There is a pressing requirement to develop new effective therapeutic and diagnostic strategies for the diagnosis and treatment of *A. fumigatus* infection (Barton, 2013; Moloney *et al.*, 2016). Significant efforts have been made to meet this goal in recent years. The following sections will discuss how proteomics has played a pivotal role in improving the understanding of *A. fumigatus* infection and response to treatment. A better understanding of a pathogen's phenotype during infection will expedite the development of targeted strategies to diagnose and treat disease.

1.2 Using proteomics to understand *A. fumigatus* infection and treatment

The virulence of *A. fumigatus* is multifactorial. Survival in its niche environment, where nutrient starvation, temperature fluctuations, and various stresses are encountered, has conferred it with a sophisticated adaptability. This adaptability to

harsh environments has translated into survival in susceptible hosts (Kwon-Chung and Sugui, 2013). The nature of its virulence means that a global investigation of the multi-faceted phenotype of *A. fumigatus* is necessary to understand it as a pathogen. Since the sequencing of the *A. fumigatus* genome, "omic" technologies have permitted this insight (Kniemeyer *et al.*, 2011; Nierman *et al.*, 2005). By analysing all of the proteins in an organism (proteome), mass spectrometry (MS)-based proteomic analysis can inform on its phenotype. A bottom-up approach is predominantly applied for the identification of fungal proteins (Doyle, 2011). In this approach proteins are digested into peptide fragments that are detected by MS (Figure 1.2). Several proteases can be used to carry out this process, but trypsin is most commonly used and cleaves peptides at the carboxyl side of lysine or arginine residues. Peptides are analysed by MS and their sequences identified using the resultant spectra. To identify their cognate protein, the sequences of these peptides are then aligned to *in silico* peptide databases from the appropriate species' proteome. Proteome databases for many species can be obtained from UniProt (http://www.uniprot.org/). For *A. fumigatus,* the *A. fumigatus* ATCC MYA-4609 (Af293) genome assembled by Nierman *et al.* (2016) is predominantly employed for sequences and identifiers. Protein identifiers are based on the open reading frame (ORF) identifier; for example, AFUA_2G07680 refers to locus number 07680 on chromosome 2 in *A. fumigatus* Af293.

Traditionally protein mixtures are separated by molecular mass alone (1-DE; 1-dimensional gel electrophoresis), or by their isoelectric point and molecular mass (2-DE; 2-dimensional gel electrophoresis), prior to in-gel digestion (Asif *et al.*, 2006; Carberry *et al.*, 2006; Kniemeyer *et al.*, 2006; Vödisch *et al.*, 2009). However, recent advances in shotgun proteomics allows for analysis of total protein content in a

complex peptide mixture without gel-based separation. If necessary, pre-fractionation of proteins or peptides can be carried out to reduce sample complexity and improve limits of detection (Washburn *et al.*, 2001; Yates *et al.*, 2009; Zhang *et al.*, 2013). Fractionation according to specific properties can provide further insight into a proteome. Shotgun proteomics has facilitated analysis of proteins previously intractable to 2-DE, such as membrane proteins, through gel-free approaches (Moloney *et al.*, 2016a; Ouyang *et al.*, 2010). However, 2-DE still plays an important role in analysing post-translational modifications and the immunoproteome (Asif *et al.*, 2010; Gautam *et al.*, 2007; Kumar *et al.*, 2011; Shi *et al.*, 2012a; Singh *et al.*, 2010a, 2010; Teutschbein *et al.*, 2016; Virginio *et al.*, 2014).

Since early global analysis of the *A. fumigatus* proteome provided reference maps (Asif *et al.*, 2006; Carberry *et al.*, 2006; Kniemeyer *et al.*, 2006; Vödisch *et al.*, 2009), MS-based proteomics has yielded significant insight into the phenotype of the organism under a variety of conditions. The following sections in this Chapter will focus on recent work that has utilised proteomics to provide new information on *A. fumigatus* relevant to infection and treatment (Moloney *et al.*, 2016).

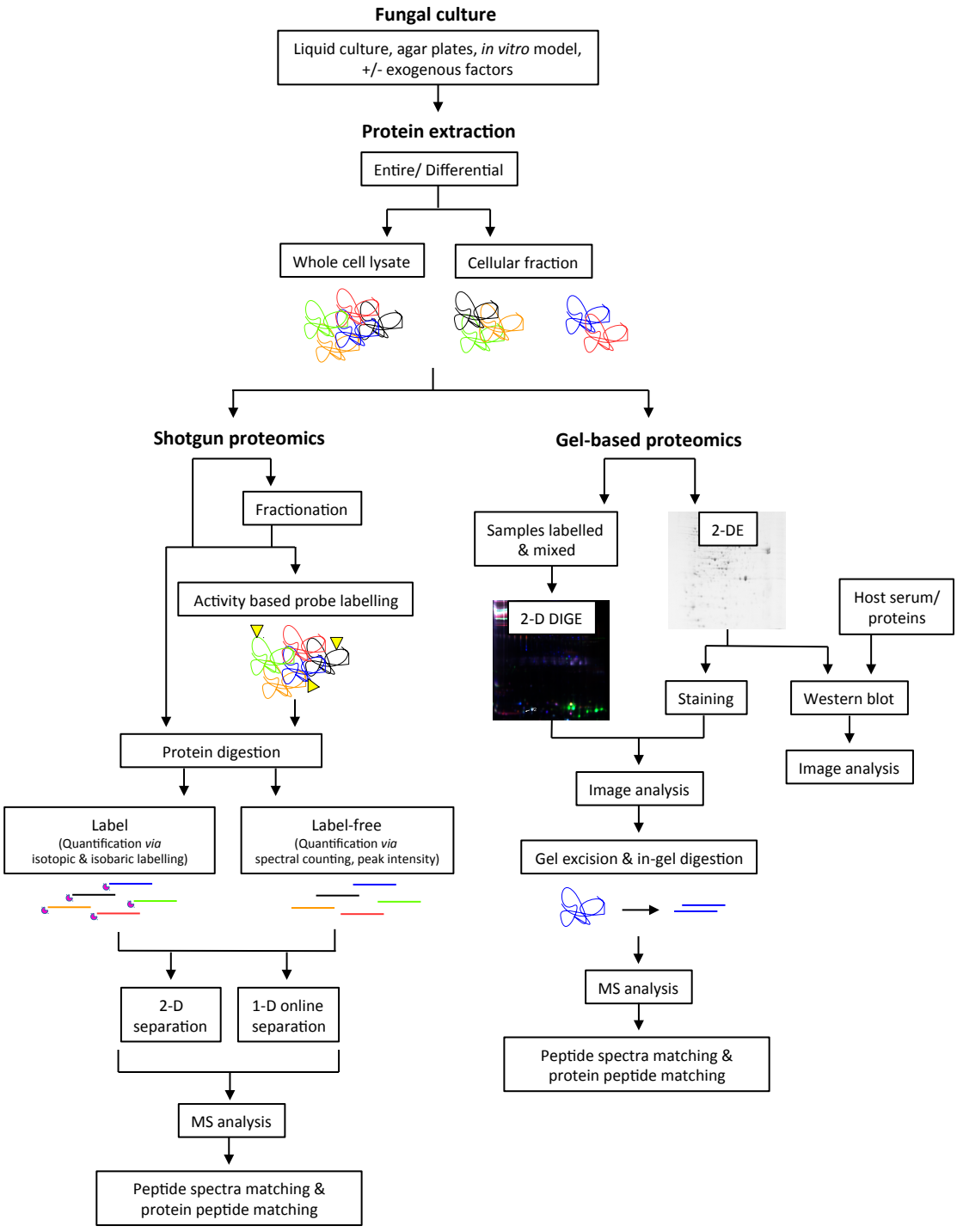

Figure 1.2 Workflow used for recent proteomic studies in *A. fumigatus*. *A. fumigatus* is cultured according to experimental requirements (liquid culture, agar plates, or *in vitro* model). Once extracted, whole cell lysates or subcellular fractions can be used in shotgun (gel-free) or gel-based proteome analysis. For shotgun proteomics, proteins can be subjected to direct enzymatic proteolysis, or first further

fractionated or probed for activity. Labeled shotgun proteomics can take the form of metabolic labels implemented at culturing, isotopic labels implemented during digestion, or isobaric labels implemented after digestion. Peptides are then analysed by MS with or without further online fractionation. For gel-based proteomics, extracted proteins can be separated by 2-DE followed by staining or transfer to membranes for host reactivity studies. Alternatively, extracted proteins can be labeled and mixed for 2-D DIGE (difference gel electrophoresis) analysis. Protein spots from 2-DE or 2-D DIGE can then be excised for in-gel proteolysis and peptides subsequently analysed by MS. MS analysed peptides are identified by peptide-spectra matching and subsequently matched to proteins using database interrogation. Figure taken and adapted from Moloney *et al.* (2016), Proteomic analysis of *Aspergillus fumigatus* - clinical implications. *Expert Review of Proteomics*, 13 (7), 635-649. DOI: dx.doi.org/10.1080/14789450.2016.1203783

1.2.1 The dynamic proteome of early development

Proteomic characterisation of *A. fumigatus* conidia at different stages of early development has revealed it to be highly dynamic (Cagas *et al.*, 2011b; Kubitschek-Barreira *et al.*, 2013; Suh *et al.*, 2012; Teutschbein *et al.*, 2010). Early work comparing resting conidia with mycelia by 2-DE with liquid chromatography mass spectrometry (LC-MS/MS) or matrix assisted laser desorption/ ionisation-time of flight (MALDI-ToF/ToF) peptide identification provided the first global insight into the conidial proteome (Asif *et al.*, 2006; Teutschbein *et al.*, 2010). However, the limitations of 2-DE in detecting low abundance proteins and resolution can make this work challenging and cumbersome. Recent work has used quantitative shotgun proteomics to provide a detailed insight into stage-specific proteomic events relevant to early host colonisation (Cagas *et al.*, 2011b; Suh *et al.*, 2012). Cagas *et al.* (2011b)

used labelled quantitative proteomics (isobaric tag for relative and absolute quantification (iTRAQ)) with MALDI-ToF/ToF detection, while in a subsequent study, Suh *et al.* (2012) used label-free quantitative analysis with LC-MS/MS to identify proteins with differential abundance over the course of early development.

Suh *et al.* (2012) identified 375 different proteins in developing conidia across several time points (0 h, 4 h, 6 h, and 8 h post-inoculation), including several proteins previously not identified in conidia (Asif *et al.*, 2006; Cagas *et al.*, 2011b; Singh *et al.*, 2010; Teutschbein *et al.*, 2010). One hundred and forty-three proteins were detected in all time points, many of which were conserved in other fungi. Proteins enriched in dormant conidia included Pep2 (AFUA_3G11400) and ConJ (AFUA_6G03210). Pep2 is a surface associated endopeptidase with increased abundance under hypoxia, it is also transcriptionally up-regulated following contact of conidia with neutrophils (Asif *et al.*, 2006; Sugui *et al.*, 2008; Teutschbein *et al.*, 2010; Vödisch *et al.*, 2009, 2011). ConJ is transcriptionally up-regulated during early murine infection (McDonagh *et al.*, 2008). The function of ConJ is not yet elucidated in *A. fumigatus*; however a homolog in *A. nidulans* has been implicated along with another Con protein in germination (Suzuki *et al.*, 2013). Several heat shock proteins (HSPs) were also enriched in resting conidia including Scf1 (AFUA_1G17370). In accordance with other studies, a superoxide dismutase, SodB (AFUA_4G11580), was also abundant in dormant conidia (Teutschbein *et al.*, 2010). In expanding conidia (4 h post-inoculation), 85 proteins showed increased abundance compared with dormant conidia including several immunoreactive proteins: Wos2/ Sba1 (AFUA_5G13920), as well as allergens, Aspf8 (AFUA_2G10100) and Aspf3 (AFUA_6G02280) (Asif *et al.*, 2010; Knutsen *et al.*, 2012). Cell wall proteins were also enriched, indicative of the functional cell wall remodelling that occurs during early germination. These

proteins included the antigenic β-1,3-endoglucanase EglC (AFUA_3G00270) (Kumar *et al.*, 2011), and Ecm33 (AFUA_4G06820) which has roles in antifungal tolerance and germination (Romano *et al.*, 2006). In hyphae with early germ tubes (6 h post-inoculation), 127 proteins showed increased abundance compared with dormant conidia including proteins shown to be transcriptionally up-regulated during early stages of murine infection including: thiazole biosynthetic protein ThiF (AFUA_6G08360), pyridoxine biosynthetic protein PyroA (AFUA_5G08090) and a pyruvate carboxylase (AFUA_4G07710) (McDonagh *et al.*, 2008). Many of the proteins enriched at 6 h were also detected at 8 h, including superoxide dismutase, SodA (AFUA_5G09240) and glucanase, BtgE (AFUA_8G05610), which are also transcriptionally up-regulated during murine infection (McDonagh *et al.*, 2008). Collectively, this has indicated the proteome of *A. fumigatus* during early development to be extremely dynamic with significant modifications occurring within the first 8 h. The enrichment of cell wall and stress proteins illustrates the dynamic remodelling and robust stress tolerance required of *A. fumigatus* conidia in the early stages of development (Suh *et al.*, 2012; Teutschbein *et al.*, 2010). The relevance of this proteome to infection is apparent based on the presence of proteins implicated in host recognition and virulence.

Given their proximity, the cell surface proteome of *A. fumigatus* during early development is pertinent to interactions with the host. In a study analysing changes in the cell surface during morphogenesis, the surface proteome of germlings (6 h post-inoculation) was compared to that of hyphae (72 h post-inoculation) (Kubitschek-Barreira *et al.*, 2013). Proteins transiently linked to the cell wall or *via* disulphide bonds were extracted. Viability and cell wall integrity was monitored to ensure membrane leakage and intracellular material from dead cells did not account for

proteins in extracts. Biotinylation of cell surface proteins prior to extraction and Western blot comparison with sodium dodecyl sulphate-polyacrylamide gel electrophoresis (SDS-PAGE) indicated no additional non-biotinylated intracellular proteins were present, thereby validating the methodology employed. Using 2D-DIGE with MALDI-ToF/ToF, 39 differentially abundant proteins were identified including proteins involved in metabolism, translation, defence and transport. Translation elongation factor, eEF3 (AFUA_7G05660) was found to be abundant on the surface of germlings but not hyphae. In *Cryptococcus neoformans* eEF3 interacts with the calcium channel, Cch1 at the plasma membrane (Liu and Gelli, 2008). As calcium is important for several cellular activities and eEF3 is not present in mammalian cells, eEF3 was proposed as a possible drug target. Interestingly, eEF3 was also identified as antigenic exclusively in patients with proven Aspergillosis so it may also represent a biomarker of early infection (Virginio *et al.*, 2014). Two putative adhesins, enolase/ Aspf22 (AFUA_6G06770) and glyceraldehyde 3-phosphate dehydrogenase (GAPDH; AFUA_5G01970), were identified from the cell-surface proteome using the fungal adhesion prediction algorithm FungalRV (Chaudhuri *et al.*, 2011). Both proteins are glycolytic enzymes and showed increased abundance in hyphae. GAPDH has been implicated in host adhesion in other species (Gozalbo *et al.*, 1998; Kinoshita *et al.*, 2008) while enolase is an allergen and has been identified among antigens expressed during IA (Denikus *et al.*, 2005). Despite having an intracellular function, surface presentation of enolase has recently been confirmed in several fungi including *A. fumigatus* using immunostaining (Funk *et al.*, 2016). As it lacks a secretory signal peptide, its non-classical secretion mechanism awaits elucidation. However, export of enolase in *Saccharomyces cerevisiae* is dependent on a N-terminal sequence including residues which are highly conserved in other fungi and thus may underlie an

export mechanism (Funk *et al.*, 2016). Comprehensive profiling of the cell-surface proteome during development has yet to be achieved, since the extraction method by Kubitschek-Barreira *et al.* (2013) did not release proteins covalently linked to carbohydrates in the cell wall, such as glycosylphosphatidylinositol (GPI)-linked proteins that are anchored in the membrane. Also, despite using an alkali extraction method, Suh *et al.* (2012) did not successfully enrich for cell wall-associated proteins based on the abundance of intracellular proteins.

The dramatic remodelling undertaken by conidia during early development is concomitant with de-masking of cell wall hydrophobin, RodA (AFUA_5G09580), and exposing pattern-associated molecular patterns (PAMPs) such as β-(1,3)-glucan, which are recognised by the host (Aimanianda *et al.*, 2009; Lee and Sheppard, 2016). Polysaccharides, including glucans such as β-1,3-glucan and α-1,3-glucan, account for a large proportion of the conidial and hyphal cell wall (Figure 1.1). Deletion of the genes (*Δags1Δags2Δags3* /*Δags*) responsible for α-1,3-glucan synthesis resulted in severely attenuated virulence *in vivo* in an immune-competent and immunocompromised murine model (Beauvais *et al.*, 2013). *Δags* conidia were also phagocytosed more efficiently by murine alveolar macrophages *in vitro*. Atomic force microscopy indicated the presence of an indeterminate material covering *Δags* conidia; however similar levels of RodA protein were isolated from *Δags* and wild-type. Interestingly, SDS-PAGE and 2-DE with MALDI-ToF/ToF analysis identified a layer of glycoproteins exclusively in NaCl extracts from *Δags* conidia. Exposure of alveolar macrophages to this extract stimulated TNFα production. In addition, there was increased expression of polysaccharide PAMPS on the surface of swollen *Δags* conidia. The authors concluded that deletion of *ags1, ags2* and *ags3* caused significant structural rearrangements of the cell wall resulting in the matrix of

glycoproteins masking the rodlet layer in the resting conidia and increased PAMP exposure in germinating conidia. This in turn, prompted rapid immunological detection and clearance of *Δags in vivo*. This work highlights the importance of cell wall carbohydrates in the conidial surface proteome and their role in evading early immune recognition during host colonisation.

1.2.2 Fungal adhesin proteins

Adhesion to host cells represents an important point in the initiation and maintenance of infection. Inhaled conidia can adhere to the mucus lining, respiratory epithelium and alveolar macrophages. Following evasion of macrophage killing and germination, invasive hyphae continue to adhere to host proteins and surface constituents. The fungal carbohydrates and proteins at the cell wall that mediate this process are referred to as adhesins (de Groot *et al.*, 2013; Latgé, 2010; Sheppard, 2011). Most fungal adhesin proteins contain a C-terminal GPI anchor to the plasma membrane, a glycosylated serine/ threonine rich domain and a N-terminal domain that mediates ligand binding (Chaudhuri *et al.*, 2011; de Groot *et al.*, 2013). Characterising host adherence mechanisms in *A. fumigatus* is warranted, as impeding this process represents a potential therapeutic strategy to prevent and/or treat infection.

Using bioinformatic analyses, Upadhyay *et al.* (2009) identified putative protein adhesins in *A. fumigatus* based on their amino acid sequence. Proteins (n = 82) were assigned a 'probability of being adhesin' (P_{ad}) value of greater than 0.9 (Upadhyay *et al.*, 2009). Cell wall protein, AfCalAp (AFUA_3G09690), with a P_{ad} = 0.94, was selected for further study. AfCalAp was found to be present on the surface of swollen conidia and to have affinity for laminin and murine lung cells (Upadhyay *et al.*, 2009). In a subsequent study, Upadhyay *et al.* showed that secreted proteins

could increase binding of conidia to the extracellular matrix (Upadhyay *et al.*, 2012). Proteins were analysed by 2-DE, and Western blot using biotinylated fibrinogen, with MALDI-ToF/ToF identification. Seven proteins with fibrinogen binding activity were identified using this approach. Proteins included pectate lyase A (PlyA; AFUA_2G00760), which had not previously been implicated in adhesion, and predicted cell wall protein β-glucosidase A (BglA/ Exg12; AFUA_1G05770) (Upadhyay *et al.*, 2012). Using a similar approach with the aim of positing a therapeutic strategy, *A. fumigatus* secreted proteins were extracted for murine immunisations and mAb development (Kumar and Shukla, 2015). Interestingly, an isolated mAb showed binding to several extracellular proteins by Western blot. After de-glycosylation of protein extracts, no binding was observed indicating the mAb was active against a glycoprotein carbohydrate moiety. Immunofluorescence indicated the presence of the mAb target antigen on the surface of conidia and hyphae. Importantly, the mAb had anti-adhesive properties *in vitro*, reducing adhesion of *A. fumigatus* conidia to fibronectin-coated plates by 70% (Kumar and Shukla, 2015). The efficacy of this mAb as a therapeutic strategy remains to be elucidated *in vivo*, but the inhibition of conidial host adhesion presents a plausible clinical application.

Fucose-specific lectin (FleA; AFUA_5G14740) was detected in the immunosecretome of *A. fumigatus* extracellular proteins probed with ABPA patient sera (Singh *et al.*, 2010a). FleA was subsequently identified in protein extracts of an *A. fumigatus* strain isolated from a cancer patient based on hemagglutination activity against rat erythrocytes (Kuboi *et al.*, 2013). Houser *et al.* (2013) characterised FleA in detail and showed the protein to have strong binding affinity for the host carbohydrate, fucose. Immunostaining indicated the presence of FleA predominantly on the surface of conidia and not hyphae. Fucose is found on the surface of many

human cells and therefore, FleA was postulated to aid initial conidial attachment to lung epithelium (Houser *et al.*, 2013). Recently, Kerr *et al.* (2016) showed that binding to mucin and macrophages is FleA-dependent. Deletion of FleA actually resulted in reduced macrophage phagocytosis and increased lung invasion in an immune-competent murine model. Hence, FleA is in fact likely not a virulence factor but a PAMP important in early host recognition of inhaled conidia (Kerr *et al.*, 2016).

The role of proteins in the adhesion of *A. fumigatus* to host cells has been further revealed using proteomics as well as other analytical techniques. However, their position as virulence factors may not be so clear cut, as elucidation of FleA functionality has shown. Furthermore, post-translational modification, in the form of protein glycosylation, has emerged as an important factor in some adhesins' functionality. Further dissection of early molecular events at the host-pathogen interface is warranted to fully understand the role of proteins in host adherence. Recent methodological advances in the recovery of membrane proteins can help facilitate this characterisation by also enabling in-depth investigations of membrane-associated adhesins (Ouyang *et al.*, 2010).

1.2.3 The secretome and proteases

Along with cell surface proteins, the secretome of *A. fumigatus* represents a focal point of the host-pathogen interface comprising various enzymes, adhesins and toxins (Osherov, 2007; Owens *et al.*, 2014). The relevance of this in host recognition is exemplified by immunoproteomic analysis which indicate the presence of many proteins reactive with IgG and IgE from ABPA, IA and aspergilloma patients (Gautam *et al.*, 2007; Kumar *et al.*, 2011; Shi *et al.*, 2012a; Singh *et al.*, 2010a). Wartenberg *et al.* (2011) comprehensively described the secreted proteome of *A.*

fumigatus grown on host-relevant substrates elastin, keratin and collagen. A protease, Alp1/ Aspf13 (AFUA_4G11800), was highly abundant following growth on protein substrates and identified as a major secreted protease. In addition to other physiological roles, an ability to hydrolyse peptides means proteases are an important family of proteins in fungi with respect to substrate degradation. Given the ease of extraction and their position at the host-pathogen interface, extracellular proteases are the best studied and many have proven to be allergenic (Yike, 2011). The secretion of allergenic proteins is particularly important in the manifestation of ABPA. In an attempt to dissect the conditions regulating their secretion, Farnell *et al.* (2012) characterised the proteolytic response of *A. fumigatus* to growth on several substrates including casein, mucin and pig lung. Extracellular proteins were separated by size exclusion chromatography, screened for proteolytic activity and analysed by SDS-PAGE with LC-MS/MS identification. The protein substrate used was found to impact the levels of protease activity, whereby growth on pig lung led to higher protease activity than that on casein, mucin or the control. The predominant class of protease also varied depending on the growth substrate. A proteolytic profile of predominantly metalloproteases, including Lap1 (AFUA_3G00650) and Mep/ Aspf5 (AFUA_8G07080), was induced on casein. Conversely, growth in pig lung favoured serine proteases, including Alp1/ Aspf13 (Farnell *et al.*, 2012), which has recently been implicated in airway hyper-responsiveness in asthma patients (Balenga *et al.*, 2015; Namvar *et al.*, 2015). Complement degrading activity for Alp1 has also been demonstrated, implicating proteases in pathogenesis (Behnsen *et al.*, 2010). By virtue of their ability to degrade macromolecules, a role for proteases in the virulence of pathogenic fungi seems plausible. However, their position as a virulence factor remains controversial. Gene deletion studies have yet to demonstrate their role in

virulence. For example, deletion of Alp1 or positive transcriptional regulator of secreted proteases PrtT did not attenuate virulence in a murine model (Behnsen *et al.*, 2010; Bergmann *et al.*, 2009; Sharon *et al.*, 2009). A proteomic and transcriptomic characterisation of Δ*prtT* indicated reduced abundance of several proteases in the secretome (Hagag *et al.*, 2012). Surprisingly, genes involved other functions such as secondary metabolism were also affected, indicating involvement of PrtT in a more complex regulatory network. Moreover, with increased expression of genes and abundance of proteins not found in wild-type, such as polysaccharide degrading enzymes, the authors speculated that the lack of virulence attenuation in Δ*prtT* may have been due to a compensatory phenotype in the mutant (Hagag *et al.*, 2012). In addition, recent work demonstrated that enolase can bind the proteolytic host protein, plasminogen, leading these authors to speculate that a commandeering of host proteolytic mechanisms may also account for tissue invasion observed in the *prtT* null strain (Funk *et al.*, 2016). Thus, the role of secreted proteases in virulence awaits unambiguous elucidation. Together, recent work has profiled the secreted proteome relevant to host colonisation and revealed mechanisms of regulation; however further work is required to improve treatment for the allergic responses associated with *A. fumigatus*.

1.2.4 The biofilm proteome

After conidial germination into hyphae, *A. fumigatus* produces an extracellular matrix, which surrounds hyphae growing in a biofilm. This extracellular matrix is composed of polysaccharides, melanin, proteins and extracellular DNA. Biofilm formation has been implicated in protection from host defences *in vivo* and significantly decreased susceptibility to antifungals (Kaur and Singh, 2014). An understanding of biofilm formation in *A. fumigatus* has only begun to emerge in recent years and proteomic

analysis serves a major tool in investigating this growth form that is highly relevant to infection. Using an *in vitro* biofilm model, Bruns *et al.* (2010) carried out a proteomic and transcriptomic characterisation of *A. fumigatus* during biofilm development compared with planktonic growth. *A. fumigatus* was grown for 24 and 48 h and proteins were extracted from mycelia. Nine proteins with differential abundance between the two growth forms were identified using 2D-DIGE with MALDI-ToF/ToF. In a similar study, 25 proteins were identified with differential abundance between the two growth states (Muszkieta *et al.*, 2013). Proteins involved in the tricarboxylic cycle, protein degradation and amino acid biosynthesis were among those with differential abundance. Interestingly, members of the gliotoxin biosynthetic gene cluster, glutathione *S*-transferase (GliG; AFUA_6G09690) and gliotoxin oxidoreductase (GliT; AFUA_6G09740) showed increased abundance during biofilm-growth (Bruns *et al.*, 2010). Induction of the gliotoxin biosynthetic gene cluster (Dolan *et al.*, 2015; Gardiner and Howlett, 2005) was verified with increased transcription of cluster members in microarray analysis and RT-PCR. Additionally, high performance liquid chromatography (HPLC) and LC-MS analysis of supernatants showed significantly higher levels of gliotoxin during biofilm-growth. Gliotoxin is a well-characterised redox-active metabolite with significantly deleterious effects on mammalian cells (Dolan *et al.*, 2015). It is regarded as an important factor contributing to the virulence of *A. fumigatus*; hence its increased production during biofilm-growth is highly relevant to infection. While, the proteomic and transcriptomic induction of the gliotoxin cluster during biofilm growth was correlated, overall there was little correlation between the two analytical formats. The authors speculated that biomolecule longevity and intrinsic differences in the analytical techniques likely underlie this. Miscorrelation such as this also indicates

that more experimental investigation of these states is required. Moreover, given the clinical relevance of the results thus far, further investigation of biofilm growth is certainly warranted.

1.2.5 The proteomic response to host-relevant stresses

1.2.5.1 Hypoxia

Even in healthy individuals, oxygen levels drop from 21% in the atmosphere to 14% in lung alveoli and as low as 2% in tissue. Such limited oxygen means that during colonisation *A. fumigatus* encounters hypoxia in the host (Grahl *et al.*, 2011). Risk groups for *A. fumigatus* colonisation such as COPD and CF patients can also experience further decreased oxygen levels in the lungs and alveolar hypoxia (Baddley, 2011; Kamath *et al.*, 2015; Tuder *et al.*, 2007). Moreover, during infection inflammation and necrosis can further restrict oxygen availability. Hence adaptation to hypoxia is likely an important trait for human pathogens. Recently, significant efforts to characterise *A. fumigatus* in response to hypoxia have been made. Proteomic analysis *via* 2D-DIGE coupled with MALDI-ToF/ToF detection has served as a major analytical tool in these studies and revealed adaptations relevant to the host-pathogen interface. Proteins involved in glycolysis, the tricarboxylic cycle, secondary metabolism and respiration were among those with differential abundance under hypoxic stress (Barker *et al.*, 2012; Vödisch *et al.*, 2011).

During hypoxia, lack of oxygen as the terminal electron acceptor of the electron transport chain in aerobic respiration prompts many microorganisms to utilise fermentation for supply of nicotinamide adenine dinucleotide (NAD^+) to adenosine triphosphate (ATP) generation *via* glycolysis. Hence, utilisation of fermentative strategies *in vivo* may be implemented when hypoxia is encountered.

Under short-term exposure to hypoxia, increased abundance of proteins PdcA (AFUA_3G11070) and AlcA (AFUA_7G01010) was observed. These proteins are involved in the conversion of pyruvate to ethanol indicating that fermentation is utilised under hypoxia (Barker *et al.*, 2012). In contrast, there was no evidence for fermentation in proteomic analysis of *A. fumigatus* under long-term hypoxic stress (Vödisch *et al.*, 2011). However, the latter work used glucose-depleted chemostatic culture conditions which may account for this lack of fermentation (Grahl *et al.*, 2012). PdcA is antigenic, indicating its synthesis at the host-pathogen interface (Teutschbein *et al.*, 2016). Moreover, recovery of ethanol from the lungs of infected mice provides evidence for the use of fermentation *in vivo* (Grahl *et al.*, 2011). While abrogation of ethanol production in *A. fumigatus* did not alter mortality in three immunologically distinct murine models, reduced fungal burden and increased inflammatory responses were observed in an alcohol dehydrogenase III (AlcC; AFUA_5G06240) deletion mutant. Thus, there is evidence to suggest the utilisation of fermentation *in vivo* during infection as a result of hypoxia.

Proteomic analysis has also revealed hypoxia-induced secondary metabolite production with members of the biosynthetic gene cluster for pseurotin A showing increased abundance under hypoxia (Vödisch *et al.*, 2011). This low oxygen-induced production was confirmed *via* reverse phase high performance liquid chromatography (RP-HPLC) analysis of culture extracts and Northern blot. Additionally, real-time polymerase chain reaction (qRT-PCR) indicated transcription of the pseurotin A biosynthetic cluster genes in lungs of infected mice. Pseurotin A has been shown to inhibit IgE activity and possess low cytotoxicity activity against lung fibroblasts (Ishikawa *et al.*, 2009; Schmeda-Hirschmann *et al.*, 2008). With induction *in vivo* during hypoxia, the immunomodulatory capacity of this secondary metabolite may aid

the pathogenesis of *A. fumigatus*. Interestingly, in an example of secondary metabolite cross-talk, deletion of *gliT* resulted in decreased expression of pseurotin A biosynthetic enzymes upon exposure to exogenous gliotoxin, and reduced production of pseurotin A relative to the wild-type (O'Keeffe *et al.*, 2014). The role of secondary metabolites, such as pseurotin A and gliotoxin, in *A. fumigatus* infection is not significantly addressed in this Chapter, but is well reviewed elsewhere (Dolan *et al.*, 2015; Heinekamp *et al.*, 2013; Owens *et al.*, 2014; Scharf *et al.*, 2014; Sheridan *et al.*, 2014).

Hypoxia-induced oxidoreductase (HorA; AFUA_4G09810) was initially identified in the proteome *A. fumigatus* conidia and subsequently shown to be increased during hypoxia (Barker *et al.*, 2012; Teutschbein *et al.*, 2010). Recent characterisation showed HorA to be localised to mitochondria and suggested a role in coenzyme Q biosynthesis (Kroll *et al.*, 2016). Decreased abundance of proteins involved in oxidative stress tolerance mechanisms was indicated by proteomic analysis of Δ*horA*. Impaired complex I activity as a result of coenzyme Q10 deficiency resulting in lower reactive oxygen species (ROS) generation may have accounted for this response. Δ*horA* also showed severely attenuated virulence in murine infection models. Importantly, HorA is a fungal-specific protein and therefore an intriguing target for novel antifungal therapy development (Kroll *et al.*, 2016). Thus, oxygen deprivation *in vivo* has emerged as an important factor within the host microenvironment. Recent proteomic analysis has shed light on the responses of *A. fumigatus* to hypoxia and revealed specific molecular adaptations undertaken by the fungus that are relevant to infection. Moreover, this insight has revealed putative drug targets specific to fungi.

1.2.5.2 Iron starvation

Iron is an essential element in all eukaryotes and therefore embedded in many biological processes. By virtue of its ability to exist in two oxidative states (Fe^{2+} and Fe^{3+}) iron can also prove deleterious in excess, through the generation of ROS *via* the Fenton and Haber-Weiss reactions (Halliwell and Gutteridge, 1984). Hence, iron-requiring organisms have developed tight regulatory systems for maintaining iron homeostasis. In fungi tight control of iron uptake is believed to largely underlie the iron homeostasis (Haas *et al.*, 2008). As with oxygen, limited supply of iron within the host represents a significant stress on invading pathogens. Restriction of iron by host elements to negate deleterious by-products means that free iron levels in humans are very low. Moreover, upon microbial challenge, the bioavailability of iron is further restricted due to an up-regulation of host iron-sequestering mechanisms in a form of 'nutritional immunity' (Cassat and Skaar, 2013). Consequently, invading microorganisms encounter an iron-starved environment during infection. The role of iron in infection will be discussed further in Section 1.3.1.

Iron starvation induces significant proteomic remodelling in *A. fumigatus.* This is evident in recent work by Mulvihill *et al.* (2017) whereby 806 proteins increased in abundance while 518 decreased in abundance in response to iron starvation. Sophisticated regulatory mechanisms in *A. fumigatus* orchestrate this adaptive response to iron starvation (Haas, 2014). This is principally mediated by the transcription factors, SreA and HapX (Haas, 2012). During iron starvation, HapX is activated and induces high affinity iron uptake systems and represses iron-consuming pathways. In contrast, during iron sufficiency, SreA is activated to repress high affinity iron uptake systems. These transcription factors also function in a negative feedback-loop, whereby HapX represses SreA expression and SreA represses HapX

expression (Haas, 2012). High affinity iron uptake systems in *A. fumigatus* include the production of low molecular mass ferric iron (Fe^{3+}) chelators, termed siderophores (Reiber *et al.*, 2005). These are secreted by *A. fumigatus in vivo* and are essential to virulence (Hissen *et al.*, 2005; Petrik *et al.*, 2010a, 2012; Schrettl *et al.*, 2004). Uptake of ferri-siderophores is mediated by a family of fungal-specific membrane transporters; siderophore iron transporters (SITs). Targeting of siderophore uptake *via* SITs represents a promising antifungal strategy, but requires further dissection (Lamb, 2015; Miethke and Marahiel, 2007).

Recently, the iron-starved microsomal proteome of *A. fumigatus* was characterized (Moloney *et al.*, 2016a). Mycelial lysates were successfully enriched for membrane proteins *via* cellular fractionation with ultracentrifugation (Ouyang *et al.*, 2010). By utilising label-free quantitative (LFQ) proteomic analysis of the microsomal cellular fraction, issues with 2-DE resolution of membrane proteins were bypassed. Microsomal proteins (n = 231) with differential abundance were detected and 96 showed increased abundance. Among these proteins were several putative transmembrane transporters, several of which were implicated in either siderophore uptake or biosynthesis in subsequent studies. Sit1 (AFUA_7G06060) was shown to be involved in the uptake of siderophores, ferrichrome and ferrioxamine B, while Sit2 (AFUA_7G04730) in the uptake of ferrichrome only (Park *et al.*, 2016). MirC (AFUA_2G05730) was implicated in the biosynthesis of intracellular *A. fumigatus* siderophore, ferricrocin (Mulvihill *et al.*, 2017). Deletion of *mirC* also resulted in decreased virulence in the model organism, *Galleria mellonella,* exemplifying the importance of iron homeostasis to virulence. Moloney *et al.* (2016b) also demonstrated that sera from healthy individuals showed higher IgG reactivity against microsomal proteins grown under iron starvation. This highlights the frequency of

normal host interaction with the *A. fumigatus* microsomal proteome and relevance of iron starvation therein.

1.2.6 Immunoproteome studies

Immunoproteomic studies have been extensively employed in a bid to identify novel clinically applicable, biomarkers of *A. fumigatus* infection. These studies typically involve the extraction of mycelial or secreted proteins following culture. Proteins are separated by 1-DE or 2-DE and subsequently transferred to nitrocellulose membranes. The membranes are then probed with sera from different patient groups (ABPA patients, high risk patients groups, proven or probable IA patients) or control sera.

Using this approach, GliT was identified as immunoreactive using IA patient sera (Shi *et al.*, 2012a). GliT was first shown to be immunoreactive with IgG from normal human sera in 2010 (Schrettl *et al.*, 2010b). Subsequently, an indirect ELISA for the detection of anti-GliT antibodies was shown to be effective for the diagnosis of IA in animal models (Shi *et al.*, 2012b). Many studies on the immunoproteome of *A. fumigatus* have utilised patient sera pools (Gautam *et al.*, 2007; Kumar *et al.*, 2011; Shi *et al.*, 2012a; Singh *et al.*, 2010; Virginio *et al.*, 2014); however there is also need to analyse individual patient serum to gain robust insight into individual biomarker frequency among patients. Using 2-DE and MALDI-ToF/ToF, Teutschbein *et al.* (2016) recently identified antigenic proteins using sera from 43 individual patients undergoing chemotherapy including 22 with probable and two with proven IA. Forty-nine antigenic proteins were identified, 31 of which had previously been identified as antigenic or allergenic in individuals with IA or ABPA (Shi *et al.*, 2012a; Singh *et al.*, 2010; Virginio *et al.*, 2014). Consistently, proteins identified as antigenic in this study were represented among the most abundant in the *A. fumigatus* proteome as detected

in other analyses (Champer *et al.*, 2012; Teutschbein *et al.*, 2010; Vödisch *et al.*, 2009). This led the authors to suggest that proteins with higher abundance are more likely to provoke an immune response *in vivo* (Teutschbein *et al.*, 2016). Supervised machine learning with a decision tree classification was used to identify proteins capable of predicting the outcome of infection. Using this approach, several proteins were shown to be associated with a positive (survival) and negative (fatal) outcome of infection including CpcB (AFUA_4G13170) and Shm2 (AFUA_3G09320), respectively. Both proteins were recombinantly expressed and exposed to peripheral blood mononuclear cells (PBMCs). Interestingly; Shm2 induced a pro-inflammatory response while CpcB did not. Given Shm2 was associated with a poor patient outcome, it is possible that Shm2 can trigger a deleterious host inflammatory response (Teutschbein *et al.*, 2016). The response associated with these proteins was in accordance with a characterisation of $CD4^+$ T cell target antigens in healthy individuals. Based on the cytokine profile induced, Shm2 was considered immunogenic while CpcB lacked induction of an effector function (Bacher *et al.*, 2014). Also apparent in work by Teutschbein *et al.* and others (Doyle, personal communication) is the anti-*A. fumigatus* antibody response present in individuals devoid of active or apparent infection. This is indicative of the ubiquity of *A. fumigatus*; however it also illustrates the need to consider antigens specific to infection as biomarkers. In a study by Virgino *et al.* (2014), sera from patients who presented with similar underlying disease but without fungal infection were used as controls in analysing the immunoproteome of *A. fumigatus* germlings. Ten of the proteins identified as antigenic had been previously proposed as biomarkers by others; however these were shown to cross-react with control sera indicating they may not be suitable in diagnosis. Furthermore, following reports of difficulty in distinguishing

between different fungi in diagnosis, the proteome was also analysed with pooled sera from patients with several other invasive fungal infections. Twenty-two proteins exhibited antigenicity, indicating that they were also unsuitable for diagnosis. Fourteen proteins were exclusively detected in the proteome probed with sera from proven cases of Aspergillosis, four of which were also immunoreactive with sera from probable Aspergillosis cases. Importantly, four proteins had not previously been proposed as possible diagnostic antigens. BLAST searches revealed that two of the proteins analysed had no homology with human proteins (Virginio *et al.*, 2014). This included eEF3, a fungal-specific protein previously proposed as a drug target with overexpression in germlings (Kubitschek-Barreira *et al.*, 2013) (above). eEF3 is involved in translation and mutations in it can deleteriously affect growth and translation (Sasikumar and Kinzy, 2014). Hence, eEF3 has emerged as a promising diagnostic antigen and drug target. Work by Teutschbein *et al.* (2016) also revealed heterogeneity in the anti-*A. fumigatus* profile in sera of individual patients with probable or proven IA, which the authors reasoned indicates that one antigen alone is unlikely to be an effective prognostic or diagnostic marker of IA. Further immunoproteomic analysis is warranted to identify more antigens, including those with immunostimulatory properties. Such studies can yield insight into to the pathology of Aspergillosis and a relatively high-throughput means of surveying candidate drug targets.

1.2.7 The proteomic response to antifungals

Antifungal resistance and host toxicity represent significant challenges in the current use of key antifungals, and proteomic analysis provides a powerful tool in characterising the effects of existing and emerging antifungals to dissect their mode of action. Furthermore, proteomic analysis of resistant strains allows elucidation of the mechanisms of resistance and can provide biomarkers.

Caspfungin (CSF) is an echinocandin that targets the fungal cell wall *via* inhibition of glucan synthesis and in doing so diminishes the cell wall stability (Valiante *et al.*, 2015). Cagas *et al.* (2011a) characterised the proteomic responses of a susceptible and resistant strain of *A. fumigatus* to CSF. The cell wall/ plasma membrane and secreted fractions at 24 and 48 h were studied as these fractions are highly exposed to the host during infection. An approach of gel-free based protein preparation with MALDI-ToF/ToF absolute quantification (iTRAQ) provided substantially better resolution than 2-DE based whole cell lysate protein analysis (Cagas *et al.*, 2011a). Using strict criteria, 122 proteins showing over a two-fold change in response to CSF were identified in the susceptible strain. Sixty-five proteins showed differential abundance in the cell wall/ plasma membrane fraction. Interestingly, 21 out of the 26 proteins with increased abundance at 24 h in the cell wall/ plasma membrane were ribosomal proteins. The authors speculated that this represented a ribosomal reprogramming response to the antifungal. Interestingly, this trend was not as striking in the resistant strain, where only four out 19 proteins with increased abundance at 24 h were ribosomal proteins implicating ribosomal protein reshuffling in susceptibility to CSF. A chitinase, ChiA1 (AFUA_5G03760), decreased over 12-fold at 24 h, which is in accordance with the increased chitin seen under exposure to CSF (Verwer *et al.*, 2012). In the secreted fraction, 57 proteins showed

differential abundance. Levels of Aspf4 and two subunits of ATP citrate lyase (Acl); Acl subunit (AFUA_6G10660) and Acl subunit 1 (AFUA_6G10650) were increased in abundance at 24 h. Both subunits have previously been implicated in other stress responses. Acl subunit 1 has been shown to increase during early responses to heat shock (Albrecht *et al.*, 2010). While Acl subunit, which has recently been identified as antigenic, decreases in response to gliotoxin exposure (Carberry *et al.*, 2012; Teutschbein *et al.*, 2016). Importantly, out of the 122 proteins with differential abundance in the susceptible strain, 103 were unchanged in the resistant strain. Several proteins, which were relatively unaltered in the resistant strain, showed over a 12-fold change in abundance in the susceptible strain. These included Aspf1 (AFUA_5G02330), mitochondrial hypoxia response domain protein (AFUA_1G12250) and citrate lyase (Cit1/ McsA; AFUA_6G03590), which may represent promising biomarkers.

Amphotericin B (AMB) is a polyene that works by binding ergosterol in the cell membrane forming channels, thereby disrupting membrane function and leading to leakage of ions and cytoplasmic material as well as ROS accumulation (Valiante *et al.*, 2015). Exposure of *A. fumigatus* to AMB resulted in differential abundance in 48 proteins when analysed by 2-DE with MALDI-ToF/ToF identification. Forty-four proteins showed increased abundance and four decreased abundance (Gautam *et al.*, 2008). Ergosterol biosynthetic protein, Erg13 (AFUA_3G10660), increased in the proteome under exposure to AMB (Gautam *et al.*, 2008). Ergosterol biosynthesis requires the input of heme as a co-factor (Shakoury-Elizeh *et al.*, 2010). Increased abundance of heme biosynthetic protein Hem13 (AFUA_1G07480) reflected this extra demand. The induction of oxidative stress defences was also observed in the proteomic analysis, with increased abundance of manganese superoxide dismutase

(Mn-SOD; AFUA_1G14550), catalase (Cat1; AFUA_3G02270) and Prx1/ LsfA (AFUA_4G08580). This supports the report that AMB driven cell membrane damage results in the generation of oxidative stress *via* ROS generation.

Itraconazole (ITC) is an azole that targets the biosynthesis of ergosterol and leads to the accumulation of toxic sterols (Valiante *et al.*, 2015). Exposure of *A. fumigatus* to ITC resulted in differential abundance of 54 proteins detected by 2-DE with MALDI-ToF/ToF identification (Gautam *et al.*, 2016). Analysis revealed 12 proteins with increased abundance and 42 with decreased abundance, representing 44 unique proteins. Similar to AMB, increased abundance of several proteins in response to oxidative stress were also observed including catalase, Cat1. Interestingly, 26 of the proteins detected had previously shown differential abundance in *A. fumigatus* in response to the anti-malarial compound, artemisinin (ART) reported to also have antifungal activity. Proteomics also represents a useful and efficient tool in investigating novel antifungals such as ART. While administration of ART alone is unlikely to be a viable therapy, Gautam *et al.* (2011) demonstrated synergy with ITC, indicating it may prove effective in combination therapy. Exposure of *A. fumigatus* to ART led to differential abundance of 85 proteins following 2-DE with MALDI-ToF/ToF identification. 29 showed increased abundance and 56 decreased (Gautam *et al.*, 2011). Decreased abundance of cell wall protein PhiA (AFUA_3G03060) suggested that cell wall remodelling was induced. Interestingly, in contrast to AMB, decreased abundance of Erg3 (AFUA_2G00320) and Hem13 (AFUA_1G07480) was also observed. Heme is required for the action of ART. Therefore, decreasing heme biosynthesis may represent a means of tolerance, followed by decreasing the abundance of heme-dependent enzymes an adaptive response. Stress-related proteins were also affected, with increased abundance of antioxidant peroxiredoxin (Prx1/

LsfA). Thus, pathways targeted by other antifungals including cell wall, ergosterol and stress were also targeted by ART.

Proteomic analysis has also provided insight into the fungal response to other putative antifungals. Screening a range of coumarin derivatives, a synthetic coumarin derivative termed SCD-1 was identified with activity against *Aspergillus* species (Gupta *et al.*, 2011). Subsequently, the proteome of *A. fumigatus* following exposure to SCD-1 was investigated to dissect its antifungal mechanism (Singh *et al.*, 2012). Cytosolic proteins were extracted from germlings and analysed by 2-DE with LC-MS/MS identification. One hundred and forty-three proteins with differential abundance were detected; 96 increased and 30 decreased in abundance. In addition, four proteins were unique to the control and 13 were unique to the SCD-1 treatment. Proteins involved in riboflavin biosynthesis (AFUA_1G06240 and AFUA_2G05820) showed decreased abundance, implicating it as a target of SCD-1. The absence of riboflavin biosynthesis in humans makes this pathway an ideal drug target with limited host toxicity. Similar to CSF, there was increased abundance of ribosomal proteins, including 60S ribosomal protein P0 (AFUA_1G05080), 40S ribosomal protein S12 (AFUA_1G05500), and 40S ribosomal protein S3 (AFUA_1G05630), indicating a ribosomal reshuffling in response to exposure. There was also increased abundance of stress proteins including antioxidant Prx1/ Lsf1 and HSPs, Hsp90 (AFUA_5G04170), Hsp88 (AFUA_1G12610) and Hsp30/ Hsp42 (AFUA_3G14540).

The proteomic analysis of *A. fumigatus* following exposure to each of these antifungal compounds has indicated some targeting of common pathways. Coping mechanisms for oxidative stress, including the induction of antioxidant proteins is evident upon exposure to all compounds. Interestingly, some of these share proteins for example, Cat1 was increased upon exposure to AMB, ITC and ART while Prx1/

LsfA was increased during AMB, ART and SCB-1 exposure. Phosphoglycerate kinase PgkA (AFUA_1G10350) showed differential abundance in response to all antifungals. Allergen enolase/ Aspf22 was also differentially abundant upon exposure to many of these compounds; with increased abundance during exposure to AMB, ART, and CMR, but decreased abundance in ITC. Enolase is classified as an allergen with a predicted adhesin motif and its increased abundance during exposure to these antifungals is therefore relevant to treatment methods in patients with ABPA (Chaudhuri *et al.*, 2011; Knutsen *et al.*, 2012).

1.3 Host-relevant adaptations to iron starvation in *A. fumigatus*

As discussed in Section 1.2.5, *A. fumigatus* must adapt to stresses within the host in order to survive during infection. In a form of 'nutritional immunity', the host restricts iron bioavailability to invading microorganisms (Cassat and Skaar, 2013). Transcriptional analysis has revealed that iron limitation induces significant alterations in ~13% of protein-encoding genes in *A. fumigatus* (Haas, 2014; Schrettl *et al.*, 2008). Hence, this host stress clearly prompts considerable phenotypic changes in *A. fumigatus.* Understanding the iron-starved phenotype of *A. fumigatus* is important to understanding its phenotype during IA so that better antifungal and diagnostic strategies can be devised.

1.3.1 Iron and infection

By virtue of its ability to exist in two oxidative states, ferrous (Fe^{2+}) and ferric (Fe^{3+}), iron is a promiscuous co-factor in biological systems, accepting or donating electrons. However, the redox capacity of iron also means it can drive the generation of deleterious reactive oxygen species (ROS) through the Fenton-Haber-Weiss sequence

resulting in formation of the highly reactive hydroxyl radical ($^{\bullet}OH$) (Aisen *et al.*, 2001; Halliwell and Gutteridge, 1984). Excess ROS generation can result in damage to lipids, DNA, and proteins. Hence, maintaining iron homeostasis is crucial in any iron-requiring organism to ensure sufficient but not deleterious levels are maintained. As discussed in Section 1.2.5.2, fungi predominantly achieve this through strict regulation of iron uptake mechanisms (Haas *et al.*, 2008).

In humans, the majority of iron is contained within erythrocytes in haemoglobin-bound heme. Heme and haemoglobin can be released into plasma from lysed erythrocytes, however they are rapidly sequestered by host proteins (e.g. haptoglobin or albumin) or taken up by cells (e.g. macrophages) (Cassat and Skaar, 2013). Any free iron circulating in plasma is bound to the glycoprotein, transferrin, which binds Fe^{3+} with high affinity. The iron-transferrin complex can then be specifically taken up into cells *via* transferrin receptor 1 (TfR1) as required (Caza and Kronstad, 2013). The majority of the iron binding sites of the transferrin pool are actually not occupied to allow for further sequestration of iron if necessary, for example during excessive iron intake (Cassat and Skaar, 2013; Caza and Kronstad, 2013). When excessive intracellular iron levels are reached, Fe^{2+} can be bound by the iron-storage protein, ferritin. Ferritin and transferrin iron storage and utilisation is regulated by the intracellular iron pool; this provides signals for the interaction of iron regulatory proteins with iron regulatory elements on TfR1 and ferritin mRNA. When intracellular iron levels are high, TfR1 synthesis is reduced thereby reducing transferrin-iron uptake, and ferritin synthesis increased thereby increasing safe intracellular sequestration of iron. Conversely, when intracellular iron levels are low, TfR1 synthesis is increased and ferritin synthesis decreased (Aisen *et al.*, 2001). As a

result of these homeostatic mechanisms, the levels of iron available to invading microorganisms in plasma are extremely low.

Upon microbial challenge there is an increase in iron-sequestering mechanisms by the host in an effort to withhold iron from the invading pathogen. This is termed 'nutritional immunity'. During infection, pro-inflammatory cytokines (e.g. IFN-γ) induce further storage of iron in ferritin and production of the regulator, hepcidin, inhibits the extracellular release of iron from cells (Cassat and Skaar, 2013; Ganz, 2009; Leal *et al.*, 2013). Lactoferrin is also released by neutrophils which, like transferrin, sequesters free iron at the site of infection (Caza and Kronstad, 2013). Consequently, upon attempts at infection, microbial pathogens enter a struggle for iron with the host and must possess a means of acquiring iron therein. This is exemplified well in two recent studies. Leal *et al.* (2013) demonstrated an increase in hepcidin levels and uptake of transferrin and lactoferrin during infection of murine corneas with *A. fumigatus*. Second, a dual RNA-seq study simultaneously analysed the transcriptional response of *Pseudomonas aeruginosa* and its murine host in response to infection (Damron *et al.*, 2016). In this study, genes involved in iron acquisition were among the most up-regulated in the pathogen transcriptome, while genes involved in iron withholding were among the most up-regulated in host transcriptome.

In addition to systems for the direct uptake of Fe^{2+} or Fe^{3+}, some microbial pathogens possess mechanisms for the direct utilisation of host iron sources. These include receptors for the uptake of iron bound to heme, haemoglobin, transferrin, or lactoferrin. In addition, some species can produce hemolysins, which are implicated in the lysis of erythrocytes for the release of iron bound to haemoglobin and heme (Crawford and Wilson, 2015). Wartenberg *et al.* (2011) identified Asp-hemolysin

(Asp-HS; AFUA_3G00590) as a predominant protein secreted by *A. fumigatus* during growth on several substrates. However, they were unable to demonstrate a role for Asp-HS in hemolysis using reverse genetic studies. In order to utilise the products of hemolysis, an organism must contain a system for the utilisation of heme or haemoglobin. Though there is evidence for this in other fungi, including *Candida albicans,* thus far, there is no evidence for such a system in *A. fumigatus* (Crawford and Wilson, 2015; Schrettl *et al.*, 2004; Vaknin *et al.*, 2014). Hence, it appears unlikely that *A. fumigatus* directly uses host iron in the form of heme or haemoglobin following hemolysis of erythrocytes.

Many bacteria and fungi can produce low molecular weight ferric iron chelators, termed siderophores, which is Greek for 'iron-carrier'. These compounds are secreted in the desferri-form and following iron chelation are taken back up *via* specific transporters. Iron is then released intracellularly and used in metabolism or stored. A role for siderophores in the virulence of several species, including *A. fumigatus,* is well defined (Caza and Kronstad, 2013; Crawford and Wilson, 2015; Haas, 2012; Moore, 2013). Siderophores produced by *A. fumigatus* can bind iron with such high affinity that they can even strip iron from transferrin (Hissen *et al.*, 2004). Siderophore production has been shown to be essential to the virulence of *A. fumigatus* and appears to represent the primary means of iron acquisition in the host (Schrettl *et al.*, 2007). Interestingly, innate immune responses exist in humans that target siderophore-mediated iron uptake. Proteins termed siderocalins, lipocalin 1 (Lcn1) and lipocalin 2 (Lcn2), are capable of binding microbial siderophores thereby preventing their uptake. Lcn2 was the first of the two siderocalins implicated in siderophore binding and is somewhat specific for bacterial catecholate-type siderophores. Deficiency in *lcn2* renders mice more susceptible to infection with

Escherichia coli (Aznar and Dellagi, 2015; Clifton *et al.*, 2009). Moreover, in the dual RNA-seq study by Damron *et al.* (2016), *lcn2* was up-regulated over 30-fold in mice following infection with *P. aeruginosa.* In contrast to Lcn2, Lcn1 binds a range of bacterial and fungal siderophores, including *A. fumigatus* siderophore, triacetylfusarinine C (TAFC). Lcn1 has been shown to inhibit the growth of *A. nidulans in vitro* and *A. fumigatus* in an *in vivo* corneal infection model (Fluckinger *et al.*, 2004; Leal *et al.*, 2013).

1.3.2 Siderophore-mediated iron uptake in *A. fumigatus*

Despite being one of the most abundant metals on earth, iron is largely found in insoluble ferric hydroxides in aerobic environments and is therefore poorly accessible to living organisms. Consequently, many iron-requiring fungi utilise high affinity iron acquisition strategies for the procurement of iron. *A. fumigatus* utilises two high affinity iron uptake mechanisms; siderophore-mediated iron uptake and reductive iron uptake (Haas, 2012). Given that restriction of free iron is employed in humans as a means of impeding the growth of invading microorganisms, high affinity iron uptake mechanisms constitute an important trait in pathogens. Though both uptake systems are up-regulated in *A. fumigatus* during infection, only siderophore-mediated iron acquisition is essential to virulence (Hissen *et al.*, 2005; Schrettl *et al.*, 2004).

A. fumigatus produces four hydroxymate type siderophores; two intracellular siderophores and two extracellular siderophores (Figure 1.3). Intracellular siderophores, ferricrocin (FC) and hydroxyferricrocin (HFC) mediate iron storage and distribution in hyphae and conidia, respectively. Extracellular siderophores, fusarinine C (FSC) and triacetylfusarinine C (TAFC) are secreted from hyphae for extracellular iron uptake (Schrettl *et al.*, 2007).

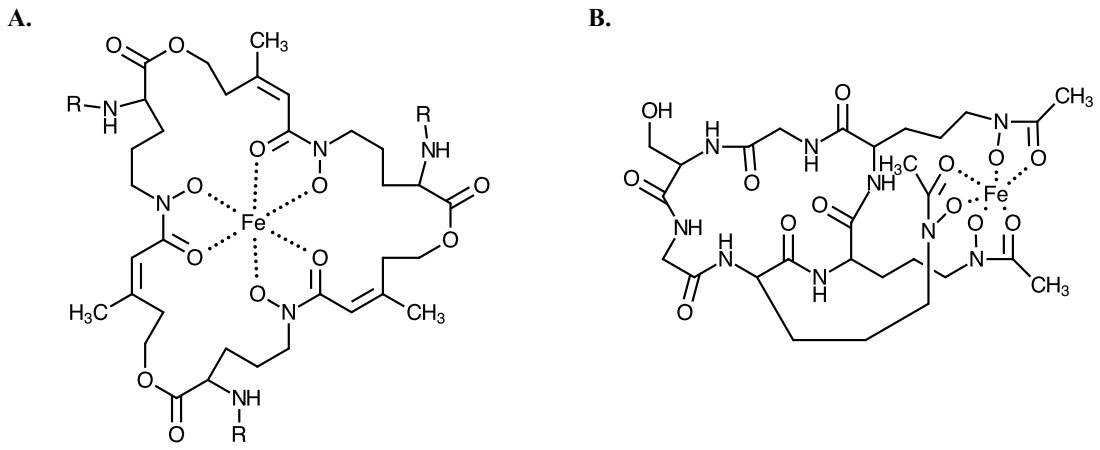

Figure 1.3 Structure of *A. fumigatus* fusarinine and ferrichrome siderophores. *A. fumigatus* utilises (A) extracellular fusarinine siderophores, FSC (R = H) and TAFC (R = acetyl), and (B) intracellular ferrichrome siderophore, FC (Haas, 2014). Images redrawn from Haas (2014) 'Fungal siderophore metabolism with a focus on *Aspergillus fumigatus*' *Natural Product Reports*, 31 (10), pp. 1266–1276. DOI:10.1039/c4np00071d. Published under the Creative Commons Attribution (Non-Commercial 3.0 Unported Licence). Published by The Royal Society of Chemistry.

Siderophore biosynthesis is initiated with the hydroxylation of ornithine by L-ornithine N^5-oxygenase, SidA, resulting in the formation of N^5-hydroxy-L-ornithine (Schrettl *et al.*, 2004). The pathway then splits for the production of extracellular or intracellular siderophores. An intermediate of the ergosterol biosynthetic pathway (mevalonate) is re-directed to extracellular siderophore biosynthesis by mevalonyl-CoA ligase, SidI, and mevalonyl-CoA hydratase, SidH, to generate anhydromevalonyl (Yasmin *et al.*, 2012). This step is carried out in peroxisomes where transacylase, SidF, also mediates adds a anhydromevalonyl group to N^5-hydroxy-L-ornithine (Gründlinger *et al.*, 2013b). The N^5-anhydromevalonyl-N^5-hydroxy-L-ornithine moiety acts as a substrate for non-ribosomal peptide synthetase (NRPS), SidD (Reiber *et al.*, 2005). SidD then directs the generation of FSC, which is comprised of three N^5-

anhydromevalonyl-N^5-hydroxy-L-ornithine groups linked by ester bonds. N^2 acetylation of FSC by SidG results in TAFC (Schrettl *et al.*, 2007). For intracellular siderophore biosynthesis, the N^5-hydroxy-L-ornithine is instead acetylated by SidL or another unknown transacylase resulting in N^5-acetyl-N^5-hydroxy-L-ornithine (Blatzer *et al.*, 2011). Along with glycine and serine, this moiety then acts as the substrate for NRPS, SidC, to generate FC (Reiber *et al.*, 2005). FC is hydroxylated by an unknown hydroxylase to generate HFC (Schrettl *et al.*, 2007). This process is summarised in Figure 1.4.

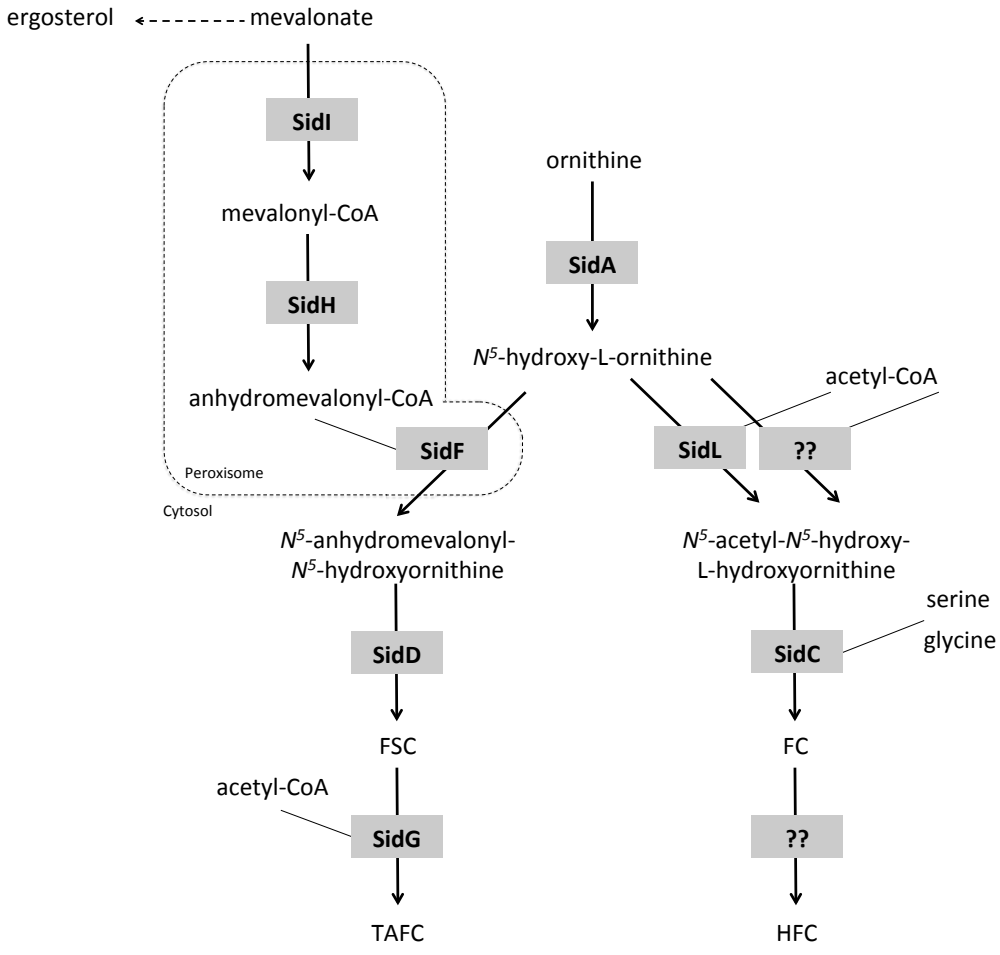

Figure 1.4 Biosynthetic pathway of siderophores in *A. fumigatus* (Haas, 2014).

A. fumigatus secretes desferri-FSC/ TAFC (FSC^{-Fe}/ $TAFC^{-Fe}$) through an unknown mechanism. FSC^{-Fe}/ $TAFC^{-Fe}$ chelate extracellular Fe^{3+} and the resulting

siderophore-iron complexes (FSC^{+Fe}/ $TAFC^{+Fe}$) are taken back up by SITs (Haas, 2014; Haas *et al.*, 2003; Philpott and Protchenko, 2008). SITs are a fungal-specific protein family within the major facilitator superfamily (MFS) (Pao *et al.*, 1998; Saier *et al.*, 1999). The *A. fumigatus* genome encodes seven putative SITs (Haas *et al.*, 2008), which include several transporters induced under iron limitation (Moloney *et al.*, 2016a). SITs are also conserved in fungi incapable of producing siderophores to permit utilisation of siderophores from other species, termed 'xenosiderophores' (Philpott and Protchenko, 2008). For example, *C. albicans* does not produce siderophores but can utilise TAFC (Crawford and Wilson, 2015). A *S. cerevisiae* strain deficient in high affinity iron acquisition was used to determine the substrate specificity of SITs from *A. nidulans*. Using this approach, MirA was found to be specific for enterobactin and MirB for TAFC (Haas *et al.*, 2003). Also using this approach in addition to reverse genetic studies, Sit1 was implicated in the uptake of ferrichrome and ferrioxamine B, and Sit2 in the uptake of ferrichrome in *A. fumigatus* (Park *et al.*, 2016). After uptake, FSC^{+Fe}/ $TAFC^{+Fe}$ are cytosolically hydrolysed by esterases and the released iron is used by metabolic machinery, stored in vacuoles or ferri-FC (FC^{+Fe}) (Gründlinger *et al.*, 2013a; Kragl *et al.*, 2007).

1.3.3 Targeting siderophore-mediated iron uptake in *A. fumigatus*

Siderophores have generated significant clinical interest because they are essential to virulence and produced *in vivo* during infection. This presents them as promising drug targets and biomarkers of infection (Haas, 2012; Hissen *et al.*, 2005; Lamb, 2015; Miethke and Marahiel, 2007; Petrik *et al.*, 2017; Schrettl *et al.*, 2004). Utilising siderophores in these capacities can be achieved through several routes (Figure 1.5). These will be further discussed throughout this section.

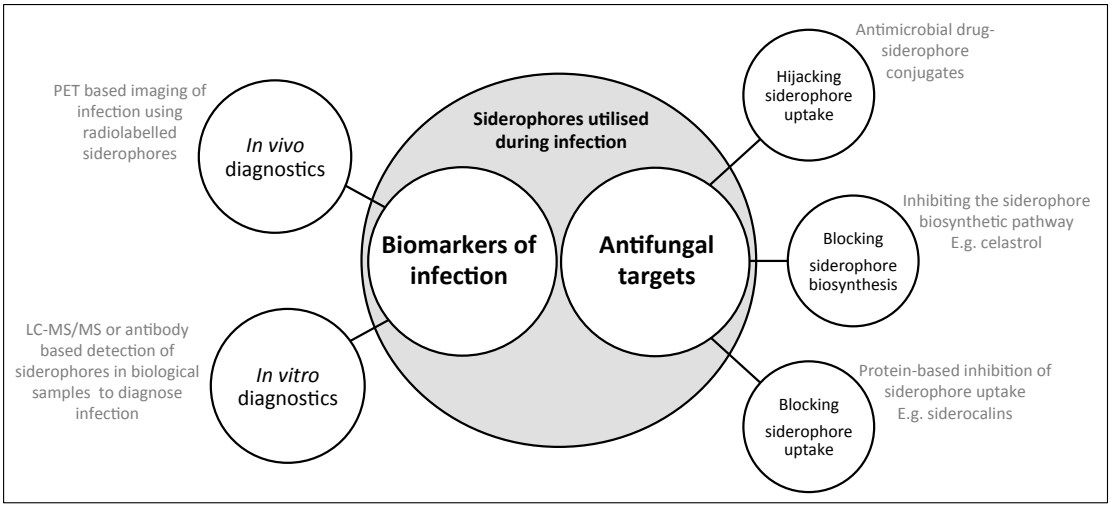

Figure 1.5 Routes for exploiting siderophore-mediated iron acquisition for diagnostic or therapeutic strategies. Siderophore production *in vivo* can be exploited as biomarkers of infection by (i) *in vivo* diagnostic strategies, or (ii) *in vitro* diagnostic strategies. Siderophore-mediated iron uptake can be exploited in an antifungal strategy by (i) hijacking siderophore uptake *via* siderophore-drug conjugates, (ii) inhibitors of the siderophore biosynthetic pathway, or (iii) impeding the uptake of siderophore following their release.

1.3.3.1 Utilising siderophores as biomarkers of infection

In addition to iron, *A. fumigatus* siderophores can also chelate radioactive metals (radiometals). Using this capacity, the utilisation of siderophores by *A. fumigatus* during infection has been directly demonstrated (Haas *et al.*, 2015; Petrik *et al.*, 2010a, 2012, 2017). Specifically, chelation of TAFC to gallium (^{68}Ga) as opposed to iron generates an effective tool for positron-emission tomography (PET)-based imaging. Gallium-TAFC chelates (^{68}Ga-TAFC) were administered to neutropenic rats with and without IA and PET imaging performed. Both showed localisation of ^{68}Ga-TAFC to kidneys and bladder following administration, indicative of renal excretion. Only rats infected with *A. fumigatus* showed ^{68}Ga-TAFC localisation to the lungs, suggesting growth and siderophore uptake by *A. fumigatus* therein (Figure 1.6). In addition to directly demonstrating siderophore-mediated iron acquisition *in vivo,* this has proven an innovative means imaging of *A. fumigatus* infection thereby providing a non-invasive *in vivo* diagnostic strategy (Petrik *et al.*, 2017). Interestingly, siderophore-gallium chelates show antimicrobial activity in other species, likely as a result of the deleterious substitution of gallium for iron in related metabolic processes (Huayhuaz *et al.*, 2017). However, as of yet, this has not been reported for *A. fumigatus.*

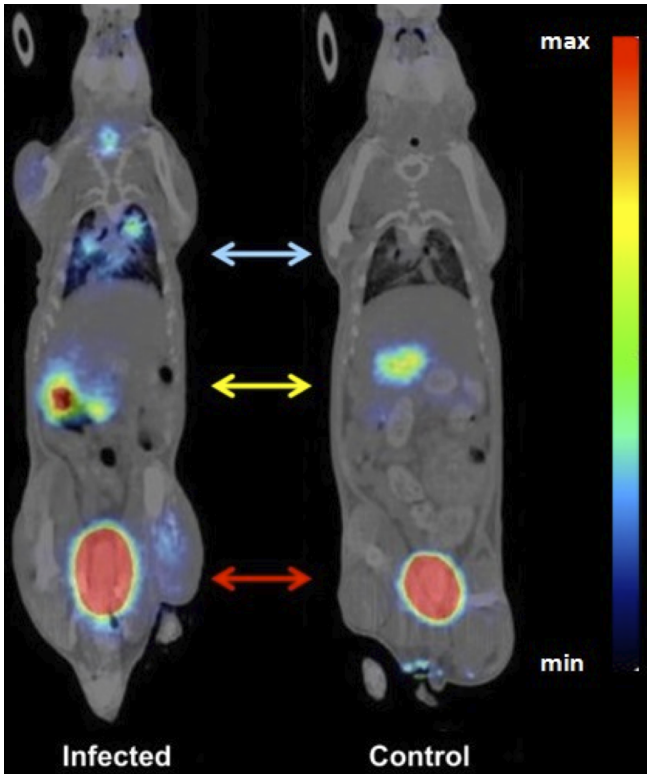

Figure 1.6 Uptake of siderophores during infection demonstrated by the uptake of ^{68}Ga-TAFC in a rat model for IA. PET imaging shows localisation of ^{68}Ga-TAFC to the lungs of rats infected with *A. fumigatus* but not in the control (blue line). Both IA infected and control rats also showed ^{68}Ga-TAFC localisation to kidneys and bladder (yellow and red lines). Image taken from Haas *et al.* (2015) 'An iron-mimicking, trojan horse-entering fungi-has the time come for molecular imaging of fungal infections?' *PLoS pathogens*, 11(1), p. e1004568. DOI: 10.1371/journal.ppat.1004568. Published under the Creative Commons Attribution License (CC BY).

Siderophores can also be implemented in an *in vitro* diagnostic strategy, whereby the detection of siderophores in biological samples (such as urine, BAL, or serum) from patients acts as a biomarker of infection (Doyle *et al.*, 2012). As discussed in Section 1.1.3.1, *in vitro* diagnostic methods currently utilised for Aspergillosis can also detect other mycoses. In contrast, detecting specific

siderophores can give more refined information on infecting species. For example, TAFC is only produced by *Aspergillus, Fusarium,* and *Nectria* species (Haas, 2014). In support of a siderophore-based diagnostic strategy, *in vitro* detection of *A. fumigatus* siderophores in mammalian host samples has recently been demonstrated (Carroll *et al.*, 2016; Luptáková *et al.*, 2017). Carroll *et al.* (2016) used LC-MS/MS for the detection and diagnosis of IA by screening for TAFC in human serum. They established a cut-off (6 ng/ ml) using negative control sera and then analysed sera from patients with suspected or proven/ probable IA. Sixty-nine percent of patients with suspected Aspergillosis (n = 51) were above the 6 ng/ ml TAFC cut-off level, while only 33% of these were positive on the GM assay. In addition, 28% of patients with proven/ probable Aspergillosis were above the 6 ng/ ml TAFC cut-off level. Luptáková *et al.* (2017) used LC-MS to detect *A. fumigatus* siderophores in the serum and urine of a rat model of Aspergillosis. Intracellular siderophore FC was present in the serum of all infected rats (n = 6). While TAFC levels in serum were below the levels of detection, both TAFC and FC were detected in the urine of all infected animals (n = 6). Importantly, no siderophores were detected in uninfected control animals (n = 3). These studies indicate promise for the use of siderophores in the non-invasive diagnosis of Aspergillosis, however further evaluation of both control and patient samples is required to validate TAFC as a biomarker of IA.

There is further evidence emerging for the use of siderophores as biomarkers of other microbial infections. Pan *et al.* (2015) used LC-MS/MS to screen mice infected with *Mycobacterium tuberculosis* for small molecules that may be used as biomarkers. They detected the siderophore, mycobactin, in the lung tissue and serum of 100% of infected mice (n = 7) but none of the controls (n = 6). Similarly, they detected mycobactin in the sputum of 90% patients with pulmonary tuberculosis (n =

10) but none of the controls (n = 10). Mycobactin was also detected in the cerebrospinal fluid of 71% of patients with tuberculous meningitis (n = 14) but none of the controls (n = 12) (Cryptococcal meningitis patients) (Pan *et al.*, 2015).

There is also evidence to suggest promise for the use of other metabolites produced by *A. fumigatus* as biomarkers of IA (Savelieff and Pappalardo, 2017). For example, the secondary metabolite, gliotoxin (GT) and its methylated derivative, bis(methylthio)gliotoxin (BmGT), are both produced by *A. fumigatus* during infection. GT has been detected using LC-MS/MS in sera from mice with IA and patients with suspected IA (Cerqueira *et al.*, 2014; Lewis *et al.*, 2005). However, BmGT is likely more stable in biological samples, because the highly reactive disulfide bridge of GT is methylated therein (Dolan *et al.*, 2014). BmGT was detected more frequently than GT in sera samples from patients at risk for IA and may represent a promising diagnostic strategy in combination with the GM assay (Domingo *et al.*, 2012; Vidal-García *et al.*, 2016). In contrast, a recent study using three mice models of immunosuppression (CGD, neutropenia, and steroid-treatment) detected GT in the lungs of all three groups, while BmGT was only consistently detected in lungs of CGD mice (Sugui *et al.*, 2017). Host status influenced the levels of both GT and BmGT. Hence, more analysis of the levels of GT/ BmGT in patient groups susceptible to IA is required before either can be implemented as a biomarker.

LC-MS/MS or HPLC analysis was implemented in the aforementioned studies to demonstrate the diagnostic potential of small molecules. While this offers the advantage of highly sensitive and effective screening during the validation of a biomarker, it is a somewhat costly procedure requiring appropriate facilities and trained operators. Point-of-care assays offering rapid results, lower associated cost and relatively easier use have potential for wider implementation. Antibodies form the

basis of many such assays, for example in the GM assay (Section 1.1.3.1). The prerequisite for this strategy is the raising of antibodies against the target molecule; however previous studies have demonstrated this to be feasible with the generation of antibodies against small molecules including siderophores (Bergeron *et al.*, 2010; Buyer *et al.*, 1990; Fox *et al.*, 2004; Howard *et al.*, 2000; Sassone-Corsi *et al.*, 2016).

1.3.3.2 Utilising siderophores in an antifungal strategy

Targeting siderophore-mediated iron acquisition as a therapeutic strategy can be achieved through several routes (Figure 1.5). Firstly, their use in siderophore-antimicrobial drug conjugates has prompted considerable research. Conjugation of an antimicrobial drug to a siderophore can improve drug delivery in a 'Trojan horse' strategy (Möllmann *et al.*, 2009). Recent work has proven this to be a viable strategy for targeting Gram negative bacteria with Gram positive antibiotics conjugated to siderophores (Ghosh *et al.*, 2017; Schalk and Mislin, 2017). However, this has yet to be demonstrated in *A. fumigatus.*

Siderophore-mediated iron acquisition can also be targeted *via* inhibition of siderophore biosynthesis (Lamb, 2015). Recently, celastrol was identified as an inhibitor of the enzyme, SidA, which mediates the first step of the siderophore biosynthetic pathway (Figure 1.4). As noted earlier, SidA is a flavin adenine dinucleotide (FAD) containing *N*-hydroxylating monooxygenase that catalyses the N^5-hydroxylation of L-ornithine. This process requires reduced nicotinamide adenine dinucleotide phosphate (NADPH). Qi *et al.* (2012) developed a chromophore that could occupy the NADPH binding site of SidA, but was displaced upon NADPH and substrate binding. This chromophore was then implemented in an assay to screen a library of compounds for small molecule inhibitors of SidA activity (Martín del

Campo *et al.*, 2016; Qi *et al.*, 2012). Using this process celastrol was identified as a SidA inhibitor. During iron starvation, celastrol was capable of inhibiting *A. fumigatus* growth, which was restored upon the addition of siderophores. Celastrol has also been investigated for anti-obesity effects in humans; therefore, the authors noted that further refinement was necessary to yield a compound with the specific SidA inhibitory activity. However, this work has demonstrated an effective strategy for the identification of siderophore biosynthesis inhibitors in *A. fumigatus*.

Similarly, statins are a collection of anti-cholesterol drugs currently administered in humans. In *A. fumigatus*, they act by inhibiting an enzyme of the ergosterol biosynthetic pathway, 3-hydroxy-3-methylglutaryl-CoA (HMG-CoA) reductase, which catalyses the generation of mevalonate. As described in Section 1.3.2, mevalonate is utilised for the siderophore biosynthesis, to the extent that under iron starvation ergosterol levels are decreased due to this diversion of mevalonate. Following this, lovastatin can inhibit extracellular siderophore production and *A. fumigatus* is more susceptible to lovastatin during iron starvation (Yasmin *et al.*, 2012). Furthermore, topical application of simvastatin to murine cornea infected with *A. fumigatus* reduced fungal growth. Importantly, this growth inhibition was somewhat restored by the addition of the exogenous siderophore, deferroxamine (Leal *et al.*, 2013). This indicates that statin-mediated growth inhibition acts by targeting siderophore biosynthesis, as well as that of ergosterol. Conversely, there was an additive inhibition of fungal growth when simvastatin was administered along with iron chelators, deferiprone.

As discussed in Section 1.3.1, the human innate response also includes elements that target siderophore utilisation in microbial pathogens *via* proteins termed siderocalins. Lcn1 and Lcn2 can bind microbial siderophores thereby impeding

siderophore-mediated iron uptake in invading microorganisms. Lcn1 is a secreted protein found in several sites of the body including tears, skin, and tracheobronchial mucosae (Dartt, 2011). Neutrophils also show constitutive expression of the *lcn1* gene (Leal *et al.*, 2013). Lcn1 contains a large cavity capable of binding a range of compounds, in addition to microbial siderophores, including retinol, cholesterol, and phosphotidylcholine (Dartt, 2011). Fluckinger *et al.* (2004) showed Lcn1 bound several bacterial and fungal siderophores, including TAFC, using a fluorescent fatty acid, 11-([5-(dimethylamino)-1-naphthalenyl]sulfonylamino) undecanoic acid (DAUDA), that could occupy the binding pocket of Lcn1. Lcn1 was also shown to inhibit TAFC-mediated growth restoration *in vitro* in a strain of *A. nidulans* deficient in siderophore biosynthesis (Δ*sidA*). Following this, Lcn1 was demonstrated to inhibit the growth of *A. fumigatus in vivo* in a mouse model of corneal infection following topical application (Leal *et al.*, 2013). Together, this work highlights that targeting siderophore biosynthesis or siderophore-mediated iron uptake in *A. fumigatus* is a plausible therapeutic strategy.

1.4 Thesis rationale and aims

As per Sections 1.1 – 1.3, *A. fumigatus* is the predominant causative agent of IA. IA carries a high mortality rate largely due a lack of diagnostic methods and limited treatment options. Iron starvation represents a prevailing stress within the host and induces significant phenotypic remodelling in *A. fumigatus*. Much of what is currently known about this response has been revealed through transcriptomic and reverse genetic studies. However, there is limited information on the proteomic response of *A. fumigatus* to iron starvation. In particular, the secreted proteome, which represents a direct facet of the host-pathogen interface. Furthermore, adaptations of *A. fumigatus* to iron starvation are crucial to its virulence, specifically the secretion of iron-

chelating siderophores. The production of these compounds *in vivo* can be clinically exploited by several means. Firstly, the detection of siderophores in patients may serve as biomarkers of IA, therefore, offering a novel diagnostic strategy. Secondly, interference with siderophore-mediated iron uptake can impede the uptake of an essential element as the basis of an anti-fungal strategy. As a consequence, the overall objectives of the work presented in this thesis were to:

i. Characterise the impact of iron starvation on proteins secreted by *A. fumigatus* and explore their relevance to the host-pathogen interface.
ii. Develop a strategy for fluorescent derivatisation of *A. fumigatus* siderophores and study their uptake.
iii. Synthesize a FSC immunogen suitable for animal immunisations. Then, using this immunogen, raise and characterise an anti-FSC antibody.
iv. Synthesize a TAFC immunogen suitable for animal immunisations. Then, using this immunogen, raise and characterise an anti-TAFC antibody.

Chapter 2

Materials and methods

Chapter 2 Materials and methods

2.1 Materials

All products listed were obtained from Sigma-Aldrich Chemical Co. Ltd. (U.K.) unless otherwise stated.

2.1.1 *A. fumigatus* Culture Media and Reagents

2.1.1.1 Malt Extract Agar (MEA)

MEA (50 g) (Oxoid Ltd, Hants, England) was added to 1 L distilled water and dissolved by stirring. The solution was sterilised by autoclaving at 115 °C for 10 min and allowed to cool to approximately 55 °C before pouring in 90 mm petri dishes under sterile conditions.

2.1.1.2 *Aspergillus* Minimal Media

2.1.1.2.1 *Aspergillus* Trace Elements without Iron

$Na_2B_4O_7 \cdot 10H_2O$ (40 mg), $CuSO_4 \cdot 5H_2O$ (400 mg), $Na_2MoO \cdot 2H_2O$ (800 mg) and $ZnSO_4 \cdot 7H_2O$ (8 g) were dissolved in order in deionised water (800 ml). A few drops of concentrated HCl were added to maintain the solution. The solution was brought to 1 L with deionised water and stored in 50 ml aliquots at -20 °C.

2.1.1.2.2 50 X *Aspergillus* Salt Solution

KCl (26 g), $MgSO_4 \cdot 7H2O$ (26 g) and KH_2PO_4 (76 g) were dissolved in deionised water (800 ml). The solution was brought to 1 L with distilled water and sterilized by autoclaving at 121 °C for 15 min. The solution was stored at 4 °C.

2.1.1.2.3 0.3 M L-Glutamine

L-Glutamine (43.8 g) was dissolved in deionised water (800 ml). HCl was added to aid dissolution. The pH was adjusted to 6.5 and final volume adjusted to 1 L with deionised water. Solution was filter sterilised and stored at room temperature.

2.1.1.2.4 0.5 M Ferrous Sulphate Heptahydrate ($FeSO_4 \cdot 7H_2O$)

$FeSO_4 \cdot 7H_2O$ (139 mg) was dissolved in deionised water (1 ml). Solution was prepared immediately before use.

2.1.1.2.5 *Aspergillus* Minimal Media Liquid

2.1.1.2.5.1 MM Liquid without Iron

50 X *Aspergillus* Salt Solution (20 ml), *Aspergillus* Trace Elements without Iron (1 ml), and Glucose (10 g) were dissolved in deionised water (800 ml). The pH of the solution was adjusted to 6.5 and final volume adjusted to 1 L with deionised water. The solution was sterilised by autoclaving at 105 °C for 30 min. The solution was allowed to cool to approximately 55 °C before filter sterilised 0.3 M L-Glutamine (66.3 ml) was added. The solution was stored at 4 °C.

2.1.1.2.5.2 MM Liquid with Iron

50 X *Aspergillus* Salt Solution (20 ml), *Aspergillus* Trace Elements without Iron (1 ml), 0.5 M $FeSO_4 \cdot 7H_2O$ (60 µl), and Glucose (10 g) were dissolved in deionised water (800 ml). The pH of the solution was adjusted to 6.5 and final volume adjusted to 1 L with deionised water. The solution was sterilised by autoclaving at 105 °C for 30 min and allowed to cool to approximately 55 °C before filter sterilised 0.3 M L-Glutamine (66.3 ml) was added. The solution was stored at 4 °C.

2.1.1.2.6 Aspergillus Minimal Media Agar

2.1.1.2.6.1 MM Agar without Iron

50 X *Aspergillus* Salt Solution (20 ml), *Aspergillus* Trace Elements without Iron (1 ml), and Glucose (10 g) were dissolved in deionised water (800 ml). The pH of the solution was adjusted to 6.5. Agar (18 g) (Fischer Scientific, UK) was added and the final volume adjusted to 1 L with deionised water. The solution was sterilised by autoclaving at 105 °C for 30 min and allowed to cool to approximately 55 °C before filter sterilised 0.3 M L-Glutamine (66.3 ml) was added. The solution was then poured into petri dishes under sterile conditions.

2.1.1.2.6.2 MM Agar with Iron

50 X *Aspergillus* Salt Solution (20 ml), *Aspergillus* Trace Elements without Iron (1 ml), 0.5 M $FeSO_4 \cdot 7H_2O$ (60 µl), and Glucose (10 g) were dissolved in deionised water (800 ml). The pH of the solution was adjusted to 6.5. Agar (18 g) (Fischer Scientific, UK) was added and the final volume adjusted to 1 L with deionised water. The solution was sterilised by autoclaving at 105 °C for 30 min and allowed to cool to approximately 55 °C before filter sterilised 0.3 M L-Glutamine (66.3 ml) was added. The solution was then poured into petri dishes under sterile conditions.

2.1.1.3 80% (v/v) Glycerol

Deionised water (20 ml) was added to glycerol (20 ml). The solution was sterilised by autoclaving at 121 °C for 15 min and stored at 4 °C.

2.1.1.4 5% (v/v) Hydrochloric Acid (HCl)

Concentrated HCl (135 ml) was slowly added to deionised water (865 ml) in a graduated cylinder (glass). Solution was stored at room temperature.

2.1.1.5 1 mM Ethylenediaminetetraacetic acid (EDTA)

0.5 M EDTA (2 ml) (Section 2.1.4.6) was added to deionised water (998 ml). The solution was prepared immediately before use and stored at room temperature.

2.1.2 Hybridoma Culture Media and Reagents

All culture media and reagents used were heated to 37 °C in a water bath prior to use with cells unless otherwise stated.

2.1.2.1 Myeloma Cell Culture Medium

Penicillin-Streptomycin (1 ml) (Gibco®), and Fetal Bovine Serum, certified, heat inactivated, US origin (10 ml) (Gibco®) were added to DMEM, high glucose, GlutaMAX™ Supplement (89 ml) (Gibco®). The solution was stored at 4 °C for up to 2 weeks and heated to 37 °C before use.

2.1.2.2 Plating Medium

Penicillin-Streptomycin (1 ml) (Gibco®), Fetal Bovine Serum, certified, heat inactivated, US origin (10 ml) (Gibco® – 10082147), 50X HAT (hypoxanthine aminopterin thymidine) supplement (2 ml) (Gibco®), and BriClone (5 ml) (NICB) were added to DMEM, high glucose, GlutaMAX™ Supplement (82 ml) (Gibco®). The solution was prepared 1 day prior to use, stored at 4 °C overnight and heated to 37 °C before use.

2.1.2.3 Hybridoma Culture Medium with 1X HT

Penicillin-Streptomycin (1 ml) (Gibco®), Fetal Bovine Serum, certified, heat inactivated, US origin (10 ml) (Gibco®), 100X HT (hypoxanthine thymidine) supplement (1 ml) (Gibco®), and BriClone (5 ml) (NICB) were added to DMEM,

high glucose, GlutaMAX™ Supplement (83 ml) (Gibco®). The solution was stored at 4 °C for up to 2 weeks and heated to 37 °C before use.

2.1.2.4 Hybridoma Culture Medium

Penicillin-Streptomycin (1 ml) (Gibco®), Fetal Bovine Serum, certified, heat inactivated, US origin (10 ml) (Gibco®), and BriClone (5 ml) (NICB) were added to DMEM, high glucose, GlutaMAX™ Supplement (84 ml) (Gibco®). The solution was stored at 4 °C for up to 2 weeks and heated to 37 °C before use.

2.1.3 Antibiotics and Supplements

All antibiotics and supplements were prepared in water, filter sterilised, and stored at -20 °C until use. Further information is provided in Table 2.1.

Table 2.1 Antibiotics and Supplements used in this study.

Condition Tested	Reagent Used	Stock Concentration	Tested Concentration
Hygromycin Resistance	Hygromycin B	100 mg/ ml (prepared in deionised water)	100 μg/ ml
Iron starvation	Bathophenanthrolinedisulfonic acid disodium salt hydrate (BPS)	1 mg/ ml (prepared in deionised water)	118 μg/ ml (200 μM)

2.1.4 Buffers and Reagents for General Use

2.1.4.1 Reagents for pH Adjustment

2.1.4.1.1 5 M Hydrochloric Acid (HCl)

Concentrated HCl (43.64 ml) was slowly added to deionised water (56.36 ml) in a graduated cylinder (glass). Solution was stored at room temperature.

2.1.4.1.2 5 M Sodium Hydroxide (NaOH)

Sodium hydroxide pellets (20 g) were added to deioinised water (80 ml) and dissolved by stirring. The final volume was adjusted to 100 ml. Solution was stored at room temperature.

2.1.4.2 Phosphate Buffered Saline (PBS)

Ten PBS tablets (Oxoid) were dissolved in deionised water (1 L). The solution was sterilised by autoclaving at 121 °C for 15 min and stored at room temperature.

2.1.4.3 PBS – Tween 20 (0.05% (v/v)) (PBST)

Tween 20 (0.5 ml) was added to 1 L PBS. The solution was sterilised by autoclaving at 121 °C for 15 min and stored at room temperature.

2.1.4.4 1 M Sodium Phosphate Monobasic

Sodium phosphate monobasic (119.98 g) was dissolved in deionised water (1 L). The solution was stored at room temperature.

2.1.4.5 1 M Sodium Phosphate Dibasic

Sodium phosphate dibasic (141.96 g) was dissolved in deionised water (1 L). The solution was stored at room temperature.

2.1.4.6 0.5 M Ethylenediaminetetraacetic acid pH 8 (EDTA)

Ethylenediaminetetraacetic acid disodium salt hydrate (186.12 g) was dissolved in deionised water (800 ml). The pH was adjusted to 8 and the final volume adjusted to 1L. The solution was stored at room temperature.

2.1.4.7 0.1 M Ethylenediaminetetraacetic acid pH 4 (EDTA)

Ethylenediaminetetraacetic acid disodium salt hydrate (18.6 g) was dissolved in deionised water (400 ml). The pH was adjusted to 4 and the final volume adjusted to 500 ml. The solution was stored at room temperature.

2.1.4.8 4-(2-Hydroxyethyl) piperazine-1-ethanesulfonic acid, N-(2-Hydroxyethyl) piperazine -N′-(2-ethanesulfonic acid) (HEPES) Glucose Buffer (HG Buffer)

HEPES (1.2 g) and glucose (10 g) were dissolved in deionised water (400 ml). The pH was adjusted to 7.2 and the final volume adjusted to 500 ml. The solution was filter sterilised and stored at 4 °C

2.1.5 Protein Extraction Reagents

2.1.5.1 100% (w/v) Trichloroacetic Acid (TCA) Solution

TCA (100 g) was gradually dissolved in deionised water (20 ml). The final volume was adjusted to 50 ml with deionised water and the solution was stored at 4 °C.

2.1.5.2 Protein Resuspension Buffer

Urea (36 g), thiourea (14.4 g), and Trizma® hydrochloride (1.6 g) were dissolved in deionised water (40 ml). The pH of the solution was adjusted to 8 and final volume adjusted to 100 ml with deionised water. The solution was stored at room temperature.

2.1.6 Protein Purification Reagents

2.1.6.1 10 mM Sodium Phosphate Monobasic

Sodium phosphate monobasic dihydrate (1.56 g) was dissolved in deionised water (1 L). The solution was sterilised by autoclaving at 121 °C for 15 min and stored at 4 °C.

2.1.6.2 10 mM Sodium Phosphate Dibasic

Sodium phosphate dibasic (1.4 g) was dissolved in deionised water (1 L). The solution was sterilised by autoclaving at 121 °C for 15 min and stored at 4 °C.

2.1.6.3 10 mM Sodium Phosphate ($NaPO_4$) 50 mM Sodium Chloride (NaCl)

10 mM sodium phosphate monobasic was added to 10 mM sodium phosphate dibasic until pH 6.5 was reached. NaCl (2.9 g per L) was dissolved in the solution. The solution was filter sterilised and sonicated in a sonication bath for 10 min. The solution was stored at 4 °C.

2.1.6.4 ÄKTA FPLC Buffers and Reagents

2.1.6.4.1 20% (v/v) Ethanol

Ethanol (200 ml) was added to deionised water (800 ml). The solution was filter sterilised and sonicated in a sonication bath for 10 min. The solution was stored at room temperature and used within 1 week.

2.1.6.4.2 Protein A Affinity Chromatography Buffers

2.1.6.4.2.1 Equilibration/ Wash Buffer

Sodium chloride (8.76 g) and sodium phosphate dibasic (2.84 g) were dissolved in deionised water (800 ml). The pH of the solution was adjusted to 8 and the final

volume adjusted to 1 L. The solution was filter sterilised and sonicated in a sonication bath for 10 min. The solution was stored at 4 °C and used within 1 week.

2.1.6.4.2.2 Elution Buffer

Sodium citrate (2.94 g) was dissolved in deionised water (80 ml). The pH of the solution was adjusted to 3.5 and the final volume adjusted to 100 ml. The solution was filter sterilised and sonicated in a sonication bath for 10 min. The solution was stored at 4 °C and used within 1 week.

2.1.6.4.2.3 Neutralisation Buffer

Trizma® hydrochloride (15.7 g) was dissolved in deionised water (80 ml). The pH of the solution was adjusted to 9 and the final volume adjusted to 100 ml. The solution was stored at 4 °C.

2.1.6.5 Magnetic Beads Purification Reagents

2.1.6.5.1 Tris Buffered Saline – Tween 20 (TBST)

Trizma® hydrochloride (1.97 g), NaCl (4.38 g), and Tween 20 (250 µl) were dissolved in deionised water (80 ml). The pH of the solution was adjusted to 7.5 and the final volume adjusted to 100 ml. The solution was stored at 4 °C.

2.1.6.5.2 Blocking Buffer

BSA (1 g) was dissolved in TBST (100 ml). The solution was filter sterilised and stored at 4 °C.

2.1.6.5.3 Wash Buffer

Trizma® hydrochloride (1.97 g), NaCl (14.61 g), and Tween 20 (250 µl) were dissolved in deionised water (80 ml). The pH of the solution was adjusted to 7.5 and the final volume adjusted to 100 ml. The solution was stored at 4 °C.

2.1.6.5.4 Elution Buffer

Glycine (1.5 g) was dissolved in deionised water (80 ml). The pH of the solution was adjusted to 2 and the final volume adjusted to 100 ml. The solution was stored at 4 °C

2.1.6.5.5 Neutralisation Buffer

Trizma® hydrochloride (15.76 g) was dissolved in deionised water (80 ml). The pH of the solution was adjusted to 9 and the final volume adjusted to 100 ml. The solution was stored at 4 °C.

2.1.7 Protein Characterisation Reagents

2.1.7.1 Bradford Solution

Bradford reagent (10 ml) (Bio-Rad) was added to PBS (40 ml). The solution was stored at 4 °C for up to 1 week.

2.1.7.2 Sodium Dodecyl Sulphate Polyacrylamide Gel Electrophoresis (SDS-PAGE) Reagents

2.1.7.2.1 1.5 M Tris-HCl pH 8.3

Trizma® hydrochloride (23.64 g) was dissolved in distilled water (60 ml). The pH of the solution was adjusted to 8.3 and the final volume adjusted to 100 ml. The solution was stored at 4 °C.

2.1.7.2.2 0.5 M Tris-HCl pH 6.8

Trizma® hydrochloride (7.88 g) was dissolved in distilled water (60 ml). The pH of the solution was adjusted to 6.8 and the final volume adjusted to 100 ml. The solution was stored at 4 °C.

2.1.7.2.3 10% (w/v) Sodium Dodecyl Sulfate (SDS)

SDS (10 g) was dissolved in distilled water (80 ml). The final volume was adjusted to 100 ml and the solution was stored at room temperature.

2.1.7.2.4 10% (w/v) Ammonium Persulphate (APS)

Ammonium persulphate (100 mg) was dissolved in distilled water (1 ml). The solution was stored at 4 °C and used within 8 h.

2.1.7.2.5 0.5% (w/v) Bromophenol Blue Solution

Bromophenol blue (100 mg) was dissolved in distilled water (20 ml). The solution was stored at 4 °C.

2.1.7.2.6 5 X Reducing Solubilisation Buffer

Glycerol (8 ml) was added to distilled water (4 ml) containing 10% (w/v) SDS (1.6 ml) and 0.5 M Tris-HCl pH 6.8 (1 ml). 2-merceptoethanol (0.4 ml) was added to the solution followed by 0.5 % (w/v) bromophenol blue solution. The solution was stored in aliquots at -20 °C.

2.1.7.2.7 5 X SDS Electrode Running Buffer

Trizma® base (30 g), glycine (144 g), and SDS (10 g) were dissolved in 1.6 L distilled water. The pH of the solution was adjusted to between 8.6 and 8.8 and the final volume adjusted to 2 l. The solution was stored at room temperature.

2.1.7.2.8 1 X SDS Electrode Running Buffer

5 X SDS electrode running buffer (200 ml) was added to distilled water (800 ml).

2.1.7.2.9 Coomassie® Blue Stain Solution

Coomassie® Brilliant Blue R (1 g) was dissolved in a solution of glacial acetic acid (100 ml), methanol (300 ml), and distilled water (100 ml). The final volume was adjusted to 1 L with distilled water and the solution was stored at room temperature.

2.1.7.2.10 Destain Solution

Glacial acetic acid (100 ml) was added to a solution of methanol (300 ml), and distilled water (600 ml). The solution was stored at room temperature.

2.1.7.3 Glucanase Assay Reagents

2.1.7.3.1 50 mM Sodium Phosphate Monobasic

Sodium phosphate monobasic dihydrate (7.8 g) was dissolved in deionised water (1 L). The solution was sterilised by autoclaving at 121 °C for 15 min and stored at 4 °C.

2.1.7.3.2 50 mM Sodium Phosphate Dibasic

Sodium phosphate dibasic (7 g) was dissolved in deionised water (1 L). The solution was sterilised by autoclaving at 121 °C for 15 min and stored at 4 °C.

2.1.7.3.3 50 mM Sodium Phosphate Buffer pH 7.4

50 mM sodium phosphate monobasic was added to 50 mM sodium phosphate dibasic until pH 7.4 was reached. The solution was stored at 4 °C.

2.1.7.3.4 50 mM Sodium Acetate Buffer pH 6

Sodium acetate (4.1 g) was dissolved in deionised water (800 ml). The pH of the solution was adjusted to 6 and the final volume adjusted to 1 L. The solution was stored at 4 °C.

2.1.7.3.5 Laminarin Solution

Laminarin (2.5 mg per ml) was dissolved in sodium acetate buffer. The solution was prepared immediately before use and stored at room temperature.

2.1.7.3.6 Glucanase Standard Solution

Glucanase (50 µl; 0.2 U/ ml) was added in sodium acetate buffer (50 µl). The solution was prepared immediately before use and stored at room temperature.

2.1.7.3.7 Ampliflu™ Red Reagent

Ampliflu™ Red reagent (5 mg) was dissolved in dimethyl sulfoxide (DMSO) (1948 µl). The solution was stored in aliquots at -20 °C until use.

2.1.7.3.8 Horse Radish Peroxidase (HRP) Solution

HRP (10 U per ml) was dissolved in sodium phosphate buffer. The solution was stored in aliquots at -20 °C until use.

2.1.7.3.9 Glucose Oxidase Solution

Glucose oxidase (1000 U per ml) was dissolved in sodium phosphate buffer. The solution was stored in aliquots at -20 °C until use.

2.1.7.3.10 Glucose Standard Solution

Glucose (72 mg per ml) was dissolved in sodium phosphate buffer. The solution was stored in aliquots at -20 °C until use.

2.1.7.3.11 Ampiflu™ Assay Mixture

Ampiflu™ Red reagent (50 µl; 10 mM), HRP solution (100 µl; 10 U/ ml), and glucose oxidase (100 µl; 100 U/ ml) were added to sodium phosphate buffer (4.75 ml). The solution was prepared immediately before use and stored at room temperature.

2.1.8 RP-HPLC Solvents

2.1.8.1 Solvent A: 0.1% (v/v) Trifluoroacetic Acid (TFA) in deionised water

TFA (1 ml) was added to 999 ml deionised water.

2.1.8.2 Solvent B: 0.1% (v/v) TFA in HPLC grade water

TFA (1 ml) was added to 999 ml HPLC grade acetonitrile.

2.1.9 Chemical Crosslinking Reagents

2.1.9.1 Buffers for Chemical Crosslinking

2.1.9.1.1 0.2 M Sodium Bicarbonate ($NaHCO_3$) Buffer

$NaHCO_3$ (1.7 g) was dissolved in deionised water (80 ml). The pH was adjusted to 8.5 and final volume bought to 100 ml. The solution was stored at room temperature.

2.1.9.1.2 0.1 M $NaHCO_3$ Buffer

0.2 M $NaHCO_3$ (10 ml) was added to deionised water (10 ml). The solution was stored at room temperature.

2.1.9.1.3 1 M Tris-HCl pH 7.2

Trizma® hydrochloride (15.7 g) was dissolved in deionised water (80 ml). The pH of the solution was adjusted to 7.2 and the final volume adjusted to 100 ml. The solution was stored at 4 °C.

2.1.9.1.4 1 M Tris-HCl pH 9

Trizma® hydrochloride (15.7 g) was dissolved in deionised water (80 ml). The pH of the solution was adjusted to 9 and the final volume adjusted to 100 ml. The solution was stored at 4 °C.

2.1.9.1.5 0.1 M Glycine pH 2

Glycine (0.1 g) was dissolved in deionised water (80 ml). The pH of the solution was adjusted to 2 and the final volume adjusted to 100 ml. The solution was stored at 4 °C.

2.1.9.1.6 0.1 M HCl

5 M HCl (10 ml) was added to deionised water (490 ml). The solution was stored at room temperature.

2.1.9.1.7 1 mM HCl

0.1 M HCl (1 ml) was added to deionised water (99 ml). The solution was stored at room temperature.

2.1.9.1.8 Standard Conjugation Buffer

Na_2HPO_4 (7.1 g), and NaCl (8.8 g) were dissolved in deionised water (800 ml). The pH of the solution was adjusted to 7.2 and the final volume adjusted to 1 L. The solution was stored at 4 °C for up to 2 months and equilibrated to room temperature before use.

2.1.9.1.9 KLH Conjugation Buffer

Na_2HPO_4 (11.8 g), NaCl (26.3 g), and EDTA (100 ml; 0.5 M) were dissolved in deionised water (300 ml). The pH of the solution was adjusted to 7.2 and the final

volume adjusted to 500 ml. The solution was stored at 4 °C for up to 2 months and equilibrated to room temperature before use.

2.1.9.1.10 PEN 6.8

KH_2PO_4 (13.61 g), NaCl (17.53 g), and EDTA (4 ml; 0.5 M) were dissolved in 1.8 L deionised water. The pH of the solution was adjusted to 6.8 and the final volume adjusted to 2 l. The solution was stored at 4 °C for up to 2 months.

2.1.9.1.11 PEN 7.8

KH_2PO_4 (13.61 g), NaCl (17.53 g), and EDTA (4 ml; 0.5 M) were dissolved in 1.8 L deionised water. The pH of the solution was adjusted to 7.8 and the final volume adjusted to 2 l. The solution was stored at 4 °C for up to 2 months.

2.1.9.1.12 Magnetic Beads Storage Buffer

0.1 M $NaHCO_3$ pH 8.5 (5 ml) was added to 0.05% sodium azide (5 ml). The solution was stored at room temperature.

2.1.9.2 Sulfo-*N*-Hydroxysuccinimide-Acetate (SNA)

SNA was dissolved in deionised water (25.9 mg per ml) with brief vortexing. The solution was prepared immediately before use.

2.1.9.3 Succinimidyl 6-(*N*-(7-Nitrobenz-2-Oxa-1,3-Diazol-5-yl)Amino) Hexanoate (NBD-X-SE)

NBD-X-SE was dissolved in DMSO (10 mg per ml) with brief vortexing. The solution was prepared immediately before use and stored in the dark.

2.1.9.4 Sulfosuccinimidyl 4-[N-maleimidomethyl]cyclohexane-1-carboxylate (Sulfo-SMCC)

Sulfo-SMCC (Thermo Fisher Scientific) was dissolved in DMSO (21 mg per ml) with brief vortexing. The solution was prepared immediately before use.

2.1.9.5 N-succinimidyl S-acetylthioacetate (SATA)

SATA (Thermo Fisher Scientific) was dissolved in DMSO (15 mg per ml unless otherwise stated) with brief vortexing. The solution was prepared immediately before use.

2.1.9.6 0.5 M Hydroxylamine

Hydroxylammonium chloride (3.47 g), triethanolamine base (13.32 ml), and EDTA (200 ml; 0.5 M) were dissolved in deionised water (80 ml). The pH of the solution was adjusted to 7 and the final volume adjusted to 100 ml. The solution was stored at room temperature. The solution was stored at 4 °C for up to 2 months

2.1.9.7 Aldrithiol^{TM}-4

Aldrithiol^{TM}-4 was dissolved in ethanol (100% (v/v)) (11 mg per ml). The solution was stored at -20 °C for up to 2 months.

2.1.10 Enzyme-linked immunosorbant assay (ELISA) Reagents

All ELISA reagents were allowed to equilibrate to room temperature before use unless otherwise stated.

2.1.10.1 Carbonate Coating Buffer

2.1.10.1.1 250 mM Sodium Carbonate (Na_2CO_3)

Na_2CO_3 (10.6 g) was dissolved in deionised water (350 ml) and the final volume was adjusted to 400 ml.

2.1.10.1.2 250 mM Sodium Bicarbonate ($NaHCO_3$)

$NaHCO_3$ (16.8 g) was dissolved in deionised water (700 ml) and the final volume was adjusted to 800 ml.

2.1.10.1.3 5 X Carbonate Coating Buffer

250 mM Na_2CO_3 was added to 250 mM $NaHCO_3$ (800 ml) until pH 9.6 was achieved. The solution was stored at 4 °C.

2.1.10.2 ELISA Wash Buffer

50X wash buffer (20 ml) (Biotrin) was added to deionised water (980 ml). The solution was stored at 4 °C.

2.1.10.3 ELISA Sera and Calibrator Buffer

BSA (1 g) was dissolved in PBST (100 ml). The solution was stored at 4 °C.

2.1.10.4 Anti-Mouse IgG Horse Radish Peroxidase (HRP) Antibody Solution

Anti-Mouse IgG-HRP (Bio-Rad) was diluted 1 in 2000 in conjugate diluent (Biotrin). The solution was stored at 4 °C.

2.1.10.5 Anti-Human IgG Horse Radish Peroxidase (HRP) Antibody Solution

Anti-Human IgG-HRP was diluted 1 in 10,000 in PBST 1% BSA. The solution was stored at 4 °C.

2.1.10.6 ELISA Blocking Solution

BSA (1 g) and sucrose (10 g) were dissolved in PBST (100 ml). The solution was stored at 4 °C.

2.1.10.7 3,3', 5,5'-Tetramethylbenzidine (TMB) Liquid Substrate

TMB (Moss Inc.) was used at the supplied concentration. The solution was stored at 4 °C.

2.1.10.8 ELISA Stop Solution

Concentrated sulfuric acid (H_2SO_4) (28.4 ml) was added to deionised water (972 ml) using a graduated cylinder (glass). The solution was stored at room temperature.

2.1.11 Mass Spectrometry Reagents

2.1.11.1 100 mM Ammonium Bicarbonate (NH_4HCO_3) Buffer

NH_4HCO_3 (400 mg) was dissolved in deionised water (50 ml). The solution was prepared immediately before use.

2.1.11.2 50 mM Ammonium Bicarbonate (NH_4HCO_3) Buffer

100 mM ammonium bicarbonate buffer (5 ml) was added to deionised water (5 ml). The solution was prepared immediately before use.

2.1.11.3 50 mM Ammonium Bicarbonate (NH_4HCO_3) Acetonitrile (50% (v/v)) Buffer

100 mM ammonium bicarbonate buffer (5 ml) was added to acetonitrile (5 ml). The solution was prepared immediately before use.

2.1.11.4 10 mM Ammonium Bicarbonate (NH_4HCO_3) Acetonitrile (10% (v/v)) Buffer

100 mM ammonium bicarbonate buffer (1 ml), acetonitrile (1 ml) were added to deionised water (8 ml). The solution was prepared immediately before use.

2.1.11.5 50 mM Tris-HCl pH 7.5

Trizma® hydrochloride (0.788 g) was dissolved in deionised water (80 ml). The pH of the solution was adjusted to 7.5 and the final volume adjusted to 100 ml. The solution was stored at 4 °C.

2.1.11.6 0.5 M Dithiothreitol (DTT) for In-Solution Digestion

DTT (77 mg) was dissolved in 50 mM ammonium bicarbonate buffer (1 ml). The solution was prepared immediately before use.

2.1.11.7 0.55 M Iodoacetamide (IAA) for In-Solution Digestion

IAA (102 mg) was dissolved in 50 mM ammonium bicarbonate buffer (1 ml). The solution was protected from the light and prepared immediately before use.

2.1.11.8 10 mM DTT for In-Gel Digestion

DTT was dissolved in 100 mM ammonium bicarbonate buffer (at 1.5 mg per 1 ml). The solution was prepared immediately before use.

2.1.11.9 55 mM IAA for In-Gel Digestion

IAA was dissolved in 100 mM ammonium bicarbonate buffer (at 10 mg per 1 ml). The solution was protected from the light and prepared immediately before use.

2.1.11.10 1% (w/v) ProteaseMAX™

ProteaseMAX™ (1 mg) (Promega) was dissolved in 50 mM ammonium bicarbonate (100 µl). The solution was kept on ice during use and any remaining solution was stored at -20 °C.

2.1.11.11 Enzymes for Protein Digestion

2.1.11.11.1 Trypsin for In-Solution Digestion

Sequencing grade Trypsin (20 µg) (Promega) was dissolved in 50 mM acetic acid (20 µl) (supplied with trypsin). The solution was prepared immediately before use and kept on ice.

2.1.11.11.2 Trypsin for In-Gel Digestion

Sequencing grade Trypsin (20 µg) (Promega) was dissolved in 10 mM ammonium bicarbonate acetonitrile (10% (v/v)) buffer (1.5 ml). The solution was prepared immediately before use and kept on ice.

2.1.11.11.3 Glu-C for In-Gel Digestion

Sequencing grade Glu-C (10 µg) (Promega) was dissolved in 10 mM ammonium bicarbonate acetonitrile (10% (v/v)) buffer (770 µl). The solution was prepared immediately before use and kept on ice.

2.1.11.11.4 Asp-N for In-Gel Digestion

Sequencing grade Asp-N (2 µg) (Roche) was dissolved in deionised water (50 µl) diluted to 13 ng/ µl in 50 mM Tris-HCl. The solution was prepared immediately before use and kept on ice.

2.1.11.12 Ion Trap: LC-MS/MS Solvents

2.1.11.12.1 Solvent A: 0.1% (v/v) Formic Acid in Deionised Water

Formic acid (1 ml) was added to deionised water (999 ml).

2.1.11.12.2 Solvent B: 0.1% (v/v) Formic Acid in Acetonitrile (90% (v/v))

Deionised water (100 ml) and formic acid (1 ml) were added to LC-MS grade acetonitrile (899 ml).

2.1.11.13 Q-Exactive: LC-MS/MS Solvents

2.1.11.13.1 Solvent A: 0.1% (v/v) TFA in Acetonitrile (3% (v/v))

LC-MS grade acetonitrile (30 ml) and TFA (1 ml) were added to deionised water (969 ml).

2.1.11.13.2 Solvent B: 0.1% (v/v) TFA in Acetonitrile (80% (v/v))

Deionised water (199 ml) and TFA (1 ml) were added to LC-MS grade acetonitrile (800 ml).

2.1.11.14 Reagents for Millipore® Ziptips

2.1.11.14.1 Resuspension Solution

TFA (5 µl) was added to deionised water (995 µl). The solution was prepared immediately before use.

2.1.11.14.2 Wetting Solution

Acetonitrile (800 µl) and TFA (1 µl) were added to deionised water (199 µl). The solution was prepared immediately before use.

2.1.11.14.3 Equilibration and Washing Solution

TFA (1 µl) was added to deionised water (999 µl). The solution was prepared immediately before use.

2.1.11.14.4 Elution solution

Acetonitrile (600 µl) and TFA (1 µl) were added to deionised water (399 µl). The solution was prepared immediately before use.

2.1.11.14.5 Loading Buffer: 0.05% (v/v) TFA in Acetonitrile (2% (v/v))

Acetonitrile (20 ml) and TFA (0.5 ml) were added to deionised water (979.5 ml).

2.2 Methods

2.2.1 Microbiological Methods – Strain Culture and Storage

Microbial strains used in this study are summarised in Table 2.2.

2.2.1.1 *A. fumigatus* Growth, Maintenance, and Storage

A. fumigatus strains were maintained on MEA (Section 2.1.1.1) or MM (Section 2.1.1.2). A sterile inoculation loop was used to inoculate agar with conidia from stocks. Plates were grown at 37 °C for 5 – 7 days. Conidia were harvested from plates by adding PBST (10 ml) to plates and bringing conidia into suspension using a sterile inoculation loop. The suspension of conidia was centrifuged (2,000 g for 10 min) and suspended in PBS (5 ml). This was repeated twice. PBS stocks of conidia were counted using a haemocytometer and stored at 4 °C. For long-term storage of stocks, the suspension of conidia (500 µl) was added to 80% glycerol (Section 2.1.1.3) (500 µl) and mixed by vortexing briefly. Glycerol stocks were snap frozen in liquid nitrogen and stored at -80 °C.

2.2.1.2 Preparation of Iron Free Glassware

Iron-free glassware was treated with 1 mM EDTA (Section 2.1.1.5) for 3 h at room temperature. After EDTA treatment, glassware was rinsed well with deionised water and then incubated overnight with 5% (v/v) HCl (Section 2.1.1.4) in a fume hood. Glassware were rinsed well with deionised water then sterilised by autoclaving at 121 °C for 15 min.

Table 2.2 Fungal strains with associated antibiotics/ supplements used in this study.

Species	Strain	Antibiotics/ Supplements	Reference
A. fumigatus	ATCC46645 wild-type	N/A	ATCC collection
A. fumigatus	ATCC46645 Δ*sidG* [1]	Hygromycin (100 μg/ ml)	Schrettl *et al.* 2007
A. fumigatus	ATCC46645 Δ*sidD* [1]	Hygromycin (100 μg/ ml)	Schrettl *et al.* 2007

[1] *A. fumigatus* Δ*sidG* and *A. fumigatus* Δ*sidD* were both very kind gifts from Professor Hubertus Haas (Division of Molecular Biology, Biocenter, Medical University Innsbruck, Innsbruck, Austria).

2.2.2 Cell Culture and Storage Methods

2.2.2.1 Cell Culture

All cells were grown at 37 °C 5% CO_2. SP/2/O-Ag 14 myeloma cells were maintained in myeloma culture medium (Section 2.1.2.1) and hybridomas were maintained in hybridoma culture medium variants (Section 2.1.2.2-2.1.2.4). SP/2/O-Ag 14 myeloma cells and hybridomas are loosely adherent and were harvested with gentle sloughing using a pipette. Cell suspensions including conditioned medium were then used to inoculate a new flask typically with a 1 in 3 dilution into fresh culture medium. For feeding, typically two thirds of the conditioned medium was removed and replaced with fresh culture medium. Cells were cultured until confluent and then used to inoculate fresh flasks (typically 75 cm^2 flasks). Hybridoma culture media was retained for screening and/ or antibody purification.

2.2.2.2 Cell Freezing

Cells (SP/2/O-Ag 14 myeloma cells and hybridomas) were frozen from several growth phases and conditions. Typically cells were grown until confluent in 75 cm^2 flasks and fed 1 day prior to freezing. Cells were harvested by sloughing into suspension using a pipette and transferred to a universal. Cell suspension was centrifuged (1,000 rpm for 1 min) and supernatant poured off. Cell pellets were gently suspended in Fetal Bovine Serum, certified, heat inactivated, US origin (0.5 ml per 75 cm^2 flask) (Gibco®) which had been cooled to 4 °C. HyClone HyCryo cryopreservation media (0.5 ml per 75 cm^2 flask) (Thermo Scientific) which had been cooled to 4 °C was added drop-wise to the cell suspension. Cell suspension was transferred to a cryovial (1 ml per cryovial) (Greiner) which was immediately placed in at -80 °C for 4 – 7 days. Cryovials were then transferred to the vapour phase of a

liquid nitrogen container for 2.5 – 3.5 h before submerging and storage in liquid nitrogen.

2.2.2.3 Cell Thawing

Cryovials were removed from the liquid nitrogen and frozen cells were gradually suspended in culture medium (10 ml) heated to 37 °C using a pipette. Cells were immediately centrifuged (1,000 rpm for 1 min) and supernatant poured off. Cells were suspended in culture medium (5 ml) and transferred to a 25 cm^2 flask. The next day, cells were fed culture medium and subsequently maintained as per Section 2.2.2.1.

2.2.3 Siderophore Analysis Methods

2.2.3.1 Siderophore Quantification

Ferri-siderophores were quantified using the molar extinction factor of 2996/ 440 nm (M^{-1} cm^{-1}) as per Schrettl *et al.* (2010). Solutions were measured using a UV Spectrophotometer (Shimadzu UV-2550) and diluted until absorbance values read between 0.2 and 1.2.

2.2.3.2 RP-HPLC Analysis of Siderophores

RP-HPLC analysis of siderophores was carried out using an Agilent Series 1200 HPLC System with a Diode Array Detector (DAD) and a Fluorescence Detector (FLD) and separation across a water: acetonitrile gradient with 0.1% (v/v) TFA (Section 2.1.8). For analysis of siderophores, gradient conditions of 5 – 55% acetonitrile over (A) 18 min or (B) 22 min at 2 ml/ min were used on a C18 column (Agilent Zorbax Eclipse XDB-C18 Semi- Preparative; 5 µm particle size; 9.4 × 250 mm) with DAD detection at 254 and 440 nm. For peak identification by LC-MS/MS, the peak associated with compound of interest was collected. The fractions were

typically evaporated to dryness or to a reduced volume in a SpeedVac™ (DNA 120; Thermo Scientific). Fractions were stored at -20 °C until preparation for LC-MS/MS analysis as per Sections 2.2.13.6 and 2.213.8.

2.2.3.3 RP-HPLC Analysis of NBD-X-SE Derivatised Siderophores

RP-HPLC analysis of NBD-X-SE derivatised siderophores was carried out using an Agilent Series 1200 HPLC System with a DAD and FLD detector and separation across a water: acetonitrile gradient with 0.1% (v/v) TFA (Section 2.1.8). For analysis of siderophores, gradient conditions of 5–100% acetonitrile over 35 min at 2 ml/ min were used on a C18 column (Agilent Zorbax Eclipse XDB-C18 Semi- Preparative; 5 μm particle size; 9.4 × 250 mm) with DAD detection at 254 and 440 nm and FLD detection at Ex/ Em 466/ 535 nm. For peak identification by LC-MS/MS, the peak associated with compound of interest was collected. The fractions were typically evaporated to dryness or to a reduced volume in a SpeedVac™ (DNA 120; Thermo Scientific). Fractions were stored at -20 °C until preparation for LC-MS/MS analysis as per Sections 2.2.13.6 and 2.213.8.

2.2.4 Siderophore Purification Methods

2.2.4.1 Sep-Pak C18 Extraction Method

A Sep-Pak C18 Vac Cartridge (50 – 200 mg bed) (Waters) was attached to a syringe (10 ml) using a screw-in adaptor. For all steps, solvent was pulled through the cartridge following application to an opening at the top of the cartridge. Flow-through was collected in a fresh syringe for each step and discarded or retained accordingly.

First, the cartridge was wet by the application of methanol (5 ml). The cartridge was then equilibrated with RP-HPLC Solvent A (10 ml) (Section 2.1.8). Next, the sample in an appropriate solvent (if necessary diluted in RP-HPLC Solvent

A) was applied to the cartridge. The cartridge was then washed with RP-HPLC Solvent A (10 ml). Methanol (5 ml) was then applied to the cartridge to elute any bound material. Elutions were collected in fractions (1 ml) and evaporated to dryness in a SpeedVac^{TM} (DNA 120; Thermo Scientific).

2.2.4.2 Sep-Pak C18 Extraction of FSC

A. fumigatus Δ*sidG* was grown in MM without iron (48 h; 37 °C; 200 rpm) (similar to Knetsch *et al* (2015)). Cultures were harvested by filtering through miracloth and supernatant was stored at -20 °C until processing. Supernatant was thawed, centrifuged (4,000 rpm for 30 min), supernatant collected and passed through 0.45 μm filters. Supernatant was then ferrated by the addition of 0.5 M $FeSO_4$ to a final concentration of 1.5 mM and left for 30 min at room temperature on a rocker in the dark. Ferrated supernatant was concentrated *via* Sep-Pak C18 cartridges as described in Section 2.2.4.1. Dried extracts were stored at -20 °C until suspension in an appropriate buffer for use.

2.2.4.3 Chloroform Extraction of FSC

Sep-Pak C18 extracted FSC (Section 2.2.4.2) was suspended in 0.1 M $NaHCO_3$ pH 8.5 (Section 2.1.9.1.2) to a final concentration of 2.9 mM FSC^{Fe+} (quantified as per Section 2.2.3.1). FSC^{Fe+} was mixed with an equal volume of chloroform in a 50 ml universal (Falcon) for 10 min at room temperature with venting. The mixture was then centrifuged (500 rpm for 10 min at 20 °C). The bottom organic layer was removed carefully with a pipette and transferred to a glass bulb for evaporation in a rotary evaporator (Section 2.2.4.5). Dried extracts were stored at -20 °C until suspension in an appropriate buffer for use.

2.2.4.4 Chloroform Extraction of TAFC

A. fumigatus was grown in MM without iron (ATCC 46645; 72 h; 37 °C; 200 rpm). Cultures were harvested by filtering through miracloth and supernatant was stored at -20 °C until processing. Supernatant was thawed, centrifuged (4,000 rpm for 30 min), and passed through 0.45 µm filters. Culture supernatant was mixed with an equal volume of chloroform in a large separatory funnel for 10 min at room temperature with venting. The mixture was allowed to settle for 0.5 – 1 h at room temperature in a fume hood. The bottom organic layer was removed by gently opening the tap and transferred to a glass bulb for evaporation in a rotary evaporator (Section 2.2.4.5). Dried extracts were suspended in deionised water and stored at -20 °C until use.

2.2.4.5 Rotary Evaporation of Organic Extraction Samples

Organic extracts (Sections 2.2.4.3 and 2.2.4.4) in a glass bulb were evaporated under a vacuum whilst rotating and submerged in a water bath set to 37 °C (Stuart RE300DB digital water bath). Dried extracts were suspended and/ or stored according to the compound.

2.2.4.6 RP-HPLC Purification of Siderophores

RP-HPLC purification of siderophores was carried out using an Agilent Series 1200 HPLC System with a DAD and FLD detector and separation across a water: acetonitrile gradient with 0.1% (v/v) TFA (Section 2.1.8). For purification of siderophores, gradient conditions of 5 – 55% acetonitrile over 22 min at 2 ml/ min on a C18 column (Agilent Zorbax Eclipse XDB-C18 Semi- Preparative; 5 µm particle size; 9.4 × 250 mm) with DAD detection at 254 and 440 nm. The peak associated with compound of interest (FSC or DAFC as per LC-MS/MS identification) was collected following repeated injection (50 – 100 µl). Fractions were either evaporated

to dryness or reduced to an appropriate volume in a SpeedVac™ (DNA 120; Thermo Scientific). Alternatively, fractions were pooled, diluted 1 in 2 in RP-HPLC Solvent A (Section 2.1.8) and following Sep-Pak C18 extraction (Section 2.2.4.1) evaporated to dryness in a SpeedVac™.

2.2.5 Siderophore Crosslinking Methods

2.2.5.1 Fluorescent Siderophore Synthesis

2.2.5.1.1 Derivatisation of FSC with NBD-X-SE

FSC^{+Fe} was extracted from fungal supernatant *via* Sep-Pak C18 concentration as per Section 2.2.4.1 – 2.2.4.2. Dried extracts were then organically extracted with chloroform (Section 2.2.4.3 and 2.2.4.5). Organic extracts were RP-HPLC purified (Section 2.2.4.6) and fractions containing FSC^{+Fe} were pooled, diluted 1 in 2 in RP-HPLC Solvent A (Section 2.1.8), and concentrated *via* Sep-Pak C18 application (Section 2.2.4.1 – 2.2.4.2). Dried extracts were suspended in 0.1 M $NaHCO_3$ pH 8.5 (Section 2.1.9.1.2) with acetonitrile 50% (v/v) at a final concentration of 2 mM for use in NBD-X-SE derivatisation. 0.88 µmoles of NBD-X-SE (34 µl; 26 mM in DMSO) (Section 2.1.9.3) was added to 0.88 µmoles of RP-HPLC purified FSC^{+Fe} (440 µl; 2 mM in 0.1 M $NaHCO_3$ with 50% (v/v) acetonitrile). Control reactions using NBD-X-SE only, organically extracted FSC^{+Fe} only, or buffers only at equivalent volumes were also conducted in parallel. The reactions were incubated for 1 h at room temperature on a rocker in the dark before RP-HPLC (Section 2.2.3.3) or LC-MS/MS analysis (Section 2.2.13.7) after RP-HPLC purification. FSC-NBD was stored at -20 °C until use in uptake studies.

2.2.5.1.2 Chelation of Iron from FSC-NBD

Removal of iron from FSC-NBD was adapted from Knetsch *et al*. (2015). 126 nmoles of FSC-NBD (68 µl) (Section 2.2.5.1.1) was added to 12.5 µmoles of EDTA pH 4 (432 µl; 0.1 M) (Section 2.1.4.6) or an equivalent volume of sodium phosphate buffer with pH adjusted to 4 (0.1 M). The reactions were mixed briefly by vortexing and incubated at 4 °C overnight (X 2). Fluorescence (Ex/Em 466/ 535) was read using a fluorescence spectrophotometer (Varian Eclipse^{TM}) and expressed as a percentage of the negative (sodium phosphate) control.

2.2.5.1.3 Generation of DAFC for NBD-X-SE Derivatisation

FSC^{+Fe} was extracted from fungal supernatant *via* Sep-Pak C18 concentration as per Section 2.2.4.1 – 2.2.4.2. Dried extracts were suspended in 0.1 M $NaHCO_3$ pH 8.5 (Section 2.1.9.1.2) at a final concentration of 5.2 mM. 104 µmoles of SNA (1.04 ml; 100 mM in deionised water) was added to 52 µmoles of Sep-Pak extracted FSC^{+Fe} (10 ml; 5.2 mM in 0.1 M $NaHCO_3$). The reaction was incubated for 1 h at room temperature on a rocker in the dark. Products were analysed by RP-HPLC (Section 2.2.3.2). Upon confirmation of maximal DAFC levels, any remaining NHS activity was quenched by the addition of 1M Tris-HCl (208 µl) (Section 2.1.9.1.3) to a 10-fold molar excess over SNA (208 µmoles). DAFC was then RP-HPLC purified from the reaction as per Section 2.2.4.6. Fractions were pooled, diluted 1 in 2 in RP-HPLC Solvent A (Section 2.1.8) and following Sep-Pak C18 extraction (Section 2.2.4.1 – 2.2.4.2) evaporated to dryness in a SpeedVac^{TM}. Dried extracts were stored at -20 °C until use in NBD-X-SE derivatisation.

2.2.5.1.4 Derivatisation of DAFC with NBD-X-SE

RP-HPLC purified DAFC was suspended in 0.1 M $NaHCO_3$ pH 8.5 (Section 2.1.9.1.2) with acetonitrile 50% (v/v) at a final concentration of 2.2 mM for use in NBD-X-SE derivatisation. 2 µmoles of NBD-X-SE (77 µl; 26 mM in DMSO) (Section 2.1.9.1) was added to 2 µmoles of RP-HPLC purified $DAFC^{+Fe}$ (923 µl; 2.2 mM in 0.1 M $NaHCO_3$ with 50% (v/v) acetonitrile) (Section 2.2.5.1.3). Control reactions using NBD-X-SE only, RP-HPLC purified $DAFC^{+Fe}$ only, or buffers only at equivalent volumes were also conducted in parallel. The reactions were incubated for 1 h at room temperature on a rocker in the dark before RP-HPLC (Section 2.2.3.3) or LC-MS/MS analysis (Section 2.2.13.8) after desalting (Section 2.2.13.4). Upon confirmation of DAFC-NBD generation, the reaction was quenched by the addition of 1M Tris-HCl. DAFC-NBD was stored at -20 °C until use in uptake studies.

2.2.5.2 Siderophore Conjugate Synthesis for ELISA plates

2.2.5.2.1 Derivatisation of BSA with SATA

SATA (299 µl; 23 mg/ ml in DMSO) was added to BSA (2 ml; 10 mg/ ml in PBS) creating a 100X molar excess of SATA to BSA. The reaction was incubated at room temperature in the dark for 1 h on a rocker, followed by rotating at 4 °C overnight. Excess SATA was removed using a Sephadex G-25 PD-10 Desalting Column (GE Healthcare Life Sciences) equilibrated with PEN 7.8 (Section 2.1.9.1.10) (normally PEN 6.8). The protein content measured by Bradford (Section 2.2.12.1) and SATA-BSA was stored at -20 °C until use.

2.2.5.2.2 Conjugation of FSC to SATA-BSA *via* SMCC

The following reactions were carried out so that SATA-BSA thiol deprotection and SMCC modification of FSC were completed simultaneously to ensure both could be

used immediately after preparation. While SATA-BSA was being demasked, the SMCC modification of FSC was carried out with the addition of 0.75 X molar excess of Sulfo-SMCC to RP-HPLC purified FSC^{+Fe} in a sodium phosphate buffer.

The thiol groups of SATA modified BSA (Section 2.2.5.2.1) were demasked by the addition hydroxylamine (0.5 M; 0.1 ml) to SATA-BSA (10 mg/ ml; 1 ml). The reaction was incubated at room temperature in the dark for 2 h on a rocker. Demasked SATA-BSA was separated from other reaction constituents using a Sephadex G-25 PD-10 Desalting Column (GE Healthcare Life Sciences) equilibrated with PEN 7.8 (Section 2.1.9.1.10) (normally PEN 6.8). The thiol content was then measured as per Section 2.2.5.5 and protein content measured by Bradford (Section 2.2.12.1).

FSC^{+Fe} was obtained from fungal supernatant *via* Sep-Pak C18 concentration as per Section 2.2.4.1 – 2.2.4.2. Extracts were RP-HPLC purified (Section 2.2.4.6) and fractions containing FSC^{+Fe} were pooled and reduced in volume in a SpeedVac™ (DNA 120; Thermo Scientific). Extracts were brought to a final concentration of 2.6 mM FSC^{+Fe} 50 mM sodium phosphate pH 7.2 for Sulfo-SMCC derivatisation. 7.1 µmoles of Sulfo-SMCC (142 µl; 50 mM in DMSO) was added to 9.45 µmoles of RP-HPLC purified FSC^{+Fe} (3.675 ml; 2.6 mM in sodium phosphate buffer). The reaction was agitated gently on a vortex at room temperature in the dark for 1 h.

4 mg of demasked SATA-BSA (2 mg/ ml; 2 ml) was added to 8.6 µmoles of the FSC-SMCC reaction (3.5 ml; 2.47 mM FSC 1.86 mM Sulfo-SMCC in sodium phosphate buffer). The reaction was incubated at room temperature in the dark for 2 h on a rocker, followed by rotating at 4 °C overnight. After conjugation, the reaction was centrifuged (2000 rpm for 10 min), the precipitate was discarded and the supernatant dialysed against PBS (Section 2.1.4.2). The conjugated siderophore

content was estimated by reading at 440 nm (Section 2.2.3.1) and protein content measured by Bradford (Section 2.2.12.1). FSC-BSA was then analysed by SDS-PAGE (Section 2.2.12.2) and stored in aliquots (1 ml) at -20 °C.

2.2.5.2.3 Conjugation of acetylated FSC to SATA-BSA *via* SMCC

The following reactions were carried out so that SATA-BSA thiol deprotection and SMCC modification of acetylated FSC^{+Fe} were completed simultaneously to ensure both could be used immediately after preparation. While SATA-BSA was being demasked, the SMCC modification of acetylated FSC^{+Fe} was carried out with the addition of equimolar Sulfo-SMCC to the acetylated FSC^{+Fe} reaction (FSC/ MAFC/ DAFC content) in a sodium phosphate buffer.

The thiol groups of SATA modified BSA (Section 2.2.5.2.1) were demasked by the addition hydroxylamine (0.5 M; 0.2 ml) to SATA-BSA (5 mg/ ml; 2 ml). The reaction was incubated at room temperature in the dark for 2 h on a rocker. Demasked SATA-BSA was separated from other reaction constituents using a Sephadex G-25 PD-10 Desalting Column (GE Healthcare Life Sciences) equilibrated with PEN 7.8 (Section 2.1.9.1.10) (normally PEN 6.8). The thiol content was then measured as per Section 2.2.5.5 and protein content measured by Bradford (Section 2.2.12.1).

FSC^{+Fe} was obtained from fungal supernatant *via* Sep-Pak C18 concentration as per as per Section 2.2.4.1 – 2.2.4.2. Extracts were RP-HPLC purified (Section 2.2.4.6) and fractions containing FSC^{+Fe} were pooled and reduced in volume in a SpeedVac™ (DNA 120; Thermo Scientific). Extracts were brought to a final concentration of 5.9 mM FSC^{+Fe} 231 mM sodium phosphate pH 7.2 for SNA acetylation. FSC^{+Fe} was acetylated *via* sequential addition of SNA (similar to as described in Section 2.2.5.1.3) with RP-HPLC monitoring until maximal DAFC

levels were obtained (43% DAFC; 29% MAFC; 17% FSC; 12% FSC). The final acetylated FSC^{+Fe} reaction was measured to be 5 mM total siderophore for Sulfo-SMCC derivatisation. 13 µmoles of Sulfo-SMCC (130 µl; 100 mM in DMSO) was added to 15.5 µmoles of the acetylated FSC^{+Fe} reaction (3.1 ml; 5 mM in sodium phosphate buffer). The reaction was agitated gently on a vortex at room temperature in the dark for 1 h.

5 mg of demasked SATA-BSA (2.5 mg/ ml; 2 ml) was added to 15 µmoles of the acetylated FSC-SMCC reaction (3 ml; 4.8 mM total siderophore 4 mM Sulfo-SMCC in sodium phosphate buffer). The reaction was incubated at room temperature in the dark for 2 h on a rocker, followed by rotating at 4 °C overnight. After conjugation, the reaction was centrifuged (2000 rpm for 10 min), the precipitate was retained and the supernatant dialysed against PBS (Section 2.1.4.1). The siderophore content was then estimated by reading at 440 nm (Section 2.2.3.1) and protein content measured by Bradford (Section 2.2.12.1). The acetylated FSC-BSA conjugate was then analysed by SDS-PAGE (Section 2.2.12.2) and stored in aliquots (1 ml) at -20 °C.

2.2.5.3 Siderophore Immunogen Synthesis

2.2.5.3.1 Derivatisation of KLH with SATA

Lyophilised KLH (20 mg) (Imject™ mcKLH in PBS; Thermo Fisher Scientific) was gently suspended in deionised water (2 ml) creating a buffer of 0.15 M NaCl 0.1 M sodium phosphate pH 7.2 at 10 mg/ ml. SATA was freshly dissolved in DMSO (15 mg/ ml) (Section 2.1.9.4). SATA (134 µl) was added to KLH (1.99 ml) creating over a 4000X molar excess of SATA to KLH. The reaction was incubated at room temperature in the dark for 2 h on a rocker. The protein content was measured by

Bradford (Section 2.2.12.1) and SATA-KLH was typically used immediately but otherwise stored at -20 °C until use

2.2.5.3.2 Conjugation of FSC to SATA-KLH *via* SMCC

The following reactions were carried out so that SATA-KLH thiol deprotection and SMCC modification of FSC^{+Fe} were completed simultaneously to ensure both could be used immediately after preparation. While SATA-KLH was being demasked, the SMCC modification of FSC^{+Fe} was carried out with the addition of 0.75X molar excess Sulfo-SMCC to the FSC^{+Fe} reaction in standard conjugation buffer pH 7.2 (Section 2.1.9.1.8).

The thiol groups of SATA modified KLH (Section 2.2.5.3.1) were demasked by the addition hydroxylamine (0.5 M; 0.4 ml) to SATA-KLH (9.4 mg/ ml; 2 ml). The reaction was incubated at room temperature in the dark for 1 h on a rocker. Demasked SATA-KLH was separated from other reaction constituents using a Sephadex G-25 PD-10 Desalting Column (GE Healthcare Life Sciences) equilibrated with KLH conjugation buffer pH 7.2 (Section 2.1.9.1.9). The thiol content was then measured as per Section 2.2.5.4 and protein content measured by Bradford (Section 2.2.12.1).

FSC^{+Fe} was obtained from fungal supernatant *via* Sep-Pak C18 concentration as per as per Section 2.2.4.1 – 2.2.4.2. Extracts were RP-HPLC purified (Section 2.2.4.6) and fractions containing FSC^{+Fe} were pooled and reduced in volume in a SpeedVac™ (DNA 120; Thermo Scientific). Extracts were brought to a final concentration of 6.5 mM FSC^{+Fe} in standard conjugation buffer pH 7.2 (Section 2.1.9.1.8) for use in Sulfo-SMCC derivatisation. 6.3 µmoles of Sulfo-SMCC (126 µl; 50 mM in DMSO) was added to 8.4 µmoles of RP-HPLC purified FSC^{+Fe} (1.292 ml;

6.5 mM in standard conjugation buffer (Section 2.1.9.1.8)). The reaction was agitated gently on a vortex at room temperature in the dark for 1 h. An aliquot was taken and quenched for later RP-HPLC analysis.

9.8 mg of demasked SATA-KLH containing 264 nmol –SH (3.13 mg/ ml; 2.2 ml in KLH conjugation buffer) was added to 7.1 μmoles of the FSC-SMCC reaction (1.2 ml; 5.9 mM FSC 4.4 mM Sulfo-SMCC (36% FSC-$(SMCC)_1$ according to RP-HPLC analysis)). The reaction was incubated at room temperature in the dark for 3 h on a rocker. Aliquots were taken at the start and end of the reaction for immediate RP-HPLC analysis. After conjugation, the reaction was centrifuged (2000 rpm for 10 min), the orange precipitate was retained and the supernatant dialysed against PBS (Section 2.1.4.2). The siderophore content was then estimated by reading at 440 nm (Section 2.2.3.1) and protein content measured by Bradford (Section 2.2.12.1). FSC-KLH was then recombined with the precipitate and stored at -20 °C until mouse immunisations.

2.2.5.3.3 Conjugation of acetylated FSC to SATA-KLH *via* SMCC

The following reactions were carried out so that SATA-KLH thiol deprotection and SMCC modification of acetylated FSC^{+Fe} were completed simultaneously to ensure both could be used immediately after preparation. While SATA-KLH was being demasked, the SMCC modification of the acetylated FSC^{+Fe} reaction was carried out with the addition of equimolar Sulfo-SMCC to the acetylated FSC^{+Fe} reaction (FSC/ MAFC/ DAFC content) in sodium phosphate buffer pH 7.2.

The thiol groups of SATA modified KLH (Section 2.2.5.3.1) were demasked by the addition hydroxylamine (0.5 M; 0.2 ml) to SATA-KLH (10 mg/ ml; 2 ml). The reaction was incubated at room temperature in the dark for 1 h on a rocker. Demasked

SATA-KLH was separated from other reaction constituents using a Sephadex G-25 PD-10 Desalting Column (GE Healthcare Life Sciences) equilibrated with KLH conjugation buffer pH 7.2 (Section 2.1.9.1.9). The thiol content was then measured as per Section 2.2.5.4 and protein content measured by A_{280}.

FSC^{+Fe} was obtained from fungal supernatant *via* Sep-Pak C18 concentration as per as per Section 2.2.4.1 – 2.2.4.2. Extracts were RP-HPLC purified (Section 2.2.4.6) and fractions containing FSC^{+Fe} were pooled and reduced in volume in a SpeedVac™ (DNA 120; Thermo Scientific). Extracts were brought to a final concentration of 5.8 mM FSC^{+Fe} in sodium phosphate buffer pH 7.2 for SNA acetylation. FSC^{+Fe} was acetylated *via* sequential addition of SNA (similar to as described in Section 2.2.5.1.3) with RP-HPLC monitoring until maximal DAFC levels were obtained (37% DAFC; 37% MAFC; 13% FSC; 12% TAFC). The acetylated FSC^{+Fe} reaction mixture was brought to 5.6 mM total siderophore for Sulfo-SMCC derivatisation. 13.4 µmoles of Sulfo-SMCC (268 µl; 50 mM in DMSO) was added to 15.1 µmoles of the acetylated FSC^{+Fe} reaction (2.7 ml; 5.6 mM). The reaction was agitated gently on a vortex at room temperature in the dark for 1 h. An aliquot was taken and quenched with an excess of Tris-HCl (1 M) for later RP-HPLC analysis.

6.4 mg of demasked SATA-KLH containing 166 nmol –SH (2.8 mg/ ml; 2.3 ml in KLH conjugation buffer) was added to 15 µmoles of the acetylated FSC-SMCC reaction (2.95 ml; 5.1 mM FSC 4.4 mM Sulfo-SMCC (14% MAFC-$(SMCC)_1$ and 10% DAFC-$(SMCC)_1$ according to RP-HPLC analysis)). The reaction was incubated at room temperature in the dark for 0.5 h on a rocker followed by rotating at 4 °C overnight. Aliquots were taken at the start and end of the reaction for immediate RP-HPLC analysis. After conjugation, the reaction was centrifuged (2000 rpm for 10

min), the orange precipitate was retained and the supernatant dialysed against PBS (Section 2.1.4.2). The siderophore content was then estimated by reading at 440 nm (Section 2.2.3.1) and protein content measured by Bradford (Section 2.2.12.1). Acetylated FSC-KLH was then recombined with the precipitate and stored at -20 °C until mouse immunisations.

2.2.5.4 Estimation of thiol content of demasked SATA modified proteins using Aldrithiol-4

Thiol groups of SATA modified protein were demasked by the addition of a volume of hydroxylamine (0.5 M) (Section 2.1.9.6) equivalent to 10% of the final reaction volume. The reaction was incubated at room temperature in the dark for 1 h.

0.5 M hydroxylamine (20 µl) was added to PEN 6.8 (980 µl) (Section 2.1.9.1.10) and 500 µl transferred to a quartz cuvette. This was used to blank the spectrophotometer at 324 nm. Aldrithiol-4 (2 µl; 11 mg/ ml) (Section 2.1.10.16) was added to the blank and after 1 min the absorbance at 324 nm was read (A_{324} Blank). PEN 6.8 (500 µl) was then used to blank the spectrophotometer at the specific λ_{max} for the protein in use ($A_{\lambda max}$ Sample). The demasked protein solution (100 µl) was added to PEN 6.8 (400 µl) and the absorbance measured ($A_{\lambda max}$ Sample). This solution was then used to blank the spectrophotometer at 324 nm. Aldrithiol-4 (2 µl; 11 mg/ ml) was added to the solution and after 1 min the absorbance at 324 nm was read (A_{324} Sample). The recorded values were then input into the below formula to calculate the number of thiol groups per protein molecule.

$$[\text{Protein}]\ \mu M = \frac{A_{\lambda max}\ \text{Sample X 5 X 1.1}}{\text{Protein extinction coefficient}}$$

$$[\text{SH}]\ \mu M = \frac{A_{324}\ \text{Sample} - A_{324}\ \text{Blank X 5 X 1.1}}{0.0198}$$

$$\textbf{Thiols per protein} = \frac{[\text{SH}]\ \mu M}{[\text{Protein}]\ \mu M}$$

2.2.5.5 Coating of Magnetic Beads with DAFC

FSC^{+Fe} was obtained from fungal supernatant *via* Sep-Pak C18 concentration as per as per Section 2.2.4.1 – 2.2.4.2. FSC^{+Fe} was acetylated *via* sequential addition of SNA (similar to as described in Section 2.2.5.1.3) with RP-HPLC monitoring until maximal DAFC levels were obtained. The acetylated FSC^{+Fe} reaction was organically extracted with an equal volume of chloroform (Section 2.2.4.3 and 2.2.4.5). If necessary, reaction was subjected to further acetylation *via* SNA addition after organic extraction. Extracts were suspended in 0.1 M $NaHCO_3$ at a final concentration of 5.2 mM and analysed by RP-HPLC to confirm maximal DAFC levels.

NHS-activated magnetic beads (Pierce™) were equilibrated to room temperature and mixed well by gentle vortexing. Beads (300 µl) were transferred to a 1.5 ml centrifuge tube in duplicate. Beads were collected in a magnetic rack and supernatant removed with a pipette. Ice-cold 1 mM HCl (1 ml) was added to beads followed by a gentle vortex for 15 sec. Beads were collected in a magnetic rack and supernatant removed. The acetylated FSC^{+Fe} reaction (300 µl; 5.2 mM in 0.1 M $NaHCO_3$) (prepared as outlined above) or sodium bicarbonate buffer (300 µl; 0.1 M $NaHCO_3$) was added to beads in singleton. Beads were incubated for 2 h while rotating at room temperature, with vortexing (for 15 sec) every 5 min for the first 30

min and then every 15 min for the remaining 1.5 h. Beads were collected in a magnetic rack, supernatant removed and retained for RP-HPLC analysis. Elution buffer (1 ml) (Section 2.1.6.5.4) was added to beads followed by vortexing (for 15 sec). Beads were collected in a magnetic rack and supernatant removed. The 0.1 M glycine elution step was repeated. Deionised water (1 ml) was added to beads followed by vortexing (for 15 sec). Beads were collected in a magnetic rack and supernatant removed. Neutralisation buffer (1 ml) (Section 2.1.6.5.5) was added to beads followed by vortexing (for 30 sec). Beads were incubated for 2 h while rotating at room temperature before collecting in a magnetic rack and removing the supernatant. Deionised water (1 ml) was added to beads followed by vortexing (for 15 sec). Beads were collected in a magnetic rack and supernatant removed. Magnetic beads storage buffer (1 ml) (Section 2.1.9.1.2) was added to beads followed by vortexing (for 15 sec). Beads were collected in a magnetic rack and supernatant removed. Magnetic beads storage buffer (300 µl) was added to beads and beads were stored at 4 °C until use.

2.2.6 Microscopic Analysis of *A. fumigatus*

2.2.6.1 Fluorescent Siderophore Uptake Studies

A. fumigatus ATCC 46645 was inoculated into MM with and without iron at 1 X 10^3 conidia/ ml in a 12 well plate (1 ml/ well) containing sterilised coverslips in each well. *A. fumigatus* was grown for 20 h at 37 °C static. Supernatant was removed and mycelia were washed four times with fresh cognate media before addition of fluorescent siderophore supplemented MM. MM with and without iron was supplemented with fluorescent siderophores at 50 µM based on the total siderophore content of the fluorescent siderophore stock (Section 2.2.5.1.1 and 2.2.5.1.4). In

addition, controls with NBD-X-SE only, siderophore only, or reaction buffer only were included at equivalent concentrations. All media was filter sterilised after treatment addition. Mycelia were incubated with treatments for 1 h at 37 °C before supernatant was removed. Mycelia were washed four times with HG Buffer (Section 2.1.4.8). Coverslips were mounted onto slides, fixed with nail varnish, and visualised using a fluorescent microscope (Olympus BX51; GFP filter: Ex/Em 492–495 nm/ 517–527 nm). All treatments were performed at least n = 2 and a minimum of 3 images were taken per replicate.

2.2.6.2 Visualisation of *A. fumigatus* using Calcofluor-White or FUN1

A. fumigatus ATCC 46645 was inoculated into MM with and without iron at 1 X 10^5 conidia/ ml in a 6 well plate (4 ml/ well) containing sterilised coverslips in each well. *A. fumigatus* was grown for 20 h at 37 °C static. Supernatant was removed and mycelia were washed with HG buffer (Section 2.1.4.8) before addition of of either (i) 20 µM FUN-1 or (ii) 20 µM FUN-1 25 µM Calcofluor-White in HG (2 ml) to each well. Mycelia were incubated with treatments for 30 min at 37 °C before supernatant was removed. Mycelia were washed four times with HG Buffer. Coverslips were mounted onto slides, fixed with nail varnish, and visualised using a fluorescent microscope (Olympus BX51; DAPI filter).

2.2.7 Disc-Based Plate Inhibtion Assay for Anti-FSC Antibodies

FSC^{+Fe} was prepared as described in Section 2.2.4.1 – 2.2.4.2. All solutions were filtered through 0.22 µm Cellulose Spin-Filters (Costar) before use. FSC^{+Fe} or PBS were added to anti-FSC IgM, GST-GtmA fusion protein (at equivalent concentration to anti-FSC IgM) or PBS to a final volume of 35 µl. The solutions were incubated for 30 min at 37 °C. *A. fumigatus* Δ*sidD* ATCC 46645 (20 µl; 5 X 10^7 conidia/ ml) was

inoculated and spread onto MM agar without iron (Section 2.1.1.2.6) supplemented with BPS (200 μM) in a 6 well plate. Assay discs (sterilised by autoclaving) (6 mm; Whatman®) were added to freshly inoculated media using a sterile forceps. Plates were allowed to dry for approximately 10 min in a laminar flow cabinet. The pre-incubated solutions (10 μl) containing (i) siderophore only, (ii) siderophore and antibody, or (iii) GST-GtmA and antibody were added to each disc. Plates were allowed to dry for approximately 20 min in a laminar flow cabinet. Plates were then incubated for 24 – 96 h at 37 °C and results recorded by photography.

2.2.8 ELISA Methods

All reagents were equilibrated to room temperature prior to use unless otherwise stated.

2.2.8.1 ELISA Plates Preparation

2.2.8.1.1 Preparation of Siderophore-BSA Coated Plates

96-well Maxisorp Nunc immunoassay plates (Thermo Fisher Scientific) were coated with 100 μl FSC- or acetylated FSC- or SATA-BSA (Section 2.2.5.2) diluted in 1X carbonate coating buffer per well (Section 2.1.10.1.3). Coating concentrations were as per Table 2.3 unless otherwise stated. Plates were sealed and incubated at 4 °C overnight. The coating solution was poured off and plates were washed four times with ELISA wash buffer (Section 2.1.10.2). ELISA blocking solution (200 μl) (Section 2.1.10.6) was added to each well, plates were sealed and incubated at 37 °C for 2 h. The blocking solution was poured off and plates were allowed to dry without seals at 37 °C overnight. Plates were sealed, packaged with desiccant sachet and stored at 4 °C until use.

Table 2.3 Coating conditions for siderophore ELISA plates.

Antigen	Coating agent	Coating conc.	Screening system
FSC	FSC-BSA	0.09 µg/ ml	For screening murine tail bleeds (selected after screening sera against a titre of coating concentrations (0.02 – 1.4 µg/ ml)).
	FSC-BSA or SATA-BSA	0.5 µg/ ml	For initial phase of hybridoma supernatant screening.
	FSC-BSA	0.09 µg/ ml	For general hybridoma supernatant screening and purified antibody analysis.
TAFC	Acetylated FSC-BSA	0.12 µg/ ml	For screening murine tail bleeds (selected after screening sera against a titre of coating concentrations (0.03 – 1.9 µg/ ml)).
	Acetylated FSC-BSA	0.12 µg/ ml	For general hybridoma supernatant screening and purified antibody analysis.

2.2.8.1.2 Preparation of Secreted Protein Coated Plates for Indirect ELISA

Similar to Moloney *et al.* (2016b) 96-well Maxisorp Nunc immunoassay plates (Thermo Fisher Scientific) were coated with 100 µl of *A. fumigatus* secreted proteins extracted from iron-starved or iron-sufficient growth (5 µg/ ml) (Section 2.2.10.2) were diluted in 1X carbonate coating buffer (Section 2.1.10.1.3). Plates were sealed and incubated at 37 °C for 1 h. The coating solution was poured off and plates were four times with ELISA wash buffer (Section 2.1.10.2). ELISA blocking solution (200 µl) (Section 2.1.10.6) was added to each well, plates were sealed and incubated at 37 °C for 2 h. The blocking solution was poured off and plates were allowed to dry without seals at 37 °C overnight. Plates were sealed, packaged with desiccant sachet and stored at 4 °C until use.

2.2.8.2 Calibrant and Sample Preparation

2.2.8.2.1 Preparation of Murine Tail Bleeds for ELISA Analysis

Tail bleeds were taken from mice and sera extracted by fractionation (by NICB, DCU as per Section 2.2.9.1). 20 µl per mouse was harvested for ELISA screening. Sera were diluted to indicated titres in PBST 1% BSA (Section 2.1.10.3).

2.2.8.2.2 Preparation of Human Sera Samples for ELISA Analysis

Human serum samples (obtained, with permission, from the Irish Blood Transfusion Service) were thawed on ice and diluted 1 in 100 in PBST 1% BSA (Section 2.1.10.3).

2.2.8.2.3 Preparation of Competitors for Competitive ELISA Analysis

FSC^{+Fe} was obtained from fungal supernatant *via* Sep-Pak C18 concentration as per Section 2.2.4.1 – 2.2.4.2. Extracts were RP-HPLC purified (Section 2.2.4.6) and

fractions containing FSC^{+Fe} were pooled and reduced in volume in a SpeedVac™ (DNA 120; Thermo Scientific). Extracts were brought to pH 7.2 in sodium phosphate buffer and quality checked by RP-HPLC analysis. TAFC was obtained as described in Section 2.2.4.4 and ferrated by the addition of $FeSO_4$ (0.5 M). BmGT and ferrichrome were purchased from Enzo Life Sciences and Sigma, respectively. Ferri-ornibactin was a kind gift from Dr Niamh Whelan and Dr Máire Callaghan (Institute of Technology, Tallaght). Subsequently, competitors were diluted to 0.1 mM in PBST 1% BSA (Section 2.1.10.3) and stored at -20 °C until use in competitive ELISA.

2.2.8.3 ELISA Procedures

2.2.8.3.1 Screening of Murine Tail Bleeds

Calibrators (50 µl) (Section 2.2.8.2.3) were added to wells of a plate coated with FSC- or acetylated FSC-BSA (Section 2.2.5.2) at concentrations indicated in Table 2.3. In the case of indirect ELISA analysis, PBST 1% BSA was used as a calibrator only. Murine tail bleeds samples (50 µl) (Section 2.2.8.2.1) were added to the wells and the plates were sealed and gently tapped. Plates were incubated at 37 °C for 1 h before serum was removed, and plates washed four times ELISA wash buffer (Section 2.1.10.2). Anti-mouse IgG-HRP (100 µl) (Section 2.1.10.4) was added to each well and plates were incubated at 37 °C for 1 h. The solution was poured off and plates were washed four times wash buffer. TMB (100 µl) (Section 2.1.10.7) was added to each well and plates were incubated at room temperature for 5 min. ELISA stop solution (100 µl) (Section 2.1.10.8) was added to each well and absorbance values were read at 450/ 620 nm (Synergy™ HT; BioTek Instruments).

2.2.8.3.2 Screening Hybridoma Supernatant by Indirect ELISA

Hybridoma culture supernatant (100 µl) was added to wells of a plate coated with FSC- or acetylated FSC-BSA (Section 2.2.5.2) at concentrations indicated in Table 2.3. Plates were incubated at 37 °C for 1 h before supernatant was removed, and plates washed four times ELISA wash buffer (Section 2.1.10.2). Anti-mouse IgG-HRP (100 µl) (Section 2.1.10.4) was added to each well and plates were incubated at 37 °C for 1 h. The solution was poured off and plates were washed four times wash buffer. TMB (100 µl) (Section 2.1.10.7) was added to each well and plates were incubated at room temperature for 5 min. ELISA stop solution (100 µl) (Section 2.1.10.8) was added to each well and absorbance values were read at 450/ 620 nm (Synergy™ HT; BioTek Instruments).

2.2.8.3.3 Screening of Hybridoma Supernatant and Purified Antibodies by Competitive ELISA

Calibrators (50 µl) (Section 2.2.8.2.3) were added to wells of a plate coated with FSC- or acetylated FSC-BSA (Section 2.2.5.2) at concentrations indicated in Table 2.3. Hybridoma culture supernatant or purified antibodies (50 µl) were then added to the wells and the plates were sealed and gently tapped. Plates were incubated at 37 °C for 1 h before supernatant was removed, and plates washed four times ELISA wash buffer (Section 2.1.10.2). Anti-mouse IgG-HRP (100 µl) (Section 2.1.10.4) was added to each well and plates were incubated at 37 °C for 40 min. The solution was poured off and plates were washed four times wash buffer. TMB (100 µl) (Section 2.1.10.7) was added to each well and plates were incubated at room temperature for 5 min. ELISA stop solution (100 µl) (Section 2.1.10.8) was added to each well and absorbance values were read at 450/ 620 nm (Synergy™ HT; BioTek Instruments).

2.2.8.3.4 Screening Human Sera for Immunoreactivity against *A. fumigatus* Secreted Proteins by ELISA

Human serum samples diluted 1 in 100 in PBST 1% BSA (100 µl) (Section 2.2.8.2.2) were added in triplicate to wells of a plate coated with *A. fumigatus* secreted proteins (Section 2.2.10.2). Plates were incubated at 37 °C for 1 h before serum was removed, and plates washed four times ELISA wash buffer (Section 2.1.10.2). Anti-human IgG-HRP (100 µl) (Section 2.1.10.4) was added to each well and plates were incubated at 37 °C for 1 h. The solution was poured off and plates were washed four times wash buffer. TMB (100 µl) (Section 2.1.10.7) was added to each well and plates were incubated at room temperature for 5 min. ELISA stop solution (100 µl) (Section 2.1.10.8) was added to each well and absorbance values were read at 450/ 620 nm (Synergy™ HT; BioTek Instruments).

2.2.9 Hybridoma Generation

2.2.9.1 Immunisation Regime

BALB/c mice (n = 3; 6 – 8 weeks old) were intraperitoneally administered the immunogen (50 µg) (Section 2.2.5.3) mixed with adjuvant, Pam3Cys in a final volume of 100 µl. Mice received 3 additional boosters of the same composition over 3 week intervals. After the third booster, tail bleeds were taken and sera isolated for polyclonal antibody analysis. A fourth and final booster was administered 3 days prior to the fusion. Immunisations were carried out at the Royal College of Surgeons (RCSI) Biomedical Research Facility, Beaumont Hospital, Dublin, Ireland; all immunisation protocols were licensed by the Department of Health and Children, Ireland (Dept. of Health license ref: B100/3676).

2.2.9.2 Fusion Procedure

The fusion procedure was carried out as described by Köhler and Milstein (1975) with some modifications. Prior to spleen removal from the sacrificed mouse, SP/2/O-Ag 14 myeloma cells from a confluent 75 cm^2 flask were harvested and centrifuged (1,000 rpm for 5 min). The supernatant was poured off and the resultant pellet of cells was suspended in DMEM (10 ml) and centrifuged again. This step was repeated and cells were suspended in DMEM (5 ml). Cells were left at 37 °C until use.

The selected BALB/c mouse was scarified by cervical dislocation, transferred to a laminar flow cabinet and the spleen removed using sterile dissection instruments. The spleen was transferred to a strainer (100 μm; BD Falcon®) in a petri dish containing DMEM (5 ml). Using the base of a plunger from a sterile syringe (10 ml), the spleen was forced through the strainer to obtain single cells. The suspension of splenocytes was transferred to a universal and the final volume adjusted to 10 ml with DMEM. Large clumps cells were allowed to settle by standing for 2 – 3 min at room temperature. Cell suspension was then centrifuged (1,000 rpm for 5 min). The supernatant was poured into a new universal and retained until the end of the fusion process as a precaution. The pellets were gently suspended in DMEM (10 ml) with a pipette. The previously prepared suspension of SP/2/O-Ag 14 myeloma cells (5 ml) was added to the splenocytes followed by gentle mixing with a pipette. This resulted in a ratio of approximately 10 SP/2/O-Ag 14 myeloma cells: 1 splenocyte. The suspension was centrifuged (1,000 rpm for 5 min). The supernatant was poured off and the resultant pellet of cells was gently suspended in DMEM (10 ml) and centrifuged again. This step was repeated and the supernatant poured off. Pre-warmed PEG (polyethylene glycol) (1 ml) (Roche) was slowly added to the mixture of cells, by gentle pipetting along the side of the universal. For 30 sec, the cells were mixed by

pasteur pipetting, while simultaneously agitating the universal by hand with a swirling motion. The pipette was removed and the universal was agitated for a further 45 sec. Plating medium (containing 1X HAT) (Section 2.2.1.2) was then added via the following steps with continuous agitation of the universal:

1. + 45 sec: plating medium (0.5 ml) was gently added.
2. + 1 min 45 sec: plating medium (1 ml) was gently added.
3. + 2 min 45 sec: plating medium (1 ml) was gently added.
4. + 3 min 45 sec: plating medium (1 ml) was gently added.
5. + 4 min 45 sec: plating medium (5 ml) was gently added.

The mixture of cells was then left at room temperature for 15 min (15 min – 1 h is appropriate). Cells were centrifuged (500 rpm for 3-5 min) and supernatant discarded. Plating medium (10 ml) was added to the pellet with mixing by gentle inversion. This mixture was added to plating medium (300 ml; 3.33 ml to 100 ml in 3 large universals) and gently mixed by inversion. The cells were then distributed across 8 X 48 well flat-bottomed cultured plates (Costar) at 0.8 ml/ well. Plates were sealed with parafilm and left undisturbed at 37 °C for 12 days.

2.2.9.3 Screening of Hybridomas

Hybridomas generated by fusing SP/2/O-Ag 14 myeloma cells to splenocytes from immunised BALB/c mice were screened using supernatant taken directly from the 48 well plates. Supernatant was screened in an indirect ELISA and an indirect competitive ELISA format for activity against their cognate hapten (according to Sections 2.2.8.3.2 and 2.2.8.3.3). Supernatant was initially screened for activity against ELISA plates coated with FSC-BSA (0.5 μg/ ml) or acetylated FSC-BSA (0.5

μg/ ml) versus plates coated with the same concentrations of SATA-BSA (Section 2.2.5.2.1). Hybridomas with reactivity against their cognate hapten but not SATA-BSA were selected and further sub-cultured before further screening for competitive activity against FSC/ TAFC. Hybridomas secreting antibodies with desired activity were selected for further subculturing.

2.2.9.4 Subculture of Hybridomas

Positive hybridoma clones (Section 2.2.9.3) were transferred from 48 well plates to 6 well plates where they were fed twice in plating medium (containing 1X HAT). Following this, they were gradually weaned into hybridoma culture medium with 1X HT. Hybridomas were then gradually weaned from hybridoma culture medium with 1X HT into hybridoma culture medium without HT over a 2-week period by gradually decreasing the amount of hybridoma culture medium with 1X HT.

2.2.9.5 Single Cell Isolation by Limiting Dilution

Hybridoma culture medium was added to the wells of a 96 well flat-bottomed culture plate (200 μl to column 1 rows A-G and 100 μl to columns 2-11 rows A-H) (Corning). Cells from a confluent flask (75 cm^2 or 25 cm^2) were sloughed and 100 μl of cell suspension was transferred to position A1 of the 96 well plate. Serial dilutions of 1 in 3 were performed going down then plate (column 1 rows A-H) followed by serial dilutions of 1 in 2 across the plate for all rows. Wells with only 1-3 colonies were marked and plates were sealed with parafilm and incubated at 37 °C for 7 – 10 days. Cells were then transferred to 25 cm^2 flasks.

2.2.9.6 Antibody Isotype Analysis

Isotyping analysis was carried out using the Isostrip™ Mouse Monoclonal Antibody Isotyping Kit (Roche). Hybridoma supernatant was typically diluted 1 in 75 in PBS before analysis as per manufacturers instructions.

2.2.10 Protein Extraction Methods

2.2.10.1 Dialysis of Protein Samples

Dialysis tubing was cut to the required size and rinsed well with distilled water. Tubing was then submerged in buffer to be used for dialysis for 10 min at room temperature. Tubing was then sealed at one end with a knot, protein sample carefully added, and then sealed on the other end. The sealed tubing containing the sample was then dialysed against a minimum of 50 volumes of appropriate buffer. Dialysis was carried out at 4 °C with stirring with a minimum of three buffer exchanges at 3 h intervals.

2.2.10.2 Secreted Protein Extraction from *A. fumigatus*

Supernatant from *A. fumigatus* ATCC 46645 liquid cultures (1 X 10^8 in 100 ml; 72 h; 37 °C; 200 rpm) grown in MM with and without iron (Section 2.1.1.2.5) were harvested by filtering through miracloth and snap frozen in liquid nitrogen. Samples were stored at -80 °C until further processing. Supernatants were thawed at 4 °C and kept on ice throughout. Samples were centrifuged (4,000 g for 30 min at 4 °C), supernatant (61.5 ml) collected and passed through 0.45 µm filters. Secreted proteins were concentrated via centrifugal filters (Amicon® 3 kDa molecular-weight cut off; Millipore) with repeated centrifugation (4,000 g for 30 min 4 °C) to a final volume of 300 – 500 µl. Protein yields were measured by Bradford Protein Assay (Section 2.2.12.2). An aliquot of each sample was taken as the enzymatically active fraction,

snap frozen in liquid nitrogen and stored at -80 °C until use. The remainder of each sample was brought to 15% TCA using 100% TCA Solution (Section 2.1.5.1) and incubated on ice in the dark for 30 min. Precipitated proteins were collected by centrifugation (13,000 rpm for 20 min at 4 °C) and supernatant discarded. Pellets were suspended in ice-cold acetone (1 ml), centrifuged again and supernatant discarded. Acetone wash steps were repeated twice more and any remaining acetone removed by drying at room temperature for approximately 10 min. Protein Resuspension Buffer (50 µl) (Section 2.1.5.2) and samples left at room temperature for approximately 10 min. Protein yields were measured by Bradford Protein Assay (Section 2.2.12.2).

2.2.11 Protein Purification Methods

2.2.11.1.1 Purification of IgM from Hybridoma Supernatant by Ammonium Sulfate Precipitation

The 7D8 hybridoma generated from the fusion of myeloma cells with FSC-KLH immunised murine splenocytes was cultured and supernatant retained for antibody purification. Hybridoma supernatant was centrifuged (2,000 rpm for 10 min) to pellet any cells and supernatant collected, passed through 0.2 µm filters and stored at 4 °C until processing. Supernatant (50 ml) was brought to 10 mM sodium phosphate pH 7 *via* the addition of sodium phosphate buffer (0.55 ml; 1 M) (Section 2.1.4.5). The supernatant was brought to 50% ammonium sulphate saturation by the addition of ammonium sulphate (15.7 g) and mixed with a magnetic stirrer for 1 h at room temperature. The mixture was then centrifuged (2,500 rpm for 25 min at 20 °C). The supernatant was poured off and retained for later analysis while the pellet was suspended in PBS (12 ml) and dialysed against PBS (Section 2.1.4.2). Dialysed

extract was centrifuged (3,000 g for 10 min at 20 °C) and supernatant collected. Protein content was measured by Bradford (Section 2.2.12.1) and analysed by SDS-PAGE (Section 2.2.12.2).

2.2.11.2 Purification of IgG from Hybridoma Supernatant by Protein A Chromatography

The 6C6 hybridoma generated from the fusion of myeloma cells with DAFC-KLH immunised murine splenocytes was cultured and supernatant retained for antibody purification. Hybridoma supernatant was centrifuged (2,000 rpm for 10 min) to pellet any cells and supernatant collected, passed through 0.2 μm filters and stored at 4 °C until processing. Immediately before purification *via* Protein A chromatography, supernatant was sonicated in a sonication bath for 10 min.

Protein A chromatography was carried out using an ÄKTA purifier with a HiTrap Protein A HP column (GE Healthcare) pre-packed with Protein A Sepharose (1 ml). The column was first equilibrated with 1 column volumes (CV) of Equilibration/ Wash Buffer (Section 2.1.6.4.2.1) at a flow rate of 1 ml/ min. Clarified hybridoma supernatant (45 ml) was applied to the Protein A column at 1 ml/ min. The flow rate was not increased above 1 ml/ min to maximise the resin capacity. An aliquot of the flow-through was retained for later analysis by ELISA (Section 2.2.8.3.3). After all the supernatant had been applied, the column was washed with 20 CV of Equilibration/ Wash Buffer. The absorbance at 280 nm was monitored to ensure it a return to baseline levels after washing. Any bound IgG was then eluted from the column using Elution Buffer (Section 2.1.6.4.2.2). Eluted IgG was collected in 0.5 ml fractions, pooled according to the absorbance at 280 nm and immediately neutralised with 1 M Tris-HCl (Section 2.1.6.4.2.3). Purified IgG was dialysed against

10 mM sodium phosphate buffer (Section 2.1.6.3) analysed by SDS-PAGE (Section 2.2.12.2) and ELISA (Section 2.2.8.3.3).

2.2.11.3 Immunoaffinity Purification of anti-TAFC IgG from Total IgG

2.2.11.3.1 Analytical Screening of anti-TAFC IgG Pull-Down Capability of DAFC Coated Magnetic Beads

All reagents were equilibrated to room temperature prior to use. DAFC activated magnetic beads or control magnetic beads (2.5 µl) (Section 2.2.5.5) were transferred to a fresh centrifuge tube. Beads were collected in a magnetic rack and supernatant removed with a pipette. Blocking Solution (100 µl) (Section 2.1.6.5.2) was added to beads followed by incubation for 15 min at room temperature while rotating. Beads were collected in a magnetic rack and supernatant removed. Protein A purified IgG (50 µl at 0.3 mg/ ml diluted in TBST) (Section 2.2.11.2) or TBST (50 µl) (Section 2.1.6.5.1) was added to beads followed by incubation for 1 h at room temperature while rotating. Beads were collected in a magnetic rack, supernatant removed and retained for later analysis by ELISA (Section 2.2.8.3.3). Wash Buffer (100 µl) (Section 2.1.6.5.3) was added to beads and following a brief vortex, the beads were collected in a magnetic rack and the supernatant was removed and discarded. The wash step was repeated another four times. Anti-Mouse IgG-HRP (100 µl) (Section 2.1.10.4) was added to beads followed by incubation for 40 min at room temperature while rotating. Beads were collected in a magnetic rack and supernatant removed. Beads were washed five times as before. TMB Liquid Substrate (100 µl) (Section 2.1.10.7) was added to beads and following a brief vortex beads were incubated for 1 min at room temperature. ELISA Stop Solution (100 µl) (Section 2.1.10.8) was added to beads and following a brief vortex beads were collected in a magnetic rack,

supernatant transferred to 96 well plate and the OD read at 450/ 620 nm (Synergy™HT; BioTek Instruments).

2.2.11.3.2 Large-Scale Immunoaffinity Purification of anti-TAFC IgG from Total IgG using DAFC Coated Magnetic Beads

The following steps were carried out with volumes distributed equally between 4 X 2 ml centrifuge tubes (Eppendorf). All reagents were equilibrated to room temperature prior to use. DAFC coated magnetic beads (200 µl) (Section 2.2.5.5) were collected in a magnetic rack and supernatant removed with pipette. Blocking Solution (8 ml) (Section 2.1.6.5.2) was added to beads followed by incubation for 15 min at room temperature while rotating. Beads were collected in a magnetic rack and supernatant removed. Protein A purified IgG (4 ml at 0.3 mg/ ml diluted in TBST) (Section 2.1.6.5.1) was added to beads followed by incubation for 2 h at room temperature while rotating. Beads were collected in a magnetic rack, supernatant removed and retained for later analysis by ELISA (Section 2.2.8.3.3). Wash Buffer (8 ml) (Section 2.1.6.5.1) was added to beads and following a brief vortex beads were collected in a magnetic rack, supernatant removed and discarded. The wash step was repeated another four times. Wash Buffer (500 µl) was added and beads were collected into a single 1.5 ml centrifuge tube. Beads were collected in a magnetic rack, supernatant removed. Elution Buffer (200 µl) (Section 2.1.6.5.4) was added to beads followed by incubation for 5 min at room temperature while rotating. Beads were collected in a magnetic rack, supernatant transferred to a fresh centrifuge tube and immediately neutralised by the addition of Neutralisation Buffer (20 µl) (Section 2.1.6.5.5). The elution step was repeated another three times. The protein content of eluted fractions determined by absorbance at 280 nm and fractions were pooled accordingly. Affinity purified IgG was analysed by ELISA (Section 2.2.8.3.3).

Eluted fractions were brought to 25% TCA using 100% TCA Solution (Section 2.1.5.1) and incubated on ice in the dark for 30 min. Precipitated proteins were collected by centrifugation (13,000 rpm for 20 min at 4 °C) and supernatant discarded. Pellets were suspended in ice-cold acetone (1 ml), centrifuged again and supernatant discarded. Acetone wash steps were repeated twice more and any remaining acetone removed by drying at room temperature for approximately 10 min. Protein Resuspension Buffer (40 µl) (Section 2.1.5.2) and samples were left at room temperature for approximately 10 min. IgG was analysed by SDS-PAGE (Section 2.2.12.2).

2.2.12 Protein Characterisation Methods

2.2.12.1 Bradford Protein Assay

Bradford reagent (Bio-Rad) was diluted 1 in 5 in PBS prior to use. The protein sample to be assayed was diluted appropriately, and 20 µl was added to Bradford reagent (980 µl) followed by mixing. The final sample (1 ml) was then transferred to a plastic 1.5 ml cuvette and incubated at room temperature for 5 min. The absorbance (595 nm) was read relative to a blank and protein concentration determined based on a standard curve. All samples were prepared and analysed in duplicate.

2.2.12.2 SDS-PAGE Analysis of Protein Samples

SDS-PAGE gels (stacking and resolving) were prepared according to Table 2.4 and Table 2.5 in a 1 mm casting plate unless otherwise stated. The gels were cast using the Mini-Protean II gel casting apparatus (Bio-Rad) according to manufacturer's instructions. Protein samples were prepared by adding one volume of 5 X Solubilisation Buffer (Section 2.1.7.2.6) to every four volumes of sample. Samples were then boiled for 5 min and centrifuged briefly before loading an appropriate

volume into the gel. A pre-stained molecular weight ladder ranging from 10 – 170 kDa (PageRuler, Thermo Scientific) (Figure 2.1) was used throughout this study. The electrophoresis tank was filled with 1X SDS Electrode Running Buffer (Section 2.1.7.2.8). Electrophoresis was carried out at 80 V for 30 min, followed by 120 V until the dye front had reached the bottom of the gel. SDS-PAGE gels were then either stained with Coomassie® Blue (Section 2.1.7.2.9).

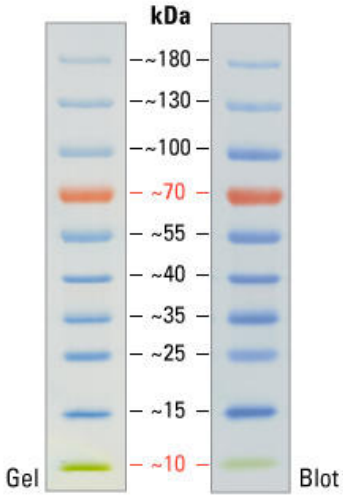

Figure 2.1 Pre-stained molecular mass protein ladder (PageRuler, Thermo Scientific) used for SDS-PAGE gels in this study.

Table 2.4 Composition of Resolving Gels for SDS-PAGE

% Acrylamide	*12%*	*12%*
Number of Minigels	**5**	**8**
1.5 M Tris HCl pH 8.3	7.0 ml	10.5 ml
10% SDS	280 µl	420 µl
30% Acrylamide, 0.8% Methylene bis-Acrylamide	11.3 ml	16.9 ml
Distilled water	9.3 ml	13.9 ml
10% Ammonium persulphate	100 µl	150 µl
TEMED	23 µl	35 µl

Table 2.5 Composition of Stacking Gels for SDS-PAGE

Number of Minigels	**5**	**8**
0.5 M Tris HCl pH 6.8	4.0 ml	5.2 ml
10% SDS	160 µl	210 µl
30% Acrylamide, 0.8% Methylene bis-Acrylamide	1.5 ml	2.0 ml
Distilled water	9.6 ml	12.8 ml
10% Ammonium persulphate	150 µl	200 µl
TEMED	15 µl	20 µl

2.2.12.3 Coomassie® Blue Staining

Following SDS-PAGE, gels were carefully removed from the electrophoresis unit and submerged in Coomassie® Blue Stain Solution (Section 2.1.7.2.9) and incubated overnight at room temperature on a rocker. Coomassie® blue stain solution was poured off and gels were then washed in distilled water. Gels were submerged in Destain Solution (Section 2.1.7.2.10) and incubated for 1 – 3 h at room temperature on a rocker. Destain solution was then poured off and gels were washed well in distilled water.

2.2.12.4 Glucanase Activity Assay

All reagents were equilibrated to room temperature before use. First, the laminarin assay was carried out, incubating the protein samples or a glucanase standard with laminarin as a substrate. Second, the glucose content these samples were estimated using an Ampliflu™ assay against a standard curve of glucose concentrations.

For the laminarin assay, the glucanase standard was diluted 0.1 U/ ml and protein samples were diluted 0.1 mg/ ml in sodium acetate buffer (Section 2.1.7.3.4). Glucanase standard (50 µl) (Section 2.1.7.3.6) or protein sample (50 µl) (Section 2.2.10.2) were then added to laminarin (200 µl; 2.5 mg/ ml) (Section 2.1.7.3.5) in a 1.5 ml centrifuge tube. Samples were briefly vortexed before incubation at 37 °C for 2.5 h. Subsequently samples were either stored at -20 °C or immediately used in the Ampiflu™ assay to estimate glucose levels.

Following incubation of protein sample or glucanase standard with laminarin, glucose levels were estimated using the Ampiflu™ Red reagent, coupled with HRP and glucose oxidase. First a 96 well plate was prepared with all reagents diluted in sodium phosphate buffer (200 µl) including (i) standard glucose (Section 2.1.7.3.10)

starting at 200 μM titred down the plate in duplicate, (ii) the glucanase standard from the laminarin assay diluted 1 in 10, 20, 40, and 80 in duplicate, (iii) the protein samples from the laminarin assay diluted 1 in 10, 20, 40, and 80 in duplicate, and (iv) a negative control of each protein sample without prior incubation with laminarin diluted 1 in 10, 20, 40, and 80 in duplicate. 50 μl of each mixture was then transferred to a new 96 well plate. Freshly prepared Ampiflu™ assay mixture (50 μl) (Section 2.1.7.3.11) was then added to each well. Plates were incubated at room temperature in the dark for 30 min. Absorbance was then read at 560 nm. Glucose content was estimated using the glucose standard curve and any background signal was subtracted from using the negative control for each protein sample, respectively.

2.2.13 Mass Spectrometry Methods

Two LC-mass spectrometers were employed for the analysis presented in this thesis:

(i) An Agilent 1200 series 6340 Ion Trap LC-MS. This LC-MS was predominantly used for metabolite mass-based identification and analysis of peptides extracted from SDS-PAGE gel bands for preliminary proteome studies. Method parameters for these analyses are outlined in Sections 2.2.13.5 and 2.2.13.6. A standard of trypsin-digested BSA or gliotoxin was analysed at the start of each run to confirm optimal machine functionality before sample analysis.

(ii) A Thermo Scientific Q Exactive connected to a Dionex Ultimate 2000 (RSLCnano) chromatography system. This LC-MS was predominantly used for shotgun proteome analysis, the analysis of peptides extracted from SDS-PAGE gel bands for antibody sequencing, and some metabolite mass-based identification. Method parameters for these analyses are outlined in

Sections 2.2.13.7 and 2.2.13.8. A standard of trypsin-digested HeLa cells were analysed at the start of each run to confirm optimal machine functionality before sample analysis.

2.2.13.1 In-Gel Digestion of SDS-PAGE Samples for Ion Trap MS Analysis

In-gel digestion of SDS-PAGE proteins was carried out as per Shevchenko *et al.* (2007). Briefly, selected bands were excised from SDS-PAGE gels and transferred to centrifuge tubes. Gel pieces were destained by the addition of 50 mM ammonium bicarbonate acetonitrile (50% (v/v)) buffer (100 µl) (Section 2.1.11.3). Samples were incubated at room temperature for 30 min with occasional vortexing. Acetonitrile (500 µl) was added and samples were incubated at room temperature until gel pieces became white and shrunken.

Any solution was then removed and replaced with trypsin solution for in-gel digestion (Section 2.1.11.11.2) in a sufficient volume to cover the gel pieces. Samples were incubated on ice for 30 min after which if the trypsin solution had been absorbed, more was added to ensure gel pieces were still covered. Samples were then incubated on ice for a further 90 min. Additional solution (100 mM ammonium bicarbonate (Section 2.1.11.1)) was added to cover gel pieces if required and samples were incubated at 37 °C overnight. Gel pieces were sonicated in a sonication bath for 10 min and centrifuged briefly. The supernatant was transferred to a fresh centrifuge tube and evaporated to dryness in a SpeedVac™ (DNA 120; Thermo Scientific). Dried samples were stored at -20 °C until the day of analysis when they were suspended in Ion Trap solvent A (20 µl) (Section 2.1.11.12.1). Solutions were filtered through 0.22 µm Cellulose Spin-Filters (Costar) before transfer into vials for injection.

2.2.13.2 In-Gel Digestion of SDS-PAGE Samples for Q-Exactive MS Analysis

In-gel digestion of SDS-PAGE proteins was carried out as per Shevchenko *et al.* (2007). Briefly, selected bands were excised from SDS-PAGE gels and transferred to centrifuge tubes. Acetonitrile (500 µl) was added and samples were incubated at room temperature for 10 min. Samples were briefly centrifuged and any solution was removed and replaced with 10 mM DTT solution for in-gel digestion (Section 2.1.11.8) in a sufficient volume to cover the gel pieces (30 – 50 µl). Samples were incubated at 56 °C for 30 min and then allowed to cool to room temperature. Acetonitrile (500 µl) was added and samples were incubated at room temperature for 10 min. Samples were briefly centrifuged and any solution was removed and replaced with 55 mM IAA solution for in-gel digestion (Section 2.1.11.9) in a sufficient volume to cover the gel pieces (30 – 50 µl). Samples were incubated at room temperature for 20 min in the dark. Acetonitrile (500 µl) was added and samples were incubated at room temperature for 10 min.

Any solution was then removed and replaced with 50 mM ammonium bicarbonate acetonitrile (50% (v/v)) buffer (100 µl) (Section 2.1.11.3). Samples were incubated at room temperature for 30 min with occasional vortexing. Acetonitrile (500 µl) was added and samples were incubated at room temperature with occasional vortexing until gel pieces became white and shrunken. Any solution was then removed and replaced with appropriate enzyme solution for in-gel digestion (trypsin, Glu-C, or Asp-N; (Section 2.1.11.11.2 - 2.1.11.11.4) in a sufficient volume to cover the gel pieces. Samples were incubated on ice for 30 min after which if the enzyme solution had been absorbed, more was added to ensure gel pieces were still covered. Samples were then incubated on ice for a further 90 min. Additional solution (100 mM ammonium bicarbonate (Section 2.1.11.1) for trypsin and Glu-C digests; 50 mM

Tris-HCl (Section 2.1.11.5) for Asp-N digests) was added to cover gel pieces if required and samples were incubated at 37 °C overnight. Gel pieces were sonicated in a sonication bath for 10 min and centrifuged briefly. The supernatant was transferred to a fresh centrifuge tube and TFA (1 µl) was added to each solution, followed by a brief vortex and incubation at room temperature for 5 min. Samples were evaporated to dryness in a SpeedVac™ (DNA 120; Thermo Scientific) and stored at -20 °C until preparation as per the ZipTip® protocol (Section 2.2.13.4).

2.2.13.3 In-Solution Digestion of Protein Samples for Q-Exactive MS Analysis

Protein samples (25 µl; 50 µg) in protein resuspension buffer (Section 2.1.5.2) were equilibrated to room temperature for 10 min to ensure urea was in solution. Ammonium bicarbonate buffer (142 µl; 50 mM) (Section 2.1.11.1) was added to samples to dilute the urea content to a final concentration of 1 M or less. DTT solution for in-solution digestion (1 µl; 0.5 M) (Section 2.1.11.6) was added to samples followed by incubation at 56 °C for 20 min. Samples were allowed to cool to room temperature after which IAA for in-solution digestion (2.7 µl; 0.55 M) (Section 2.1.11.7) was added and samples incubated at room temperature for 15 min in the dark. DTT for in-solution digestion (13 µl; 0.5 M) (Section 2.1.11.6) was added to samples followed by incubation at 56 °C for 20 min to quench any excess IAA activity.

Following reduction and alkylation, ProteaseMAX (1 µl; 1% (w/v)) and trypsin for in-solution digestion (1.8 µl; 1 µg/ µl) were added to samples followed by incubation at 37 °C overnight. The next day, TFA (1 µl) was added to each sample, followed by a brief vortex and incubation at room temperature for 5 min. Samples

were evaporated to dryness in a SpeedVac™ (DNA 120; Thermo Scientific) and stored at -20 °C until preparation as per the ZipTip® protocol (Section 2.2.13.4).

2.2.13.4 ZipTip® Pipette Tip Protocol

The sample was suspended in resuspension buffer (20 µl) (Section 2.1.11.14.1) and sonicated for 2 min to aid pellet resuspension. The sample was then centrifuged briefly to collect the solution. The Ziptip was wet by aspirating and dispensing wetting solution (10 µl) (Section 2.1.11.14.2) into the tip using a pipette. This was repeated five times. The ZipTip was then equilibrated by aspirating and dispensing equilibration solution (10 µl) (Section 2.1.11.14.3) into the tip. This was repeated five times. To bind the sample to the ZipTip, the resuspended sample (10 µl) was aspirated and dispensed from the tip. This was repeated 10 times. The ZipTip was then washed by aspirating and dispensing washing solution (10 µl) (Section 2.1.11.14.3) into the tip. This was repeated five times. To elute the sample from the ZipTip, elution solution (10 µl) (Section 2.1.11.14.4) was aspirated and dispensed from the tip into a new centrifuge tube. This was repeated five times. The eluted samples were evaporated to dryness in a SpeedVac™ (DNA 120; Thermo Scientific) and stored at -20 °C until further processing. On the day of analysis, the sample was resuspended in loading buffer (15 µl) (Section 2.1.11.14.5) and sonicated for 2 min. The sample was then centrifuged (13,400 rpm for 10 min) and supernatant (10 µl) transferred to a vial for injection.

2.2.13.5 Ion Trap: LC-MS/MS Analysis of Peptide Mixtures

For Ion Trap LC-MS/MS analysis of peptides, samples were first diluted appropriately into water formic acid (Section 2.1.11.12.1) and then spin filtered (0.2 µm; Costar) before injection. LC-MS/MS analysis was carried out on a nanoflow

Agilent 1200 LC system and subjected to tandem mass spectrometry using an Agilent 6340 Ion Trap LC-MS System (Agilent Technologies). Samples were applied to a Zorbax 300 SB-C18 HPLC-Chip with a 40 nl enrichment column and a 75 µm x 43 mm (5 µm particle and 300 Å pore size) analytical column with water formic acid (Section 2.1.11.12.1). Peptides were separated and eluted over an increasing acetonitrile gradient (5 – 50%) over 12 min at a flow rate of 4 µl/ min with a post-run of 7 min. The mass spectrometer was operated in positive mode with MS^n carried out the three most abundant precursor ions at each time point. Singly charged ions were excluded from analysis.

2.2.13.6 Ion Trap: LC-MS/MS Analysis of Metabolites

For Ion Trap LC-MS/MS analysis of metabolites, samples were first diluted appropriately into water formic acid (Section 2.1.11.12.1) and then spin filtered (0.2 µm; Costar) before injection. LC-MS/MS analysis was carried out on a nanoflow Agilent 1200 LC system and subjected to tandem mass spectrometry using an Agilent 6340 Ion Trap LC-MS System (Agilent Technologies). Samples were applied to a Zorbax SB-C18 HPLC-Chip with a 40 nl enrichment column and a 75 µm x 43mm (5 µm particle and 300 Å pore size) analytical column with water formic acid (Section 2.1.11.12.1). Metabolites were separated and eluted over an increasing acetonitrile gradient (30 – 70%) over 12 min at a flow rate of 4 µl/ min with a post-run of 7 min. The mass spectrometer was operated in positive mode with MS^n carried out the two most abundant precursor ions at each time point. Singly charged ions were not excluded from analysis and the precursor *m/z* range was 50 – 2200. Integrated peak intensity values were then analysed for the *m/z* corresponding to the metabolite of interest from the total ion chromatogram (TIC) or extracted ion chromatogram (EIC). The *m/z* corresponding to particular masses of interest were evaluated using an adduct

calculator generated by Huang *et al.* (1999) (www.lc-ms.nl/ESI-MS-adducts.xls) (Huang *et al.*, 1999).

2.2.13.7 Q-Exactive: LC-MS/MS Analysis of Peptide Mixtures

Peptide samples were analysed on a Thermo Scientific Q Exactive mass spectrometer connected to a Dionex Ultimate 3000 (RSLCnano) chromatography system. Each sample was loaded onto an EASY-Spray PepMap RSLC C18 Column (75 μm x 500 mm), and was separated by an increasing acetonitrile gradient over (A) 20 min or (B) 120 min at a flow rate of 250 nL/min. The mass spectrometer was operated in positive mode with MS^n carried out the 15 most abundant precursor ions at each time point. Singly charged ions were excluded from analysis.

2.2.13.8 Q-Exactive: LC-MS/MS Analysis of Metabolites

Peptide samples were analysed on a Thermo Scientific Q Exactive mass spectrometer connected to a Dionex Ultimate 3000 (RSLCnano) chromatography system. Each sample was loaded onto an EASY-Spray PepMap RSLC C18 Column (75 μm x 500 mm), and was separated by an increasing acetonitrile gradient over 14 min at a flow rate of 250 nL/min. The mass spectrometer was operated in positive mode with MS^n carried out the five most abundant precursor ions at each time point. Singly charged ions were not excluded from analysis and the precursor *m/z* range was 300 – 2000. Integrated peak intensity values were then analysed for the *m/z* corresponding to the metabolite of interest from the total ion chromatogram (TIC) or extracted ion chromatogram (EIC). The *m/z* corresponding to particular masses of interest were evaluated using an adduct calculator generated by Huang *et al.* (1999) (www.lc-ms.nl/ESI-MS-adducts.xls) (Huang *et al.*, 1999).

2.2.14 Bioinformatic Analysis

2.2.14.1 Protein identification using Mascot

Peptide-spectral matching and protein-peptide matching of raw files from Ion Trap LC-MS/MS analysis of in-gel digests were carried out using MASCOT (http://www.matrixscience.com/). Peptides from the MS^n were matched using MASCOT MS/ MS ion searching with interrogation of the NCBI database for protein identification. Search parameters included: mass tolerance (Da) of 2 for precursor ions and 1 for product ions, carbamidomethylation of cysteines as a fixed modification, oxidation of methionines as a variable modification, maximum 2 missed cleavage sites, and peptide charge of 1+, 2+, or 3+. Proteins were specifically analysed for features and/ or functions in UniProt (http://www.uniprot.org/) or AspGD (http://www.aspgd.org/).

2.2.14.2 Label-free quantitative proteomic (LFQ) analysis using MaxQuant and Perseus

Peptide-spectral matching and protein-peptide matching of raw files from Q-Exactive analysis of LFQ proteomic studies were carried out using MaxQuant (version 1.5.0.0; http://maxquant.org) (Tyanova *et al.*, 2015). This utilised the Andromeda database search to match MS/MS data with the *A. fumigatus* Af293 reference proteome (UP000001530 - *Neosartorya fumigata* (strain ATCC MYA-4609/ Af293/ CBS 101355/ FGSC A1100) from UniProt (http://www.uniprot.org/). Search parameters included: peptide tolerance (ppm) of 20 for the first search peptide and 4.5 for the main search peptide, carbamidomethylation of cysteines as a fixed modification, oxidation of methionines and acetylation of N-termini as variable modifications, maximum 2 missed cleavage sites, and minimum 1 peptide detected per protein. The

maximum protein/ peptide FDRs were set to 1% based on a comparison to a reverse database (decoy database). The LFQ algorithm was used to generate normalised spectra intensities to infer relative protein abundance.

Subsequently, protein groups were exported and processed in Perseus (version 1.5.5.0; http://www.coxdocs.org/doku.php?id=:perseus:start) for data filtering (Tyanova *et al.*, 2016b). Proteins (i) identified as contaminants, (ii) only identified by a modification site, or (iii) identified by the decoy database were removed. Extracted LFQ intensities measured for each run were grouped according to experimental grouping conditions, for example, iron-deplete and iron-replete. For secretome analysis, LFQ intensities were scaled to the total protein yield in a 100 ml culture volume for both conditions thereby normalising protein abundances to the original total protein yields. This was carried out using the Perseus Plugin, Proteomic Ruler, utilising the 'Total Protein Approach' proposed by Wiśniewski *et al.* (2012) (Wiśniewski *et al.*, 2012, 2014). Only proteins identified in a minimum of three replicates from either group were selected for analysis. Protein abundances were $\log_2$ transformed. Qualitative results were generated by the unique abundance of a protein to either condition. A 2-sample t test was performed to identify proteins with significant ($p < 0.05$) and differential ($\log_2$ fold change: > 2 or < -2) abundance between conditions for quantitative results. Enrichment for Gene Ontology (GO) cellular compartment, molecular function, and biological process categories were carried out using FungiFun2 (https://elbe.hki-jena.de/fungifun/fungifun.php) with a Fischer's exact test ($p < 0.05$) (Priebe *et al.*, 2015). Proteins were then specifically analysed for features and/ or functions in UniProt (http://www.uniprot.org/) or AspGD (http://www.aspgd.org/).

2.2.14.3 Assembly of antibody sequences using PEAKS

2.2.14.3.1 Data analysis

Analysis of LC-MS/MS spectra associated with antibodies was carried out using PEAKS and based on the ALPS system based on that outlined by Tran *et al.* (2016). Raw files for the same band digested with three different enzymes were imported into PEAKS Studio (version 8.0) together and treated as a single sample. Generally, an error tolerance of 10 ppm and 0.02 Da was permitted for the precursor and fragment ions, respectively. Modifications included: carbamidomethylation (fixed), oxidation of methionines (variable), and deamidation of asparagine/ glutamine (variable). At most, three modifications were permitted per peptide. Local confidence scores of peptides identified by *de novo* sequencing were accepted if above 50%. Three lists of peptides were generated for each sample as outlined below.

(i) ***de novo* sequencing results**: Mass spectra were subjected to *de novo* sequencing as per above parameters and exported for the first list. List was termed 'DN'.

(ii) **Standard database search results paired with remaining unmatched over *de novo* sequencing results**: A database search was performed using PEAKS DB with a database from Tran *et al*. 2016 comprised of murine antibody sequences including common contaminants. Once the antibody isotype was determined to be IgG_{2a}, additional sequences (IgG_{2a} κ antibodies) from abYsis (www.abysis.org) were added to the database and another search carried out - this was used to generate the second peptide list (Swindells *et al.*, 2017). Peptides were refined to include those with an FDR of less than 1%. List was termed 'DB'.

(iii) **SPIDER database search results paired with remaining unmatched over *de novo* sequencing results**: A SPIDER database search was performed which

allows for *de novo* sequencing and database errors. It works by matching *de novo* tags to database proteins while incorporating potential protein mutations and sequencing errors then generating a putative true protein sequence. The SPIDER search was carried out using the Tran *et al.* (2016) database with the additional Abysis entries as defined above (ii). Peptides were refined to include those with an FDR of less than 1%. List was termed 'DBS'.

The three peptide lists were exported with the area and residue confidence score associated with each peptide. Peptides matching contaminants were removed and peptides assembled using the ALPS.jar tool from Tran *et al*. (2016). ALPS.jar assembles peptides using a weighted de Bruijn graph construction accounting for the area and peptide confidence scores. Peptides were assembled with a *k*-mer length of 6. Sequence outputs were subjected to a BLAST search and any peptide matching a contaminant was removed. Peptides found matching IgG_3 antibodies were also removed.

2.2.14.3.2 Peptide assembly

Peptides generated from the ALPS assembly along with peptides manually extracted from database hits in Section 2.2.14.3.1 were collected. Peptide lists were refined to reduce redundancy and remove contaminants. A putative sequence was assembled by aligning the sequences with several template antibody sequences. This was done using multiple sequence alignment tools (Clustal Omega or MUSCLE) in R (using bioconductor package, msa) or online to assemble overlapping residues and a putative sequence. Details of the enzyme and search method used to obtain the sequence were also exported.

2.2.15 Software Graphing and Statistical Analysis

All statistical analyses were carried out using Graphpad Prism version 7.0 using stated tests. Graphs were generated Graphpad Prism version 7.0 or Microsoft Excel. RP-HPLC chromatograms were generated in R version 3.4.1. Multiple sequence alignment figures were generated in R version 3.4.1 using the 'msa' package version 1.8.0. Chemical structure schematics were generated in ChemDoodle version 8.1.0.

Chapter 3

Iron starvation induces a host-relevant secretomic remodelling of the cell surface in *A. fumigatus*

Chapter 3 Iron starvation induces a host-relevant secretomic remodelling of the cell surface in *A. fumigatus*

3.1 Introduction

Secretome constituents are highly influential on the interactions between fungi and their environment. Along with the cell wall proteome, the secretome is particularly relevant to infection acting as a proteomic interface between the host and pathogen (McCotter *et al.*, 2016). Moreover, due to the wide range of niches occupied by fungi there is great functional diversity in fungal secretomes (Lowe *et al.*, 2012). Proteins are typically secreted for roles in nutrient acquisition, host interactions, virulence, and/ or cell surface remodelling (McCotter *et al.*, 2016).

As a saprophyte, *A. fumigatus* is predominantly found on decaying plant and organic matter. Survival here requires the secretion of a suite of enzymes for the degradation of complex materials, such as proteins and carbohydrates, to provide carbon, nitrogen, and other nutrients (Dagenais and Keller, 2009; Tekaia and Latgé, 2005). In addition to nutrient acquisition, these enzymes also function in processes of growth and maintenance, for example in cell wall remodelling and protein turnover (McCotter *et al.*, 2016; Yike, 2011). Fungal proteases, which are involved in peptide hydrolysis and protein degradation, have attracted attention as potential virulence factors in mammalian hosts whereby protease-mediated tissue destruction can aid invasion and dissemination (Dagenais and Keller, 2009; Yike, 2011). For example, Alp1/ Aspf13 (AFUA_4G11800), can degrade complement components and disturb the airway epithelium (Balenga *et al.*, 2015; Behnsen *et al.*, 2010; Namvar *et al.*, 2015). However, gene deletion studies have not yet provided evidence supporting a role for proteases in virulence (Bergmann *et al.*, 2009; Sharon *et al.*, 2009).

Interestingly, an ortholog of the aspartic protease, CtsD (AFUA_4G07040) which is expressed during *A. fumigatus* infection of *G. mellonella,* was recently shown to be required for virulence in *C. neoformans* (Clarke *et al.*, 2016; Vickers *et al.*, 2007). The role for proteases as allergens that can deleteriously exacerbate allergic responses and induce inflammatory responses is more defined (Yike, 2011). In fact, studies on the *A. fumigatus* secretome show that it contains many proteins reactive with human IgE as well as IgG (Gautam *et al.*, 2007; Shi *et al.*, 2012a; Singh *et al.*, 2010a).

Various factors can have a regulatory effect on the fungal secretome and alterations in many of these are encountered in host including, pH, temperature, nutrient availability, and oxidative stresses (McCotter *et al.*, 2016). Several studies have demonstrated the secretomic remodelling of *A. fumigatus* in response to host-relevant substrates (Farnell *et al.*, 2012; Wartenberg *et al.*, 2011). However, no study has characterised the *A. fumigatus* secretome in response to iron starvation. Given the importance of iron to microbial infection and influence of iron availability on the proteome of *A. fumigatus*, characterisation of the iron-deplete secretome is warranted to dissect pathogen adaptations that are relevant to infection (Cassat and Skaar, 2013; Moloney *et al.*, 2016a; Mulvihill *et al.*, 2017). Following this, the objectives of the work presented in this chapter were to:

i. Investigate and validate a method for the isolation of secreted proteins from *A. fumigatus* suitable for both native protein analysis and LC-MS/MS based shotgun analysis.

ii. Analyse the proteins secreted by *A. fumigatus* in response to iron starvation by LC-MS/MS.

iii. Bioinformatically characterise the secretome in response to iron starvation and validate observations.

3.2 Results

3.2.1 Preliminary characterisation of the iron-starved secretome

Following growth of *A. fumigatus* for 72 h in liquid culture under iron-deplete and -replete conditions, secreted proteins were extracted as described in Section 2.2.10.2. Several extraction methods were initially trialled. These included lyophilisation and direct TCA precipitation of culture supernatant, similar versions of which have been successfully use by others for secretome studies (Adav *et al.*, 2015; Liu *et al.*, 2013; Upadhyay *et al.*, 2012; Wartenberg *et al.*, 2011). However, lyophilised supernatants proved somewhat intractable to protein recovery, while direct TCA precipitation was highly inefficient at protein extraction from large culture volumes. It was found that concentration *via* centrifugal filters with a 3 kDa molecular mass cut-off (Amicon® 3 kDa molecular-weight cut off; Millipore) was effective at concentrating proteins, which has also been implemented in other fungal secretome studies (Sorgo *et al.*, 2011). This meant that proteins were isolated in their native form thereby also allowing for enzymatic studies. Subsequently, TCA precipitation facilitated sample clean-up and concentration of proteins sufficient for gel-based and gel-free proteome analysis. The protein concentrations were estimated by Bradford assay after centrifugal filter-mediated concentration (before TCA precipitation) to estimate total protein yields during iron-deplete and –replete growth ($n = 4$) (Figure 3.1). There was a protein yield of 91 ± 17.53 µg/ 100 ml during iron-deplete growth and 496 ± 50.75 µg/ 100 ml during iron-replete growth. This indicated a significantly reduced level of protein secretion ($p < 0.0001$; unpaired t-test) during iron starvation, with 5.45 times less total protein secreted during iron starvation.

To investigate if a lowered biomass accounted for the reduced levels of protein secretion under iron starvation, mycelia were washed and lyophilised to dryness to estimate dry weight. Surprisingly, there was no significant difference in the biomass in response to iron starvation (Figure 3.2). This is in contrast to the reduced biomass observed by others in iron-deplete growth at 24 h growth (Wiemann *et al.*, 2014). To validate the biomass levels at 72 h, *A. fumigatus* was grown in the same conditions for 24 h and biomass measured. This did indicate significantly ($p < 0.005$; unpaired t-test) reduced biomass during iron starvation (Figure 3.3). All raw data associated with the preliminary characterisation is found in the Appendices in Supplementary Table 1-3.

Centrifugal filter extracted protein samples were subsequently subjected to TCA precipitation and SDS-PAGE analysis. This indicated differential abundance of several proteins between the two conditions (Figure 3.4). Protein bands were excised and digested with trypsin for Ion-Trap LC-MS/MS identification as described in Sections 2.2.13.1 and 2.2.13.5. Successfully identified proteins are listed in Table 3.1.

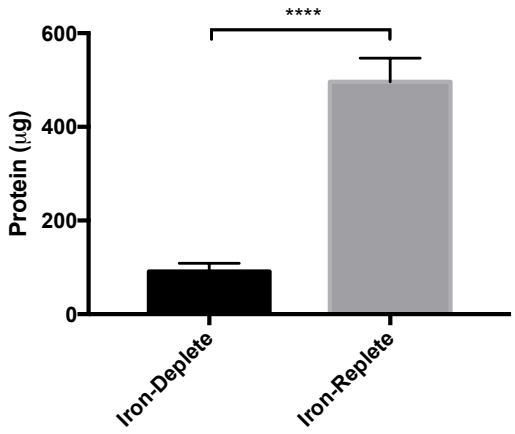

Figure 3.1 Total secreted protein yields following growth in iron-deplete or –replete media for 72 h (100 ml cultures; $n = 4$). Following secreted protein extraction

via centrifugal filter concentration, total protein yields were determined by Bradford assay. There was significantly less secreted protein present during iron starvation ($p < 0.0001$; unpaired t-test).

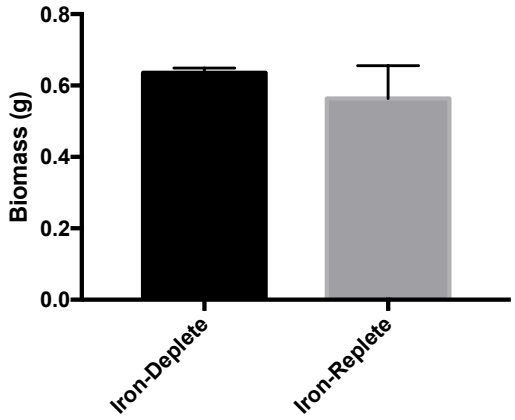

Figure 3.2 Biomass of *A. fumigatus* following growth in iron-deplete or –replete media for 72 h (100 ml cultures; $n = 4$). No significant difference was observed in the mycelial biomass yields following growth in iron-deplete and –replete media for 72 h.

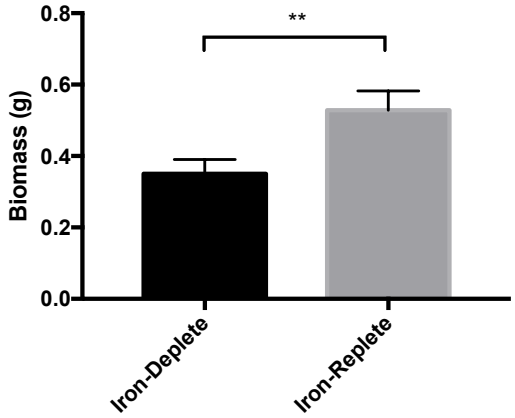

Figure 3.3 Biomass of *A. fumigatus* following growth in iron-deplete or –replete media for 24 h (50 ml cultures; $n = 3$). There was significantly reduced biomass in response to iron starvation at 24 h growth ($p < 0.005$; unpaired t-test).

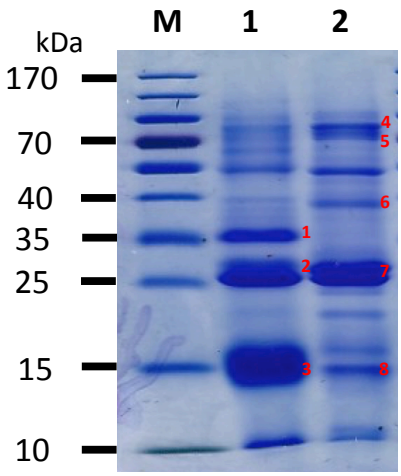

Figure 3.4 SDS-PAGE analysis of secreted proteins isolated from iron-deplete and -replete growth (20 µg loading). M: Molecular mass marker. 1: Secreted proteins from iron-deplete growth. 2: Secreted proteins from iron-replete growth. Bands numbered in red were excised and identified by LC-MS/MS analysis (Table 3.1).

Table 3.1 Identification of iron-deplete and –replete secretome proteins from SDS-PAGE following Ion Trap LC-MS/MS analysis (Figure 3.4).

Protein description	Score[1]	Peptides	Coverage (%)[2]	tMW	Name	Accession	Band no.
Probable pectate lyase A[a]	491	6	34	33858	PlyA	AFUA_2G00760 [a]	1
Uncharacterized protein	163	2	10	30101	-	AFUA_2G15420	2
Probable pectate lyase A[a]	67	1	6	33858	PlyA	AFUA_2G00760 [a]	3
bifunctional catalase-peroxidase Cat2	277	4	9	83824	Cat2	AFUA_8G01670	4
mycelial catalase Cat1	395	5	9	79918	Cat1	AFUA_3G02270	5
class V chitinase ChiB1	284	4	18	47706	ChiB1	AFUA_8G01410	6
alkaline serine protease Alp1	125	1	8	42164	Alp1	AFUA_4G11800	7
Asp-hemolysin	216	3	32	15303	Asp-HS	AFUA_3G00590	8

[1] Mascot protein score. [2] Coverage (%) refers to the % of the protein sequence represented in identified peptides. [a] The same protein (PlyA) was identified for bands 1 and 3.

3.2.2 Label-free quantitative proteomics indicates significant secretome remodelling in response to iron starvation

Secreted proteins were extracted from *A. fumigatus* grown in iron-deplete or –replete media for 72 h. Proteins were extracted from the supernatant as described in Section 2.2.10.2 and prepared for LFQ proteomic analysis as described Sections 2.2.13.3 and 2.2.13.7. To obtain a meaningful LC-MS/MS analysis of the protein content of each sample, 500 ng of tryptic peptides were injected for each sample. Matching of spectra to peptides, and matching of peptides to proteins were carried out in MaxQuant against a database of the *A. fumigatus* Af293 proteome (UniProt). After identification, MaxQuant uses peptide intensities as a proxy for protein abundances (Tyanova *et al.*, 2016a). These values are subsequently used in the program, Perseus, for the comparative analysis of protein abundances in response to iron starvation (Tyanova *et al.*, 2016b). However, due to the significant difference in total protein yield between iron-deplete and -replete growth (Figure 3.1), whereby there was 5.45 times less total protein secreted during iron starvation, an injection of equal protein content (500 ng each) would over represent the proteins present during iron starvation. Hence, during data processing in Perseus, protein abundances were scaled to the total protein yield in a 100 ml culture volume for both conditions thereby normalising protein abundances to the original total protein yields. This was carried out using the Perseus Plugin, Proteomic Ruler, utilising the 'Total Protein Approach' proposed by Wiśniewski *et al.* (2012). This showed that a protein's relative abundance within a protein fraction is related to its relative MS signal within the total MS signal (Wiśniewski *et al.*, 2012, 2014).

In total, 398 proteins were detected in either iron-deplete or –replete growth (min. $n = 3$ in either condition) following processing of raw data through MaxQuant

and Perseus (Section 2.2.14.2) (Appendices, Supplementary Table 4). Scatterplot analysis comparing the intensities of individual proteins between different sample pairs indicated strong correlation between replicates (> 0.971), but only moderate correlation when comparing the iron-deplete secretome to the iron–replete secretome (< 0.403) (Figure 3.5). The top ten most abundant proteins detected in this work, in either iron-deplete or –replete growth are listed in Table 3.2. Remarkably high sequence coverage was obtained for many of these proteins, for example peptides detected matching superoxide dismutase, SodC (AFUA_5G09240), amounted to 99.4% sequence coverage for this 15.966 kDa protein.

Comparative qualitative analysis indicated 216 proteins were either unique to or absent from iron-deplete growth, with 105 proteins uniquely detected in iron-deplete growth and 111 uniquely detected in iron-replete growth (Figure 3.6) (Appendices, Supplementary Table 5). Quantitative analysis using a t-test indicated 115 proteins showed differential abundance ($\log_2$ fold change > 2 or < -2; $p < 0.05$) in response to iron starvation, with 15 showing increased abundance and 100 decreased abundance (Figure 3.7) (Appendices, Supplementary Table 6). Proteins unique or absent following iron-deplete growth in the qualitative data were also termed to be increased or decreased in abundance as opposed to unique or absent to avoid false reports of absence in cases where protein levels were below instrument detection limits. Thus, collectively, 120 proteins showed increased abundance and 211 decreased abundance in response to iron starvation.

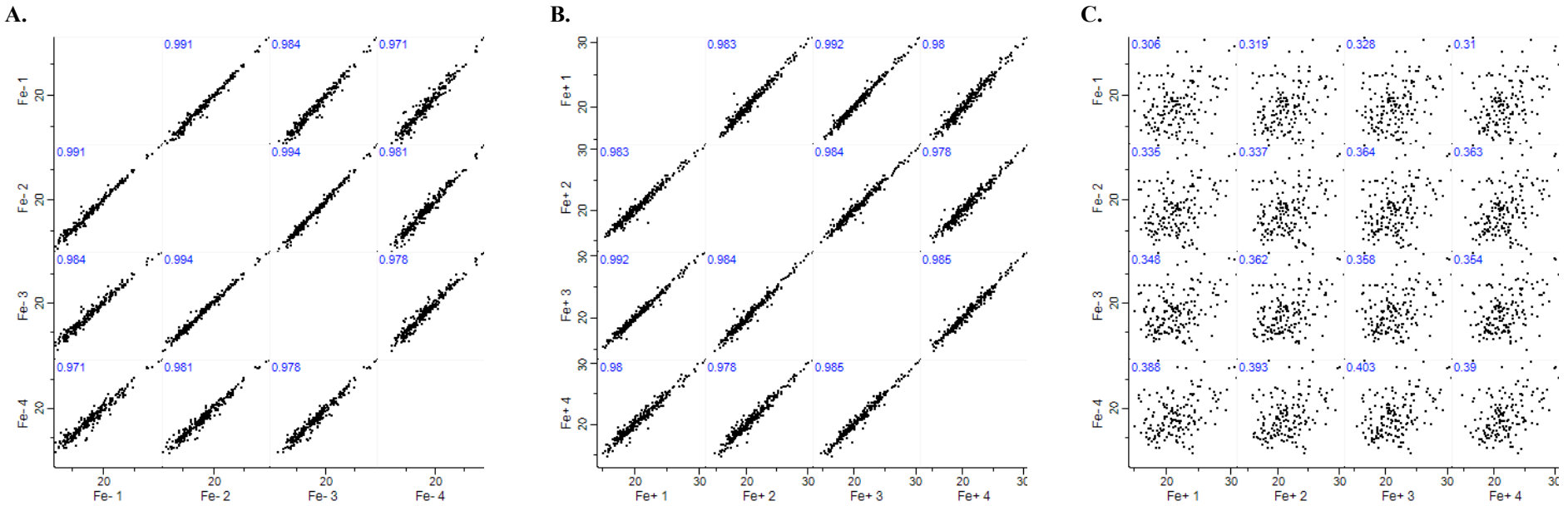

Figure 3.5 Scatterplot analysis comparing the intensity (log_2) values of individual proteins between different sample pairs. (A) Scatterplot of protein intensities comparing replicates from the iron-deplete secretome. (B) Scatterplot of protein intensities comparing replicates from the iron-replete secretome. (C) Scatterplot of protein intensities comparing the iron-deplete secretome to the iron–replete secretome. The Pearson correlation coefficient is depicted in the top left corner of each plot and indicates strong correlation between replicates of the iron-deplete or –replete secretome (> 0.971), but only moderate correlation when comparing the iron-deplete secretome to the iron–replete secretome (< 0.403).

Table 3.2 The top ten most abundant proteins detected in the *A. fumigatus* secretome during iron-deplete and/or -replete growth (listed in order of protein intensity).

Protein description	Intensity	Peptides	Coverage (%)[1]	SP[2]	Name	Accession
Probable glucan endo-1,3-β-glucosidase EglC	3.7×10^{11}	23	33.2	SP	EglC/ Bgt2	AFUA_3G00270[b,c]
Probable pectate lyase A	3.5×10^{11}	36	68.8	SP	PlyA	AFUA_2G00760[b,e]
FG-GAP repeat protein	3.3×10^{11}	36	89.9	SP	-	AFUA_1G04130[b,c]
Ribonuclease (mitogillin)	2.6×10^{11}	25	83	SP	MitF/ Aspf1	AFUA_5G02330[b,c]
Superoxide dismutase [Cu-Zn]	1.3×10^{11}	24	99.4	-	SodC	AFUA_5G09240
Alkaline protease 1 (ALP)	1.1×10^{11}	25	53.6	SP	Alp1/ Aspf13	AFUA_4G11800[a]
Catalase B	5.0×10^{10}	74	66.2	SP	CatB/ Cat1	AFUA_3G02270[b]

Protein description	Intensity	Peptides	Coverage (%)[1]	SP[2]	Name	Accession
Cell wall protein	4.6×10^{10}	17	74.4	SP	-	AFUA_3G01130
Elastase inhibitor AFUEI	4.2×10^{10}	6	70.1	SP	-	AFUA_3G14940
Probable glycosidase Crf1	4.1×10^{10}	21	45.6	SP	Crf1	AFUA_1G16190[b]

[1] Coverage (%) refers to the % of the protein sequence represented in identified peptides. **[2]** Indicates the presence of a signal peptide sequence on the protein. [a] Defined as a fungal allergen. [b] Demonstrated to bind human IgE. [c] Demonstrated to bind human IgG. [d] Immunoreactive with sera of rabbits exposed to *A. fumigatus*. [e] Capable of adhering to fibrinogen.

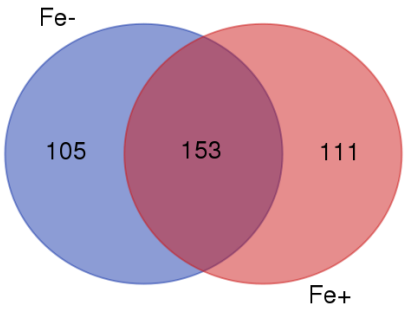

Figure 3.6 Venn diagram depicting proteins detected in both the iron-deplete and –replete secretome (n = 153), or unique to the iron-deplete secretome (n = 105), or unique to the iron-replete secretome (n = 111).

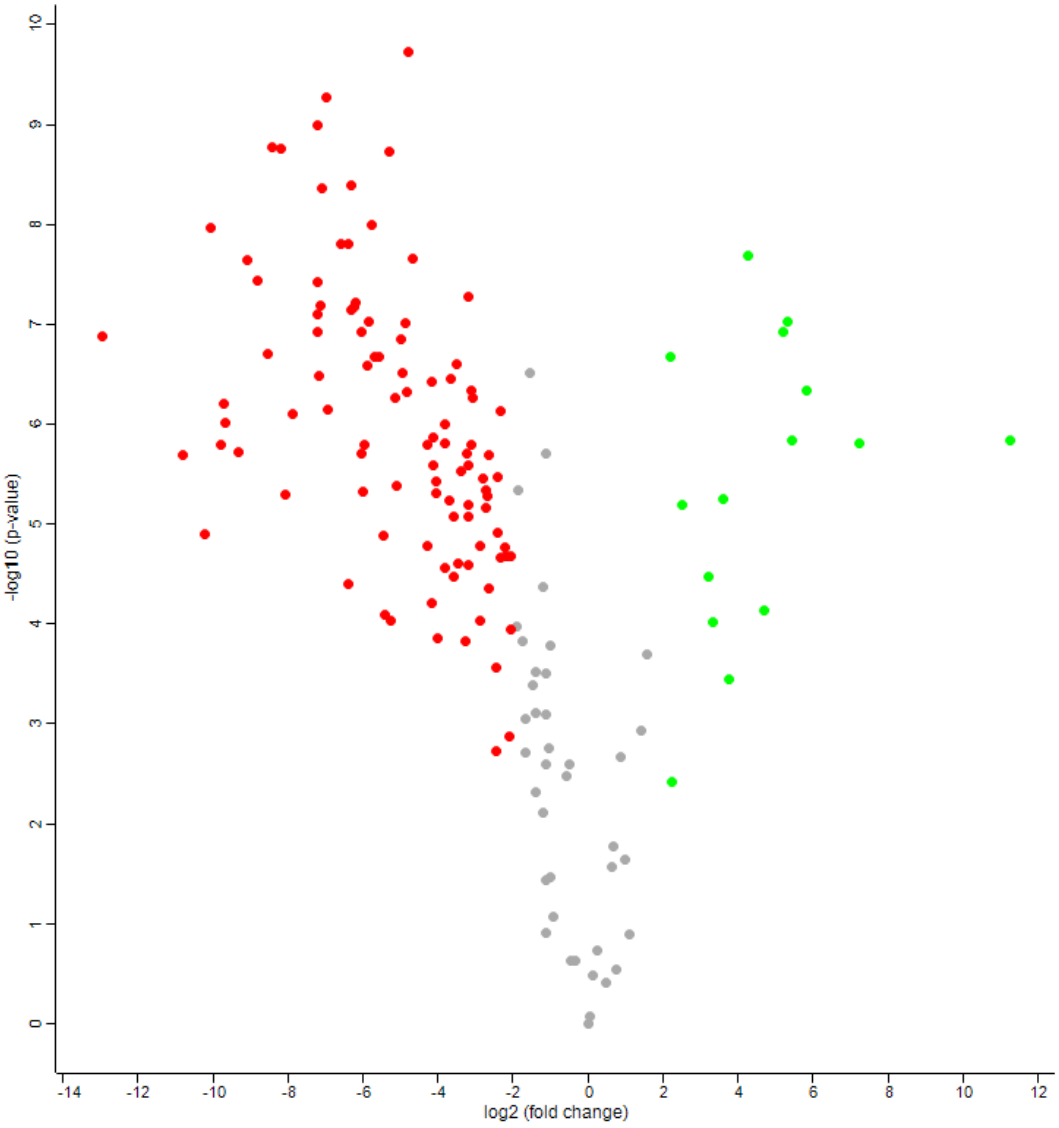

Figure 3.7 Scatterplot analysis of secretome proteins in response to iron starvation ($\log_2$ fold change versus $-\log_{10}$ *p*-value) (min. $n = 3$ in each condition). Proteins detected during both iron-deplete and -replete growth but with differential abundance in response to iron starvation ($\log_2$ fold change > 2 or < -2; $p < 0.05$; 2-sample t-test) are marked in green (increased abundance) or red (decreased abundance).

Of the 398 proteins detected in total, 160 were predicted to contain a signal peptide according to UniProt database interrogation. Of proteins with increased abundance in response to iron starvation, 52% (n = 62) contained signal peptides, while of those with decreased abundance, 30% (n = 63) contained signal peptides (Figure 3.8).

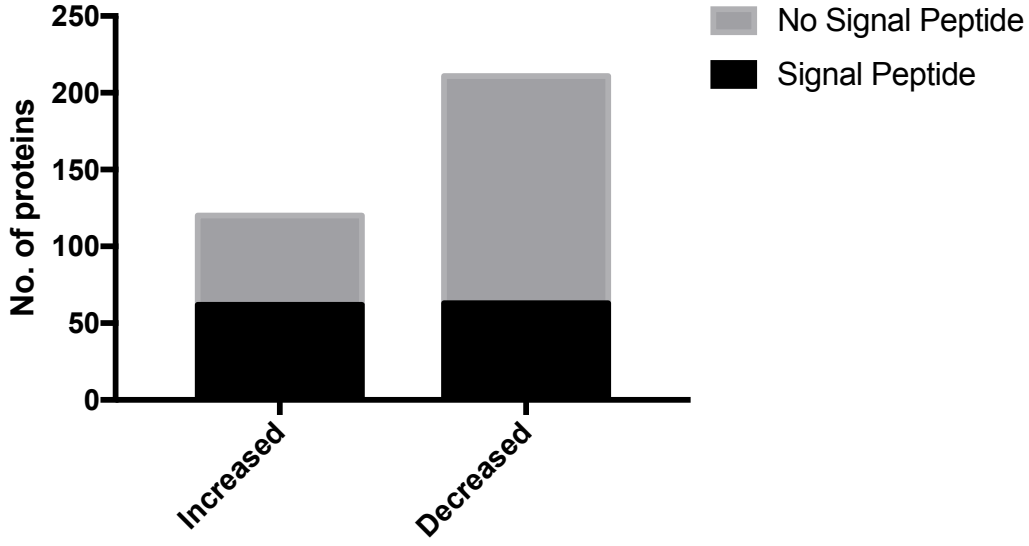

Figure 3.8 Abundance of signal peptide-containing proteins in proteins with increased or decreased abundance in response to iron starvation. Of the 120 proteins with increased abundance in response to iron starvation, 62 (52%) contained signal peptides; whereas of the 211 proteins with decreased abundance, 63 (30%) contained signal peptides.

Proteins with differential abundance in response to iron starvation were initially investigated globally for enrichment of GO categories using FungiFun2 (https://elbe.hki-jena.de/fungifun/fungifun.php) with a Fischer's exact test for enrichment ($p < 0.05$) (Appendices, Supplementary Table 7 and 8) (Priebe *et al.*, 2015). The most significantly represented GO cellular compartment category represented was 'extracellular region' for proteins with both increased abundance (n = 26) and decreased abundance (n = 44) in response to iron starvation. Among the top most significantly represented GO molecular function categories in proteins with increased abundance were; structural constituent of ribosome (n =11), cation binding (n = 7), IgE binding (n = 3), carbohydrate binding (n = 3), cellulase activity (n = 3), endo-1,4-β-xylanase activity (n = 2), and fibrinogen binding (n = 2) (Figure 3.9 A). Among the top most significantly represented GO molecular function categories in proteins with decreased abundance were; cation binding (n = 14), pyridoxal phosphate binding (n = 11), hydrolase activity, hydrolyzing O-glycosyl compounds (n = 10), peptidase activity (n = 6), carbohydrate binding (n = 6), and metal ion binding (n = 5) (Figure 3.9 B).

A.

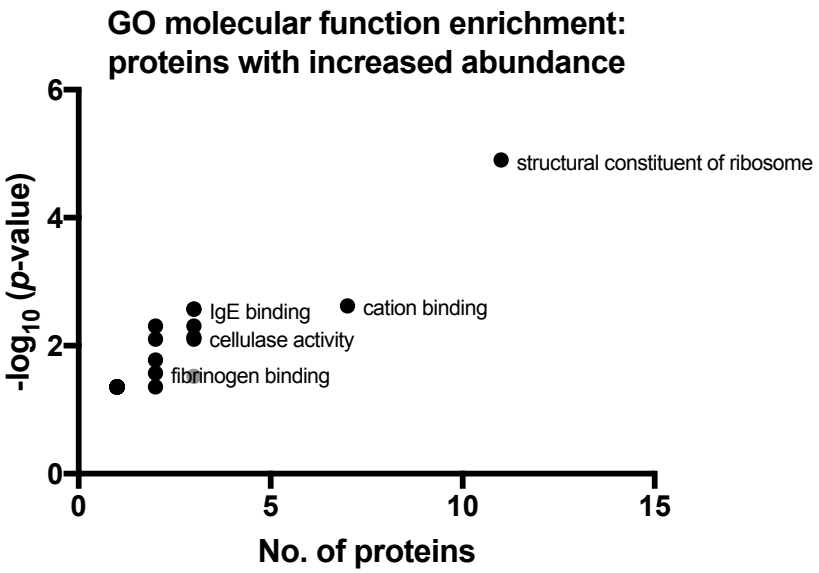

B.

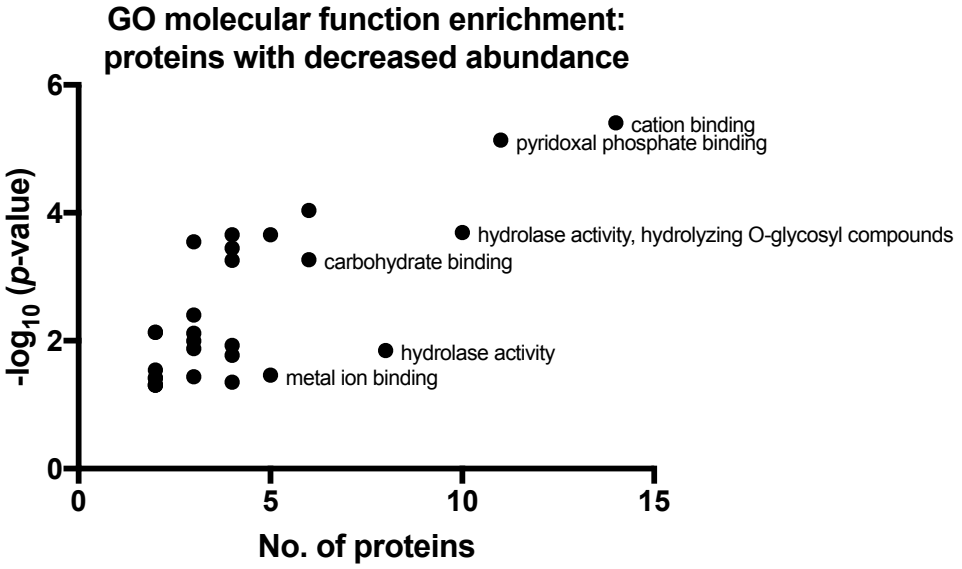

Figure 3.9 GO molecular function categories enriched significantly ($p < 0.05$; Fischer's exact test) in proteins with (A) increased, or (B) decreased abundance in response to iron starvation.

3.2.3 Iron starvation increases the abundance of proteins implicated in host recognition

Enrichment analysis indicated the GO molecular function categories of 'IgE binding' and 'fibrinogen binding' were significantly represented in the iron-deplete secretome (Figure 3.9 A; Appendices, Supplementary Table 7). Further database interrogation indicated that 29 of the proteins with increased abundance in response to iron starvation had previously been implicated in host recognition by others (Table 3.3). Proteins either (i) defined as allergens (Abad *et al.*, 2010), (ii) recognised by IgG or IgE in human sera including from patients with proven IA, probable IA, or ABPA (Singh *et al.*, 2010a, 2010; Teutschbein *et al.*, 2016; Virginio *et al.*, 2014), (iii) recognised by IgG, IgA, or IgM in rabbit sera following challenge with *A. fumigatus* (Asif *et al.*, 2010), or (iv) capable of adhering to fibrinogen (Upadhyay *et al.*, 2012) were considered to be implicated in host recognition.

Table 3.3 Secretome proteins with increased abundance in response to iron starvation previously implicated in host recognition (as defined in Section 3.2.3). Proteins are listed in order of accession ID.

Protein description	Fold change[1]	Peptides	Coverage (%)[2]	Name	Accession	Reference
40S ribosomal protein S3	Unique	3	13.5	-	AFUA_1G05630	(Singh *et al.*, 2010)[b]
Elongation factor 1-alpha	Unique	3	9.7	Tef1	AFUA_1G06390	(Teutschbein *et al.*, 2016)[c]
Pyruvate dehydrogenase E1 component subunit alpha	Unique	2	6.5	-	AFUA_1G06960	(Virginio *et al.*, 2014)[c]
Phosphoglycerate kinase	Unique	7	17.7	PgkA	AFUA_1G10350	(Asif *et al.*, 2010; Singh *et al.*, 2010; Teutschbein *et al.*, 2016; Virginio *et al.*, 2014)[b,c,d]
1,3-β-glucanosyltransferase Bgt1	Unique	18	53.4	Bgt1	AFUA_1G11460	(Singh *et al.*, 2010a)[b,c]
Isocitrate dehydrogenase [NAD] subunit, mitochondrial	Unique	2	3.1	-	AFUA_1G12800	(Singh *et al.*, 2010)[b]
Transketolase	Unique	2	3.7	-	AFUA_1G13500	(Teutschbein *et al.*, 2016)[c]

Protein description	Fold change[1]	Peptides	Coverage (%)[2]	Name	Accession	Reference
Probable pectate lyase A	↑ 2.51	36	68.8	PlyA	AFUA_2G00760	(Singh *et al.*, 2010a; Upadhyay *et al.*, 2009) [b,c,e]
Peptidyl-prolyl cis-trans isomerase	↑ 5.84	14	46.3	Cyp4/ Aspf11	AFUA_2G03720	(Abad *et al.*, 2010) [a]
Allergen Aspf4	Unique	8	32.3	Aspf4	AFUA_2G03830	(Abad *et al.*, 2010) [a]
Antigenic mitochondrial protein HSP60	Unique	2	3.9	Hsp60	AFUA_2G09290	(Asif *et al.*, 2010; Virginio *et al.*, 2014) [c,d]
Translation elongation factor EF-2 subunit	Unique	2	2.3	-	AFUA_2G13530	(Singh *et al.*, 2010; Teutschbein *et al.*, 2016; Virginio *et al.*, 2014)[b,c]
Class V chitinase	Unique	4	16.9	-	AFUA_3G07160	(Singh *et al.*, 2010a) [b,c]
Fructose-bisphosphate aldolase, class II	Unique	6	21.1	-	AFUA_3G11690	(Asif *et al.*, 2010; Singh *et al.*, 2010; Teutschbein *et al.*, 2016; Virginio *et al.*, 2014) [b,c]
Phosphoglucomutase	↑ 2.23	13	31.2	PgmA	AFUA_3G11830	(Asif *et al.*, 2010; Teutschbein *et al.*, 2016) [c,d]

Protein description	Fold change[1]	Peptides	Coverage (%)[2]	Name	Accession	Reference
Uncharacterized protein	Unique	4	9.2	GlfA	AFUA_3G12690	(Teutschbein *et al.*, 2016) [c]
Allergen Aspf7	Unique	5	16.3	Aspf7	AFUA_4G06670	(Abad *et al.*, 2010) [a]
Glycerol dehydrogenase (GldB)	Unique	3	13.8	GldB	AFUA_4G11730	(Teutschbein *et al.*, 2016) [c]
Glyceraldehyde-3-phosphate dehydrogenase	Unique	2	6.8	GpdA	AFUA_5G01970	(Asif *et al.*, 2010; Singh *et al.*, 2010) [b,d]
Ribonuclease (mitogillin)	↑ 11.26	25	83	MitF/ Aspf1	AFUA_5G02330	(Abad *et al.*, 2010; Singh *et al.*, 2010a) [a,b,c]
Heat shock protein 90	Unique	3	5.7	Hsp90/ Aspf12	AFUA_5G04170	(Abad *et al.*, 2010; Singh *et al.*, 2010; Virginio *et al.*, 2014) [a,b,c]
Woronin body protein HexA	Unique	2	2.8	HexA	AFUA_5G08830	(Teutschbein *et al.*, 2016) [c]
ATP synthase subunit beta	Unique	8	18.7	-	AFUA_5G10550	(Asif *et al.*, 2010; Singh *et al.*, 2010; Virginio *et al.*, 2014) [b,c,d]
Uncharacterized protein	↑ 5.21	5	38.5	-	AFUA_6G00180	(Upadhyay *et al.*, 2012) [e]

Protein description	Fold change[1]	Peptides	Coverage (%)[2]	Name	Accession	Reference
Peroxiredoxin Pmp20	Unique	6	36.3	Pmp20/ Aspf3	AFUA_6G02280	(Abad *et al.*, 2010; Asif *et al.*, 2010; Teutschbein *et al.*, 2016) [a,c,d]
Pyruvate kinase	Unique	2	6.5	-	AFUA_6G07430	(Asif *et al.*, 2010) [d]
Malate dehydrogenase	Unique	10	36.8	-	AFUA_7G05740	(Asif *et al.*, 2010; Singh *et al.*, 2010a, 2010) [b,d]
ATP synthase subunit alpha	Unique	11	20.3	-	AFUA_8G05320	(Teutschbein *et al.*, 2016) [c]
Probable beta-glucosidase BtgE	Unique	8	19.3	BtgE	AFUA_8G05610	(Virginio *et al.*, 2014) [c]

[1] Fold change refers to $\log_2$ fold change in protein abundance in response to iron starvation. [2] Coverage (%) refers to the % of the protein sequence represented in identified peptides. [a] Defined as a fungal allergen. [b] Demonstrated to bind human IgE. [c] Demonstrated to bind human IgG. [d] Immunoreactive with sera of rabbits exposed to *A. fumigatus*. [e] Capable of adhering to fibrinogen.

3.2.4 Increased immunoreactivity against proteins isolated from iron-deplete growth

To validate the observation of an increased abundance of proteins involved in host recognition in response to iron starvation, an indirect ELISA was developed for the detection of human antibodies against secreted proteins (Section 2.2.8). Secreted proteins grown in iron-deplete or –replete conditions were isolated as described for the LFQ proteomic analysis (Section 2.2.10.2). Proteins were coated onto ELISA plates and probed with individual human serum samples (obtained, with permission, from the Irish Blood Transfusion Service) (n = 41) followed by an anti-human IgG antibody (Figure 3.10). A paired t-test comparing the signal generated in all sera samples on iron-deplete versus –replete coated plates indicated significantly (p < 0.0001) higher signal from plates coated with iron-deplete proteins (Figure 3.11) (Appendices, Supplementary Table 9). This suggested more human IgG binding to secreted proteins isolated from iron starved growth.

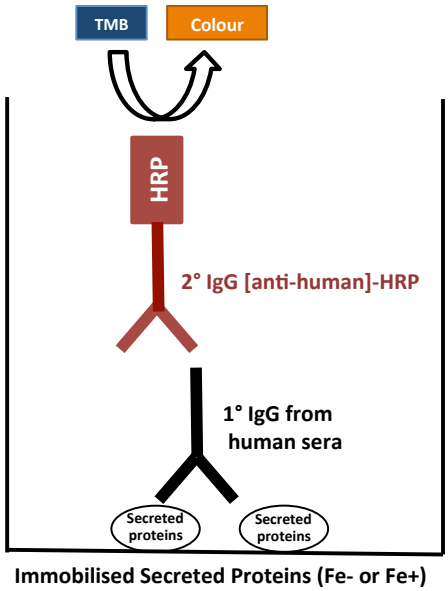

Figure 3.10 ELISA principle. Secreted proteins from iron-deplete or –replete growth were coated onto wells of ELISA plates. Human sera were subsequently

added to wells individually. Recognition of coated proteins by IgG results in immobilisation of the antibody to the plate such that it resists removal upon washing. The 1° antibody is then detected by an anti-human IgG antibody conjugated to HRP (2°) which similarly immobilises on the plate. After substrate (TMB) addition, HRP forms a coloured product generating a signal output readable at 450 nm after the reaction is stopped.

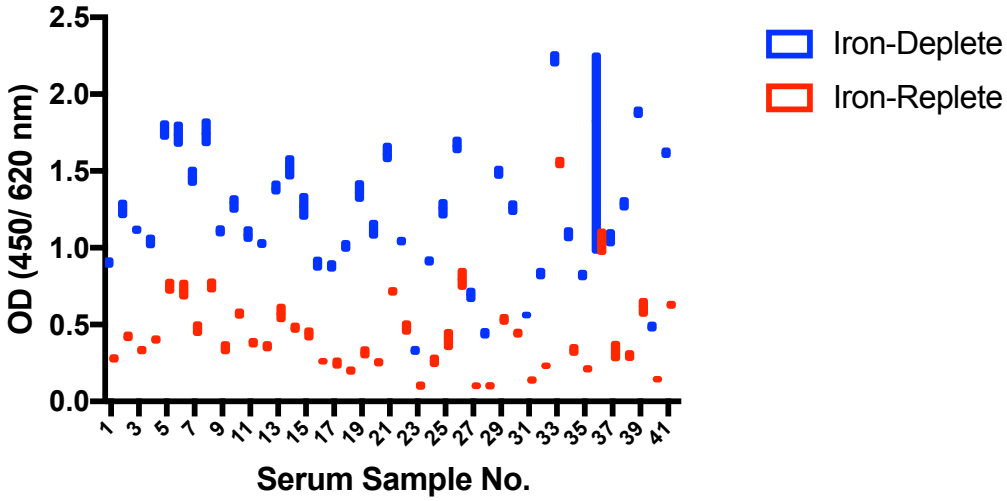

Figure 3.11 Indirect competitive ELISA analysis for the detection of human IgG against secreted proteins indicates more immunoreactivity against proteins secreted during iron starvation. Human sera (n = 41; with three technical replicates) were analysed by indirect ELISA for immunoreactivity against secreted proteins. A paired t-test comparing the signal generated in all sera samples (n = 41) on iron-deplete versus –replete coated plates indicated significantly (p < 0.0001) higher signal on plates coated with iron-deplete proteins. Sample 36 (biological sample 69) showed a wide deviation as a result of one of the technical replicates.

3.2.5 Iron starvation induces differential abundance of proteins involved in cell wall remodelling

There was evidence for a cell wall remodelling in response to iron starvation in the *A. fumigatus* secretome. Interestingly, a sensor of the cell wall integrity pathway, Wsc1 (AFUA_4G13670), was uniquely detected in the secretome during iron starvation. Several other members of this signal transduction pathway have previously been shown to increase in abundance in response to iron starvation (Moloney *et al.*, 2016a; Mulvihill *et al.*, 2017). Analysis of the secretome also indicated the differential abundance of many enzymes involved in remodelling polysaccharide components of the fungal cell wall including enzymes acting on chitin and glucan (Section 3.2.5.1 and 3.2.5.2).

3.2.5.1 Iron starvation induces differential abundance of chitinases

Chitinases, ChiA1 (AFUA_ 5G03760) and ChiB1 (AFUA_8G01410) showed a 5.41 and 7.21 log_2 fold decrease in response to iron starvation, respectively, in addition to a class V chitinase (AFUA_6G09310) which showed a 3.39 log_2 fold decrease in abundance (Table 3.4). While, another class V chitinase (AFUA_3G07160) was uniquely detected during iron starvation (Table 3.4). To qualitatively investigate this, *A. fumigatus* was grown in MM with and without iron and stained with the chitin binding stain, Calcofluor-white (n = 1) (Figure 3.12) (Section 2.2.6.2). This indicated increased staining during iron-deplete growth suggesting a higher chitin content or exposure therein.

Table 3.4 Proteins acting on chitin (n = 4) with differential abundance in response to iron starvation.

Protein description	Fold change[1]	Peptides	Coverage (%)[2]	Name	Accession
Class V chitinase	↓ 3.39	18	21.7	-	AFUA_6G09310
Endochitinase B1	↓ 7.21	16	44.6	ChiB1	AFUA_8G01410
Endochitinase A1	↓ 5.41	5	5.2	ChiA1	AFUA_5G03760
Class V chitinase	Unique	4	16.9	-	AFUA_3G07160

[1] Fold change refers to $\log_2$ fold change in protein abundance in response to iron starvation. [2] Coverage (%) refers to the % of the protein sequence represented in identified peptides.

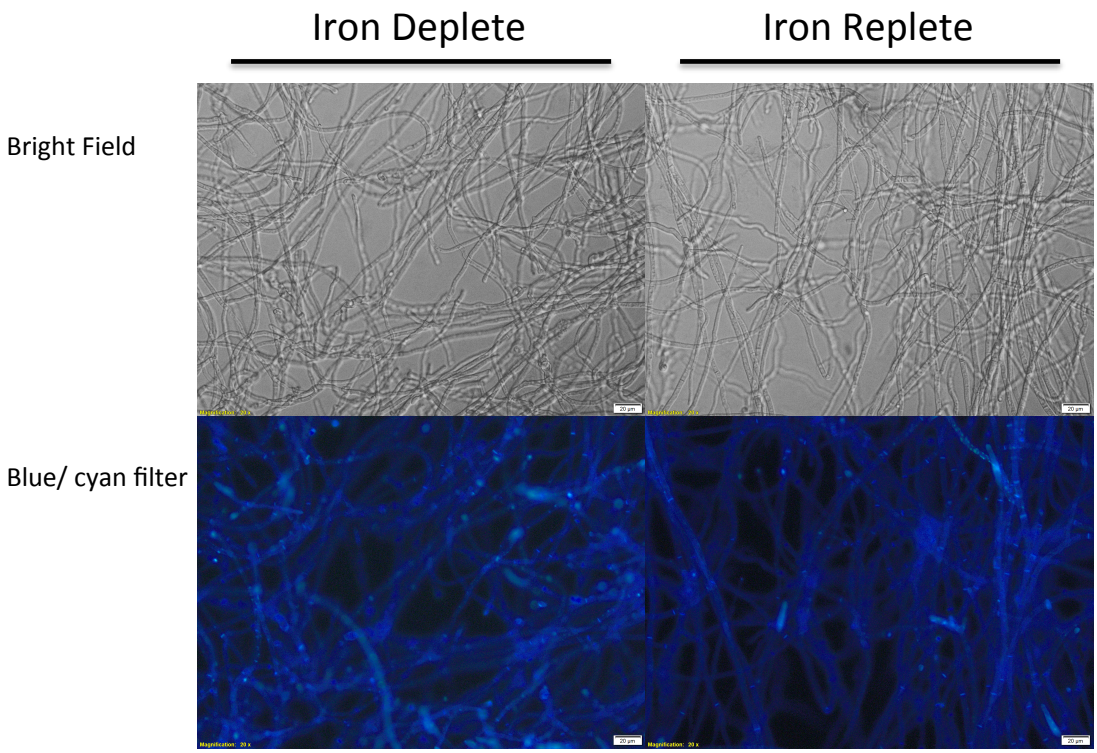

Figure 3.12 *A. fumigatus* was grown in iron-deplete or -replete MM iron and stained with Calcofluor-white. Staining indicated more intensity in mycelia from iron-deplete growth. Bar = 20 µm.

3.2.5.2 Iron starvation induces differential abundance of enzymes acting on glucan

There was differential abundance of many of the enzymes reported to act on glucan chains in the fungal cell wall (Mouyna *et al.*, 2013) (Table 3.5 and 3.6). Specifically, there was an increased abundance of enzymes predominantly involved in glucan chain elongation, crosslinking, and branching; whereas there was decreased of abundance of predominantly glucanases, which can hydrolyse glucan. To explore any differential glucanase activity, a glucanase activity assay was carried out using secreted proteins (Section 2.2.12.4). *A. fumigatus* supernatant proteins from iron-deplete and –replete growth (n = 4) were isolated without TCA precipitation to preserve native conformation and therefore function (Section 2.2.10.2). Extracts were incubated with laminarin in parallel with a glucanase standard. Subsequently, glucose content was estimated using an Ampliflu^{TM} red assay. Glucanase activity (mU/ mg protein) was estimated based on the activity of the glucanase standard. This assay was carried out by Rose Waldron (Maynooth University). This indicated significantly ($p < 0.0001$; unpaired t-test) reduced glucanase activity during iron starvation, with 181.9 ± 24.69 mU/ mg glucanase activity during iron-deplete growth, but 722.6 ± 58.08 mU/ mg glucanase activity during iron-replete growth (Figure 3.13) (Appendices, Supplementary Table 10-11).

Table 3.5 Proteins with predicted roles in cell wall remodelling (n = 5) with increased abundance in response to iron starvation.

Protein description	Role in cell wall[1]	Fold change[2]	Peptides	Coverage (%)[3]	Name	Accession
1,3-β-glucanosyltransferase Bgt1	Glucan branching	Unique	18	53.4	Bgt1	AFUA_1G11460
Probable β-glucosidase BtgE	Glucan branching	Unique	8	19.3	Scw11	AFUA_8G05610
Cell wall glucanase/allergen F16-like	Glucan crosslinking	Unique	5	15.7	Crh1	AFUA_6G03230
Probable glycosidase Crf2	Glucan crosslinking	↑ 5.44	12	18.7	Crh2	AFUA_2G03120 [a]
Protein Ecm33	Cell wall integrity	Unique	6	20.4	Ecm33	AFUA_4G06820 [a]

[1] Role in cell wall according to (Mouyna *et al.*, 2013) (excluding Ecm33). [2] Fold change refers to $\log_2$ fold change in protein abundance in response to iron starvation. [3] Coverage (%) refers to the % of the protein sequence represented in identified peptides. [a] Predicted to contain a GPI attachment sequence.

Table 3.6 Proteins with predicted roles in cell wall remodelling (n = 10) with decreased abundance in response to iron starvation.

Protein description	Role in cell wall[1]	Fold change[2]	Peptides	Coverage (%)[3]	Name	Accession
Glucanase	Exo β(1–3) glucanase	Absent	3	9.8	Exg3	AFUA_7G05610
Exo-β-1,3-glucanase	Exo β(1–3) glucanase	↓ 4.14	11	22.5	Exg6	AFUA_6G13270
Exo-β-1,3-glucanase	Exo β(1–3) glucanase	Absent	5	8.8	Exg7	AFUA_3G07520
Exo-β-1,3-glucanase Exg0	Exo β(1–3) glucanase	↓ 2.64	16	23.4	Exg8	AFUA_1G14450
Endo-1,3-β-glucanase Engl1	Endo β (1–3) glucanase	Absent	15	17.5	Engl1	AFUA_1G04260
Endo-1,3(4)-β-glucanase	Endo β (1–3) glucanase	Absent	6	28.1	Eng7	AFUA_3G03080
Probable β-glucosidase A	Exo-β–glucanase	↓ 6.93	17	26.7	Exg12	AFUA_1G05770
Probable β-glucosidase L	Exo-β–glucanase	↓ 4.04	44	63.9	Exg13	AFUA_7G06140

Protein description	Role in cell wall[1]	Fold change[2]	Peptides	Coverage (%)[3]	Name	Accession
Probable glucan endo-1,3-β-glucosidase EglC	Glucan branching	↓ 2.65	23	33.2	EglC/ Bgt2	AFUA_3G00270 [a]
1,3-β-glucanosyltransferase	Glucan elongation	↓ 4.06	3	7.8	Gel5	AFUA_8G02130 [a]

[1] Role in cell wall according to (Mouyna *et al.*, 2013). [2] Fold change refers to $\log_2$ fold change in protein abundance in response to iron starvation. [3] Coverage (%) refers to the % of the protein sequence represented in identified peptides. [a] Predicted to contain a GPI attachment sequence

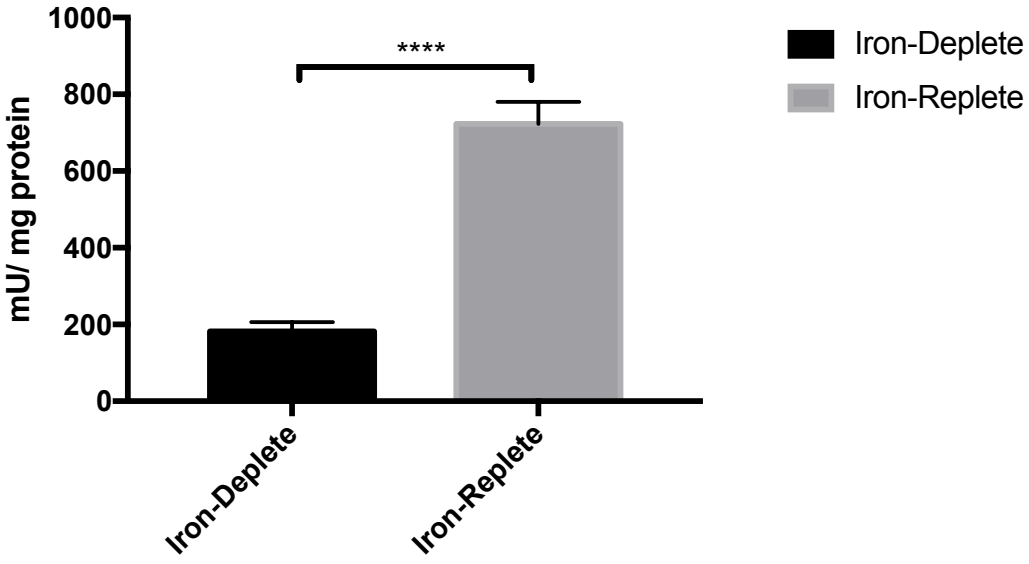

Figure 3.13 Glucanase activity of secreted proteins isolated from iron-deplete and –replete growth. There was significantly reduced glucanase activity (mU/ mg) in response to iron starvation ($p < 0.0001$; unpaired t-test).

3.3 Discussion

Along with the cell wall, the secretome represents a focal point of the host-pathogen interface during infection. Following this, several studies have focused on characterising the secretome of *A. fumigatus* (Farnell *et al.*, 2012; Gautam *et al.*, 2007; Kumar *et al.*, 2011; Shi *et al.*, 2012a; Singh *et al.*, 2010a; Upadhyay *et al.*, 2012; Wartenberg *et al.*, 2011). The bioavailability of iron is a key factor in microbial infection, with mechanisms of nutritional immunity acting to deprive iron from invading microorganisms (Cassat and Skaar, 2013; Crawford and Wilson, 2015). Moreover, low iron availability induces significant global transcriptomic and proteomic remodelling in *A. fumigatus* (Haas, 2014; Moloney *et al.*, 2016a; Mulvihill *et al.*, 2017; Schrettl *et al.*, 2008, 2010). Hence, study of the iron-starved secretome in *A. fumigatus* is warranted to dissect and understand adaptations of *A. fumigatus* at the host-pathogen interface. To this end, *A. fumigatus* was grown in iron-deplete and –replete media, secreted proteins were extracted and analysed by LFQ proteomics. Comparative analysis indicated significant secretome remodelling in response to iron starvation. GO enrichment analysis indicated the cellular compartment of 'extracellular' was the most significantly represented in either protein set (Section 3.2.2). In addition, various GO molecular function categories were differentially enriched under both conditions (Figure 3.9). Detailed comparative analysis indicated an increased abundance of many proteins implicated in host recognition (Section 3.2.3). Furthermore, there was differential abundance of various cell wall enzymes and evidence for induction of the cell wall remodelling in response iron starvation (Section 3.2.5).

Despite no significant difference in the biomass between iron-deplete and –replete growth, there was significantly less total secreted protein yield in response to

iron starvation (Section 3.2.1). LFQ proteomic analysis identified 398 proteins in total (min. n = 3 in either condition). There was high correlation between replicates (Pearson correlation coefficient > 0.971), but only moderate correlation between the two conditions (< 0.403). Comparative proteome analysis indicated 120 proteins with increased abundance and 211 with decreased abundance in response to iron starvation (Section 3.2.2). Fifty-two percent of the proteins with increased abundance had signal peptides, while 30% of proteins with decreased abundance had signal peptides (Figure 3.8). Proteins destined for classical secretion contain a signal peptide sequence that directs them to the ER for co-translational entry. They are subsequently transported *via* vesicles to the Golgi where they are sorted before transport again through vesicles to the plasma membrane for externalisation (Lodish, 2000). Many proteins lacking signal peptide sequences are often found in the secretome and likely represent unconventional secretion mechanisms (McCotter *et al.*, 2016). However, they may also represent protein release from dead, lysed cells. Interestingly, the observation of a higher relative abundance of signal peptide containing proteins during iron-deplete growth suggests an iron-sensitive regulatory mechanism for the unconventional secretion of proteins.

Among the ten most abundant proteins identified in this work (Table 3.2), nine had previously been detected in the supernatant of *A. fumigatus*; EglC (AFUA_3G00270), PlyA (AFUA_2G00760), AFUA_1G04130, MitF/ Aspf1 (AFUA_5G02330), SodC (AFUA_2G11800), Alp1/ Aspf13, CatB/ Cat 1 (AFUA_3G02270), AFUA_3G01130, and Crf1 (AFUA_1G16190) were previously detected in secretomic studies by Singh *et al.* (2010), Wartenberg *et al.* (2011), Farnell *et al*. (2012), or Upadhyay *et al.* (2012). Recently, Teutschbein *et al*. (2016) suggested that the relative abundance of proteins within the *A. fumigatus* proteome

impacted the host serological response; whereby highly abundant proteins are more likely to induce a humoral immune response (Teutschbein *et al.*, 2016). In support of this, seven of the ten most abundant proteins observed here in secretome have been somehow implicated in host recognition. Alp1/ Aspf13 is designated as a fungal allergen (Abad *et al.*, 2010). It was detected during both iron-deplete and –replete growth but showed decreased abundance (8.8 $\log_2$ fold) in response to iron starvation. Alp1/ Aspf13 has been identified as a major secreted protein in several studies and was detected in the *A. fumigatus* secretome during growth on elastin, collagen, and keratin, as well as in media containing casein, pig lung, and mucin (Farnell *et al.*, 2012; Wartenberg *et al.*, 2011). The position of Alp1/ Aspf13 as a major secreted protein is supported by its persistent presence during iron-deplete and –replete growth despite the dramatic proteome remodelling between these two conditions (Figure 3.5). SodC was also shown to be immunoreactive using sera from rabbits exposed to *A. fumigatus* (Asif *et al.*, 2010). MitF/ Aspf1 is another fungal allergen and showed increased abundance (11.26 $\log_2$ fold) in response to iron starvation (Abad *et al.*, 2010). Singh *et al.* (2010) also identified MitF/ Aspf1, along with EglC, CatB/ Cat1, and AFUA_1G04130 in the *A. fumigatus* secretome and found them to be reactive with IgG and IgE from ABPA patient sera (Singh *et al.*, 2010a). Crf1 and PlyA were also immunoreactive with IgE from ABPA patient sera and detected in the secretome during growth in elastin, collagen, and keratin (Singh *et al.*, 2010a; Wartenberg *et al.*, 2011). PlyA was also shown to bind blood clotting glycoprotein, fibrinogen, in the secretome and increased in abundance in response to iron starvation (2.51 $\log_2$ fold) (Upadhyay *et al.*, 2012).

In addition to proteins among the top ten most abundant (MitF/ Aspf1 and PlyA), a further 27 proteins with increased abundance under iron starvation have been

implicated in host recognition. These proteins are listed in Table 3.3. Many of these are designated as fungal allergens including, Aspf1, Aspf3 (Pmp20), Aspf4, Aspf7, Aspf11 (Cyp4), and Asp12 (Abad *et al.*, 2010). In addition, a further 11 proteins listed in Table 3.3 were shown to be immunoreactive with human IgE, several of which were previously identified in the *A. fumigatus* secretome including AFUA_1G11460, AFUA_2G00760, AFUA_3G07160, and AFUA_5G02330 (Singh *et al.*, 2010a, 2010). Twenty of the proteins listed in Table 3.3 have been shown to be immunoreactive with human IgG (Singh *et al.*, 2010a, 2010; Teutschbein *et al.*, 2016; Virginio *et al.*, 2014). Interestingly, two of these human IgG-reactive proteins (AFUA_2G09290 and AFUA_5G10550) were shown to be exclusively immunoreactive with sera from a patient with proven IA and not with control sera or sera from patients with other mycoses (Virginio *et al.*, 2014).

To confirm the induction of a more immunoreactive secretome during iron starvation, an indirect ELISA for the detection of antibodies against secreted proteins was developed (Section 2.2.8). The principle of this ELISA is illustrated in Figure 3.10. This ELISA was subsequently used to screen individual human sera from the general population (n = 41). There was significantly more immunoreactivity against proteins isolated from iron-deplete growth ($p < 0.0001$; paired t-test), which was similarly observed for iron-deplete microsomal proteins by Moloney *et al.* (2016b). This suggests that the antigenic proteins produced by *A. fumigatus* during iron starvation are more relevant to host recognition and, therefore, attempts at host colonisation. Given the frequency of spore inhalation by humans, a high prevalence of immunoreactivity against *A. fumigatus* in the general population is unsurprising and has been observed in other proteomic studies (Latgé, 1999; Moloney *et al.*, 2016). Upon attempts at host colonisation as well as dissemination within the host, the

bioavailability of iron dictates the secretomic constituents of *A. fumigatus*. In response to iron starvation, there is clearly a dramatic reshuffling of protein abundances. This, in turn, directs the predominant antigens against which the serological response of the host is raised. As a result, we show that the proteins with higher abundance during iron starvation are typically more immunoreactive with sera from either the general population or ABPA/ IA patients.

In addition to proteins capable of interacting with antibodies, two of the proteins with increased abundance under iron starvation have been shown to bind fibrinogen (PlyA, 2.51 $\log_2$ fold; AFUA_6G00180, 5.21 $\log_2$ fold) (Table 3.3) (Upadhyay *et al.*, 2012). Fibrinogen is a glycoprotein involved in blood clotting and binding to this protein is speculated to aid host adherence. Mechanisms of host adherence such as this are believed to be important in establishing and maintaining infection for *A. fumigatus* (Moloney *et al.*, 2016; Upadhyay *et al.*, 2009, 2012). Adhesins are the collective term given to the proteins and carbohydrates that mediate this process and many adhesins are cell wall related proteins (de Groot *et al.*, 2013). Interestingly, there was differential abundance of many proteins involved in cell wall processes under iron starvation (Section 3.2.5). Cell wall proteins are typically expected to be associated with the plasma membrane or cell wall; however their presence in fungal culture supernatants has been reported by others (Adav *et al.*, 2013, 2015; Ene *et al.*, 2012; Sorgo *et al.*, 2011). This may be a result of phospholipase-mediated cleavage of GPI anchored proteins from the cell surface. Such cleavage may act as a means of regulating GPI protein attachment, whereby cleavage can function in signal transduction or release of the protein for a secondary function (Paulick and Bertozzi, 2008). Alternatively, the action of culture shaking may encourage the release of proteins from the cell wall into the supernatant.

In *C. albicans,* the differential abundance of cell wall enzymes in the secretome has been associated with concomitant cell wall remodelling in several studies (Ene *et al.*, 2012; Heilmann *et al.*, 2013; Sorgo *et al.*, 2011). Similarly, in this work the secretomic profile of *A. fumigatus* under iron starvation suggested an iron-responsive cell wall remodelling (Section 3.2.5). Cell wall related proteins with increased abundance were predominantly involved in glucan chain branching, elongation, or crosslinking (Table 3.5). For example, Crh1 and Crh2, function in cross-linking glucan and chitin chains in fungi and were increased in abundance (Free, 2013). In contrast, proteins with decreased abundance were predominantly involved in hydrolysing β-1,3-glucan chains as glucanases (Table 3.6). For example, exo-β–glucanases, Exg3, Exg6, Exg7, Exg8, Exg12, and Exg13. Following this, a decreased level of glucanase activity under iron starvation was verified using an *in vitro* assay with native secreted proteins. This indicated four times less glucanase activity (mU/ mg) under iron starvation (Figure 3.13). There was also a decreased abundance of three chitinases (ChiA1, ChiB1, and AFUA_6G09310) and increased abundance of only one class V chitinase (AFUA_3G07160) in response to iron starvation (Table 3.4). Calcofluor staining qualitatively supported an increased presence or exposure of chitin in mycelia following culture under iron starvation (Figure 3.12). Such an orchestrated restructuring of enzymatic activity suggested a targeted remodelling of the cell wall during iron starvation, with a reduced cell wall softening by glucanases or chitinases and increased action of glucan branching, elongation, or crosslinking enzymes. This may reflect reduced growth during iron starvation, as cell wall softening may be important during morphogenetic events including conidial germination and subsequent hyphal growth (Mouyna *et al.*, 2013).

Notably, a similar pattern in the abundance of proteins is observed in the fungal response to azoles (Amarsaikhan *et al.*, 2017; Gautam *et al.*, 2016; Sorgo *et al.*, 2011). Azoles are a class of anti-fungal compounds that inhibit the biosynthesis of ergosterol – an integral component of the fungal cell membrane (Valiante *et al.*, 2015). During iron starvation, the production of iron-chelating compounds, siderophores, for iron uptake in *A. fumigatus* depletes ergosterol levels. This is because the siderophore biosynthetic pathway utilises an ergosterol intermediate (mevalonate) resulting in lower levels of ergosterol in the cell membrane (Section 1.3.2) (Yasmin *et al.*, 2012). Gautam *et al.* (2016) analysed the proteome of *A. fumigatus* in response to itraconazole and 13 of the proteins they identified were also differentially abundant in response to iron starvation. Specifically, nine proteins mutually decreased in abundance in response to itraconazole exposure and iron starvation, and three proteins mutually increased in abundance. Only one protein (Fpr1A; AFUA_6G12170) showed an opposing change, with an increase in response to iron starvation, but a decrease upon itraconazole exposure. A recent study Amarsaikhan *et al.* (2017) analysed the proteomic response of *A. fumigatus* to voriconazole. Thirty-two of the proteins they identified were also differentially abundant in response to iron starvation; 13 of these mutually decreased and six mutually increased. Among the proteins with mutually increased abundance were the 1,3-β-glucanosyltransferase, Bgt1, and conidial hydrophobin, RodB (AFUA_1G17250) (Amarsaikhan *et al.*, 2017). Sorgo *et al.* (2011) characterised the secretome of *C. albicans* in response to fluconazole exposure. This work identified a similar pattern in the abundance of cell wall related proteins in response to the membrane-perturbing antifungal. Orthologs of Ecm33 and Bgt1 (Bgl2) in *C. albicans* with increased abundance also showed increased abundance under iron starvation

(Table 3.5). Similarly, orthologs of Engl1 (Eng1) and ChiA1 (Cht2) showed decreased abundance, also observed in *A. fumigatus* in response to iron starvation (Table 3.6) (Sorgo *et al.*, 2011). Azole exposure alters the cell wall glucan and chitin composition in *Candida* species, presumably by an indirect cell wall remodelling response to membrane perturbation (Pfaller and Riley, 1992). Sorgo *et al.* (2011) proposed a compensatory response was responsible for the proteomic cell wall remodelling observed in *C. albicans* in response to fluconazole. It is noteworthy that subsequent work by Sorgo and colleagues also demonstrated cell wall remodelling in *C. albicans* in response to iron starvation (Sorgo *et al.*, 2013). However, they noted that the cell wall profile observed herein was actually not analogous to that during impaired membrane integrity. This contrasting response to iron starvation between the two species actually lends further supports the role of ergosterol in the cell wall remodelling in *A. fumigatus*, as *C. albicans* does not produce siderophores and therefore does not suffer ergosterol depletion to the same extent under iron starvation.

The stress responses to iron starvation and azole exposure in *A. fumigatus*, therefore, share some features. In particular, the cell wall integrity pathway is activated during iron starvation and its disruption increases susceptibility to azoles (Dichtl *et al.*, 2012; Jain *et al.*, 2011). The pathway is comprised of a mitogen-activated protein kinase (MAPK) signalling cascade initiated at the cell surface by transmembrane sensors (Wsc1, Wsc2, and MidA) in response to various stresses. Sensor activation results in the activation of Rho1, which activates a protein kinase C (PkcA), this in turn triggers the phosphorylation of a series of three MAPKs (Bck1, Mkk2, and finally MpkA) (Figure 3.14). After phosphorylation, MpkA translocates to the nucleus where it regulates the expression of genes involved in an array of processes including cell wall morphogenesis, carbohydrate metabolism, amino acid

metabolism and secondary metabolism, including siderophores (Dichtl *et al.*, 2016; Jain *et al.*, 2011; Valiante *et al.*, 2015). Importantly, Jain *et al.* (2011) demonstrated MpkA can repress siderophore biosynthesis during iron starvation in a bid to regulate energy utilisation.

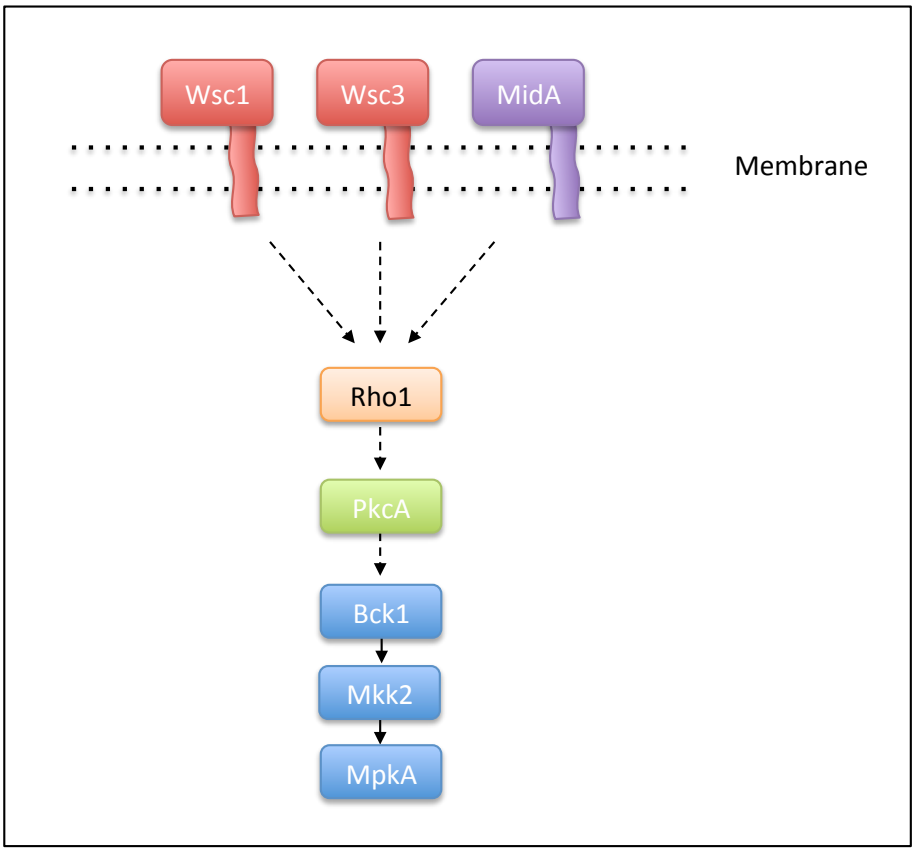

Figure 3.14 The cell wall integrity pathway in *A. fumigatus*. The pathway is initiated at the cell surface by transmembrane sensors (Wsc1, Wsc2, and MidA). These lead to the activation of Bck1-Mkk2-MpkA kinase modules through a signalling cascade. After phosphorylation, MpkA moves to the nucleus, where it regulates the expression genes involved in range of processes (Dichtl *et al.*, 2016; Valiante *et al.*, 2015).

Interestingly, a sensor of the cell wall integrity pathway, Wsc1 (AFUA_4G13670), was detected uniquely in the iron-deplete secretome (Appendices,

Supplementary Table 4). Other members of this pathway also showed increased abundance in response to iron starvation in the microsomal and mycelial proteome, including PkcA, Rho1, and the sensor, MidA (Moloney *et al.*, 2016a; Mulvihill *et al.*, 2017). A mutual activation of this pathway during iron starvation and azole exposure suggests the induction of cell wall remodelling in response to the impaired cell membrane integrity caused by ergosterol depletion. Thus, a compensatory cell wall remodelling response in *A. fumigatus* would account for the orchestrated reshuffling of cell wall modelling enzymes observed herein.

Together, this exploration of the secretomic response of *A. fumigatus* to iron starvation has yielded novel insight into proteomic adaptations at the host-pathogen interface. The increased abundance of proteins implicated in host recognition and increased immunoreactivity of iron-deplete secreted proteins validates the importance of this phenotype to host recognition. Furthermore, the induction of a cell remodelling response is evident in the proteomic and enzymatic alterations in response to iron starvation.

Chapter 4

Fluorescent derivatisation of *A. fumigatus* siderophores

Chapter 4 Fluorescent derivatisation of *A. fumigatus* siderophores

4.1 Introduction

A. fumigatus utilises two high affinity iron uptake systems: reductive iron assimilation and siderophore-mediated iron uptake (Haas *et al.*, 2008). Though both systems are up-regulated *in vivo* during infection, only siderophore-mediated iron acquisition is essential to virulence (Hissen *et al.*, 2005; Schrettl *et al.*, 2004). Siderophores are low molecular weight compounds capable of chelating ferric iron. They are secreted in the desferri form and following iron chelation, taken back up for direct use in metabolism or intracellular storage.

A. fumigatus produces four hydroxymate type siderophores; two intracellular ferrichrome siderophores (FC and HFC) and two extracellular fusarinine siderophores (FSC and TAFC) (Figure 1.3). FC functions in intracellular iron storage and distribution within hyphae, and HFC functions in iron storage within conidia (Schrettl *et al.*, 2007) . In contrast, FSC and TAFC are secreted in the desferri form through an unknown mechanism. After iron chelation, uptake of the siderophore-iron complex is mediated by specific transporters of the SIT protein subfamily (Haas *et al.*, 2003; Philpott and Protchenko, 2008). SITs are conserved across fungi, even in species incapable of producing siderophores and many microorganisms will also take up siderophores produced by other species (Lesuisse *et al.*, 2001; Pao *et al.*, 1998; Saier *et al.*, 1999). In *A. fumigatus*, MirB has been shown to be involved in the uptake of TAFC, FC, and coprogen (Haas *et al.*, 2003; Raymond-Bouchard *et al.*, 2012). Sit1 is involved in uptake of ferrichrome and ferrioxamine B, and Sit2 in the uptake of ferrichome (Park *et al.*, 2016). Subsequent to the uptake of FSC^{+Fe} and $TAFC^{+Fe}$, the siderophores are enzymatically hydrolysed in the cytosol by SidJ and EstB,

respectively (Gründlinger *et al.*, 2013a; Kragl *et al.*, 2007). The iron is then either used in metabolism or transferred to FC or vacuoles for storage. The fate of desferri-ligands following hydrolysis is still poorly defined, but there is evidence to suggest they are recycled and/ or excreted (Haas, 2014; Moore, 2013). Fluorescent derivatisation of siderophores or siderophore analogues has the potential to provide significant insight into the processing and iron release from siderophores following uptake. This has been demonstrated in several fungal species. For example, Larcher *et al.* (2013) demonstrated uptake of ferrioxamine derivatised with 7-nitrobenz-2-oxa-1,3-diazole (NBD) in *Rhizopus arrhizus* (Larcher *et al.*, 2013; Lytton *et al.*, 1991). Uptake of a ferrichrome analogue (B9) labelled with anthracene (B9-ANT) or lissamine rhodamine B (B9-LRB) was demonstrated in *Ustilago maydis* (Ardon *et al.*, 1997, 1998). Uptake of another ferrichrome analogue and ferrioxamine labelled with NBD was also demonstrated in *C. albicans* and *S. cerevisiae* (Froissard *et al.*, 2007; Ouchetto *et al.*, 2005).

As discussed in Section 1.3.3.1, siderophores can be implemented in a PET-based strategy for a non-invasive method of diagnosing fungal infection. Gallium-TAFC chelates (^{68}Ga-TAFC) were taken up by *A. fumigatus* in infected rats thereby providing a means of localising infection using PET imaging (Haas *et al.*, 2015; Petrik *et al.*, 2010a, 2012, 2017). Clinical interest in siderophores has also evolved and the application of siderophore-radiometal chelates extends further than imaging of infection (Petrik *et al.*, 2017). Synthesis of ^{68}Ga-FSC labelled with RGD (arginine-glutamic acid-aspartic acid) peptides yielded a siderophore-radiometal chelate (^{68}Ga-FSC-$(RGD)_3$) capable of binding $\alpha_V\beta_3$ (an integrin found on the surface of endothelial cells during angiogenesis and associated with tumour metastasis) *in vivo* (Knetsch *et al.*, 2015; Zhai *et al.*, 2015). FSC is a cyclic tripeptide comprised of three N^5-

anhydromevalonyl-N^5-hydroxyornithine groups linked by ester bonds (Figure 1.3). This structure makes it an ideal compound for such work, as in addition to a radiometal chelating ability; it possesses three primary amine groups free for modification. The authors utilised these amine groups for linkage of FSC to RGD peptides thereby conferring the $\alpha_V\beta_3$ binding capacity. This work effectively demonstrates the diverse capacity for modification and utilisation of FSC.

There is a range of amine-reactive compounds commercially available. Hence, FSC is an ideal source for studies requiring semi-synthetic derivatives to biochemically investigate or utilise siderophores with a fusarinine moiety. The majority of these amine-reactive compounds contain NHS esters which can react with nucleophiles to form an acylated product with the release of the NHS group (Figure 4.1) (Hermanson, 2008). NHS esters primarily react with amines forming a stable amide bond. They can also react with thiol and hydroxyl groups, however the resulting bonds are unstable. Amine reaction with NHS esters is temperature and pH sensitive and competes with hydrolysis of the NHS ester. The degree of hydrolysis is limited at pH close to neutral. Most NHS ester reactions are carried out at pH 7.0 – 9.0 in non-amine containing buffers such as phosphate, carbonate-bicarbonate, HEPES, or borate buffers for 30 – 60 min at room temperature (Hermanson, 2008).

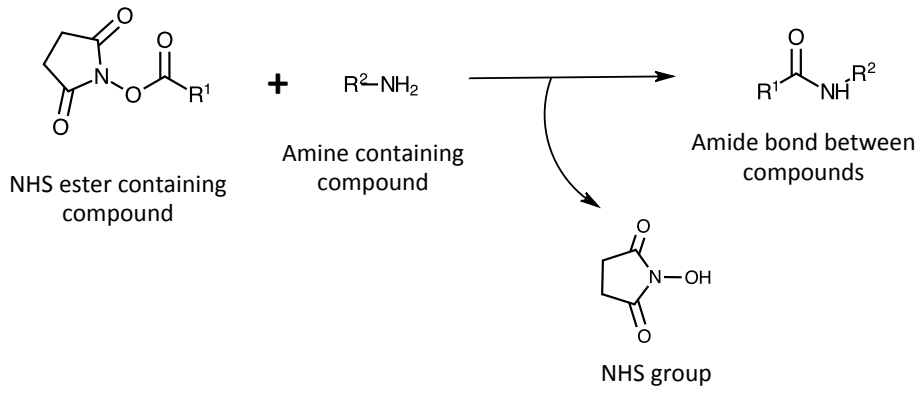

Figure 4.1 The reaction of an amine-containing compound with a NHS ester-containing reagent forming an amide bond with the release of a NHS group (Hermanson, 2008).

There is a current gap in the knowledge of the processes following ferri-siderophore uptake in *A. fumigatus*. Investigations herein can provide an insight into siderophore-mediated iron uptake mechanisms, which are critical to the virulence of *A. fumigatus*. With this in mind, the objectives of the work presented in this chapter were to:

i. Develop a strategy for the fluorescent derivatisation of FSC.

ii. Develop a semi-synthetic analogue of TAFC suitable for common cross-linker modification including fluorescent derivatisation.

iii. Functionally validate the uptake of fluorescently derivatised siderophores in *A. fumigatus.*

4.2 Results

4.2.1 Fluorescent derivatisation of FSC

4.2.1.1 Strategy for fluorescently labelling FSC

FSC is a cyclic tripeptide comprised of three N^5-anhydromevalonyl-N^5-hydroxyornithine groups linked by ester bonds (Haas, 2014). FSC has three free amines (-NH_2) that are acetylated by the acetyltransferase, SidG, to generate the more stable TAFC (Figure 1.3). As these functional groups do not participate in iron binding, amine conjugation represented the most feasible means of fluorescent derivatisation while retaining FSC functionality. NBD has been successfully used in fluorescently derivatising siderophores in other species (Ardon *et al.*, 1998; Froissard *et al.*, 2007; Larcher *et al.*, 2013; Noël *et al.*, 2011; Ouchetto *et al.*, 2005). Furthermore, NBD is commercially available in an amine-reactive succinimidyl-ester derivative (NBD-X-SE) (Life Technologies). Hence, linking FSC to NBD *via* a primary amine was chosen as the premise of this work for the fluorescent derivatisation of FSC.

In the desferri- form, FSC possesses three free hydroxyl (-OH) groups that function in iron chelation. Previous work in our group and by others has shown that the –OH groups of FSC can react with NHS esters (Hermanson, 2008). Thus, to avoid interference with iron binding, it was necessary to ferrate FSC prior to modification to protect the –OH groups. FSC^{+Fe} was extracted as outlined in Section 2.2.4 and RP-HPLC purified for NBD-X-SE derivatisation as illustrated in Figure 4.2. Generation of FSC-$(NBD)_1$ was confirmed *via* RP-HPLC and LC-MS/MS analysis before use in functional studies.

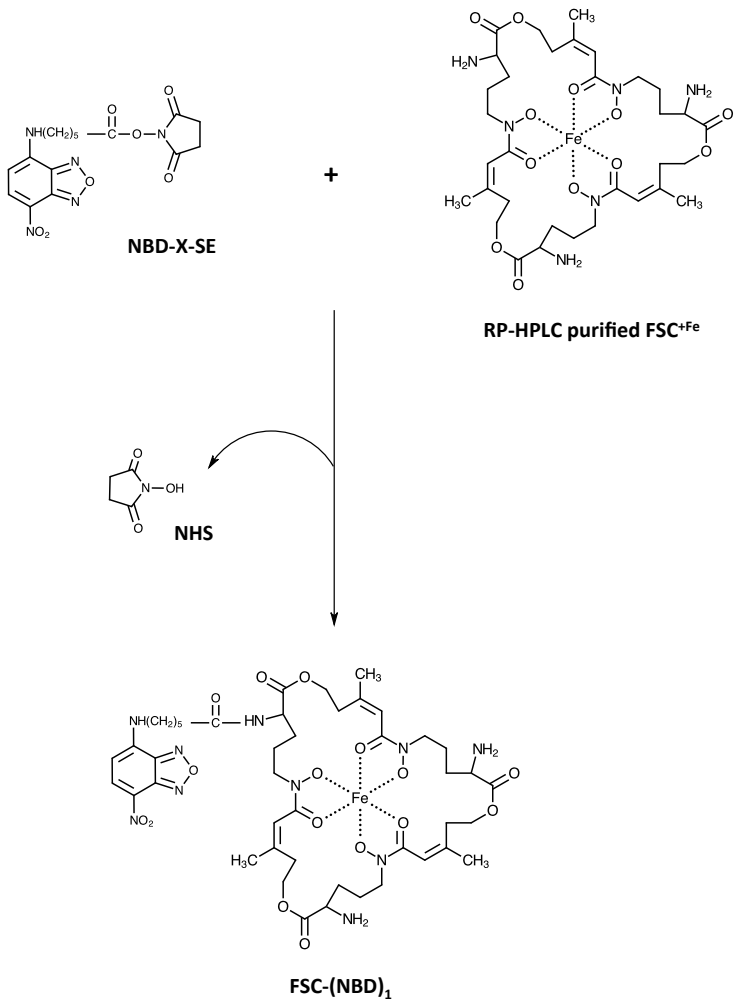

Figure 4.2 FSC^{+Fe} derivatisation with NBD-X-SE. RP-HPLC purified FSC^{+Fe} possesses three amines free for conjugation to NBD in the generation of FSC-$(NBD)_1$. NBD-X-SE reacts with one such amine, with the loss of an NHS, to link NBD to FSC.

4.2.1.2 Purification of FSC^{+Fe}

A. fumigatus Δ*sidG* was grown in MM without iron. Supernatant was ferrated and concentrated *via* Sep-Pak C18 cartridges as described in Sections 2.2.4.1 – 2.2.4.2. Dried extracts were suspended in 0.1 M $NaHCO_3$ pH 8.5. FSC is quite labile and linearised N^5-anhydromevalonyl-N^5-hydroxyornithine dimers and trimers (Fusarinine A and Fusarinine B) are often also recovered from culture supernatant (Renshaw *et al.*, 2002). To remove any linearised fusarinines, Sep-Pak C18 column purified FSC was organically extracted with 1:1 volume of chloroform (Section 2.2.4.3). After evaporating to dryness in a rotary evaporator, organic extracts were subjected to RP-HPLC purification to isolate pure FSC^{+Fe} (Sections 2.2.4.6). All steps of the purification process were monitored by RP-HPLC analysis with DAD detection at 440 nm (Figure 4.3) as described in Section 2.2.3.3. The peak associated with FSC^{+Fe} was fraction collected and analysed by LC-MS/MS to confirm its identity (Section 2.2.13.5). Identity of FSC^{+Fe} was confirmed by detection of a doubly charged ion (M: 779.3, $[M+2H]^{2+}$: observed *m/z* 390.7; expected *m/z* 390.7) (Figure 4.4).

A.

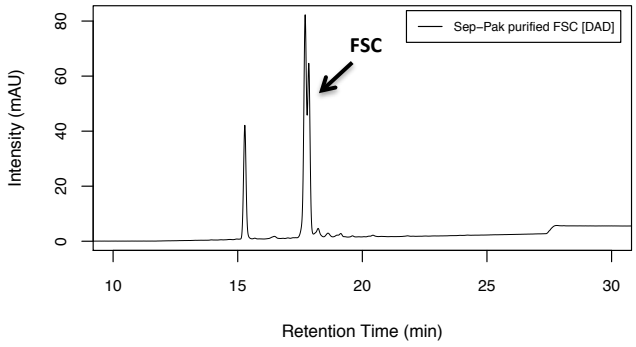

B.

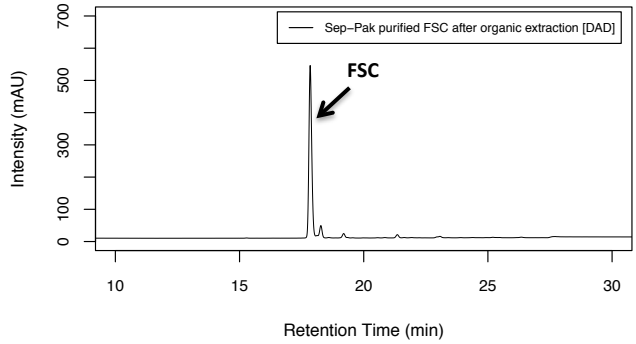

C.

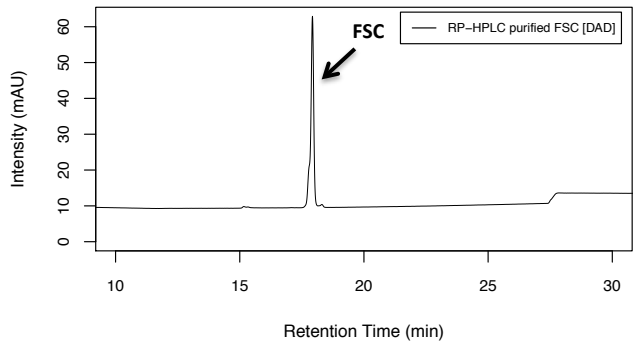

Figure 4.3 RP-HPLC analysis with DAD detection (440 nm) of FSC^{+Fe} after (A) concentration of culture supernatants through Sep-Pak C18 cartridges, (B) organic extraction with chloroform, and (C) RP-HPLC purification.

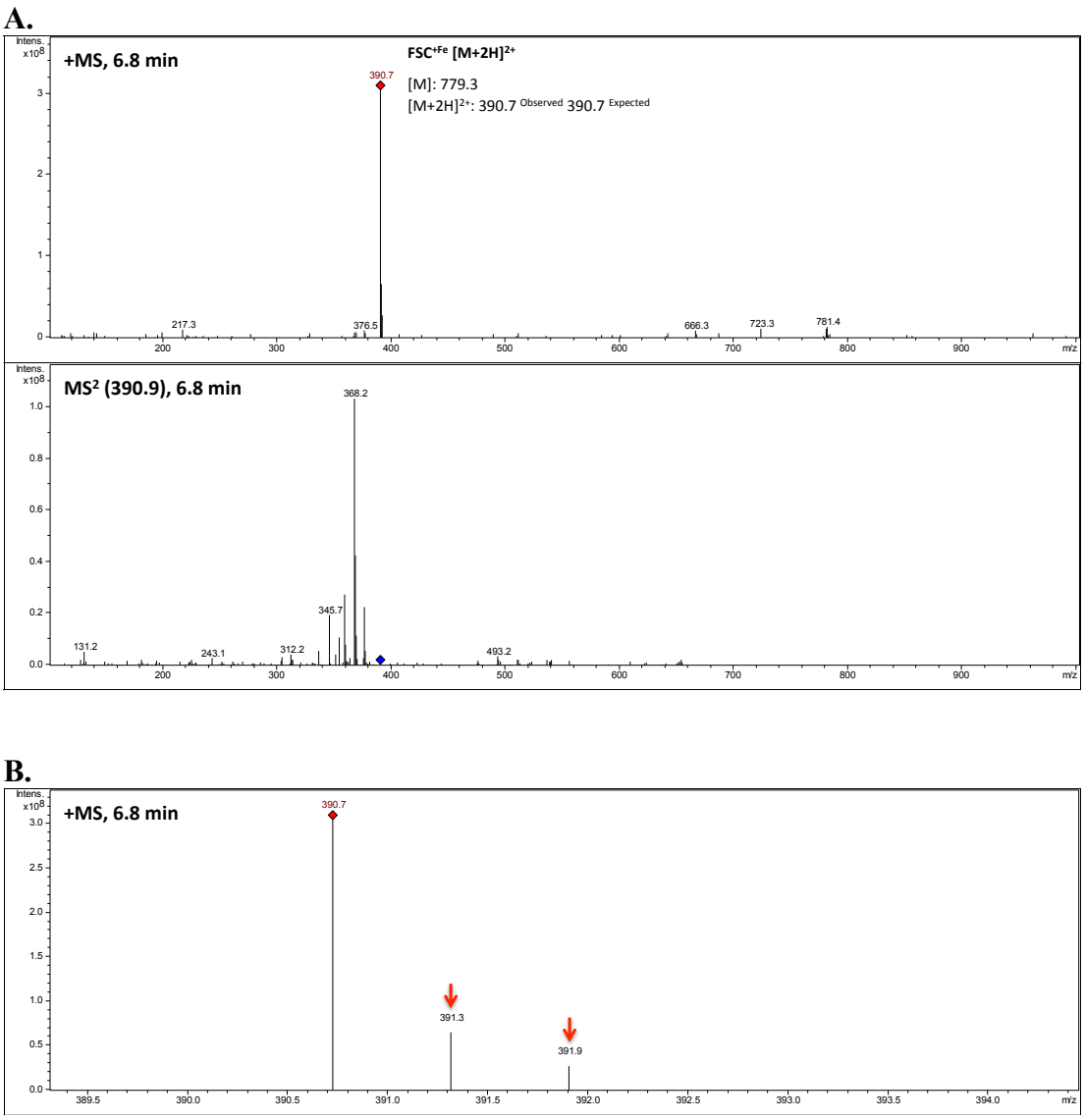

Figure 4.4 LC-MS/MS identification of FSC^{+Fe}. Peak associated with FSC^{+Fe} was fraction collected during RP-HPLC analysis and analysed by LC-MS/MS. (A) MS (total ion chromatogram) spectrum shows the detection of FSC^{+Fe} as a doubly charge ion (M: 779.3, $[M+2H]^{2+}$: observed *m/z* 390.7; expected *m/z* 390.7). MS2 spectrum shows the fragmentation of precursor ion. (B) Increments of approx. +0.5 in observed *m/z* are indicative of C_{13} isotope incorporation in a doubly charged ion.

4.2.1.3 Derivatisation of FSC^{+Fe} with NBD-X-SE

Micro-precipitation is often observed in organic solvent solubilised NHS esters upon their addition to an aqueous reaction buffer (Hermanson, 2008). The addition of DMSO solubilised NBD-X-SE to FSC^{+Fe} in either sodium phosphate or sodium carbonate buffer to a final DMSO content of 10% resulted in significant precipitation. Fluorophore modification of oligonucleotides using a DMSO solubilised NHS ester (CyDye® NHS ester; GeneCopoeia) can be effectively carried out in a sodium bicarbonate buffer with acetonitrile (33%). Similarly, NBD-Cl modification of desferrioxamine was carried out in a sodium bicarbonate buffer with methanol (33%) (Lytton *et al.*, 1991). FSC is quite soluble in organic solvents including acetonitrile. Thus, a similar approach was trialled with FSC-NBD labelling. RP-HPLC purified FSC^{+Fe} was suspended in 0.1 M $NaHCO_3$ with 50% (v/v) acetonitrile. In this case, addition of DMSO solubilised NBD-X-SE to a final DMSO content of 7% (v/v) did not result in any precipitation.

To negate the effects of photobleaching and potential FSC instability, the FSC-NBD reaction was used after preparation without further purification. This prompted several considerations. Firstly, the reaction of FSC^{+Fe} and NBD-X-SE would generate several products: mono-, di-, and tri-labelled FSC^{+Fe} (FSC-$(NBD)_1$, FSC-$(NBD)_2$ and FSC-$(NBD)_3$). The consequences of di- and tri-labelling of FSC with NBD-X-SE (FSC-$(NBD)_2$ and FSC-$(NBD)_3$) on siderophore uptake were unclear; however FSC-$(NBD)_1$ would most closely resemble the native siderophore thereby increasing the likelihood of cognate transporter recognition. Secondly, the presence of free unreacted FSC^{+Fe} could compete with FSC-$(NBD)_1$ for uptake by *A. fumigatus*. Thus, it was necessary to maximise the generation of FSC-$(NBD)_1$ as opposed to FSC-$(NBD)_2$ and FSC-$(NBD)_3$, while minimising levels free FSC^{+Fe}.

Modification of FSC^{+Fe} with an equimolar concentration of NBD-X-SE yielded maximum levels of FSC-$(NBD)_1$ compared with other reaction components and products (Figure 4.5 E and F). The reaction conditions are outlined in Section 2.2.5.1.1. Controls using the same reaction conditions excluding NBD-X-SE (Figure 4.5 A and B), or FSC^{+Fe} (Figure 4.5 C and D), or both were also set up. All reactions were monitored by RP-HPLC analysis with DAD detection at 440 nm and FLD detection at Ex/ Em 466/ 535 nm (Figure 4.5) as described in Section 2.2.3.3. The peak associated with FSC-$(NBD)_1$ was fraction collected and analysed by LC-MS/MS to confirm its identity (Section 2.2.13.7). Generation of FSC-$(NBD)_1$ was confirmed by detection a doubly charged ion (M: 1055.4, $[M+2H]^{2+}$: observed *m/z* 528.7; expected *m/z* 528.7) (Figure 4.6).

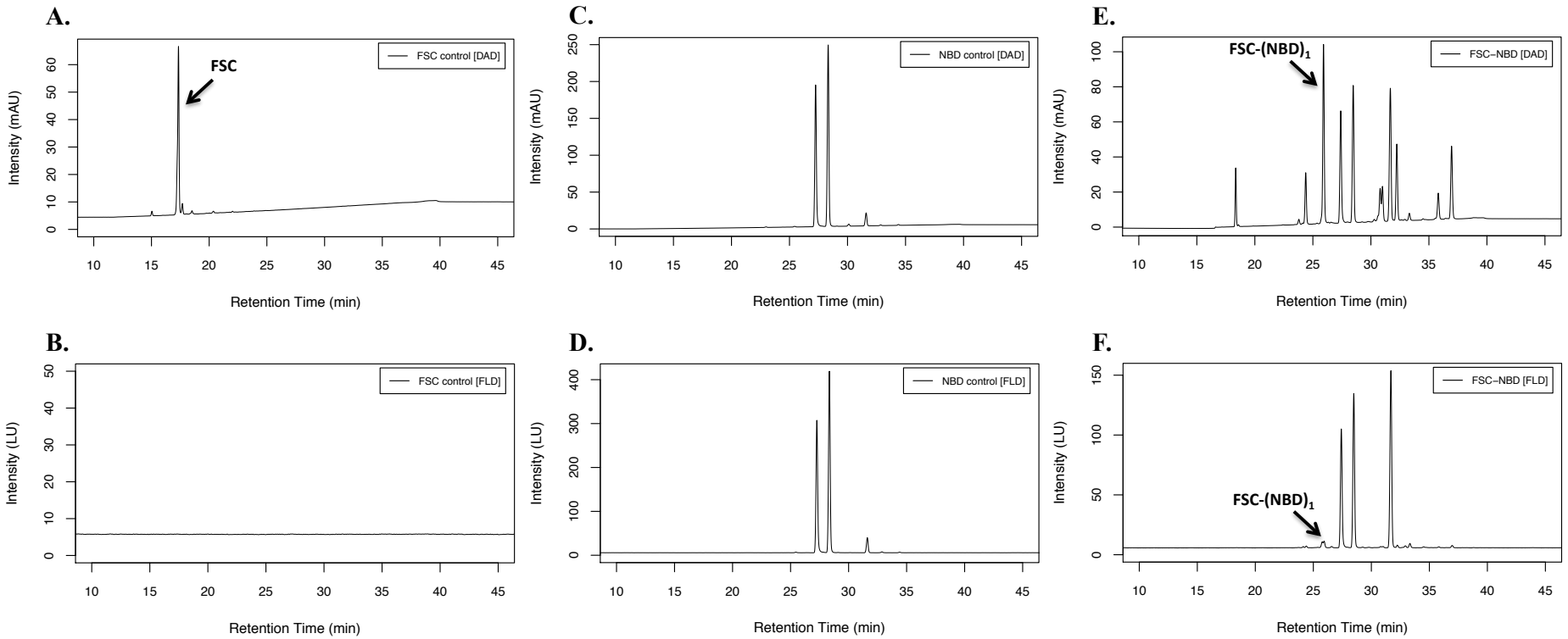

Figure 4.5 RP-HPLC analysis of FSC^{+Fe} derivatisation with NBD-X-SE using DAD (440 nm) and FLD (Ex/ Em 466/ 535 nm) detection. (A & B) FSC^{+Fe} only control shows a single peak (FSC^{+Fe}) with DAD but no FLD detection. (C & D) NBD-X-SE only control shows unreacted fluorophore with DAD and FLD detection. (E & F) FSC-NBD reaction shows the generation of several new peaks with DAD detection and a single new peak with FLD detection ($FSC\text{-}(NBD)_1$).

A.

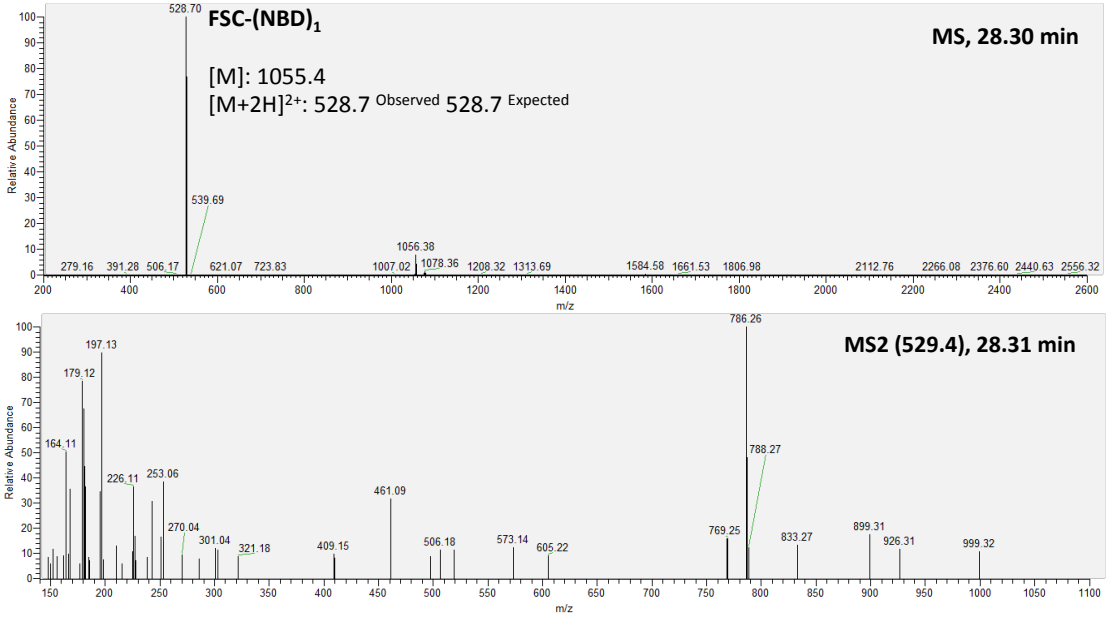

B.

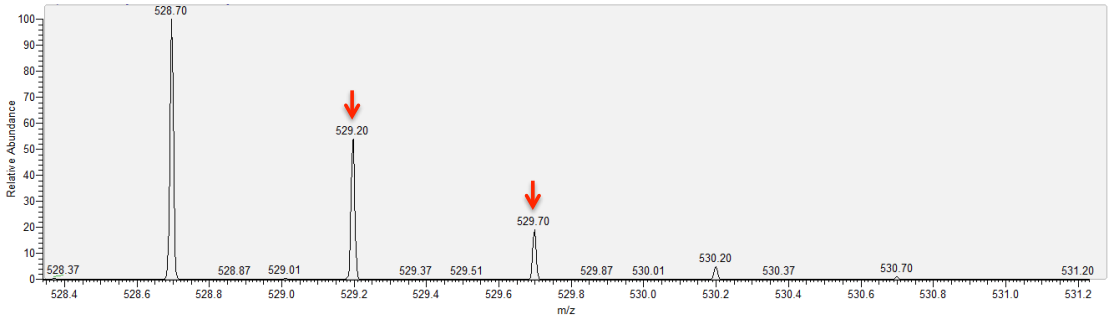

Figure 4.6 LC-MS/MS identification of FSC-$(NBD)_1$. Peak associated with FSC-$(NBD)_1$ was fraction collected during RP-HPLC analysis and analysed by LC-MS/MS. (A) MS (extracted ion chromatogram for *m/z* 528 – 530) spectrum shows the detection of FSC-$(NBD)_1$ as a doubly charged ion (M: 1055.4, $[M+2H]^{2+}$: observed *m/z* 528.7; expected *m/z* 528.7). MS2 spectrum shows the fragmentation of precursor ion (B) Increments of approx. +0.5 in observed *m/z* are indicative of C_{13} isotope incorporation in a doubly charged ion.

4.2.1.4 The presence of iron quenches the fluorescence of FSC-NBD

RP-HPLC analysis indicated that the cumulative FLD signal of the FSC-NBD reaction (4105 LU) showed a reduction in intensity compared with the NBD-X-SE control (7550 LU). In particular, the peak associated with FSC-$(NBD)_1$ showed little FLD signal despite strong DAD detection (Figure 4.5). Other NBD derivatised siderophores have been shown to exhibit a quenching of fluorescence upon iron chelation (Ardon *et al.*, 1998; Froissard *et al.*, 2007; Lytton *et al.*, 1991). As FSC-$(NBD)_1$ was ferrated prior to derivatisation it was necessary to remove iron to observe any impact of iron chelation on fluorescence.

FSC-NBD was incubated with either EDTA or sodium phosphate buffer as per Section 2.2.5.1.2 (adapted from Knetsch *et al.,* 2015). After incubation, fluorescence signal was measured (Ex/ Em 466/ 535 nm) and expressed relative to the control (Figure 4.7). Removal of iron *via* EDTA chelation led to a 52% increase in fluorescence signal indicating that iron chelation quenches fluorescence in FSC-NBD.

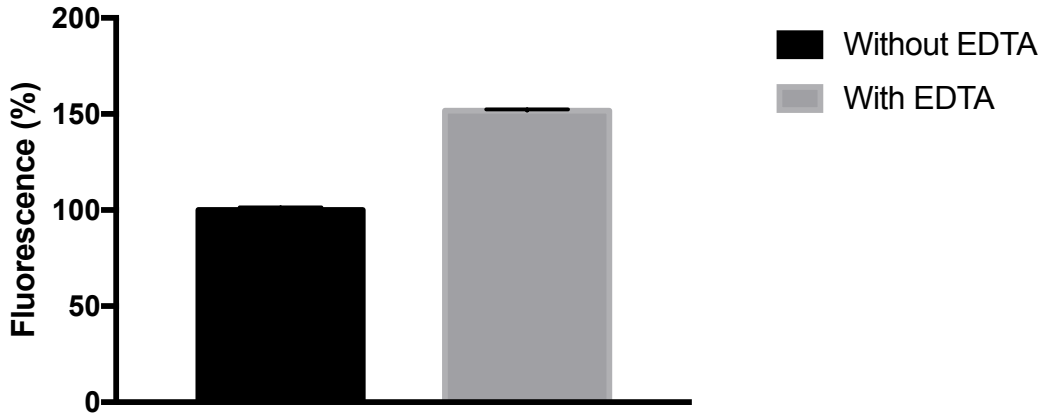

Figure 4.7 Fluorescence of FSC-NBD increases upon incubation with EDTA.

4.2.2 FSC-NBD is taken up by *A. fumigatus* under iron starved but not sufficient growth

To observe the uptake of FSC-NBD by *A. fumigatus*, uptake studies were set up in 12 well plates as described in Section 2.2.6. MM, with and without iron, was supplemented with fluorescent siderophores at 50 μM based on the total siderophore content of the FSC-NBD reaction or an equivalent volume of controls (FSC only/ NBD only/ buffer only). Fluorescence was observed in the vacuoles of hyphae incubated with FSC-NBD during growth without iron only (Figure 4.8).

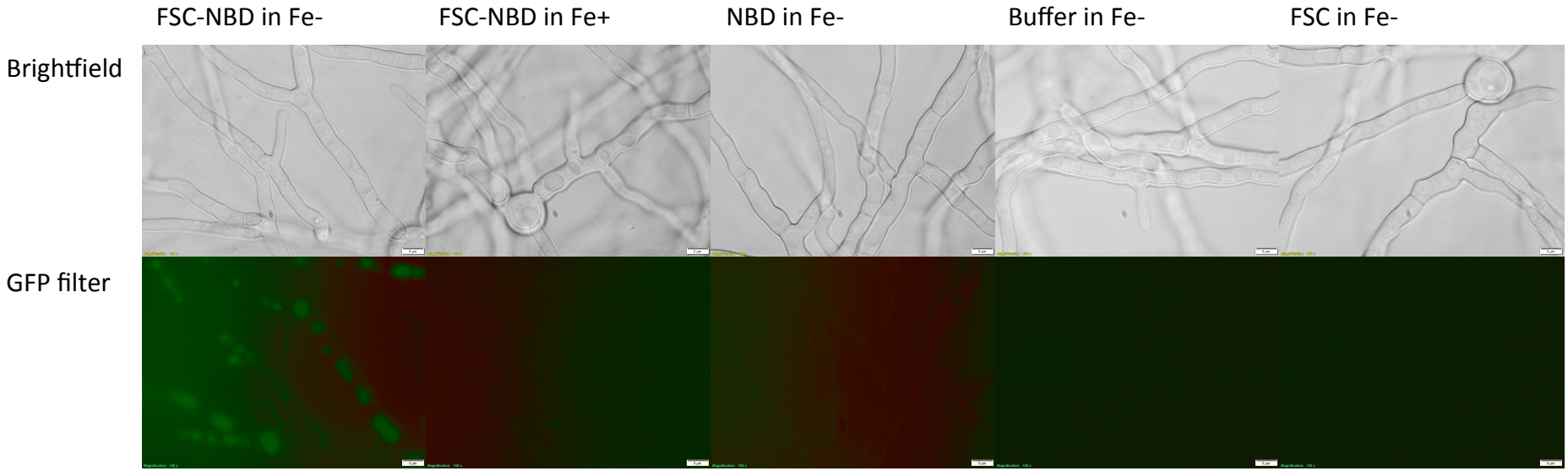

Figure 4.8 Uptake of FSC-NBD by *A. fumigatus*. *A. fumigatus* was grown in MM with (Fe+) and without iron (Fe-) followed by incubation with FSC-NBD or controls (NBD, Buffer, or FSC) at a equivalent concentration for 1 h. After washing, mycelia were viewed by fluorescent microscopy. Fluorescence was observed to localise to vacuoles after incubation with FSC-NBD only when grown without iron. Bar = 5 μm.

4.2.3 Development of a TAFC analogue suitable for cross-linker modification

4.2.3.1 Strategy for generating diacetylfusarinine C (DAFC)

TAFC possesses limited functional groups for standard crosslinker modification. Though crosslinkers are available for the modification of –OH groups, such modification would be unsuitable, as it would interfere with the iron-binding region of TAFC (Figure 1.3). FSC, however, possesses three easily modified amines, and thus could be used to create a semi-synthetic TAFC analogue. By acetylating two amine groups, generating diacetylfusarinine C (DAFC); a third amine group is still available for further NHS ester modification (Figure 4.9).

Sulfo-NHS-Acetate (SNA) is an amine-reactive acetylation agent commonly used for blocking primary amines during crosslinking reactions (Hermanson, 2008). As with other NHS ester containing compounds, SNA reacts with amines at pH 7 – 9 and releases NHS in the process (Figure 4.1). Reacting FSC^{+Fe} with SNA can result in the formation of several products; mono-, di-, and tri-acetylated fusarinine C (MAFC, DAFC, and TAFC) (Figure 4.9). Purification of DAFC from this reaction yielded a semi-synthetic TAFC analogue with only one free amine for derivatisation with NBD-X-SE (Figure 4.10). Generation of DAFC and DAFC-NBD were confirmed *via* RP-HPLC and LC-MS/MS analysis before use in functional studies.

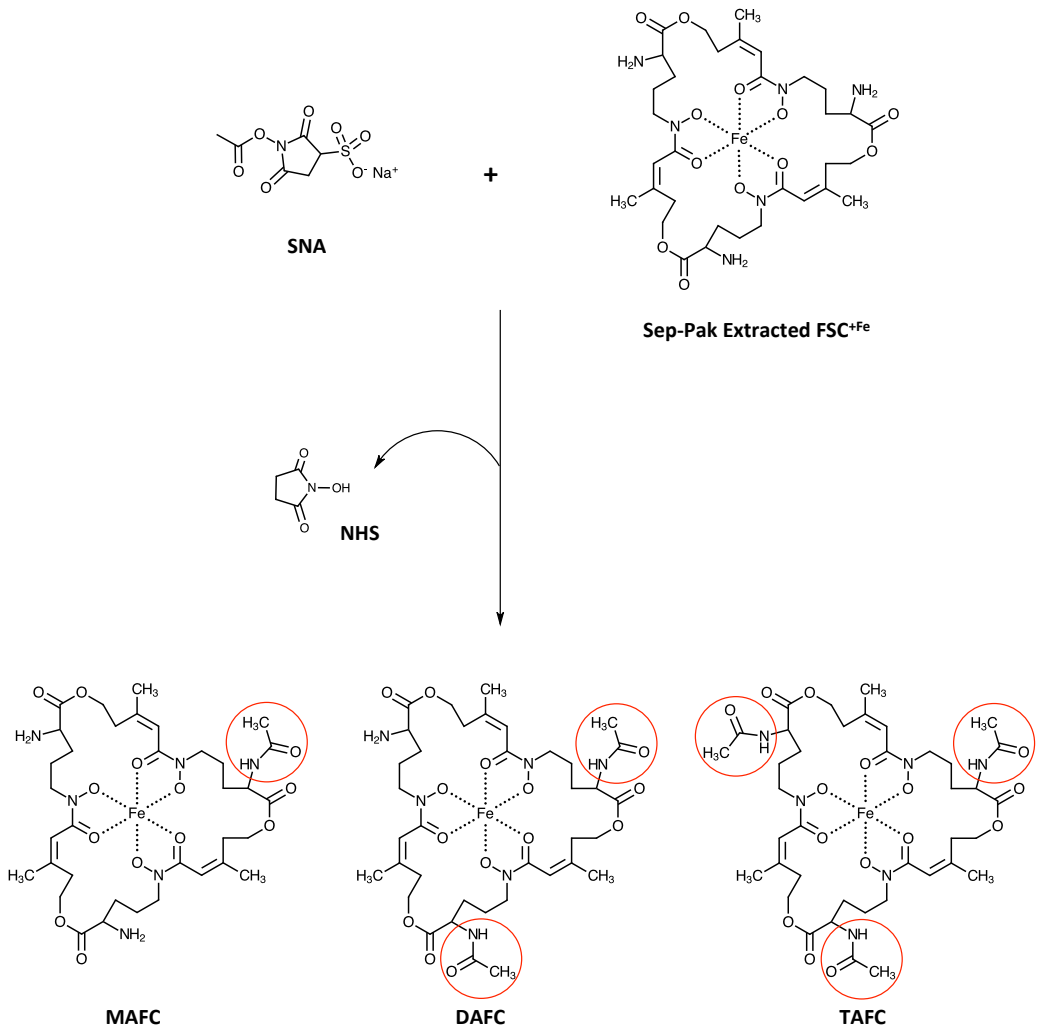

Figure 4.9 FSC^{+Fe} derivatisation with SNA. Sep-Pak extracted FSC^{+Fe} possesses three amines free for derivatisation with SNA in the generation of MAFC, DAFC, and TAFC. SNA acetylates amines with the loss of an NHS group.

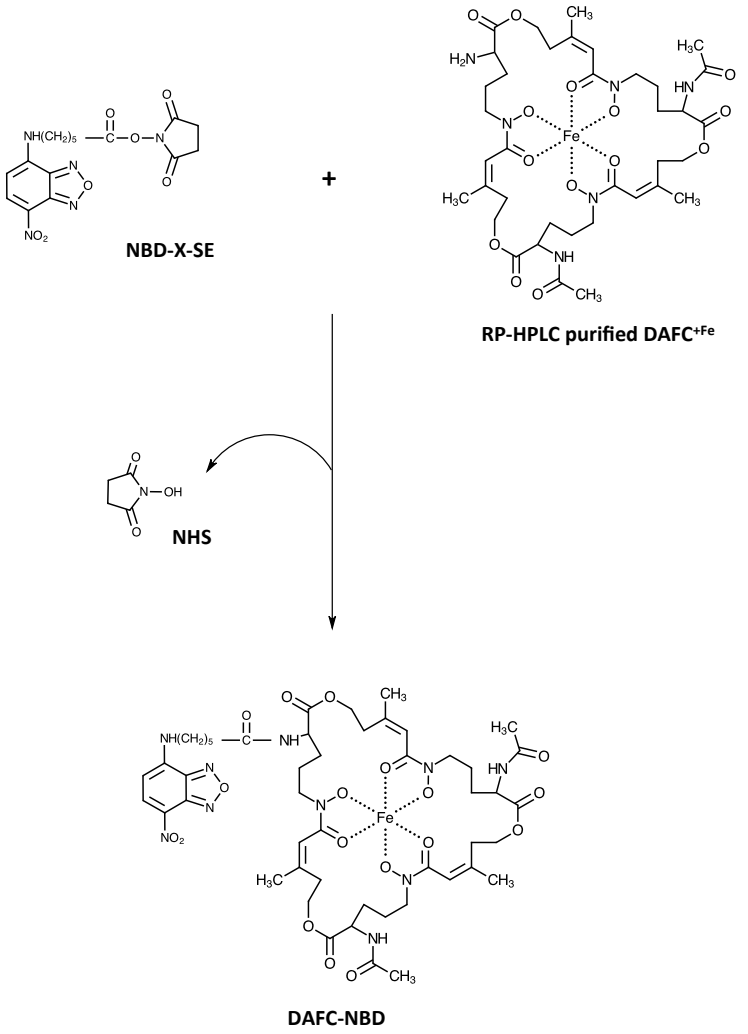

Figure 4.10 DAFC^{+Fe} derivatisation with NBD-X-SE. RP-HPLC purified DAFC^{+Fe} possesses a single amine free for derivatisation with NBD-X-SE in the generation of DAFC-$(NBD)_1$. NBD-X-SE reacts with this amine, with the loss of an NHS, to link NBD to DAFC.

4.2.3.2 Acetylation of FSC with SNA

FSC^{+Fe} was extracted from culture supernatant as described in Section 2.2.4.1 – 2.2.4.2. Dried extracts were suspended in 0.1 M $NaHCO_3$ and modified with a 2-fold molar excess of SNA (Section 2.2.5.1.3). The reactions were monitored by RP-HPLC analysis (Figure 4.11). Peaks associated with MAFC and DAFC were fraction

collected and identified by LC-MS/MS analysis (Figure 4.12 – 4.13). TAFC was identified based on the retention time of an in-house RP-HPLC standard. LC-MS/MS analysis of SNA- and SidG-generated (produced by *A. fumigatus*) TAFC indicated a shared retention time, *m/z*, and fragmentation pattern (Figure 4.14). DAFC was RP-HPLC purified from the reaction (Figure 4.15) for NBD-X-SE derivatisation (Section 4.2.3.3).

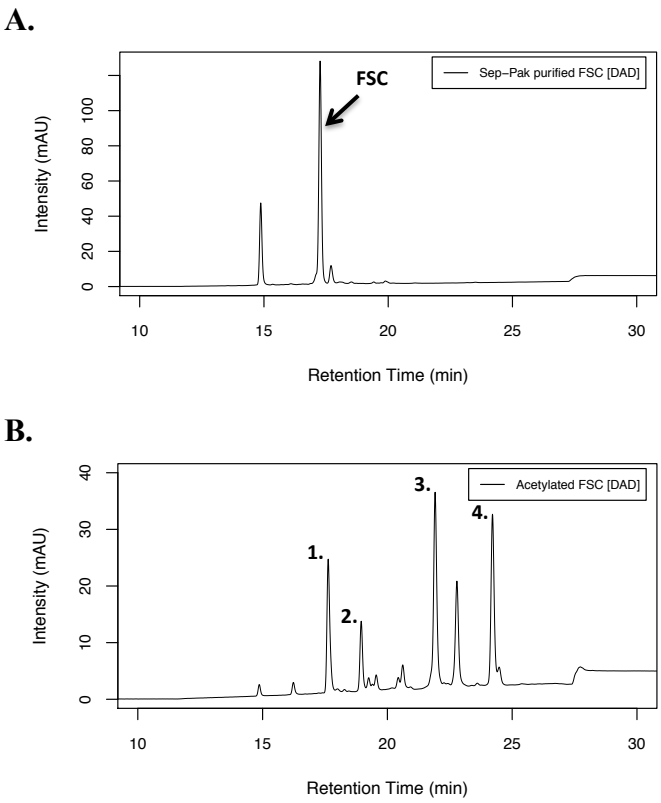

Figure 4.11 RP-HPLC analysis with DAD detection (440 nm) of FSC^{+Fe} (A) before and (B) after SNA acetylation (**1.** FSC^{+Fe}, **2.** $MAFC^{+Fe}$, **3.** $DAFC^{+Fe}$, and **4.** $TAFC^{+Fe}$).

A.

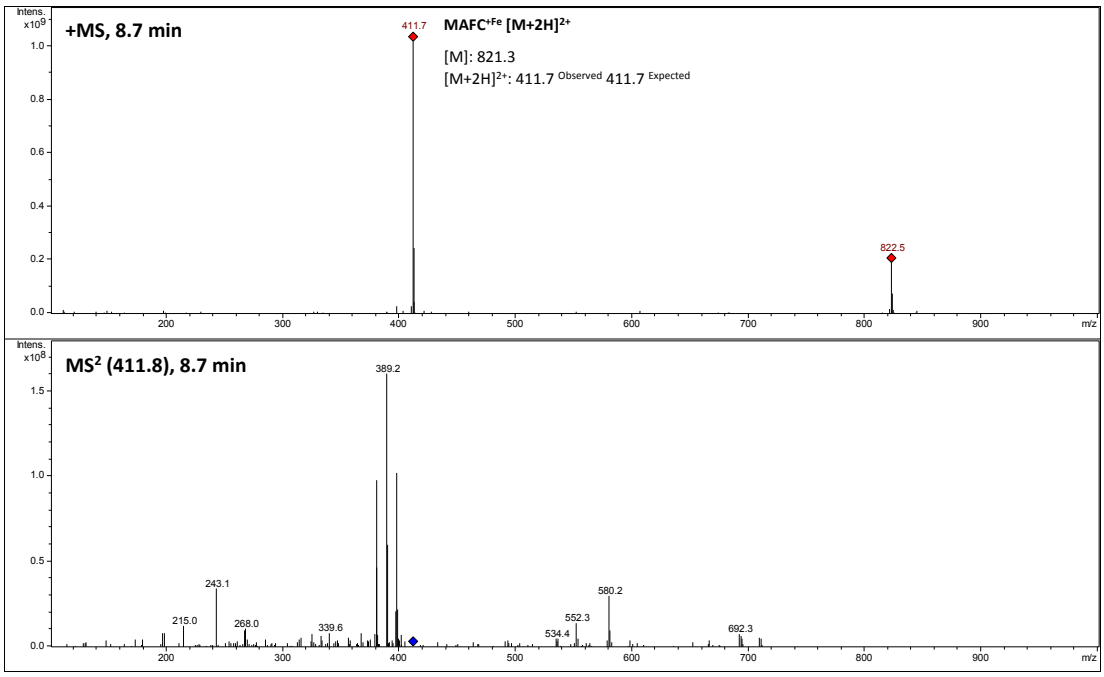

B.

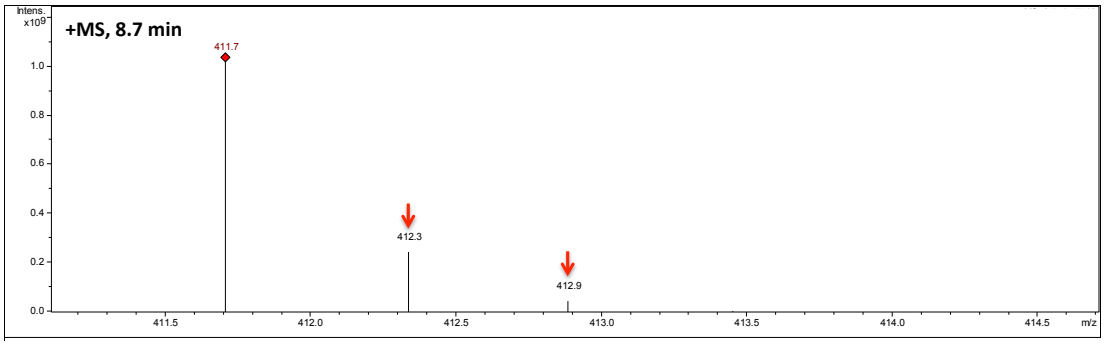

Figure 4.12 LC-MS/MS identification of MAFC^{+Fe}. Peak associated with MAFC^{+Fe} (**2.** in Figure 4.11) was fraction collected during RP-HPLC analysis and analysed by LC-MS/MS. (A) MS spectrum (total ion chromatogram) shows the detection of MAFC^{+Fe} as a doubly charge ion (M: 821.3, $[M+2H]^{2+}$: observed *m/z* 411.7; expected *m/z* 411.7). MS2 spectrum shows the fragmentation of precursor ion. (B) Increments of approx. +0.5 in observed *m/z* are indicative of C_{13} isotope incorporation in a doubly charged ion.

A.

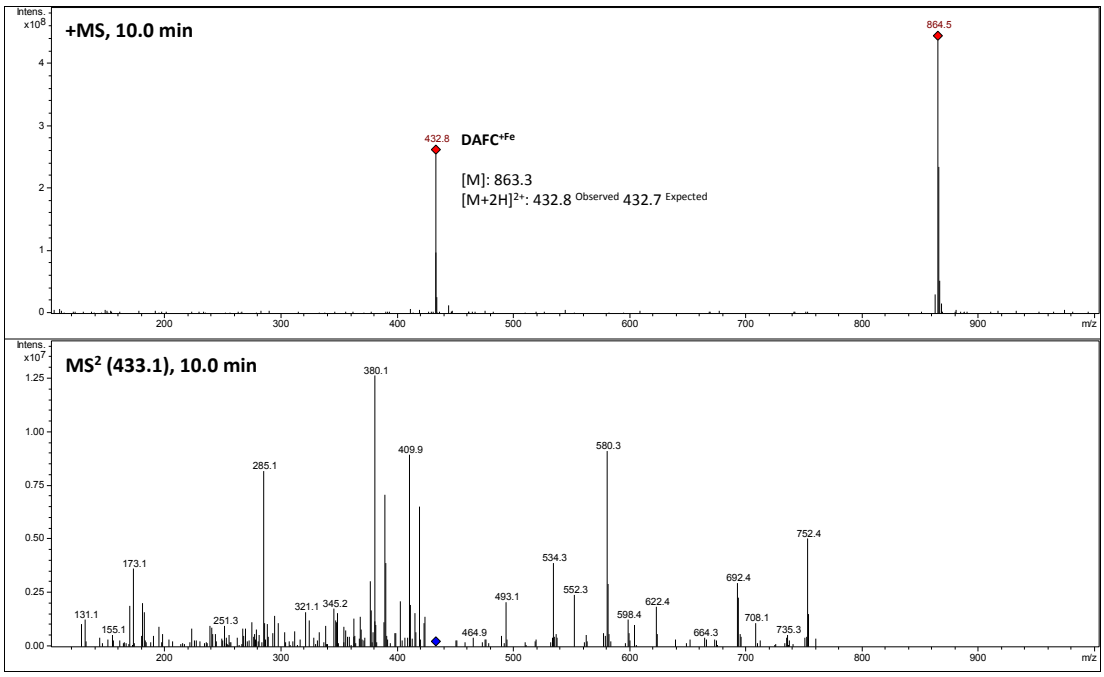

B.

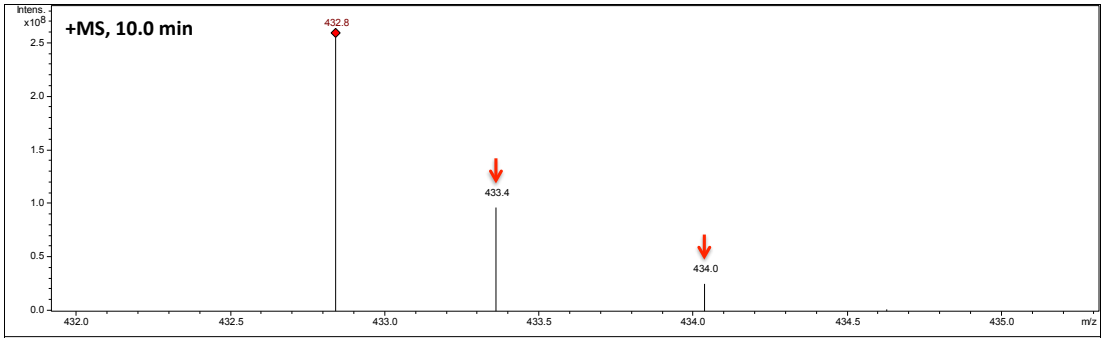

Figure 4.13 LC-MS/MS identification of DAFC^{+Fe}. Peak associated with DAFC^{+Fe} (**3.** in Figure 4.11) was fraction collected during RP-HPLC analysis and analysed by LC-MS/MS. (A) MS spectrum (total ion chromatogram) shows the detection of DAFC^{+Fe} as a doubly charge ion (M: 863.3, $[M+2H]^{2+}$: observed *m/z* 432.8; expected *m/z* 432.7). MS2 spectrum shows the fragmentation of precursor ion. (B) Increments of approx. +0.5 in observed *m/z* are indicative of C_{13} isotope incorporation in a doubly charged ion.

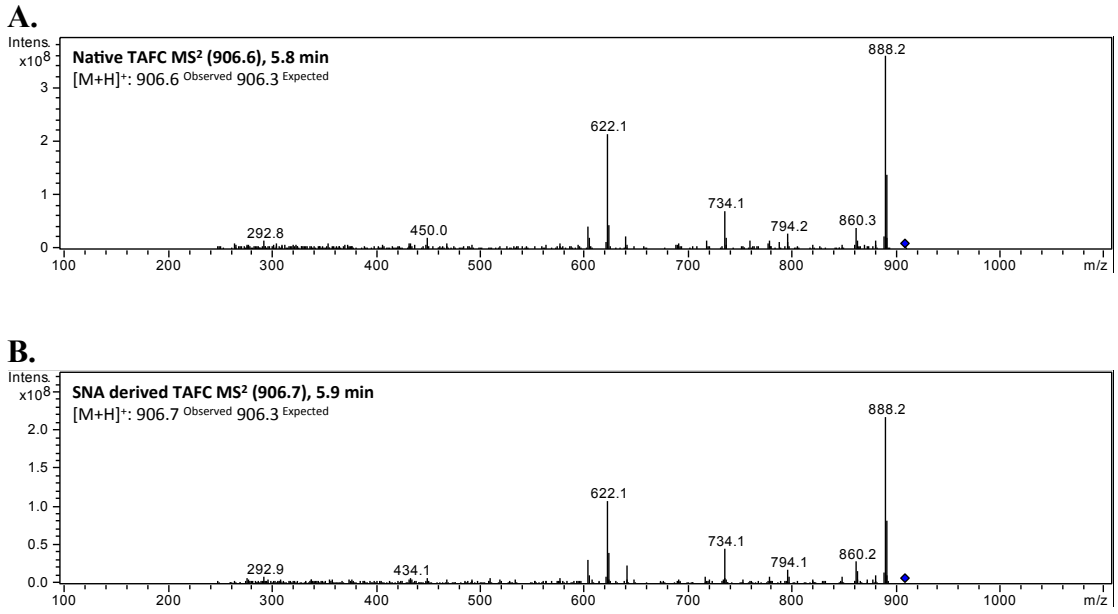

Figure 4.14 LC-MS/MS analysis of (A) native TAFC extracted from *A. fumigatus* supernatant and (B) TAFC derived from SNA acetylation of FSC. TAFC derived from SidG and SNA acetylation share fragmentation patterns when analysed by LC-MS/MS.

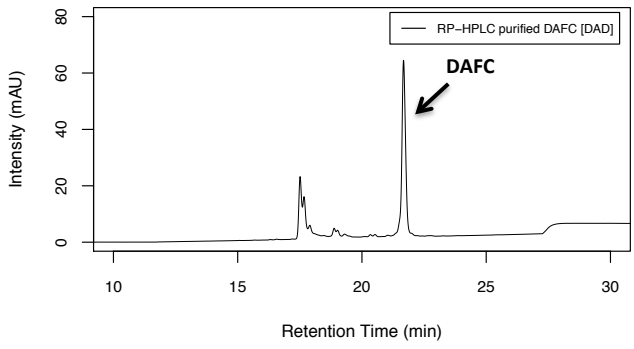

Figure 4.15 RP-HPLC analysis with DAD detection (440 nm) of $DAFC^{+Fe}$ after RP-HPLC purification.

4.2.4 Fluorescent derivatisation of DAFC

Similar to the fluorescent derivatisation of FSC (Section 4.2.1.3), RP-HPLC purified $DAFC^{+Fe}$ was suspended in 0.1 M $NaHCO_3$ with 50% (v/v) acetonitrile. Modification of DAFC was carried out with an equimolar concentration of NBD-X-SE as outlined in Section 2.2.5.1.4. Controls using the same reaction conditions excluding either $DAFC^{+Fe}$ or NBD-X-SE or both were also set up. All reactions were monitored by RP-HPLC analysis with DAD detection at 440 nm and FLD detection at Ex/Em 466/535 nm (Figure 4.16) as described in Section 2.2.3.3. Similar to that observed in FSC-NBD (Section 4.2.1.4), RP-HPLC analysis indicated that the cumulative FLD signal of the DAFC-NBD reaction (2261 LU) showed a reduction in intensity compared with the NBD-X-SE control (6018 LU). The DAFC-NBD reaction was analysed by LC-MS/MS (Section 2.2.13.3.1 and 2.2.13.7). Generation of DAFC-NBD was confirmed by detection a singly charged ion (M: 1139.4, $[M+H]^+$: observed *m/z* 1140.4; expected *m/z* 1140.4) (Figure 4.17).

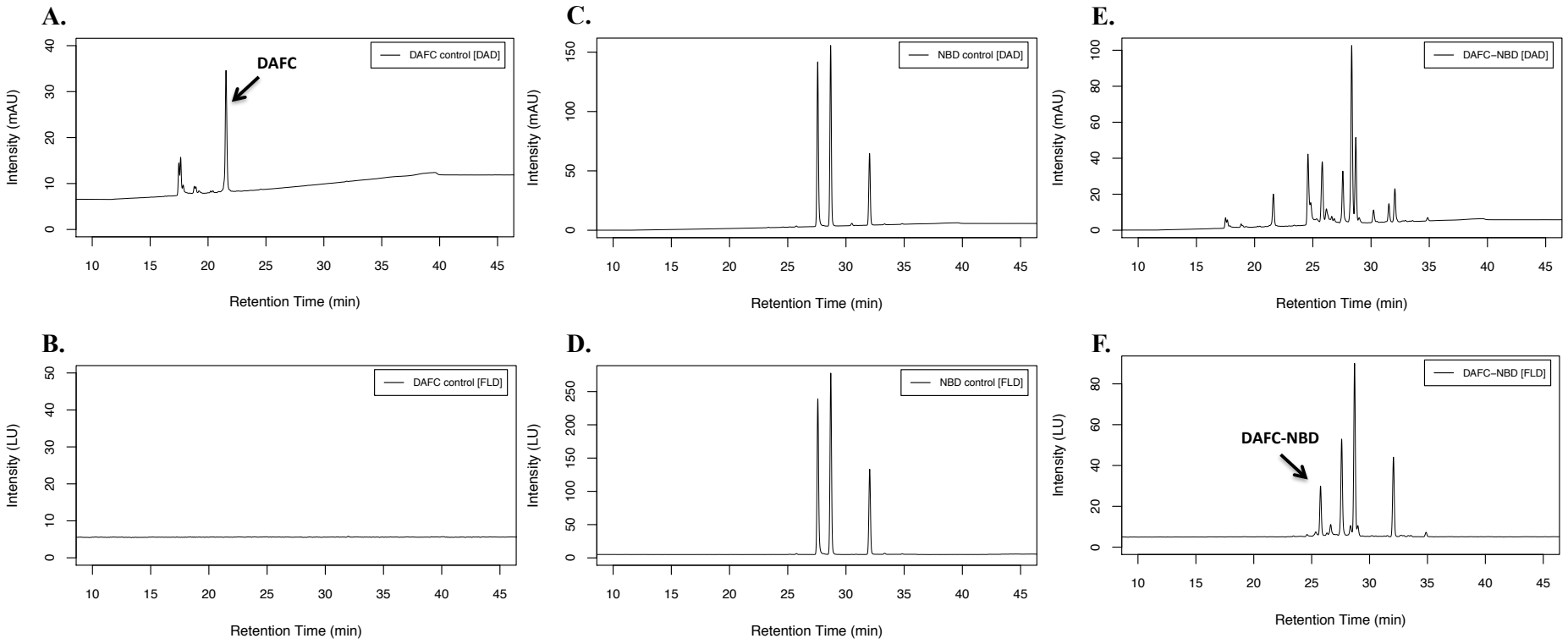

Figure 4.16 RP-HPLC analysis of DAFC^{+Fe} derivatisation with NBD-X-SE using DAD (440 nm) and FLD (Ex/ Em 466/ 535 nm) detection. (A & B) DAFC^{+Fe} only control shows RP-HPLC purified DAFC^{+Fe} with DAD but no FLD detection. (C & D) NBD-X-SE only control shows unreacted fluorophore with DAD and FLD detection. (E & F) DAFC-NBD reaction shows the generation of a new peak with DAD detection and FLD detection (DAFC-NBD).

A.

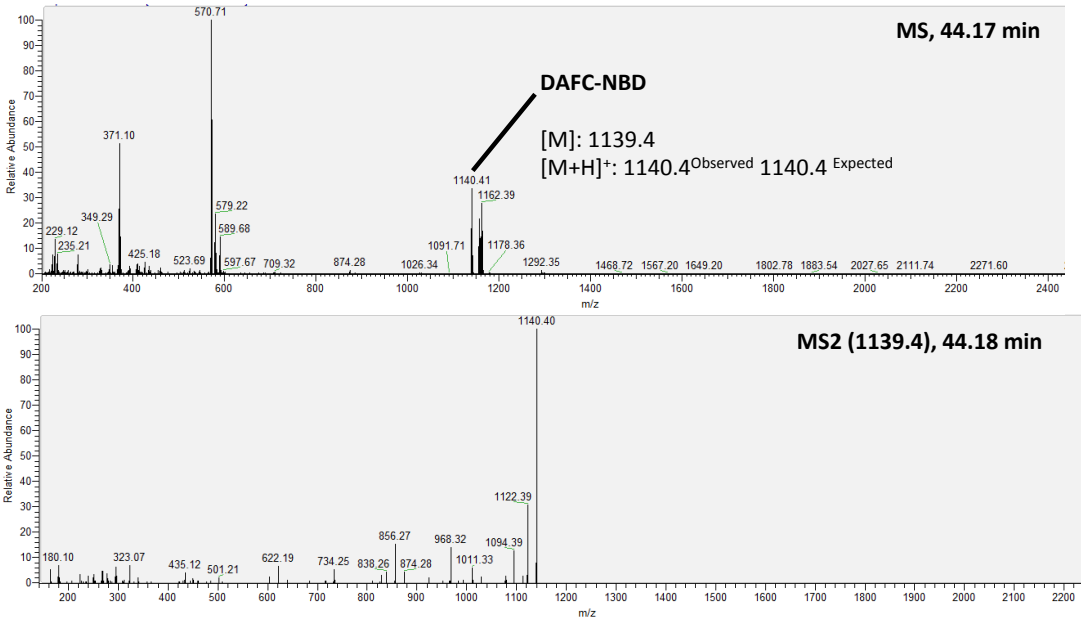

B.

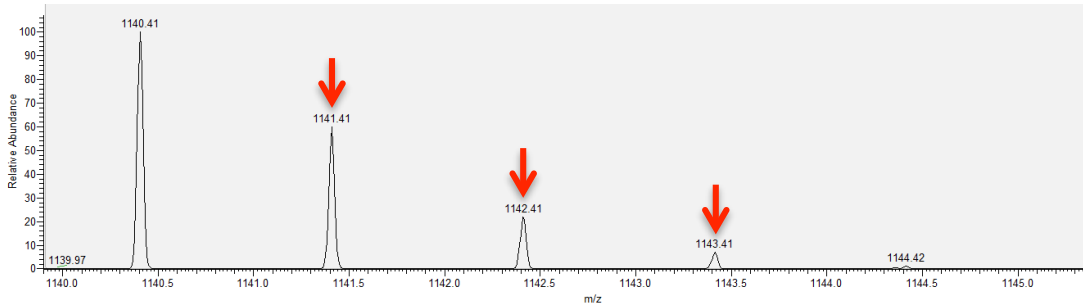

Figure 4.17 LC-MS/MS identification of DAFC-NBD. DAFC-NBD reaction was analysed by LC-MS/MS. (A) MS (extracted ion chromatogram for *m/z* 1139 – 1142) spectrum shows the detection of DAFC-NBD as a singly charged ion (M: 1139.4, $[M+H]^+$: observed *m/z* 1140.4; expected *m/z* 1140.4). MS2 spectrum shows the fragmentation of precursor ion. (B) Increments of approx. +1.0 in observed *m/z* are indicative of C_{13} isotope incorporation in a singly charged ion.

4.2.5 DAFC-NBD is taken up by *A. fumigatus* under iron starved but not sufficient growth

To observe the uptake of DAFC-NBD by *A. fumigatus*, uptake studies were set up in 12 well plates as described in Section 2.2.6. MM, with and without iron, was supplemented with DAFC-NBD at 50 μM (based on the total siderophore content of the DAFC-NBD reaction) or an equivalent volume of controls (TAFC only/ NBD only/ buffer only). Fluorescence was observed in the vacuoles of hyphae incubated with DAFC-NBD during growth without iron only (Figure 4.18).

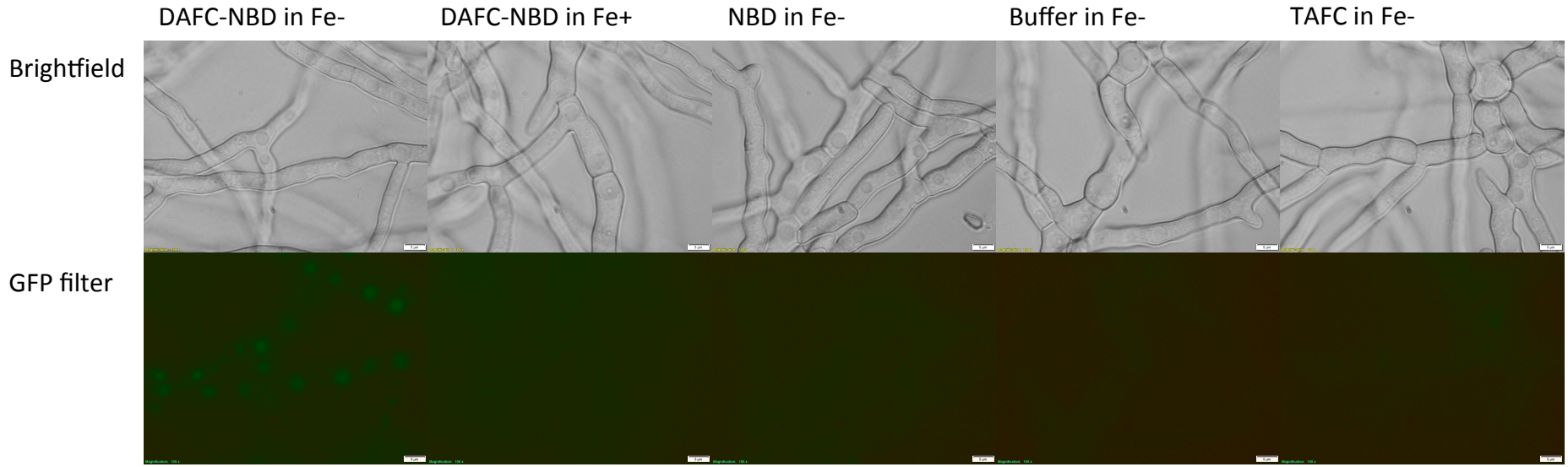

Figure 4.18 Uptake of DAFC-NBD by *A. fumigatus*. *A. fumigatus* was grown in MM with (Fe+) and without (Fe-) iron followed by incubation with DAFC-NBD or controls (NBD, Buffer, or TAFC) at a equivalent concentration for 1 h. After washing, mycelia were viewed by fluorescent microscopy. Fluorescence was observed to localise to vacuoles after incubation with DAFC-NBD only when grown without iron. Bar = 5 μm.

4.3 Discussion

The mechanisms of ferri-siderophore uptake and utilisation in *A. fumigatus* have been considerably elucidated by Haas and co-workers (reviewed in Haas, 2012, 2014). However, there remains a gap in the knowledge on the fate of siderophores and the sites for iron exchange following hydrolysis. To this end, fluorescent derivatives of *A. fumigatus* siderophores were generated. FSC^{+Fe} was RP-HPLC purified and linked to the fluorophore, NBD, *via* NHS ester-mediated primary amine conjugation. Amine linkage ensured that the iron-chelating capacity of FSC remained intact. Generation of FSC-$(NBD)_1$ was confirmed *via* RP-HPLC and LC-MS/MS analysis with detection of FSC-$(NBD)_1$ as a doubly charged ion (M: 1055.4, $[M+2H]^{2+}$: observed *m/z* 528.7; expected *m/z* 528.7). FSC^{+Fe} was also used to create semi-synthetic TAFC analogue, DAFC, by acetylating two of the three free amines with SNA. Generation of DAFC was confirmed *via* RP-HPLC and LC-MS/MS analysis with detection of $DAFC^{+Fe}$ as a doubly charge ion (M: 863.3, $[M+2H]^{2+}$: observed *m/z* 432.8; expected *m/z* 432.7). Similar to FSC-NBD generation, RP-HPLC purified DAFC was linked to NBD *via* NHS ester-mediated primary amine conjugation. Generation of DAFC-NBD was confirmed by detection of DAFC-NBD as a singly charged ion (M: 1139.4, $[M+H]^{+}$: observed *m/z* 1140.4; expected *m/z* 1140.4). Uptake studies in *A. fumigatus* with both FSC- and DAFC-NBD showed a localisation of fluorescence to vacuoles within hyphae exclusively during iron-starved growth.

Conjugation of the siderophore, desferrioxamine, to NBD by Lytton *et al.* (1991) *via* an amine was found to increase the siderophore's lipophilicity (Lytton *et al.*, 1991). The authors concluded this was responsible for the increased membrane permeation observed in desferrioxamine-NBD compared with non-labelled desferrioxamine. The localisation of fluorescence to vacuoles in the work presented in

this chapter could be speculated to have arisen from a similar non-specific membrane permeation of FSC-/ DAFC-NBD. However, during iron starvation, *A. fumigatus* has been shown to undergo significant transcriptional and proteomic remodelling (Moloney *et al.*, 2016a; Mulvihill *et al.*, 2017; Schrettl *et al.*, 2008, 2010). Specifically, microsomal proteins, including a suite of putative and proven siderophore transporters are uniquely present or increased in abundance during iron starvation (Haas *et al.*, 2003; Moloney *et al.*, 2016a; Mulvihill *et al.*, 2017; Park *et al.*, 2016; Raymond-Bouchard *et al.*, 2012; Schrettl *et al.*, 2008, 2010). Uptake of FSC- and DAFC-NBD occurred exclusively during iron-starved growth and not during iron-sufficient growth. This suggests that uptake is dependent on this suite of transporters and not a result of non-specific membrane permeation.

Fluorescently derivatised siderophores have also been observed to localise to vacuoles or vesicles following uptake in other species, including siderophores labelled with fluorophores other than NBD, such as anthracene and lissamine rhodamine B (Ardon *et al.*, 1997, 1998; Froissard *et al.*, 2007; Ouchetto *et al.*, 2005). The localisation of ferrichrome-NBD to "*peri*-vacuolar vesicles" in *C. albicans* and *S. cerevisiae* supported the concept of endocytosis-mediated siderophore uptake (Ouchetto *et al.*, 2005). In *S. cerevisiae*, SITs have been observed to localise intracellularly to endosome-like vesicles that translocate to the plasma membrane upon exposure to their cognate siderophores (Kim *et al.*, 2002). A similar mechanism was observed with MirB in *A. fumigatus.* During iron starvation MirB was found at or near the plasma membrane in vesicles/ aggregates (Raymond-Bouchard *et al.*, 2012). However, when intracellular iron levels were high, MirB was distributed to vesicles throughout the cytoplasm. Thus, in contrast to yeast, low intracellular iron levels and not substrate exposure induce MirB translocation to the plasma membrane. Recently,

Park *et al.* (2016) demonstrated a role for transporters, Sit1 and Sit2, in siderophore uptake in *A. fumigatus*. Sit1 was shown to be involved in the uptake of ferrichrome and ferrioxamine B, while Sit2 was involved in the uptake of ferrichrome only. In contrast to MirB, Sit1 and Sit2 did translocate to the plasma membrane upon substrate (ferrichrome) exposure (Park *et al.*, 2016). Following SIT mediated uptake, FSC^{+Fe}/ $TAFC^{+Fe}$ are enzymatically hydrolysed. This process is mediated by EstB for $TAFC^{+Fe}$ hydrolysis and SidJ for FSC^{+Fe} hydrolysis (Gründlinger *et al.*, 2013a; Kragl *et al.*, 2007). Deficiency in either enzyme resulted in decreased FSC^{+Fe}/ $TAFC^{+Fe}$ hydrolysis; however it did not completely abolish hydrolysis. Following release, iron is either directly used in metabolism, transferred to FC, or transported to vacuoles *via* iron transporter CccA (Gsaller *et al.*, 2012). Ferrated hydrolysis products have been shown to accumulate in FC- and CccA-deficient strains. Thus, the transfer of iron to FC or vacuoles must precede any further processing of siderophore degradation products (Gsaller *et al.*, 2012). Given that iron chelation quenched NBD fluorescence in FSC- and DAFC-NBD (Sections 4.2.1.4 and 4.2.4), the vacuole-localised fluorescence observed in this work is likely a result of desferri-siderophores or desferri-siderophore degradation products. Siderophore hydrolysis in *A. fumigatus* occurs cytosolically and iron removal occurs after this process upon transfer to FC/ vacuoles/ metabolism. Thus, the fluorescence observed herein is unlikely to be a result of vacuolar enclosed ferri-siderophores immediately following uptake, but instead to represent siderophore degradation products after hydrolysis and iron removal.

The subsequent fate of siderophore degradation products remains poorly defined; however they are thought to be recycled or excreted (Haas, 2014; Moore, 2013). There is evidence for a recycling of TAFC degradation products in *Aspergillus*

species. *A. nidulans* deficient in siderophore production (Δ*sidA*) was actually able to synthesize FC following supplementation with $TAFC^{+Fe}$ (Eisendle *et al.*, 2003). This suggests an enzymatic ability to recycle N^5-hydroxyornithine groups from siderophore degradation products (Figure 1.4). In addition, the limited recovery of intracellular $TAFC^{-Fe}$ and the presence of siderophore degradation products in the culture supernatant of *A. fumigatus* together suggest a rapid excretion and following uptake, degradation and re-excretion (Kragl *et al.*, 2007). Given, degradation products are still capable of chelating iron; their compartmentalisation or rapid excretion following iron removal is rational (Kragl *et al.*, 2007). Compartmentalisation of siderophore degradation products to vacuoles would prevent further deleterious iron chelation in the cytosol. Such compartmentalisation has been observed in *Aspergillus* species for self-protection from harmful secondary metabolites, for example in aflatoxin biosynthesis (Chanda *et al.*, 2009; Roze *et al.*, 2011). Notably, in *M. tuberculosis,* deficiency in siderophore exporters resulted in impaired growth upon exogenous exposure to ferri-siderophores. The authors concluded that blocking the siderophore recycling pathway resulted in a toxic intracellular accumulation of desferri-siderophores (Jones *et al.*, 2014). Thus, a compartmentalisation of desferri-siderophore degradation products in *A. fumigatus* is plausible and likely accounts for the fluorescence observed in vacuoles in this work (summarised in Figure 4.19).

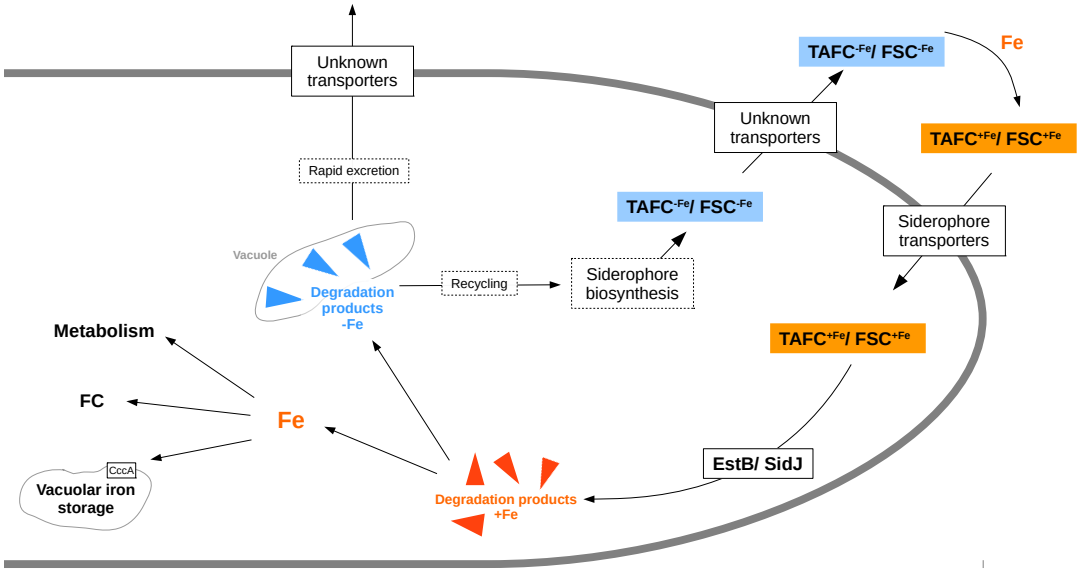

Figure 4.19 Proposed involvement of vacuoles in the processing of siderophores. After siderophore biosynthesis, FSC and TAFC are excreted in the desferri-form (FSC^{-Fe}/ $TAFC^{-Fe}$) for extracellular iron chelation. Ferri-siderophores (FSC^{+Fe}/ $TAFC^{+Fe}$) are taken up *via* SITs and hydrolysed in the cytosol by SidJ or EstB to yield ferri-siderophore degradation products. Iron is transferred to either metabolism, or FC/ vacuolar storage, while desferri-siderophore degradation products are compartmentalised in vacuoles. Degradation products are then either (i) recycled as part of the siderophore biosynthetic pathway by providing N^5-hydroxyornithine groups (supplementing *de novo* N^5-hydroxyornithine), or (ii) rapidly excreted. Image adapted and redrawn from Haas (2014) 'Fungal siderophore metabolism with a focus on *Aspergillus fumigatus*' *Natural Product Reports*, 31 (10), pp. 1266–1276. DOI:10.1039/c4np00071d. Published under the Creative Commons Attribution (Non-Commercial 3.0 Unported Licence). Published by The Royal Society of Chemistry.

Importantly, uptake of FSC- and DAFC-NBD indicates a practical validity to the use of modified siderophores as anti-fungal drugs in a 'Trojan Horse' strategy specifically against *A. fumigatus*. Significant efforts in this domain have yielded

siderophore-drug conjugates with efficacy in several species (Ghosh *et al.*, 2017; Schalk and Mislin, 2017); however this has yet to be realised in *A. fumigatus.* In the work presented in this chapter, uptake of FSC and DAFC was preserved despite amine conjugation to NBD. Thus, a similar approach using an anti-fungal instead of NBD-X-SE warrants investigation. In general, fluorescently labelled siderophores also provide a method to investigate therapeutic strategies targeting siderophore uptake. For example, human protein, Lcn1, which can sequester siderophores from several species and inhibit fungal growth *in vivo* (Fluckinger *et al.*, 2004; Leal *et al.*, 2013). Possessing an additional *in vitro* method to evaluate such potential therapeutics can serve to expedite screening pipelines.

This work has provided new insight into the uptake and subsequent fate of the siderophore-iron complex and commenced a practical realisation of a 'Trojan horse' antifungal strategy in *A. fumigatus.* Moreover, validating the recognition of amine-linked siderophores by their cognate transporters indicates the preservation of crucial epitopes/ structural moieties. Consequently, the NHS ester-mediated modification of FSC *via* amine groups provides the basis for (i) derivatives for FSC studies, (ii) synthesizing a semi-synthetic TAFC analogue *via* SNA acetylation, and (iii) the consequent derivatives for TAFC studies. These can be used in the experimental development of other applications, importantly including conjugation of *A. fumigatus* siderophores to carrier proteins for immunogen preparation.

Chapter 5

Development and characterisation of an anti-FSC IgM

Chapter 5 Development and characterisation of an anti-FSC IgM

5.1 Introduction

A. fumigatus can effect various forms of disease in humans, particularly when the immune system or lung function are compromised in some way. IA is the most serious of these diseases and carries a high mortality rate in at-risk patient groups (Baddley, 2011; Kousha *et al.*, 2011). Lack of early diagnostic methods and limited treatment options largely underlie this high mortality rate. Thus, there is a requirement for novel strategies for diagnosing and treating disease caused by *A. fumigatus*. Siderophores are produced and utilised *in vivo* and their production is essential to the virulence of many microorganisms. Hence, exploiting siderophore systems represents an appealing basis to meet this need (Haas, 2012; Lamb, 2015; Miethke and Marahiel, 2007). Moreover, developing antibodies against siderophores simultaneously provides the basis for both a siderophore-based diagnostic strategy and immunotherapeutic strategy.

Antibodies are widely employed in ELISA systems for the detection of disease biomarkers. For example, the GM assay is routinely utilised in conjunction with other screening methods for the diagnosis of *A. fumigatus* infection (Section 1.1.3.1) (Barton, 2013). This assay uses a sandwich ELISA format with antibodies capable of detecting GM in serum or BAL (Barton, 2013). Recently, the capacity of siderophores for diagnosing microbial infection has been explored using MS detection. TAFC was detected in serum from patients with suspected Aspergillosis (in 69% of samples tested) and proven/ probable Aspergillosis (in 28% of samples tested) (Carroll *et al.*, 2016). Intracellular siderophore, FC was detected in the serum of a rat model of Aspergillosis (Luptáková *et al.*, 2017). Furthermore, in the same study, both TAFC

and FC were detected in the urine of infected rats. Importantly, no siderophores were detected in uninfected animals in this work. Though this is promising, further sample analysis is required to validate the use of siderophores as biomarkers of Aspergillosis. The use of *M. tuberculosis* siderophore, mycobactin, for diagnosing pulmonary tuberculosis and tuberculous meningitis also shows promise. One-hundred percent of patients with pulmonary tuberculosis and 71% of patients with tuberculous meningitis contained mycobactin in sputum and CSF samples, respectively, while there was no mycobactin detected in control samples (Pan *et al.*, 2015). LC-MS/MS based screening strategies offer many advantages, including the highly sensitive detection of small molecules. However, its application is restricted to hospitals with such instruments as well as trained operators. In contrast, antibodies can easily be implemented in point-of-care assays reducing cost and time for diagnosis. Hence, while LC-MS/MS analysis can offer significant insight into the validity of a biomarker during development studies, antibodies are favoured for the actual utilisation of the biomarker in a diagnostic assay.

In mammals, the restriction of free iron forms the basis of a nutritional immunity, depriving pathogens of an essential element to impede their growth (Cassat and Skaar, 2013; Crawford and Wilson, 2015). As a result, a struggle for iron ensues during the path of microbial infection, with iron-sequestering strategies implemented by both pathogen and host. As discussed in Section 1.3.1, humans can produce siderocalins, Lcn1 and Lcn2, which can sequester microbial siderophores. Recently, the application of Lcn1 in reducing *A. fumigatus* corneal infection was demonstrated (Leal *et al.*, 2013). This suggests validity to the concept of targeting siderophore uptake *via* proteinaceous sequestration of siderophores. Generating an antibody

against siderophores can yield a protein with similar activity to siderocalins but with higher specificity. Therefore, allowing highly targeted growth inhibition.

Small molecules, such as siderophores, are typically incapable of independently eliciting an immune response. In order to raise antibodies against such a small molecule (referred to as hapten upon conjugation to a carrier protein), it must first be linked to a protein that is in itself quite immunogenic. When used in immunisations, the carrier protein raises an immune response, resulting in the formation of B-lymphocytes producing antibodies against both the hapten and carrier protein. The most commonly used carrier proteins include keyhole limpet hemocyanin (KLH), ovalbumin, BSA, and thyroglobulin (Hermanson, 2008).

Haptens are commonly linked to carrier proteins *via* heterobifunctional crosslinkers for immunogen preparations. Heterobifunctional crosslinkers possess two different reactive groups, which can link to functional groups, such as thiols, amines, or hydroxyl groups, on target molecules. Amine linkage *via* NHS esters is one of the most common strategies utilised in bioconjugation. Using NHS esters, mutually reactive groups can be introduced onto both the hapten and carrier protein through amine linkage. Subsequently, combining the molecules allows covalent conjugation of the two molecules (Hermanson, 2008). For example, crosslinkers, *N*-succinimidyl-*S*-acetylthioacetate (SATA) and succinimidyl-4-(*N*-maleimidomethyl)cyclohexane-1-carboxylate (SMCC) are commonly utilised together in bioconjugation applications. SATA has an amine-reactive NHS ester on one end and a protected thiol group on the other end. Protection of the thiol group facilitates the preservation of thiol groups during storage of SATA-modified proteins. Hence, proteins can be modified with SATA and stored as stocks. When required, the thiol group can be deprotected. SMCC also has an amine-reactive NHS ester on one end as well as a thiol-reactive

maleimide on the other end. Though SMCC is water insoluble, a water soluble analogue, sulfosuccinimidyl-4-(*N*-maleimidomethyl)cyclohexane-1-carboxylate (Sulfo-SMCC) is also available. Both can be solubilised in an organic solvent such as DMSO prior to addition to an aqueous reaction containing the molecule to be labelled. Subsequently, coupling of the maleimide and thiol groups occurs from pH 6.5 – 7.5 yielding a stable thioether bond (Hermanson, 2008).

There is a need to develop novel diagnostic and therapeutic strategies against *A. fumigatus* infection. The use of siderophores as biomarkers of infection and the targeting of siderophore-mediated iron uptake as an anti-fungal strategy both present promising solutions to this need. The generation of anti-siderophore antibodies has potential to provide the basis for both strategies. *A. fumigatus* produces two extracellular siderophores, FSC and TAFC. This chapter focuses on FSC while Chapter 6 similarly focuses on TAFC. The objectives of the work presented in this chapter were to:

i. Develop a FSC immunogen suitable for murine immunisations.

ii. Develop a competitive FSC ELISA for (A) screening for antibody production in murine sera, (B) screening for antibody production in hybridoma supernatant, and (C) detecting FSC in *A. fumigatus* culture supernatants.

iii. Generate mAbs directed against FSC.

iv. Purify and characterise the anti-FSC antibody.

5.2 Results

5.2.1 Development of a FSC immunogen

5.2.1.1 Strategy for generating FSC antibodies

As a small molecule, FSC is likely incapable of independently eliciting an immune response. Hence, to generate a FSC immunogen it was necessary to conjugate FSC to an immunogenic carrier protein. In this case, KLH was selected due to its immunogenicity and available functional groups for crosslinking. KLH is isolated from *Megathura crenulata* and is a very large (molecular mass of 4.5 X 10^5 – 1.3 X 10^7) multi-subunit protein that can easily dissociate into highly immunogenic smaller subunits. Moreover, it is commonly used as a carrier protein, therefore, established methods are available for its use in immunogen preparation (Hermanson, 2008).

As discussed in Chapter 4, FSC is a cyclic tripeptide comprised of three N^5-anhydromevalonyl-N^5-hydroxyornithine groups linked by ester bonds (Haas, 2014). The presence of three free amine groups means FSC may be particularly amenable to modification with NHS esters. This was explored by the generation of several compounds in Chapter 4, including FSC-$(NBD)_1$ and DAFC-$(NBD)_1$, in which siderophore uptake was preserved despite fluorophore conjugation. There are a variety of NHS ester-based crosslinker strategies suitable for conjugating small molecules to carrier proteins in immunogen synthesis. For this work, a heterobifunctional crosslinking strategy was employed, whereby mutually reactive crosslinkers were independently introduced into the carrier protein and hapten, subsequently, the two were combined and linked together. Doyle *et al.* (2011) demonstrated a similar strategy to this for conjugation of FSC to BSA. First, KLH

was modified with an amine-reactive crosslinker (SATA), introducing protected thiol groups. A thiol-reactive maleimide group was then introduced into FSC *via* Sulfo-SMCC. After deprotection of the thiol groups in SATA-KLH, the maleimide group introduced to FSC permits conjugation to the carrier protein *via* a stable thioether bond (summarised in Figure 5.1).

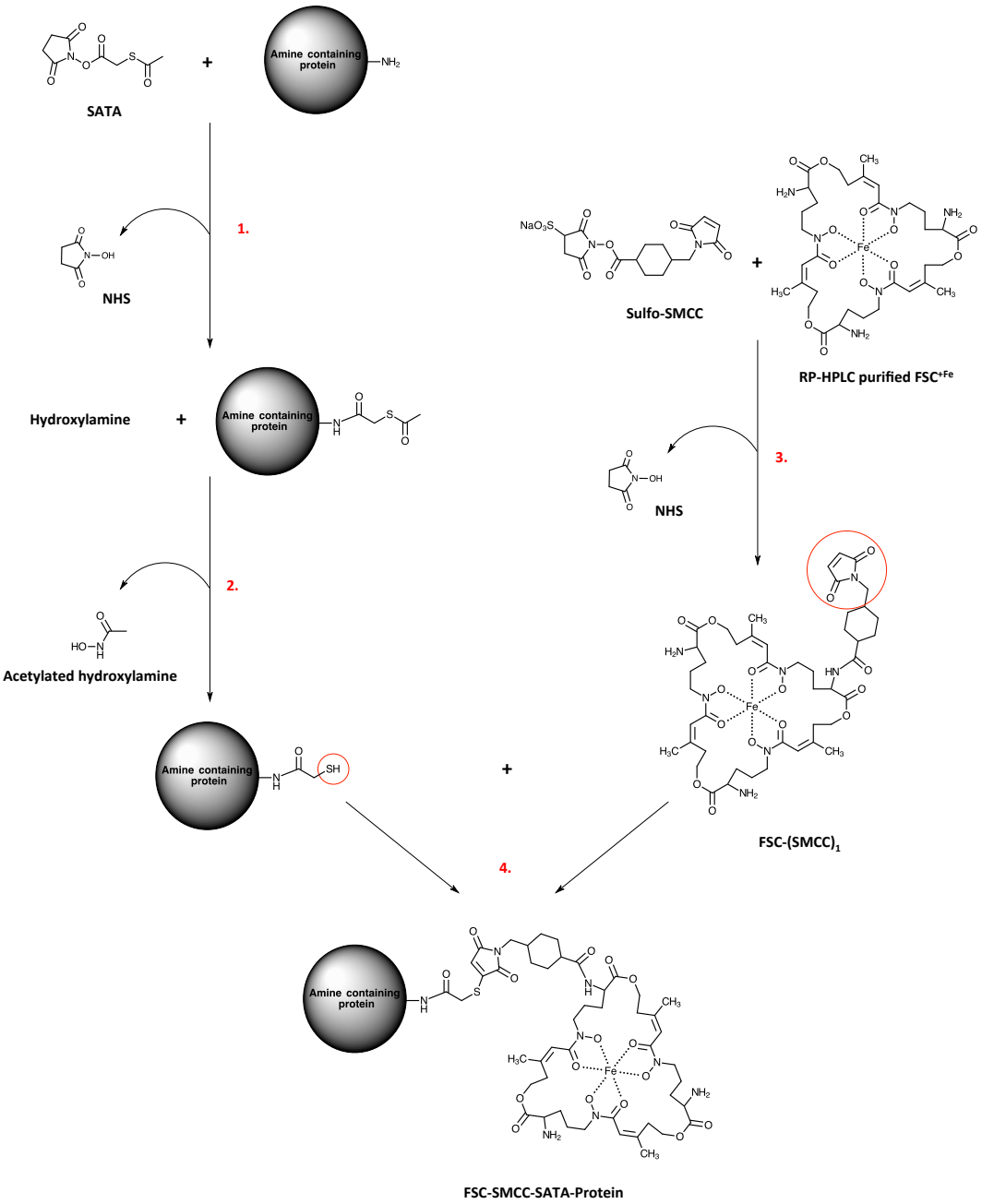

Figure 5.1 Strategy for the development of FSC immunogen. **1.** KLH is modified with SATA *via* NHS ester linkage to amine groups, introducing protected thiol groups. **2.** Thiol groups of SATA-KLH are deprotected with hydroxylamine. Excess SATA and hydroxylamine are removed by gel filtration. **3.** FSC is modified with Sulfo-SMCC introducing a thiol-reactive maleimide group. **4.** When combined, the thiol group of SATA-KLH can form a stable thioether bond with the maleimide group of FSC-SMCC. Excess unconjugated siderophore/ crosslinker are then removed by dialysis.

5.2.1.2 Demonstrating modification of FSC with Sulfo-SMCC

Before proceeding to the conjugation of FSC to KLH *via* SMCC and SATA, it was first necessary to confirm that Sulfo-SMCC could activate FSC and introduce the thiol-reactive maleimide group. For the generation of FSC-$(SMCC)_1$ a similar rationale to that of FSC-$(NBD)_1$ synthesis was employed (Section 4.2.1.1), whereby (i) FSC^{+Fe} was utilised for NHS ester modification to avoid the modification of –OH groups in FSC^{-Fe}, (ii) FSC^{+Fe} was modified with limiting amounts of Sulfo-SMCC to limit generation of FSC-$(SMCC)_2$ and FSC-$(SMCC)_3$, aimed at preserving native epitopes as much as possible, and (iii) FSC-SMCC was prepared without further purification to negate effects of instability (in this case maleimide group instability).

RP-HPLC purified FSC^{+Fe} was incubated with Sulfo-SMCC equimolar to the moles of FSC^{+Fe} to demonstrate the generation FSC-$(SMCC)_1$ and FSC-$(SMCC)_2$ (similar to Section 2.2.5.3.2). All reactions were monitored by RP-HPLC analysis with DAD detection at 440 nm as described in Section 2.2.3.2 (Figure 5.2). The peaks associated with FSC-$(SMCC)_1$ and FSC-$(SMCC)_2$ were fraction collected and analysed by LC-MS/MS to confirm their identity (as per Section 2.2.13.6). Generation of FSC-$(SMCC)_1$ was confirmed by detection of a doubly charged ion (M: 998.4, $[M+2H]^{2+}$: observed *m/z* 500.1; expected *m/z* 500.2) (Figure 5.3). Generation of FSC-$(SMCC)_2$ was confirmed by detection of a doubly charged ion (M: 1217.5, $[M+2H]^{2+}$: observed *m/z* 609.7; expected *m/z* 609.7) (Figure 5.4). RP-HPLC analysis indicated 38% of the FSC^{+Fe} was converted to FSC-$(SMCC)_1$ and 16% was converted to FSC-$(SMCC)_2$ (Figure 5.2).

A.

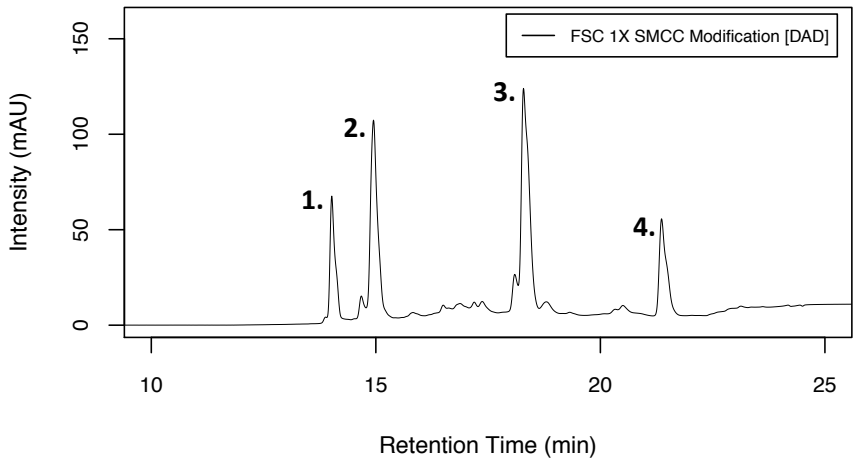

B.

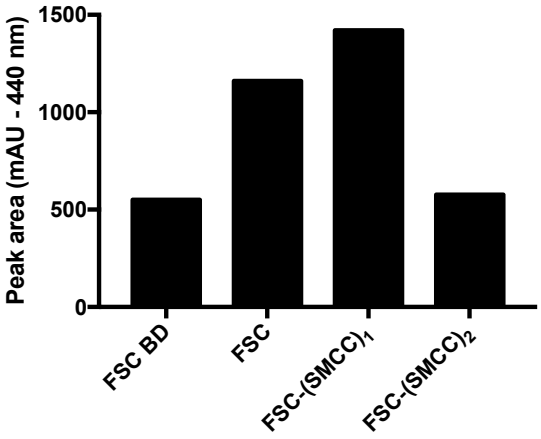

Figure 5.2 (A) RP-HPLC analysis with DAD detection (440 nm) shows the formation of FSC-$(SMCC)_1$ and FSC-$(SMCC)_2$ following incubation of RP-HPLC purified FSC^{+Fe} with Sulfo-SMCC (**1.** FSC breakdown product (FSC BD), **2.** FSC, **3.** FSC-$(SMCC)_1$, and **4.** FSC-$(SMCC)_2$). (B) Graphical representation of the peak area (mAU – 440 nm) associated with FSC BD, FSC, FSC-$(SMCC)_1$, and FSC-$(SMCC)_2$.

A.

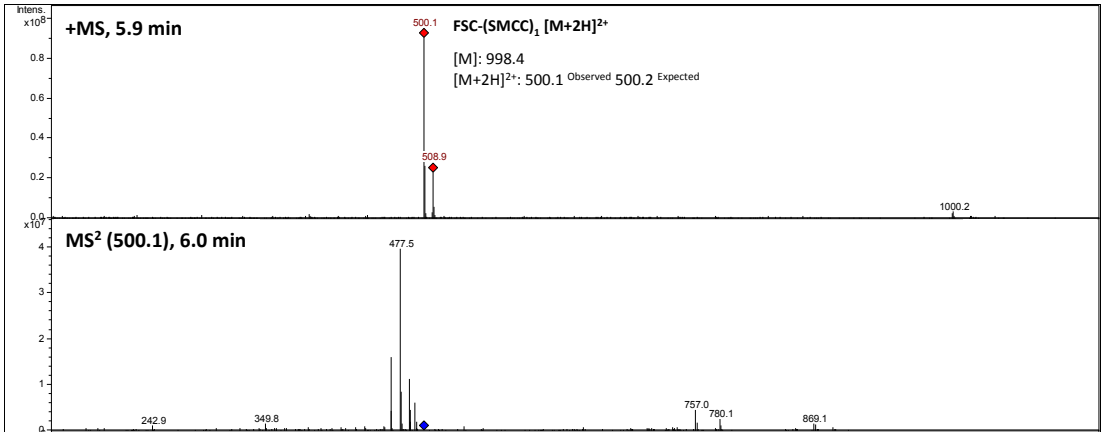

B.

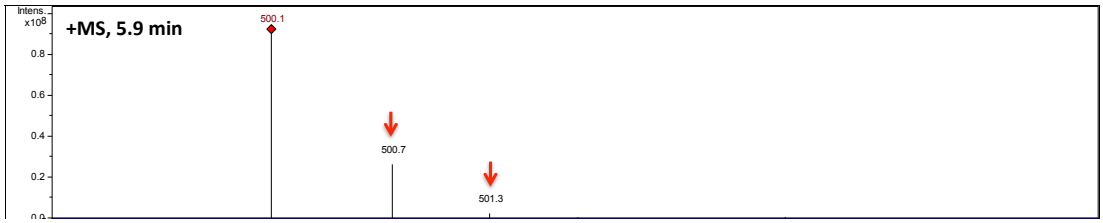

Figure 5.3 LC-MS/MS identification of FSC-$(SMCC)_1$. Peak associated with FSC-$(SMCC)_1$ (**3.** in Figure 5.2 A) was fraction collected during RP-HPLC analysis and analysed by LC-MS/MS. (A) MS (extracted ion chromatogram for *m/z* 498 – 502) spectrum shows the detection of FSC-$(SMCC)_1$ as a doubly charged ion (M: 998.4, $[M+2H]^{2+}$: observed *m/z* 500.1; expected *m/z* 500.2). MS2 spectrum shows the fragmentation of precursor ion (B) Increments of approx. +0.5 in observed *m/z* are indicative of C_{13} isotope incorporation in a doubly charged ion.

A.

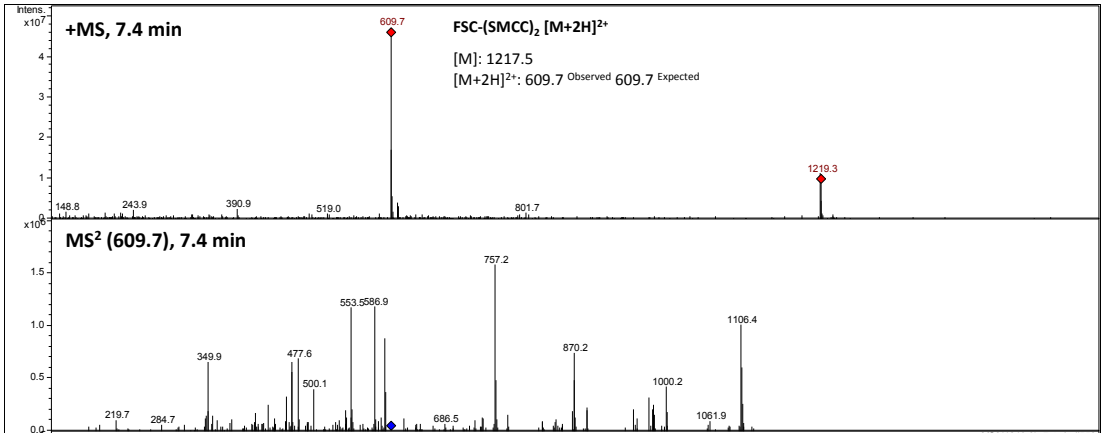

B.

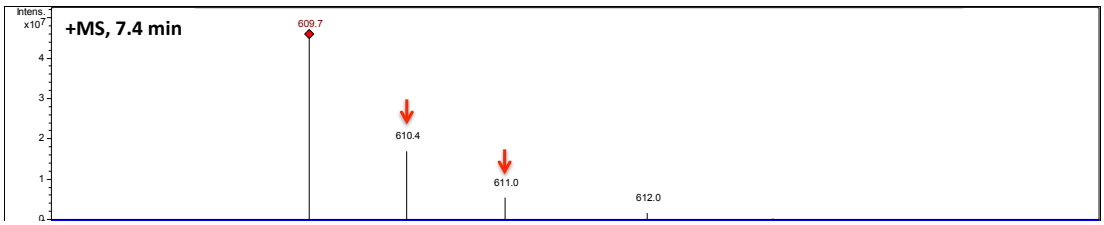

Figure 5.4 LC-MS/MS identification of FSC-$(SMCC)_2$. Peak associated with FSC-$(SMCC)_2$ (**4.** in Figure 5.4 A) was fraction collected during RP-HPLC analysis and analysed by LC-MS/MS. (A) MS (extracted ion chromatogram for *m/z* 608 – 612) spectrum shows the detection of FSC-$(SMCC)_1$ as a doubly charged ion (M: 1217.5, $[M+2H]^{2+}$: observed *m/z* 609.7; expected *m/z* 609.7). MS2 spectrum shows the fragmentation of precursor ion (B) Increments of approx. +0.5 in observed *m/z* are indicative of C_{13} isotope incorporation in a doubly charged ion.

5.2.1.3 Conjugation of FSC-SMCC to SATA-KLH

Section 5.2.1.2 demonstrated FSC modification with Sulfo-SMCC whereby generation of FSC-$(SMCC)_1$ and FSC-$(SMCC)_2$ were confirmed by LC-MS/MS and RP-HPLC analysis. Following this, Sulfo-SMCC was deemed appropriate for use in a conjugation strategy to link FSC to SATA-modified KLH.

FSC^{+Fe} was RP-HPLC purified and derivatised with a 0.75X molar excess of Sulfo-SMCC, as described in Section 2.2.5.3.2, to yield FSC-$(SMCC)_1$ while minimising formation of FSC-$(SMCC)_2$. The resultant reaction was analysed by RP-HPLC to confirm the formation of FSC-$(SMCC)_1$ and showed that 36% of the FSC^{+Fe} was converted to FSC-$(SMCC)_1$ while only 8% was converted to FSC-$(SMCC)_2$ (Figure 5.5). Demasking of SATA-KLH was confirmed by measuring the thiol content of the demasked SATA-KLH before conjugation to be 92 μmoles per μmole KLH (as per Section 2.2.5.4). The FSC-SMCC reaction mixture was immediately added to demasked SATA-KLH with approx. 10X molar excess of FSC-$(SMCC)_1$ to thiol groups. The reaction was allowed to proceed at room temperature for 3 h (Section 2.2.5.3.2). For comparative analytical purposes, a small scale of the sample and a negative control (using FSC^{+Fe} without Sulfo-SMCC modification) were also conducted in parallel.

Utilising the λ_{max} of ferri-siderophores (440 nm), spectrophotometry was primarily used to determine successful conjugation. Following the conjugation reaction, the small-scale sample and negative control were purified by PD10 separation and the OD (440 nm) and protein content measured from each fraction to determine the OD/ mg of protein. Fractions from the small-scale sample showed an average OD of 0.595/ mg protein while the negative control showed an OD of 0.125/

mg of protein (Figure 5.6). This indicated the successful conjugation of FSC-$(SMCC)_1$ to KLH whereby without Sulfo-SMCC in the reaction, any free FSC^{+Fe} was not conjugated and removed following a size exclusion separation. Similarly, after conjugation, the large-scale sample was dialysed against PBS to remove any unconjugated FSC^{+Fe}/ FSC-$(SMCC)_1$/ FSC-$(SMCC)_2$. The OD (440 nm) and Bradford assay were used to determine the siderophore and protein content to be 330 μM and 0.85 mg/ ml respectively, indicating conjugation of 338 nmol FSC^{+Fe} per mg KLH. RP-HPLC analysis of the large-scale conjugation over the course of the conjugation showed a 16% reduction in the amount of free FSC-$(SMCC)_1$ in the reaction also indicative of conjugation (Figure 5.7). Finally, upon the addition of FSC-SMCC to SATA-KLH, significant orange precipitation was observed. Extensive modification of proteins during crosslinking can affect protein solubility, thus such precipitation suggests significant conjugation of FSC-$(SMCC)_1$ to SATA-KLH.

A.

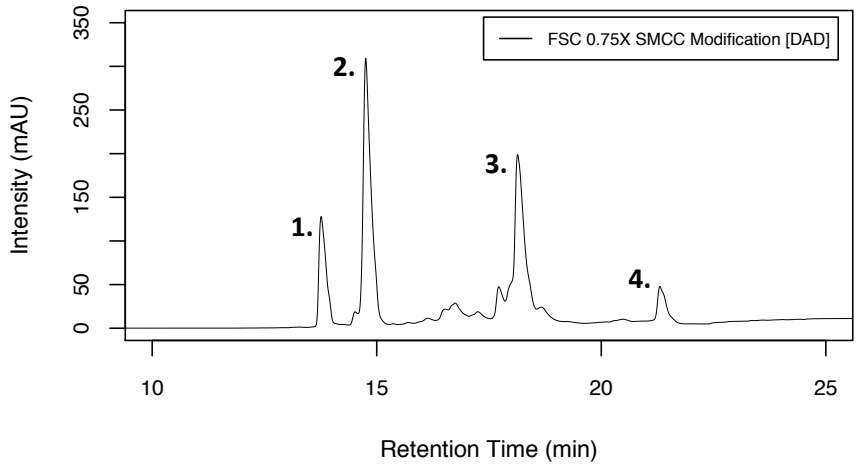

B.

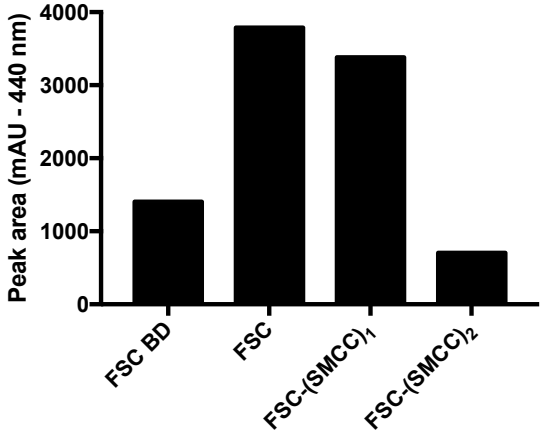

Figure 5.5 (A) RP-HPLC analysis with DAD detection (440 nm) shows the formation of FSC-$(SMCC)_1$ for conjugation to SATA-KLH (**1.** FSC breakdown product (FSC BD), **2.** FSC, **3.** FSC-$(SMCC)_1$, and **4.** FSC-$(SMCC)_2$). (B) Graphical representation of the peak area (mAU – 440 nm) associated with FSC BD, FSC, FSC-$(SMCC)_1$, and FSC-$(SMCC)_2$.

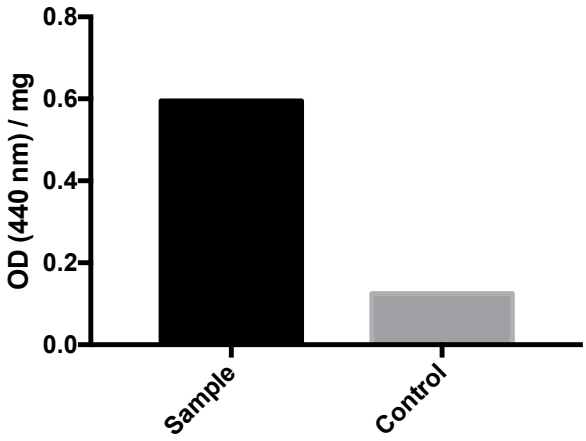

Figure 5.6 A small-scale sample and negative control (omitting Sulfo-SMCC) were also conducted in parallel for comparative analysis to confirm conjugation *via* measurement of the λ_{max} of ferri-siderophores (440 nm). After PD10 separation, the OD/ mg of protein was determined and showed an average of 0.595/ mg in the small-scale sample and 0.125/ mg in the control.

A.

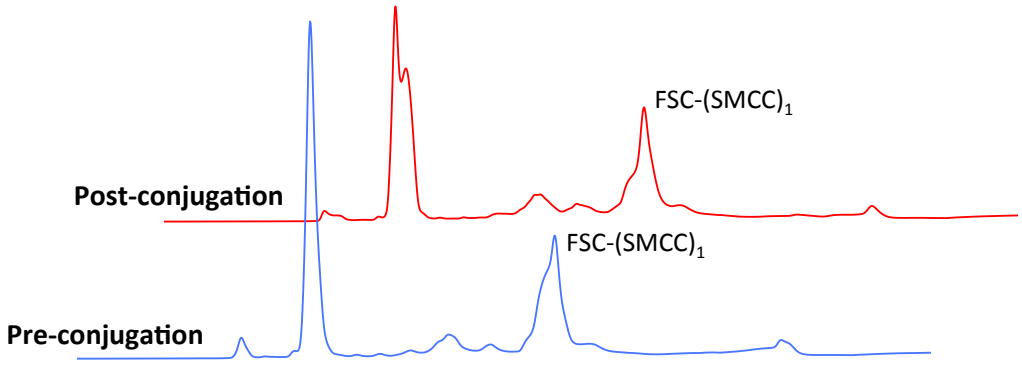

B.

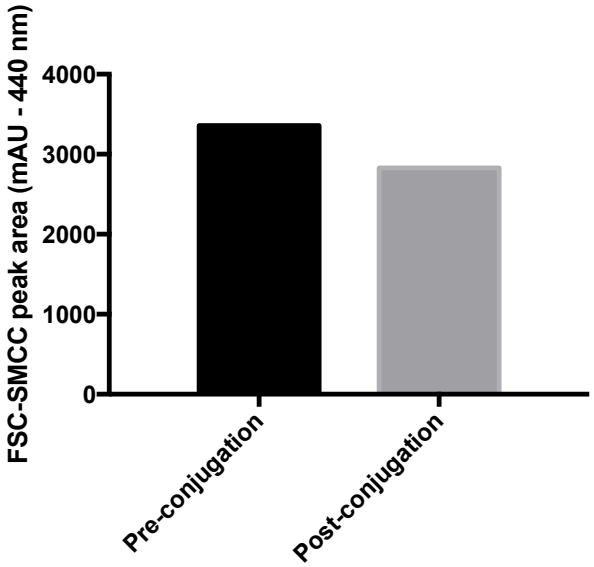

Figure 5.7 (A) RP-HPLC analysis with DAD detection (440 nm) shows a reduction in the levels of FSC-$(SMCC)_1$ over the course of the conjugation (3 h). (B) Graphical representation of the peak area (mAU – 440 nm) associated with FSC-$(SMCC)_1$ over the course of the conjugation.

5.2.2 Immunisation of mice

The FSC-KLH immunogen (50 µg soluble and insoluble fractions) (Section 5.2.1.3) was mixed with adjuvant, Pam3Cys in a final volume of 100 µl and intraperitoneally administered to BALB/c mice (n = 3; 6 – 8 weeks old). Mice received three additional boosters of the same composition over 3 week intervals. After the third booster, tail bleeds were taken and sera isolated for polyclonal antibody analysis. A fourth and final booster was also administered 3 days prior to the fusion.

5.2.3 Development of an ELISA for the detection of anti-FSC antibodies

5.2.3.1 Assay principle

The primary basis for screening anti-FSC antibodies was by either (i) indirect ELISA, or (ii) competitive ELISA using plates coated with FSC^{+Fe} conjugated to BSA and free competing FSC^{+Fe}. The principle of these assays is described in Figure 5.8.

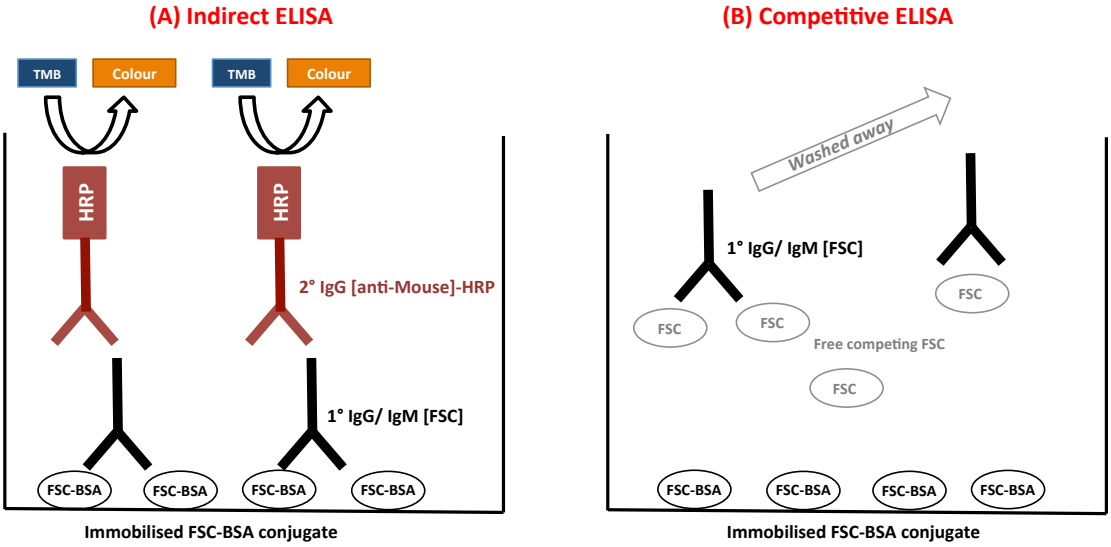

Figure 5.8 ELISA principle. (A) In an indirect ELISA, anti-FSC antibodies (1°) bind FSC-BSA coated wells of an ELISA plate. Binding to the plate immobilises the antibody so that it resists removal upon washing. The 1° antibody is then bound by an anti-mouse IgG antibody conjugated to HRP (2°) which similarly immobilises on the plate. After substrate (TMB) addition, HRP forms a coloured product generating a signal readable at 450 nm after stopping the reaction. (B) In contrast, when competing FSC is added before the 1° antibody, it competes with FSC-BSA on the plate for 1° antibody binding. Upon binding to the competitor, the anti-FSC antibody no longer immobilises on the plate and is washed away. Subsequently, the 2° antibody has no site for immobilisation and is also washed away. Consequently, there is less/ no colour development upon substrate addition and a lower signal.

5.2.3.2 Conjugation of FSC-SMCC to SATA-BSA

Coating ELISA plates is based on the adsorption of coating antigens to the polystyrene material. It is typically more suitable for small molecules to be coated to plates *via* a carrier protein so that more epitopes of the molecule are accessible to the probing antibody (Daven, 2009). Following this, FSC^{+Fe} was conjugated to BSA for ELISA plate coating. Similar to the FSC-KLH immunogen preparation, FSC^{+Fe} was RP-HPLC purified and derivatised with a 0.75X molar excess of Sulfo-SMCC as described in Section 2.2.5.2.2. This was immediately added to demasked SATA-KLH and the reaction was allowed to proceed at room temperature for 2 h followed by overnight at 4 °C (Section 2.2.5.2.2). SDS-PAGE analysis of the resultant conjugate indicated an increased molecular mass in comparison to BSA or SATA-BSA (Figure 5.9). Similar to FSC-$(SMCC)_1$ conjugation to KLH, using the λ_{max} of ferri-siderophores (440 nm), spectrophotometry was used as a measure of successful conjugation. Following the reaction, the sample was dialysed against PBS. The OD (440 nm) and Bradford assay were used to determine the siderophore and protein content to be 177 µM and 0.8 mg/ ml respectively, indicating conjugation of 221 nmol FSC^{+Fe} per mg BSA.

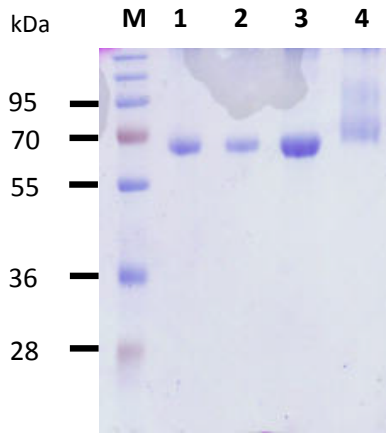

Figure 5.9 SDS-PAGE analysis of FSC^{+Fe}-BSA. M: Molecular mass marker. 1: Unmodified BSA. 2: SATA-BSA (masked). 3. SATA-BSA (demasked). 4. FSC^{+Fe}-BSA.

5.2.4 Screening strategy

The strategy for screening for anti-FSC antibodies is summarised in Figure 5.10. After immunisations, a tail bleed was taken to screen for polyclonal antibodies by competitive FSC ELISA. By screening the mice at this stage it was possible to select the best mouse with which to proceed to hybridoma generation. After assay optimisation and screening (Section 5.3.4), mouse D was selected for spleen removal and hybridoma generation as described in Section 2.2.9. Hybridoma supernatant was screened directly; initially by indirect ELISA using plates coated with FSC-BSA or SATA-BSA (as the negative control). Given antibody production levels were unknown *a priori*, higher coating concentrations were utilised to detect low-level antibody production. Any hybridomas positively selected were sub-cultured and screened again by competitive ELISA as optimised for tail bleed screening. From these, the best antibody producers were selected for cloning.

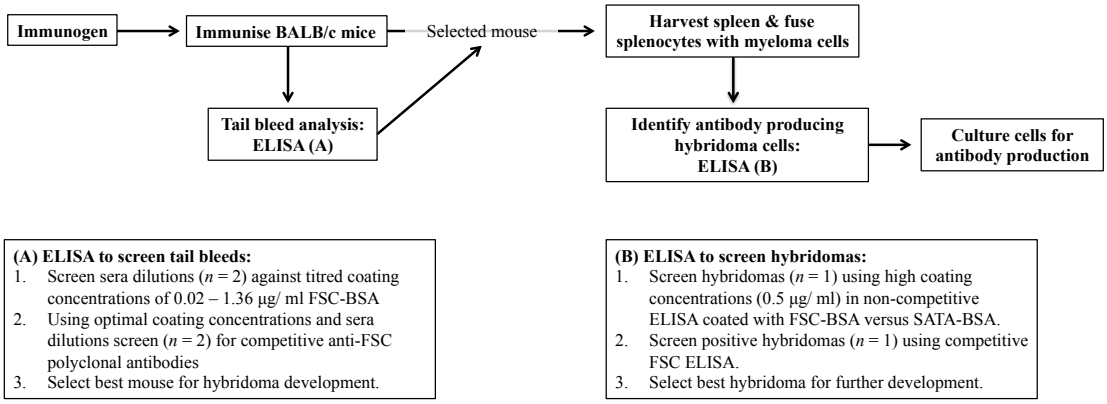

Figure 5.10 Schematic of overall screening strategy for screening for (i) anti-FSC antibodies in tail bleeds, and (ii) anti-FSC hybridomas.

5.2.5 Screening of murine sera

5.2.5.1 Optimisation of ELISA coating concentration

To establish a suitable ELISA coating concentration, murine tail bleed sera from mice D and E were analysed on ELISA plates (n = 2) coated with a titred range of FSC-BSA concentrations (0.02 – 1.36 µg/ ml) (Section 5.2.3.2). Sera were diluted 1 in 25,600, 1 in 40,000, or 1 in 80,000 and an indirect ELISA carried out as per Section 2.2.8. A coating concentration of 0.09 µg/ ml paired with a sera dilution of 1 in 80,000 showed a mean OD (450/ 620 nm) of 1.4 and 1.9 for mice D and E respectively (Figure 5.11) (Appendices, Supplementary Table 12). A coating concentration of 0.09 µg/ ml was selected for all further ELISA analysis.

A.

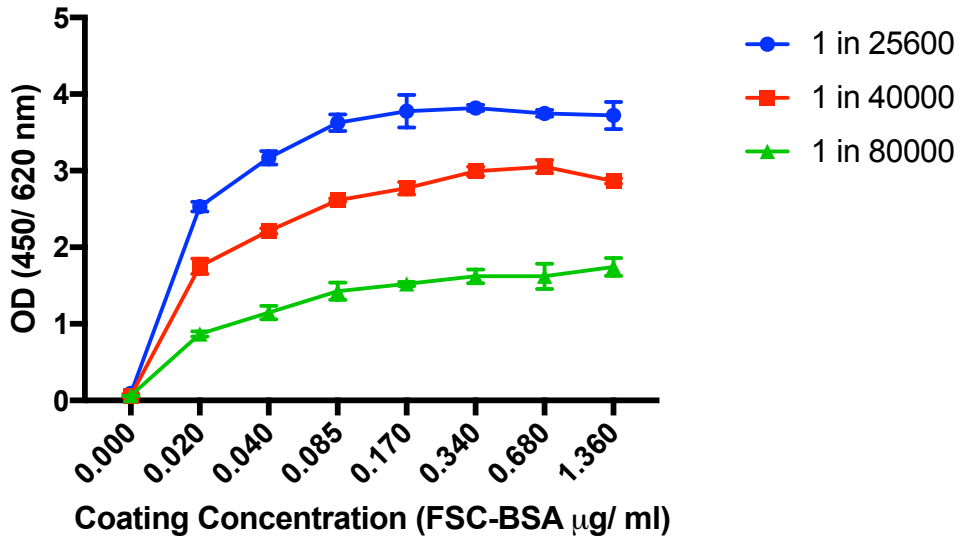

B.

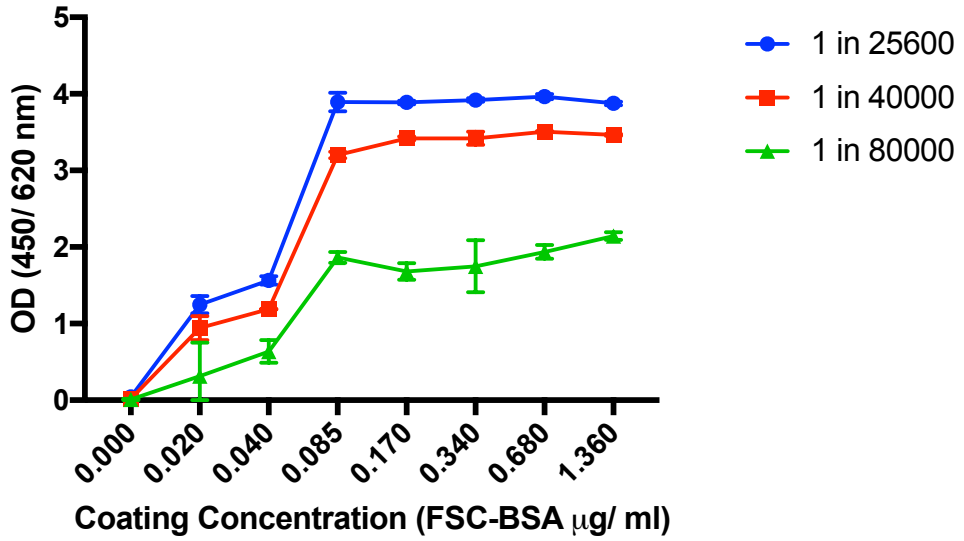

Figure 5.11 Indirect FSC ELISA analysis of murine tail bleeds. Sera from (A) mouse D and (B) mouse E were analysed on ELISA plates coated with a titre of FSC-BSA concentrations to establish a suitable coating concentration at several sera dilutions (1 in 25,600, 1 in 40,000, and 1 in 80,000). A coating concentration of 0.09 μg/ ml was selected for further ELISA analysis.

5.2.5.2 Mouse D produces competitive anti-FSC polyclonal antibodies

Murine tail bleed sera were analysed by competitive FSC ELISA to establish if mice D and E possessed competitive anti-FSC antibodies. Tail bleed sera was diluted 1 in 100,000 and analysed by competitive FSC ELISA (n = 2) with a coating concentration of 0.09 µg/ ml. Mouse D showed a somewhat decreasing OD (450/ 620 nm) with increasing free competing FSC concentration ($OD_{450/620}$ 1.31 at 0 µM FSC and 0.98 at 100 µM FSC) indicative of the presence of competitive anti-FSC antibodies; whereas mouse E did not show competition (Figure 5.12) (Appendices, Supplementary Table 13). Mouse D was selected for further analysis.

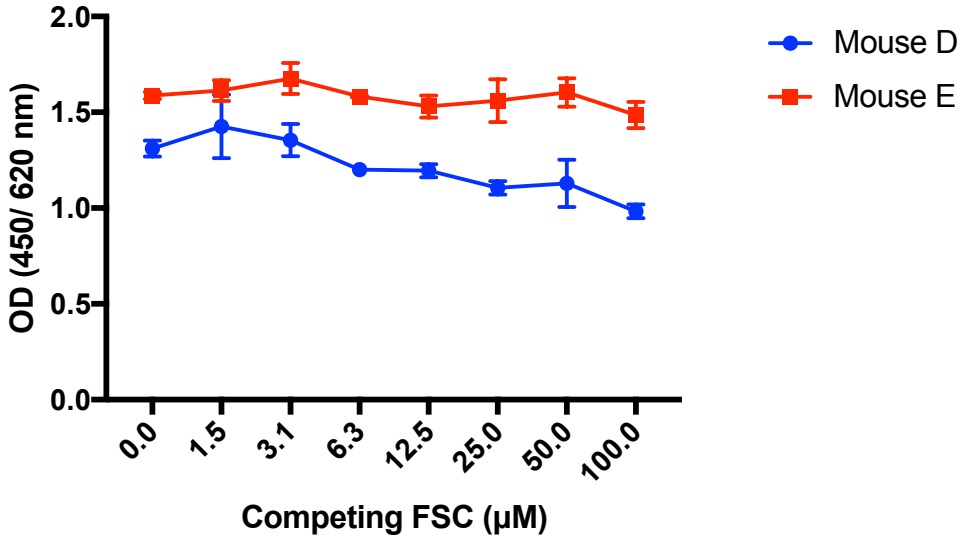

Figure 5.12 Competitive FSC ELISA analysis of murine tail bleeds. Tail bleeds from mice D and E were analysed by competitive FSC ELISA. Serum from mouse D showed decreasing OD (450/ 620 nm) with increasing competing FSC concentration ($OD_{450/620}$ 1.31 at 0 µM FSC and 0.98 at 100 µM FSC); whereas mouse E serum did not show competition.

5.2.5.3 Mouse D produces competitive and specific anti-FSC polyclonal antibodies

The polyclonal antibodies present in sera from mouse D were next tested for specificity for FSC compared with other competitors including free iron, and *A. fumigatus* metabolite, bis(methylthio)gliotoxin (BmGT). Tail bleed serum was diluted 1 in 100,000 and analysed by competitive ELISA (n = 2) with a coating concentration of 0.09 µg/ ml. Serum analysis indicated the presence of competitive anti-FSC antibodies that showed no competition against free iron or BmGT at the same concentration (Figure 5.13). This indicates that the polyclonal antibodies are not just non-specifically competing with FSC. A pre-bleed taken from one of the two mice prior to FSC-KLH immunisation was diluted 1 in 100,000 and also analysed. This showed no binding to FSC-BSA on ELISA plates (Figure 5.13) (Appendices, Supplementary Table 14).

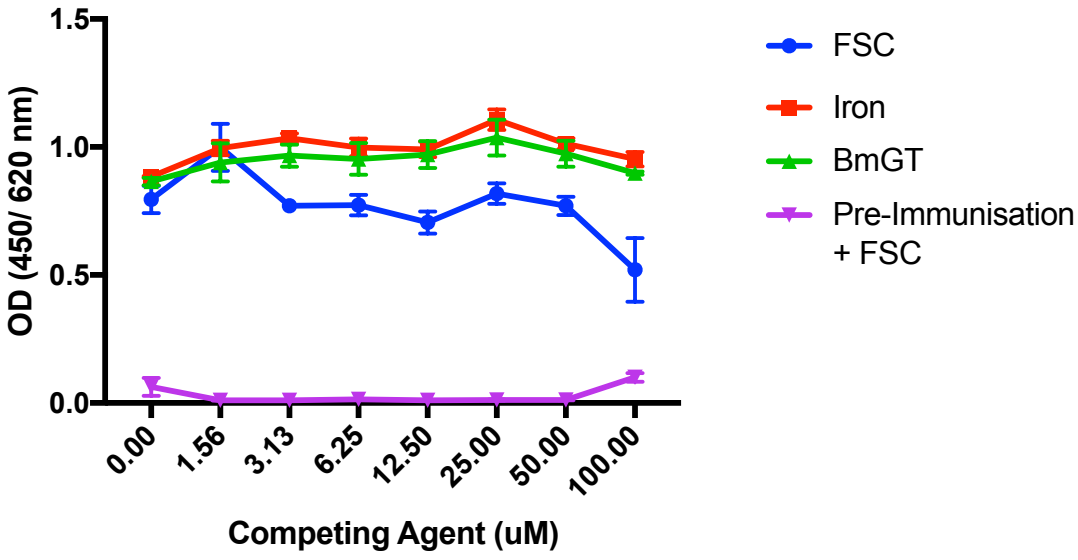

Figure 5.13 Competitive ELISA analysis to establish specificity of anti-FSC polyclonal antibodies. Tail bleeds from mouse D were analysed by competitive ELISA with competitors; FSC, iron, and BmGT. Only addition of competing FSC

resulted in a decreased OD (450/ 620 nm). Pre-immunisation control sera was also analysed and showed no affinity for FSC-BSA coated ELISA plates.

5.2.6 Generation of hybridomas producing anti-FSC antibodies

After immunisations and tail bleed analysis, mouse D was selected for the development of anti-FSC producing hybridomas. A fourth and final booster of the FSC-KLH immunogen (50 μg) (Section 5.2.1.3) was mixed with adjuvant, Pam3Cys in a final volume of 100 μl and intraperitoneally administered to BALB/c mice 3 days prior to the fusion. The mouse was sacrificed and spleen removed. Splenocytes were fused with SP2/0 myeloma cells as per Section 2.2.9.2 (Köhler and Milstein, 1975). This fusion was carried out by Dr Andrew McCann, NICB, DCU.

5.2.6.1 Fusion efficiency

Following the fusion of the spleen from mouse D with SP/2/O-Ag 14 myeloma cells, as per Section 2.2.8.2, a 78.6% fusion efficiency was observed with 338 out of 430 wells of 48 well plates showing hybridoma generation.

5.2.6.2 Screening of hybridomas following fusion

Screening of hybridomas was carried out in two stages; indirect ELISA, and then by competitive ELISA (Section 5.2.4; Figure 5.10). In the first stage, the hybridoma supernatant was screened by indirect ELISA against plates coated with high concentrations (0.5 μg/ ml) of FSC-BSA versus SATA-BSA to crudely identify antibodies with specificity for FSC and not the crosslinker, SATA. Hybridomas with a relatively high affinity for FSC-BSA and limited or no affinity for SATA-BSA were regarded as positive. In total, 316 hybridoma supernatants were screened this way and 60 hybridomas were transferred to 6 well plates for further subculturing and screening (Appendices, Supplementary Table 15). Figure 5.14 shows the OD (450/ 620 nm) readings obtained from this screen for hybridomas that were ultimately selected and carried forward; 2B6, 5C2, 7D8, and 5B7.

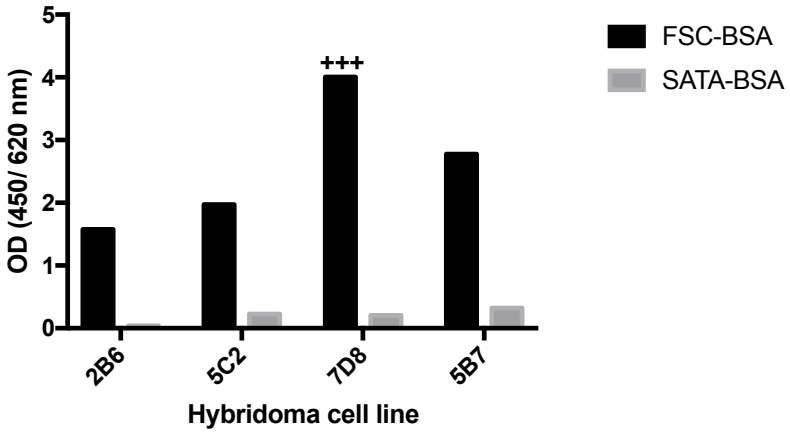

Figure 5.14 Indirect ELISA screening of supernatant from hybridomas 2B6, 5C2, 7D8, and 5B7. Hybridoma supernatant was screened using ELISA plates coated with FSC-BSA or SATA-BSA. Hybridomas with supernatant showing a relatively high affinity for FSC-BSA and limited or no affinity for SATA-BSA were regarded as positive and moved to 6 well plates. The OD (450/ 620 nm) for supernatant collected from hybridoma 7D8 was too high for the spectrophotometer to read and is instead represented by the max. OD of 4 with "+++".

Any hybridomas positively identified from first screening stage were sub-cultured according to Section 2.2.8.4. Subsequently, hybridoma supernatants were screened by competitive ELISA (n = 1) using the coating conditions optimised for tail bleed screening (Section 5.2.5.1) with or without free competing FSC (at 100 μM only). Figure 5.15 shows the OD (450/ 620 nm) readings obtained from this screen for hybridomas 2B6, 5C2, 7D8, and 5B7 (Appendices, Supplementary Table 16). All hybridoma supernatants exhibited some degree of competition for free FSC whereby signal (OD 450/ 620 nm) was reduced upon the addition of FSC (100 μM). The signal for hybridoma 7D8 was still very high suggesting high levels of antibody production. Though competing FSC only reduced the signal by 11% for 7D8, this may have

resulted from excessive levels of antibody. Hybridomas, 2B6, 5C2, 7D8, and 5B7 were all subjected to cloning by limiting dilution (Section 2.2.9.5).

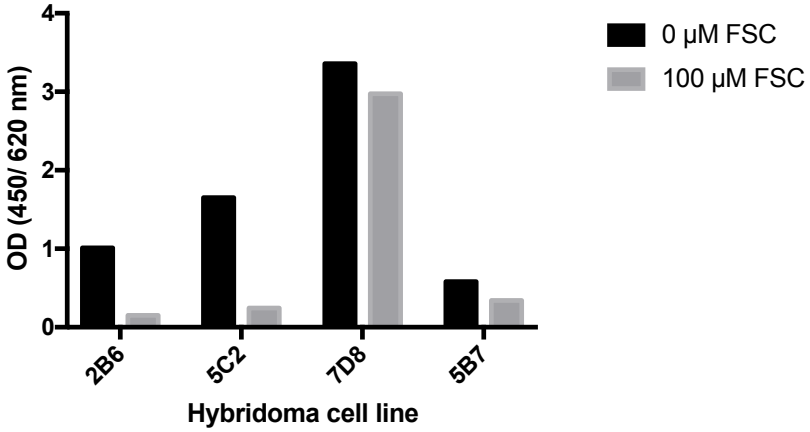

Figure 5.15 Competitive ELISA screening of supernatant from hybridomas 2B6, 5C2, 7D8, and 5B7. Hybridoma supernatant was screened by competitive FSC ELISA, by addition to ELISA plates wells with and without 100 µM FSC. All hybridomas showed some degree of competition for free FSC.

Following the cloning of 2B6, 5C2, 7D8, and 5B7, supernatant of clones and cognate parents were screened by competitive ELISA. Six monoclonal hybridomas were screened in total. Only one retained production of anti-FSC antibodies, which was cloned from the 7D8 parent hybridoma (Figure 5.16) (Appendices, Supplementary Table 17). Despite repeated efforts, we were unable to isolate an additional monoclonal anti-FSC antibody producing hybridoma. Thus, the monoclonal hybridoma of 7D8 (7D8-C) was sub-cultured for antibody purification and characterisation.

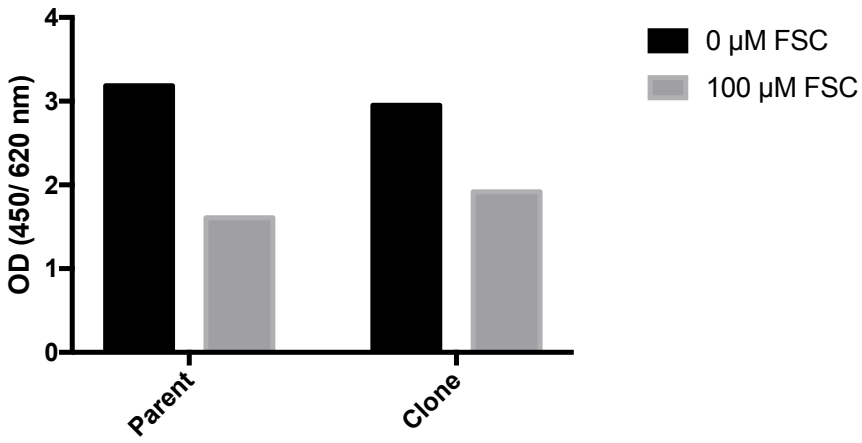

Figure 5.16 Competitive ELISA screening of 7D8 hybridoma cloning. Supernatant from the 7D8 clone and cognate parent (mean of 5 culture flasks) were screened by competitive FSC ELISA. This clone retained the anti-FSC antibody production associated with the parent.

5.2.7 The 7D8-C hybridoma produces competitive anti-FSC IgM

The 7D8-C hybridoma was maintained as described in Section 2.2.2 with growth in Hybridoma Culture Medium (Section 2.1.2.4). Any culture supernatant was retained for characterisation or antibody purification. Antibody isotyping analysis was carried out using the Isostrip™ Mouse Monoclonal Antibody Isotyping Kit (Roche) (Section 2.2.9.6) and indicated 7D8-C hybridoma to be producing IgM antibodies with a κ light chain (Figure 5.17). Analysis of culture supernatant by competitive FSC ELISA indicated the hybridoma produced competitive anti-FSC antibodies whereby supernatant showed decreasing OD (450/ 620 nm) with increasing competing FSC concentration (Figure 5.18) (Appendices, Supplementary Table 18).

Figure 5.17 Isostrip analysis of 7D8-C hybridoma supernatant indicated it produces an IgM heavy chain and κ light chain.

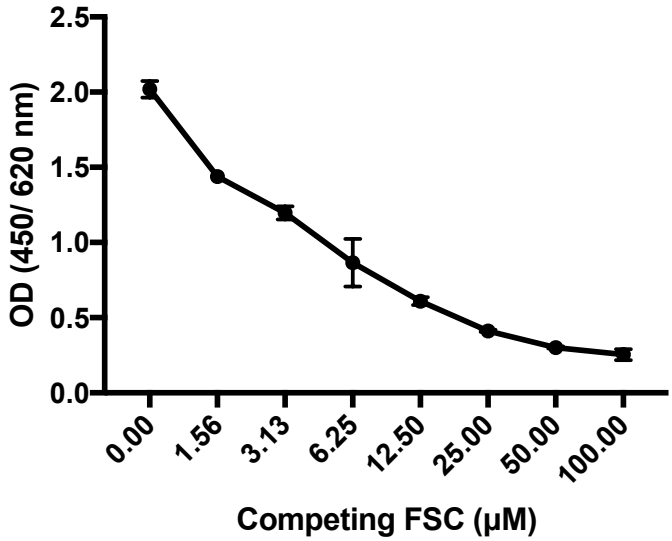

Figure 5.18 Competitive FSC ELISA analysis of 7D8-C hybridoma supernatant. Culture supernatant from 7D8-C was analysed by competitive FSC ELISA. Supernatant showed decreasing OD (450/ 620 nm) with increasing competing FSC concentration (mean $OD_{450/620}$ 2.02 at 0 μM FSC and 0.25 at 100 μM FSC).

5.2.8 Purification of anti-FSC IgM

Supernatant was collected from hybridoma 7D8-C and IgM was collected by ammonium sulphate precipitation as per Section 2.2.11.1. Supernatant before and after ammonium sulphate precipitation were analysed by competitive FSC ELISA (*n* = 2) and indicated successful complete collection of anti-FSC antibody (Figure 5.19) (Appendices, Supplementary Table 19). Purified IgM was also analysed by reducing SDS-PAGE in which heavy, light, and J chains were visible (Figure 5.20).

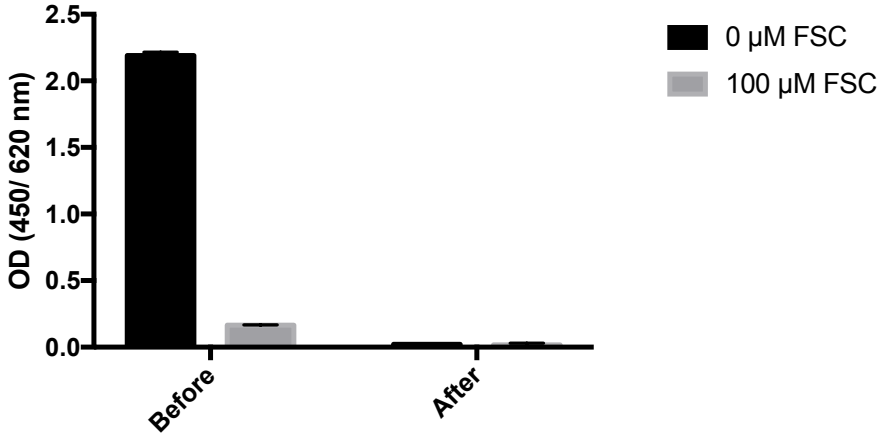

Figure 5.19 Competitive FSC ELISA analysis of 7D8-C hybridoma supernatant before and after ammonium sulphate precipitation shows anti-FSC antibody activity before but not after purification. This indicates successful purification of the anti-FSC antibody from hybridoma supernatant.

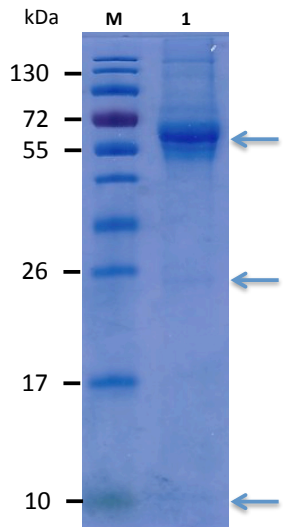

Figure 5.20 IgM was analysed by SDS-PAGE after ammonium sulphate precipitation from hybridoma supernatant. M: Molecular mass ladder. 1: Anti-FSC IgM. Arrows indicate positions of heavy, light, and J chains respectively.

5.2.9 Development of a competitive FSC ELISA with purified anti-FSC IgM

Purified IgM (n = 2) was analysed to determine the optimal concentration of IgM for ELISA analysis. IgM (3.9 – 2000 μg/ ml) was added to ELISA plates coated with 0.09 μg/ ml FSC-BSA (as previously used in hybridoma and tail bleed screening for competitive ELISA) (Figure 5.21) (Appendices, Supplementary Table 20). A concentration of 500 μg/ ml was selected for further ELISA analysis.

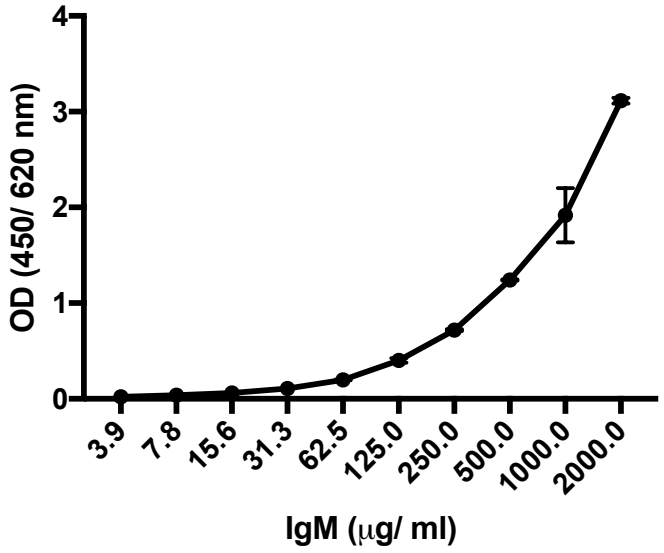

Figure 5.21 Optimisation of IgM concentration for competitive FSC ELISA analysis. IgM was titred (3.9 – 2000 μg/ ml) and added to FSC-BSA coated ELISA plates to determine the optimal concentration of IgM to use for further ELISA analysis. A concentration of 500 μg/ ml was selected for all further ELISA analysis.

Using the optimised IgM concentration (500 µg/ ml) along with the previously optimised coating conditions, anti-FSC IgM was subjected to further characterisation. To establish the extent of its specificity for FSC, the IgM was screened by competitive FSC ELISA using FSC along with several other competitors (TAFC, BmGT, ferrichrome, and ferri-ornibactin). The IgM exhibited high specificity for FSC, showing competition for FSC, but not the other metabolites (Figure 5.22) (Appendices, Supplementary Table 21).

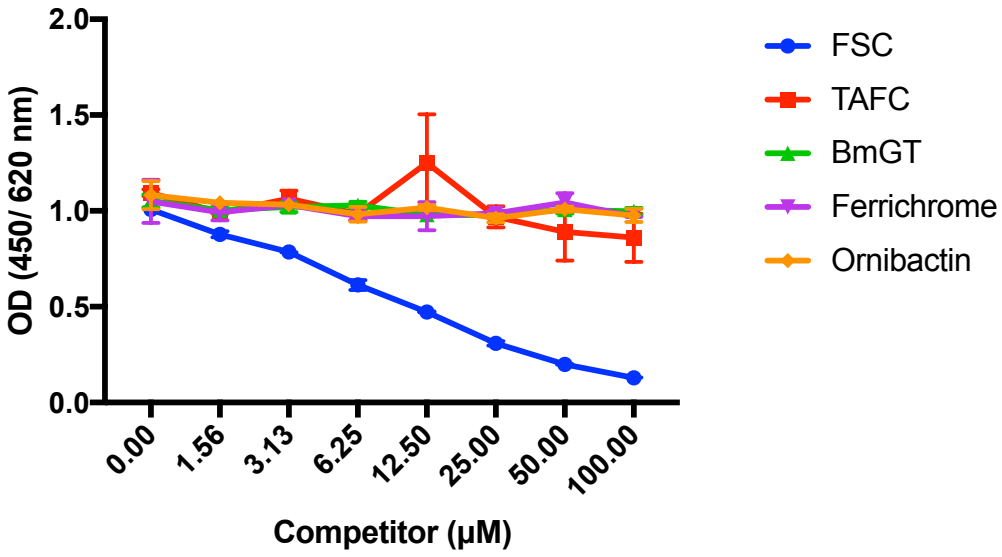

Figure 5.22 Competitive ELISA analysis indicates high specificity for FSC. Purified IgM was analysed by competitive ELISA with a titre (1.56 – 100 µM) of several competitors: ferri-fusarinine C (FSC), ferri-triacetylfusarinine C (TAFC), BmGT, ferrichrome, and ferri-ornibactin on FSC-BSA coated ELISA plates. IgM shows competition with FSC (mean $OD_{450/620}$ 1.01 at 0 µM FSC and 0.13 at 100 µM FSC), but not other metabolites.

Competitive FSC ELISA analysis indicated the antibody was capable of detecting concentrations of FSC as low as 1.56 µM (Figures 5.22). The IgM was also screened against supernatant from *A. fumigatus* Δ*sidG* grown for 72 h in iron-deplete MM as a competitor. The fungal supernatant was ferrated in excess (similar to Section 2.2.4.2) and quantified as per Section 2.2.3.1 and added to the ELISA as a competitor alongside RP-HPLC purified FSC. Anti-FSC IgM showed similar competition for RP-HPLC purified FSC as ferrated Δ*sidG* supernatant at equivalent concentrations (Figure 5.23) (Appendices, Supplementary Table 22).

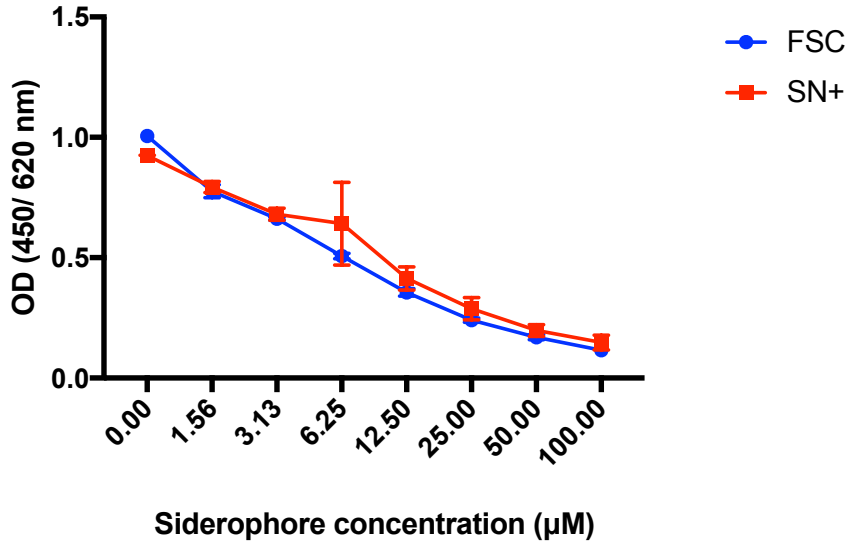

Figure 5.23 Competitive FSC ELISA analysis using purified anti-FSC IgM. IgM purified from 7D8-C culture supernatant was analysed by competitive FSC ELISA using RP-HPLC purified FSC (FSC) and ferrated *A. fumigatus* Δ*sidG* supernatant (SN+). IgM showed decreasing OD (450/ 620 nm) with increasing competing FSC concentration from (i) FSC (mean $OD_{450/620}$ 1.01 at 0 µM FSC and 0.12 at 100 µM FSC) and (ii) SN+ (mean $OD_{450/620}$ 0.925 at 0 µM FSC and 0.15 at 100 µM FSC).

5.2.10 *In vitro* assessment of growth inhibitory potential of anti-FSC IgM

To investigate the effect of anti-FSC IgM on the growth of *A. fumigatus*, an assay strategy was devised using *A. fumigatus* Δ*sidD* (Schrettl *et al.*, 2007). *A. fumigatus* Δ*sidD* is a gene deletion strain for the NRPS, SidD, and is incapable of producing extracellular siderophores FSC and TAFC (Figure 1.4). Absence of the production of extracellular siderophores was confirmed with spectrophotometric (440 nm) analysis of culture supernatants (data not shown). First, a growth assay was established whereby the application of exogenous FSC^{+Fe} restored growth of *A. fumigatus* Δ*sidD*. *A. fumigatus* Δ*sidD* was streaked onto MM agar without iron (supplemented with iron chelators, BPS; ensuring only siderophore-mediated iron uptake was utilised) to which sterile assay discs were added. Subsequently, a titre of FSC^{+Fe} amounts (5 – 100 pmol) was added to each disc (n = 2) (FSC^{+Fe} was extracted as described in Section 2.2.4.2). Plates were grown at 37 °C for 48 h. Exogenous FSC^{+Fe} was found to visibly restore the growth of Δ*sidD* at 20, 50, and 100 pmol per disc (Figure 5.24).

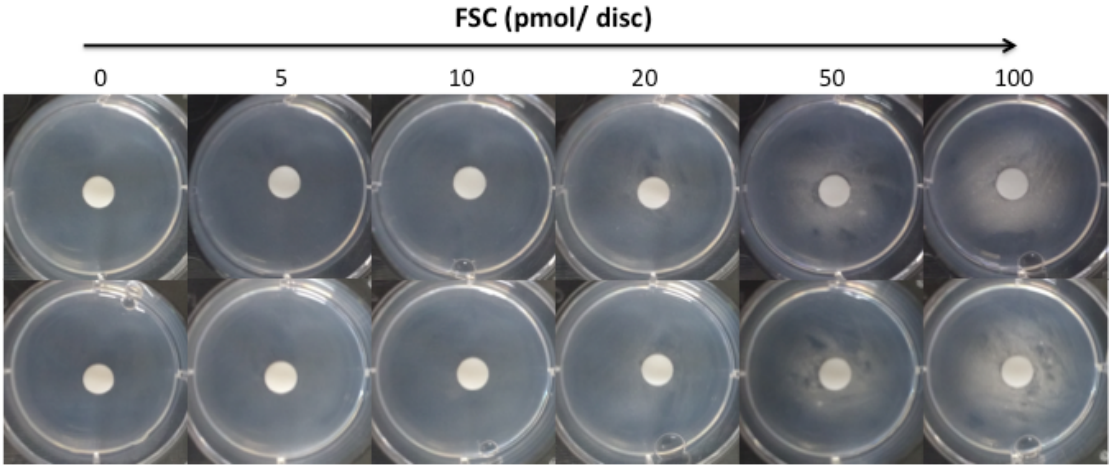

Figure 5.24 A growth assay was established using *A. fumigatus* Δ*sidD* streaked on MM without iron. Discs supplemented with a titre of FSC amounts (5 – 100 pmol/ disc) were subsequently added and plates were incubated at 37 °C for 48 h.

Exogenous supplementation of FSC^{+Fe} (20, 50, and 100 pmol) was found to restore growth of *A. fumigatus* Δ*sidD* at 48 h.

Next, the effect of anti-FSC IgM on FSC^{+Fe}-mediated growth restoration was investigated. Prior to addition to discs, FSC^{+Fe} was pre-incubated with (i) PBS, (ii) anti-FSC IgM, or (iii) GST-GtmA fusion protein (at an equivalent protein concentration to the IgM as a negative control) ($n = 3$). Plates were grown at 37 °C for 48 h or 96 h. Anti-FSC IgM showed visible inhibition of FSC-mediated growth restoration of *A. fumigatus* Δ*sidD* at a ratio of 50 pmol IgM/ 20 pmol FSC per disc after 96 h of growth (Figure 5.25). As this assay was only qualitative in nature and quantitative analysis was not possible, the reduction in growth was verified by the blind observations of two other individuals.

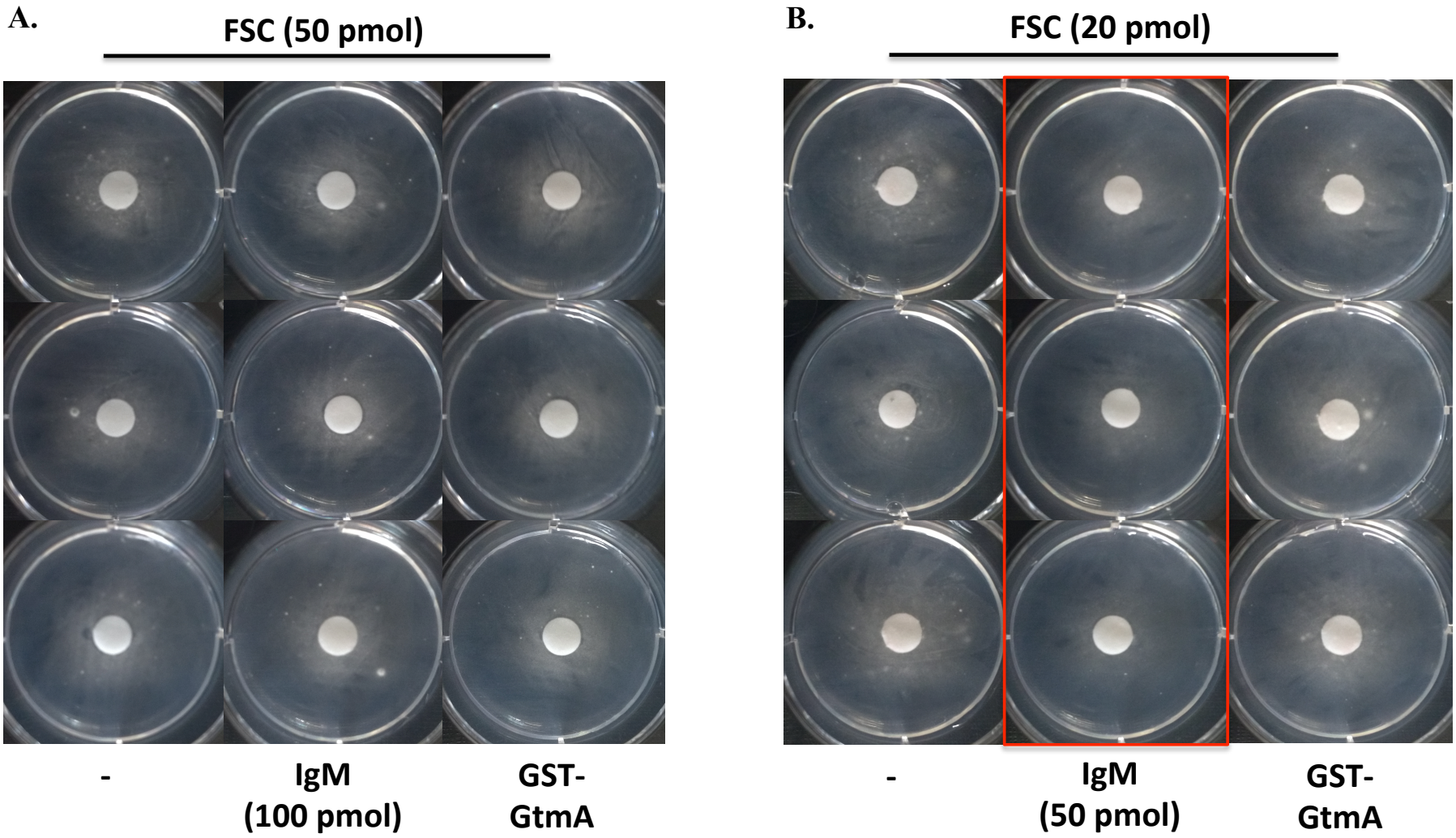
A.
FSC (50 pmol)
-
IgM
(100 pmol)
GST-
GtmA
B.
FSC (20 pmol)
-
IgM
(50 pmol)
GST-
GtmA

Figure 5.25 A growth assay was established using *A. fumigatus* Δ*sidD* grown on MM without iron with discs supplemented with (i) FSC only, (ii) FSC mixed with anti-FSC IgM, or (iii) FSC mixed with GST-GtmA (at an equivalent protein concentration to the IgM). Plates were subsequently grown for (A) 48 h, or (B) 96 h. Anti-FSC IgM inhibits FSC-mediated growth restoration of *A. fumigatus* Δ*sidD* at a ratio of 50 pmol IgM/ 20 pmol FSC per disc after 96 h of growth (highlighted in red).

5.3 Discussion

There is a need to develop novel diagnostic and therapeutic strategies against *A. fumigatus* and siderophores show promise for the basis of such strategies. To this end antibodies were raised against one of the siderophores excreted by *A. fumigatus*, FSC^{+Fe}. To generate a FSC immunogen suitable for immunisations, FSC was conjugated to KLH *via* heterobifunctional crosslinkers, Sulfo-SMCC and SATA, respectively (Section 5.2.1). Generation of FSC-$(SMCC)_1$ was confirmed by RP-HPLC analysis. The peak associated with FSC-$(SMCC)_1$ was identified by LC-MS/MS with detection of a doubly charged ion (M: 998.4, $[M+2H]^{2+}$: observed *m/z* 500.1; expected *m/z* 500.2). After deprotection, thiol incorporation in SATA-KLH was estimated at 92 μmoles per μmole KLH. Successful conjugation of FSC-SMCC to SATA-KLH was measured by quantifying the incorporation of FSC using the λ_{max} of ferri-siderophores (440 nm), with an estimated 338 nmol FSC^{+Fe} per mg KLH (Section 5.2.1.3). The FSC-KLH immunogen was then used to immunise BALB/c mice ($n = 3$).

Tail bleeds were taken from the immunised mice ($n = 2$) and a strategy was developed to screen for polyclonal anti-FSC antibodies. Because generating antibodies with competitive anti-FSC activity was an objective of this work, a competitive FSC ELISA format was developed for screening the murine sera (Section 5.2.3). By screening the mice at this stage, it was possible to select the best mouse possessing antibodies with competitive anti-FSC activity with which to proceed to hybridoma generation. The principle of this ELISA is illustrated in Figure 5.8. It is typically more suitable for small molecules to be coated to ELISA plates *via* a carrier protein so that the molecule's epitopes are accessible to the probing antibody (Daven, 2009). Hence, FSC^{+Fe} was conjugated to BSA *via* Sulfo-SMCC and SATA

modification, respectively, for coating ELISA plates (Section 5.2.3.2). As the same crosslinkers for the immunogen were used to generate this conjugate, another advantage of using the competitive ELISA format was that antibodies reactive against the crosslinkers would not be selected. Such antibodies would bind the FSC-BSA on the plate, but would not show competition for FSC. Successful conjugation of FSC-SMCC to SATA-BSA was measured by quantifying the incorporation of FSC using the λ_{max} of ferri-siderophores (440 nm), with an estimated 221 nmol FSC^{+Fe} per mg BSA (Section 5.2.3.2). FSC-BSA was then coated onto wells of an ELISA plate in a titre of concentrations (0.02 – 1.36 μg/ ml) and probed with murine sera to identify to optimal coating conditions (Section 5.2.5.1). A coating concentration of 0.09 μg/ ml was selected for further analysis. This was used in the competitive FSC ELISA with the inclusion of titre of competing FSC (100 – 1.56 μM). Using this format, sera from mouse D showed competitive anti-FSC activity (Section 5.2.5.2). Furthermore, when the serum was screened with the competing FSC exchanged for free iron or *A. fumigatus* metabolite, BmGT, competition was not observed. This indicated that the polyclonal antibodies in mouse D were not non-specifically competing with FSC. Furthermore, tail bleeds taken from a FSC-KLH immunised mouse prior to immunisation showed no affinity for FSC-BSA on the plate.

Mouse D was selected for sacrifice and splenectomy to develop hybridomas. A fusion efficiency of 78.6% was observed and resultant hybridomas were screened for anti-FSC antibody production. Screening was conducted in two stages (Section 5.2.4). First, the hybridoma supernatant was screened using an indirect ELISA without a competitor using plates coated with a high concentration of FSC-BSA (0.5 μg/ ml) so that any low level of anti-FSC antibody production could be detected. The supernatant was also screened on plates coated with SATA-BSA (0.5 μg/ ml) as a

negative control, to identify antibodies reactive against SATA or BSA. In total, 316 hybridoma supernatants were screened this way and 60 hybridomas were selected for further sub-culture. Second, the hybridoma supernatant was screened using the competitive FSC ELISA, as optimised for the tail bleed analysis. Four hybridomas were carried forward from this work, 2B6, 5C2, 7D8, and 5B7. One of these parent hybridomas was successfully cloned to establish a stable monoclonal antibody producing hybridoma, 7D8-C (Section 5.2.6.2).

The 7D8-C hybridoma was further sub-cultured and any supernatant collected. Isostrip (Roche) analysis indicated it was an IgM with a κ light chain (Figure 5.17). Further competitive ELISA analysis of the supernatant indicated the antibody could detect FSC at as low as 1.56 μM (Figure 5.18). The anti-FSC IgM was purified from culture supernatant by ammonium sulphate precipitation and analysed by SDS-PAGE (Figures 5.19 and 5.20). The use of this IgM in a competitive FSC ELISA was established. After assay optimisation, ELISA analysis again indicated the antibody could detect FSC at as low as 1.56 μM (Figure 5.22). Exchange of the FSC competitor for other microbial siderophores (ferrichrome or ornibactin) or BmGT at equivalent concentrations resulted in no competition (Figure 5.22). Hence, the antibody was highly specific for FSC^{+Fe}. Interestingly, there was no competition for $TAFC^{+Fe}$ suggesting the epitope against which the antibody is directed is not the iron-binding region. Moreover, it suggests that the acetylation of the amine groups in TAFC is pertinent to siderophore antigenicity. To validate the ability of the ELISA to detect FSC in biological samples, ferrated supernatant from iron-deplete culture of *A. fumigatus* Δ*sidG* was added to the assay in parallel with RP-HPLC purified FSC^{+Fe} at an equivalent concentration. *A. fumigatus* Δ*sidG* cannot produce TAFC and produces FSC at high levels during iron-deplete growth (Schrettl *et al.*, 2007). The anti-FSC

IgM was able to detect FSC in *A. fumigatus* Δ*sidG* culture supernatant at comparable levels to RP-HPLC purified FSC^{+Fe} (Figure 5.23).

To investigate the ability of anti-FSC IgM to impede the uptake of FSC, an *in vitro* bioassay was developed using *A. fumigatus* Δ*sidD* (Schrettl *et al.*, 2007). *A. fumigatus* Δ*sidD* is deficient in the NRPS, SidD, and is therefore unable to produce either extracellular siderophore (FSC or TAFC). First, *A. fumigatus* Δ*sidD* was grown on MM agar without iron (with BPS) with discs supplemented with a titre of FSC^{+Fe} amounts (5 – 100 pmol/ disc). This demonstrated a concentration-dependent restoration of growth upon the addition of FSC^{+Fe}. Growth was visibly restored around the discs at 20, 50, and 100 pmol/ disc (Figure 5.24). After trialling several conditions, it was demonstrated that pre-incubation of FSC^{+Fe} with anti-FSC IgM (at 20 pmol FSC + 50 pmol IgM per disc) did not restore growth after 96 h; whereas when FSC^{+Fe} was similarly pre-incubated PBS or GST-GtmA (fusion protein) growth was restored (Figure 5.25). This indicates that anti-FSC IgM is capable of impeding the uptake of FSC^{+Fe} to *A. fumigatus* Δ*sidD* and in doing so is able to inhibit FSC-mediated growth restoration.

Targeting the biosynthesis or uptake of siderophores has long been considered a viable antimicrobial strategy in *A. fumigatus*. While there is evidence for its validity in the reduced virulence of strains deficient in siderophore biosynthesis (Schrettl *et al.*, 2007), evidence for an effective therapeutic approach directly targeting siderophores is lacking. One promising avenue, for this antimicrobial approach, comes in the form of a human protein, Lcn1. In a bioassay similar to that of Section 5.2.10, growth of a strain of *A. nidulans* deficient in siderophore biosynthesis was restored by supplementation with TAFC. However, when the TAFC was pre-incubated with Lcn1, it failed to restore growth (Fluckinger *et al.*, 2004). This

suggests an Lcn1-mediated inhibition of siderophore uptake, similar to that observed for anti-FSC IgM. However, the inhibition of siderophore-mediated iron uptake by anti-FSC IgM was demonstrated in a strain with intracellular siderophore biosynthesis intact. Hence, it specifically indicates the targeting of extracellular siderophores. Importantly, topical application of recombinant Lcn1 was effective in reducing *A. fumigatus* corneal infection in a murine model (Leal *et al.*, 2013). Hence, proteinaceous targeting of siderophore uptake represents a plausible anti-fungal target *in vivo*.

This work has demonstrated the generation of anti-siderophore antibodies against *A. fumigatus* extracellular siderophore, FSC. Following purification, antibody characterisation indicated the antibody was a highly specific anti-FSC IgM capable of detecting FSC at concentrations as low as 1.56 μM. Furthermore, anti-FSC IgM has demonstrated the use of anti-siderophore antibodies in impeding siderophore uptake in *A. fumigatus.*

Chapter 6

Development and characterisation of an anti-TAFC IgG

Chapter 6 Development and characterisation of an anti-TAFC IgG

6.1 Introduction

A. fumigatus excretes two extracellular siderophores, FSC and TAFC. Chapter 5 focused on the results associated with the synthesis of a FSC immunogen as well as development and characterisation of an anti-FSC IgM. This chapter focuses on the same strategy, but against TAFC. TAFC is produced at much higher amounts by *A. fumigatus* during iron-deplete growth (Moloney *et al.*, 2016a; Schrettl *et al.*, 2007). Moreover, it was TAFC that was detected in mammalian host samples using MS (Carroll *et al.*, 2016; Luptáková *et al.*, 2017). Carroll *et al.* (2016) detected TAFC in sera from patients with suspected, or probable/ proven Aspergillosis, while Luptáková *et al.* (2017) detected TAFC in the urine of a rat model of Aspergillosis. TAFC was also implemented in a PET-based imaging strategy of *A. fumigatus* infection whereby uptake of ^{68}Ga-TAFC was demonstrated *in vivo* to localise to infected tissue in a rat model of Aspergillosis (Haas *et al.*, 2015; Petrik *et al.*, 2010b, 2012, 2017). Hence, much of the work demonstrating the role of siderophores in *A. fumigatus* infection was carried out in respect to TAFC. In addition, TAFC is more stable than FSC, which is likely to improve its recovery from biological samples (Renshaw *et al.*, 2002). TAFC, therefore, represents the more promising of the two extracellular siderophores, particularly for the basis of a diagnostic strategy.

Due to the nature of hybridoma generation, whereby murine splenocytes are fused to myeloma cells generating a single cell with multiple nuclei, there is an inherent instability in hybridomas. Hence, when a hybridoma producing an antibody with clinical application is isolated, it is often prudent to promptly obtain the antibody sequence. This preserves the antibody by permitting long-term storage and large-scale

production in a suitable vector system. Antibody sequencing can be achieved through several routes using genomic and proteomic approaches (Georgiou *et al.*, 2014). To sequence an antibody of known isotype from a monoclonal hybridoma, Sanger sequencing of heavy and light chain sequences is quite effective. This can use isotype-specific degenerate primers to independently amplify the heavy and light chain sequences from hybridoma cDNA. For example, Robinson *et al.* (2015) used degenerate primers for the amplification of IgG_{2a} heavy chain and κ light chain sequences from hybridoma cDNA. They subsequently expressed a humanised full-length version of the antibody in *E. coli* (Robinson *et al.*, 2015). Recently, advances in LC-MS/MS have permitted direct sequencing of the antibody itself. As the antibody sequence is novel, database interrogation cannot be used to obtain the full-length sequence. Instead, *de novo* sequencing of the peptide-derived MS spectra coupled with a database of template antibody sequences can be utilised (Castellana *et al.*, 2011; Guthals *et al.*, 2017; Tran *et al.*, 2016). In doing so, conserved regions can be mapped to the database, while novel sequences of variable domains can be identified with *de novo* sequencing. In this method, the same protein is typically independently digested with several proteolytic enzymes of differing specificity to generate overlapping fragments thereby improving the protein coverage. One shortcoming of *de novo* sequencing is that it is prone to identification errors. Tran *et al.* (2016) recently outlined the ALPS system, which assembles peptides using a weighted de Bruijn graph construction incorporating the *de novo* peptides' area and confidence scores. They demonstrated the use of this system in sequencing both mouse and human antibodies. While these methods are suitable for screening cDNA from monoclonal hybridomas or a homogenous antibody preparation, in order to screen a repertoire of cells or antibodies the methods must be adapted (Georgiou *et*

al., 2014). This area is currently advancing considerably and the high-throughput ability to sequence antibody repertoires is becoming increasingly feasible. For example, targeted repertoire screening can be used, whereby human antibodies can be isolated by immunoaffinity purification of serum using the antigen of interest. MS based sequencing then permits further work including recombinant expression of the antibody for *in vitro* analysis of activity (Guthals *et al.*, 2017).

The objectives of the work presented in this chapter were to:

i. Develop a TAFC immunogen suitable for murine immunisations.

ii. Develop a competitive TAFC ELISA for (A) screening for antibody production in murine sera, (B) screening for antibody production in hybridoma supernatant, and (C) detecting TAFC in culture supernatants.

iii. Generate mAbs directed against TAFC.

iv. Purify and characterise the anti-TAFC antibody.

v. Identify the putative N- and C-terminal residues of the anti-TAFC antibody fragment antibody binding (Fab) region for the basis of a proteogenomic antibody sequencing strategy.

6.2 Results

6.2.1 Development of a TAFC immunogen

6.2.1.1 Strategy for generating TAFC antibodies

A similar strategy to that employed for FSC (Chapter 5) was used to develop the TAFC immunogen. Conjugation of the siderophore to the carrier protein, KLH, was mediated by heterobifunctional crosslinkers, Sulfo-SMCC and SATA, respectively.

As discussed in Chapter 4, TAFC possesses limited functional groups for standard crosslinker modification. However, by acetylating two amine groups using SNA, generating DAFC; a third amine group is still available for further NHS ester modification. This strategy was used to generate a semi-synthetic TAFC analogue suitable for fluorophore derivatisation, generating DAFC-NBD. Despite the amine modifications, uptake of DAFC-NBD was preserved under iron starvation. A similar strategy was utilised to generate the TAFC immunogen in this Chapter, whereby acetylated FSC was conjugated to the carrier protein, KLH. FSC acetylated with SNA generates a heterogeneous mixture of FSC, MAFC, DAFC, and TAFC (collectively termed acetylated FSC). This yields a reaction mixture with three compounds capable of reacting with NHS esters and therefore, carrier protein crosslinking; FSC, MAFC, and DAFC (Figure 4.9). It was decided to not RP-HPLC purify DAFC from this reaction mixture and generate a heterogeneous immunogen predominantly containing MAFC-KLH and DAFC-KLH. In doing so, the immunised mice could potentially raise both FSC and TAFC antibodies. Both antibodies could then later be selected for during hybridoma generation should the FSC antibody development from Chapter 5 be unsuccessful. The strategy for generating the TAFC immunogen is summarised in Figure 6.1.

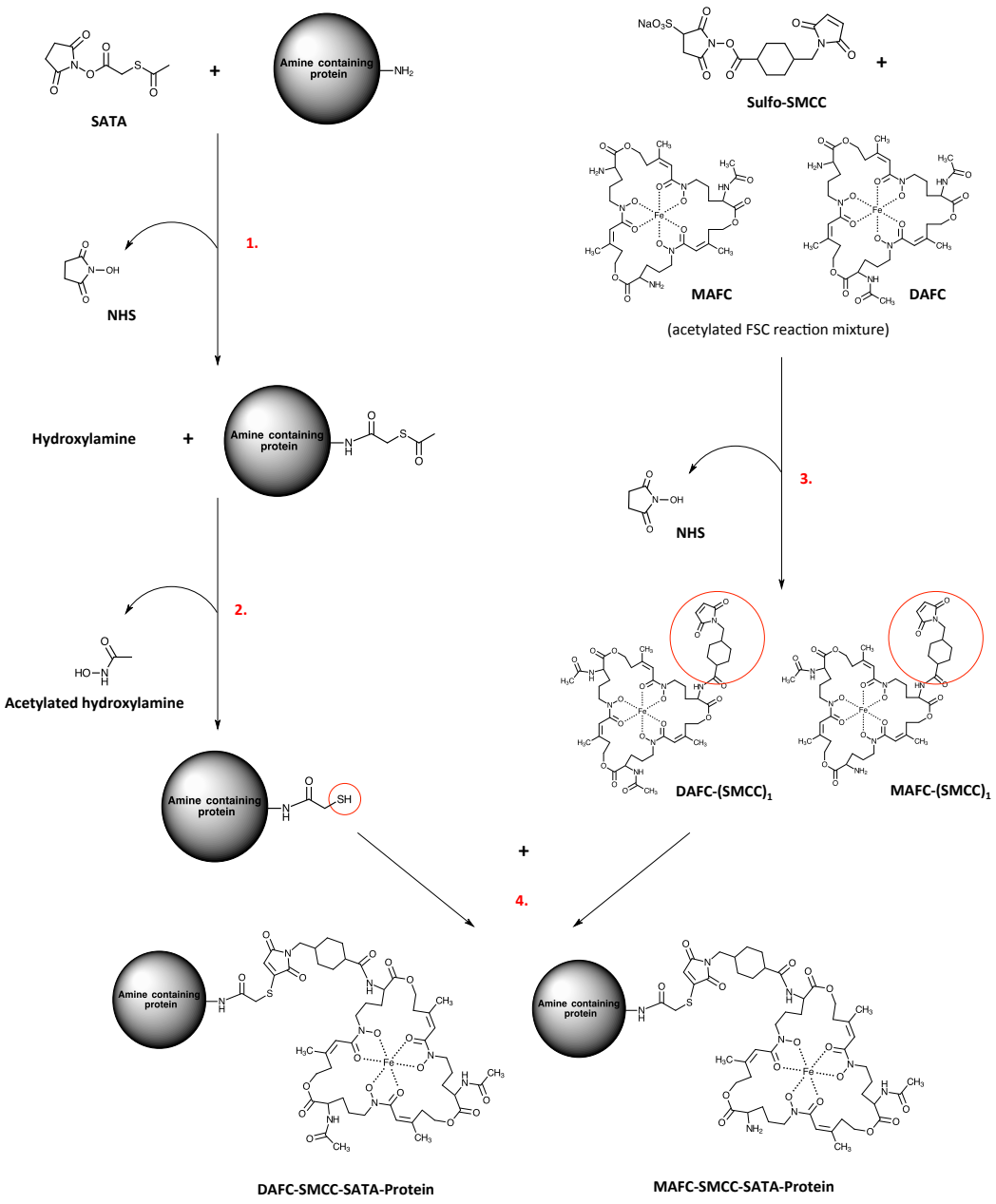

Figure 6.1 Strategy for the development of a TAFC immunogen. **1.** KLH is modified with SATA *via* NHS ester linkage to amine groups, introducing protected thiol groups. **2.** Thiol groups of SATA-KLH are deprotected by hydroxylamine. Excess SATA and hydroxylamine are removed by gel filtration. **3.** Acetylated FSC is modified with Sulfo-SMCC introducing a thiol-reactive maleimide group and generating MAFC-$(SMCC)_1$ and DAFC-$(SMCC)_1$. **4.** When combined, the thiol group of SATA-KLH can form a stable thioether bond with the maleimide group of

MAFC-SMCC or DAFC-SMCC. Excess unconjugated siderophore and crosslinker are then removed by dialysis.

6.2.1.2 Demonstrating modification of acetylated FSC with Sulfo-SMCC

Before proceeding to the conjugation of acetylated FSC to KLH *via* SMCC and SATA, it was first necessary to confirm that Sulfo-SMCC could link to acetylated FSC and introduce the thiol-reactive maleimide group. RP-HPLC purified FSC^{+Fe} was acetylated *via* the sequential addition of SNA with RP-HPLC monitoring until maximal DAFC levels were obtained (similar to Section 2.2.5.3.3) (Figure 6.2). Subsequently, the acetylated FSC^{+Fe} was incubated with a 1.1X molar excess of Sulfo-SMCC relative to the moles of FSC, MAFC, and DAFC present (according to RP-HPLC analysis) to demonstrate the generation MAFC-$(SMCC)_1$ and DAFC-$(SMCC)_1$. All reactions were monitored by RP-HPLC analysis with DAD detection at 440 nm (Figure 6.3) as described in Section 2.2.3.2. The peaks associated with MAFC-$(SMCC)_1$ and DAFC-$(SMCC)_1$ were fraction collected and analysed by LC-MS/MS to confirm their identity (Section 2.2.13.6). Generation of MAFC-$(SMCC)_1$ was confirmed by detection of a doubly charged ion (M: 1040.4, $[M+2H]^{2+}$: observed *m/z* 521.1; expected *m/z* 521.2) (Figure 6.4). Generation of DAFC-$(SMCC)_1$ was confirmed with detection of a singly charged ion (M: 1082.4, $[M+H]^{+}$: observed *m/z* 1083.4; expected *m/z* 1083.4) (Figure 6.5). RP-HPLC analysis indicated 23% of the total siderophore was converted to MAFC-$(SMCC)_1$, 25% to DAFC-$(SMCC)_1$ and 3% to FSC-$(SMCC)_2$ (Figure 6.3).

A.

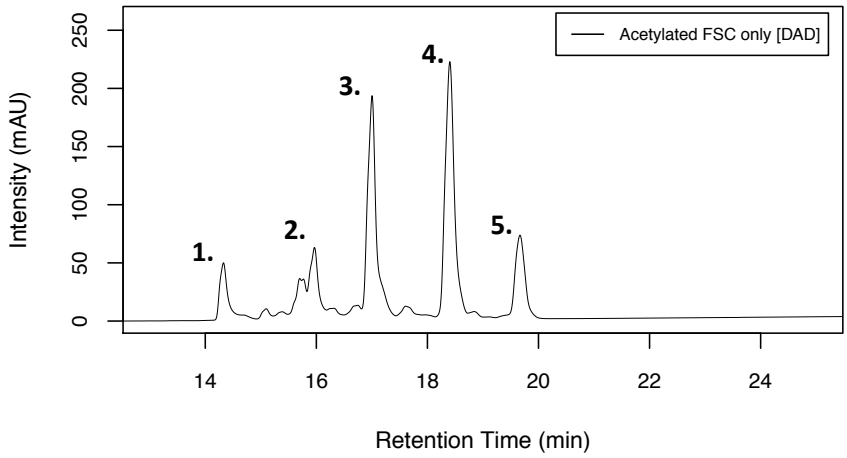

B.

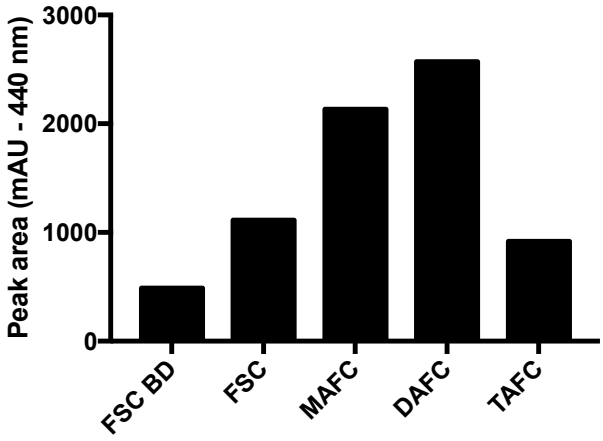

Figure 6.2 (A) RP-HPLC analysis with DAD detection (440 nm) shows the formation of MAFC and DAFC following sequential acetylation of RP-HPLC purified FSC^{+Fe} with SNA (**1.** FSC BD, **2.** FSC, **3.** MAFC, **4.** DAFC, and **5.** TAFC). (B) Graphical representation of the peak area (mAU – 440 nm) associated with all siderophores.

A.

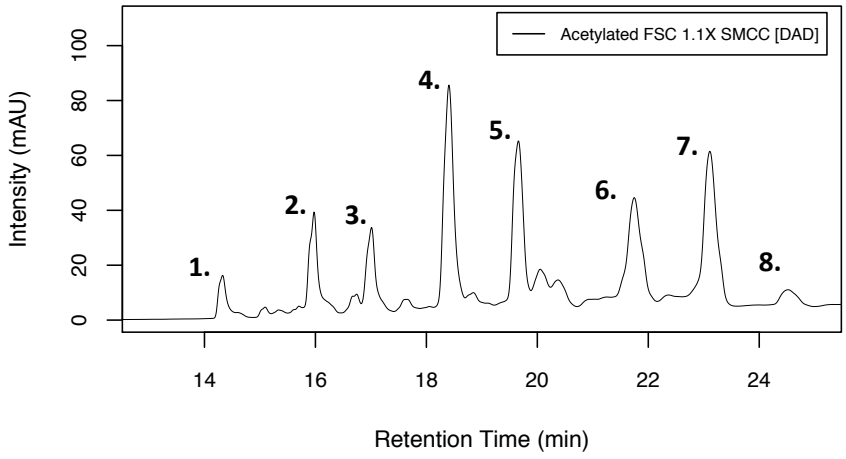

B.

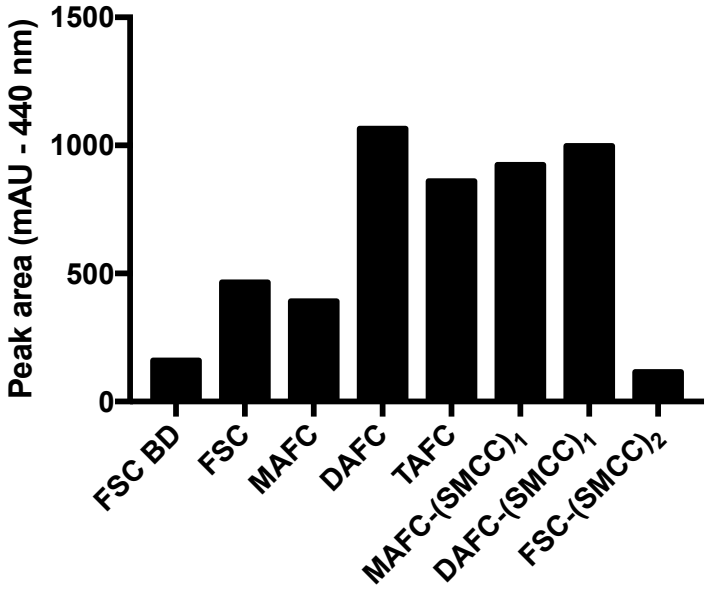

Figure 6.3 (A) RP-HPLC analysis with DAD detection (440 nm) shows the formation of MAFC-$(SMCC)_1$ and DAFC-$(SMCC)_1$ following incubation of acetylated FSC^{+Fe} with Sulfo-SMCC (**1.** FSC BD, **2.** FSC, **3.** MAFC, **4.** DAFC, **5.** TAFC, **6.** MAFC-$(SMCC)_1$, **7.** DAFC-$(SMCC)_1$, and **8.** FSC-$(SMCC)_2$). (B) Graphical representation of the peak area (mAU – 440 nm) associated with all siderophores.

A.

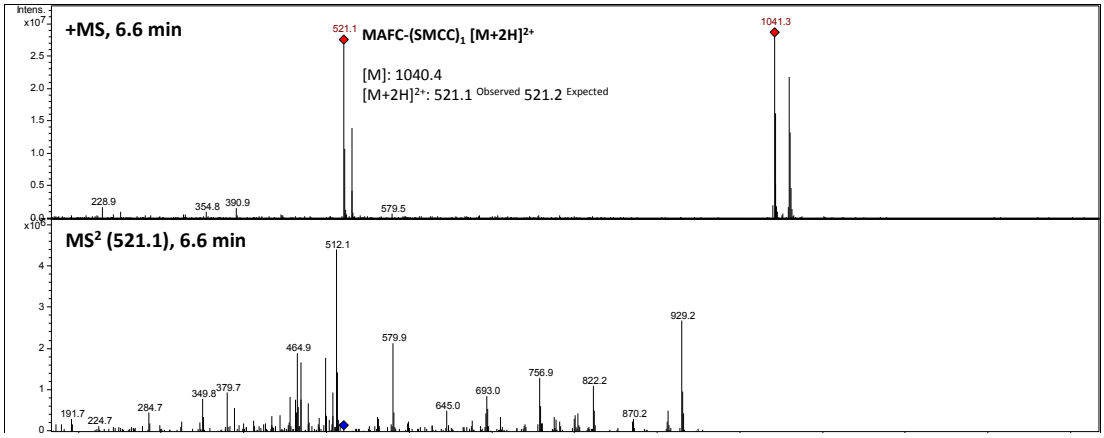

B.

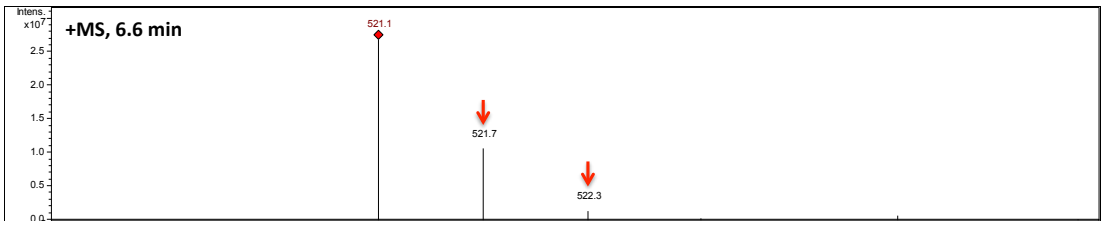

Figure 6.4 LC-MS/MS identification of MAFC-(SMCC)$_1$. Peak associated with MAFC-(SMCC)$_1$ (peak **6.** in Figure 6.3 A) was fraction collected during RP-HPLC analysis and analysed by LC-MS/MS. (A) MS (extracted ion chromatogram for *m/z* 518 – 524) spectrum shows the detection of MAFC-(SMCC)$_1$ as a doubly charged ion (M: 1040.4, $[M+2H]^{2+}$: observed *m/z* 521.1; expected *m/z* 521.2). MS2 spectrum shows the fragmentation of precursor ion. (B) Increments of approx. +0.5 in observed *m/z* are indicative of C_{13} isotope incorporation in a doubly charged ion.

A.

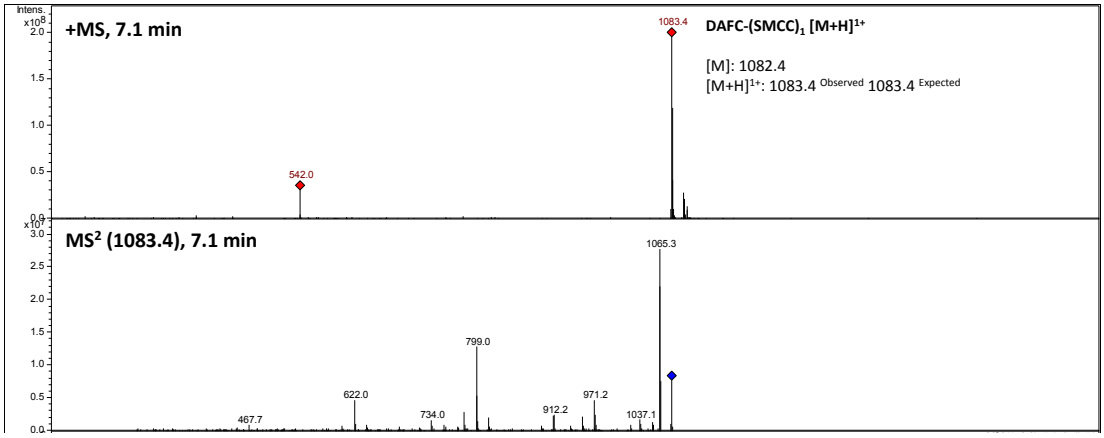

B.

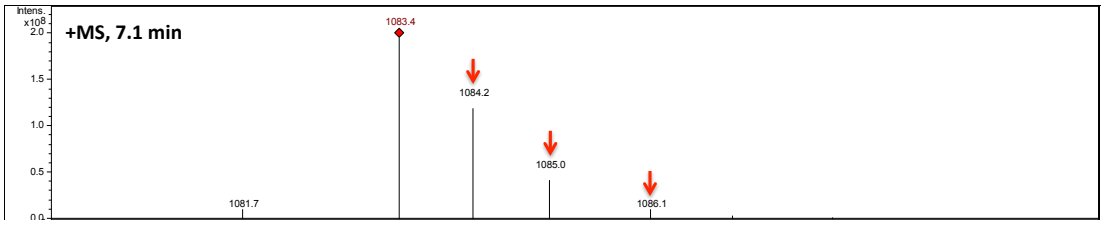

Figure 6.5 LC-MS/MS identification of DAFC-(SMCC)$_1$. Peak associated with DAFC-(SMCC)$_1$ (peak **7.** in Figure 6.3 A) was fraction collected during RP-HPLC analysis and analysed by LC-MS/MS. (A) MS (extracted ion chromatogram for *m/z* 1081 – 1085) spectrum shows the detection of DAFC-(SMCC)$_1$ as a singly charged ion (M: 1082.4, $[M+H]^+$: observed *m/z* 1083.4; expected *m/z* 1083.4). MS2 spectrum shows the fragmentation of precursor ion. (B) Increments of approx. +1.0 in observed *m/z* are indicative of C_{13} isotope incorporation in a singly charged ion.

6.2.1.3 Conjugation of acetylated FSC-SMCC to SATA-KLH

Section 6.2.1.2 demonstrated acetylated FSC activation with Sulfo-SMCC whereby generation of MAFC-$(SMCC)_1$ and DAFC-$(SMCC)_1$ were confirmed by LC-MS/MS and RP-HPLC analysis. Following this, Sulfo-SMCC was deemed appropriate for use in a conjugation strategy to link acetylated FSC to SATA-modified KLH.

FSC^{+Fe} was RP-HPLC purified and acetylated *via* sequential addition of SNA (Section 2.2.5.3.3). This was analysed by RP-HPLC to estimate relative levels of FSC, MAFC, DAFC, and TAFC (Figure 6.6). Subsequently, the acetylated FSC was derivatised by the addition of Sulfo-SMCC equimolar to the moles of FSC, MAFC, and DAFC (Section 2.2.5.3.3). An aliquot of the reaction was quenched and later analysed by RP-HPLC, which indicated that 14% and 10% of the total siderophore was converted to MAFC-$(SMCC)_1$ and DAFC-$(SMCC)_1$, respectively (Figure 6.7). Demasking of SATA-KLH was confirmed by measuring the thiol content of the demasked SATA-KLH before conjugation to be 88 µmoles per µmole KLH (as per Section 2.2.5.4). The acetylated FSC-SMCC reaction mixture was immediately added to demasked SATA-KLH with at least 10X molar excess of MAFC-$(SMCC)_1$ and DAFC-$(SMCC)_1$ each to total thiol groups. The reaction was allowed to proceed at room temperature for 2 h followed by overnight at 4 °C (Section 2.2.5.3.3). For comparative analytical purposes, a small scale of the sample and a negative control (using acetylated FSC^{+Fe} without Sulfo-SMCC modification) were also conducted in parallel.

Similar to the conjugation of FSC-$(SMCC)_1$ to SATA-KLH (Section 5.2.1.2), measurement of the λ_{max} of ferri-siderophores (440 nm) by spectrophotometry was primarily used to determine successful conjugation. Following the conjugation

reaction, the small-scale sample and negative control were purified by PD10 separation and the OD (440 nm) and protein content measured from each fraction to determine the OD/ mg of protein. Fractions from the small-scale sample showed an average OD of 0.22/ mg protein while the negative control showed an OD of 0.09/ mg of protein (Figure 6.8). This indicated successful conjugation whereby without Sulfo-SMCC in the reaction any free unconjugated siderophore was removed following a size exclusion separation. After conjugation, the large-scale conjugation reaction was dialysed against PBS to remove any unconjugated siderophore. The OD (440 nm) and Bradford assay were used to determine the siderophore and protein content to be 181 μM and 1.4 mg/ ml respectively, indicating conjugation of 129 nmol siderophore per mg KLH. Unfortunately, the RP-HPLC column failed during analysis of conjugation at the start of the reaction. Hence, no T0 is available, only RP-HPLC carried out at the end of the conjugation, which is depicted in Figure 6.9. Consequently, RP-HPLC analysis was not a suitable measure for successful conjugation. Similar to FSC-$(SMCC)_1$ conjugation to SATA-KLH, the addition of acetylated FSC-SMCC to SATA-KLH resulted in significant orange precipitation indicative of ferri-siderophore crosslinking to SATA-KLH.

A.

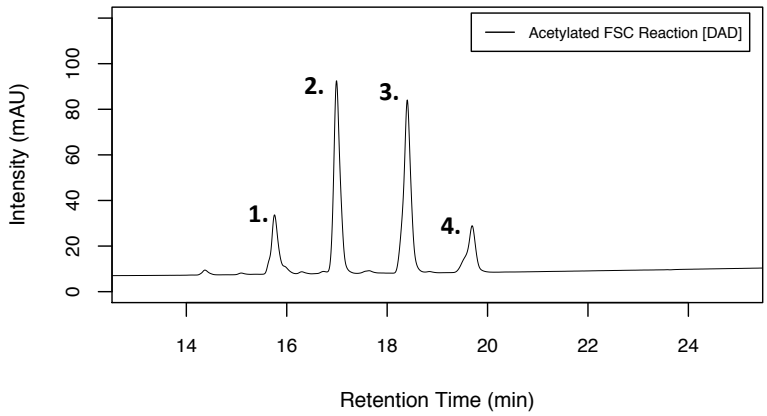

B.

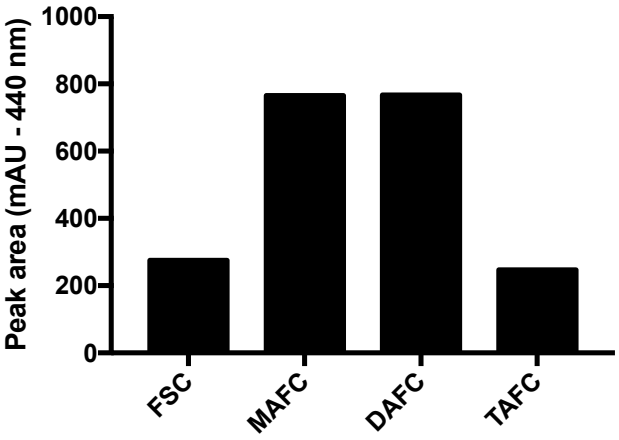

Figure 6.6 (A) RP-HPLC analysis with DAD detection (440 nm) shows the formation of MAFC and DAFC for Sulfo-SMCC derivatisation (**1.** FSC, **2.** MAFC, **3.** DAFC, and **4.** TAFC). (B) Graphical representation of the peak area (mAU – 440 nm) associated with FSC, MAFC, DAFC, and TAFC.

A.

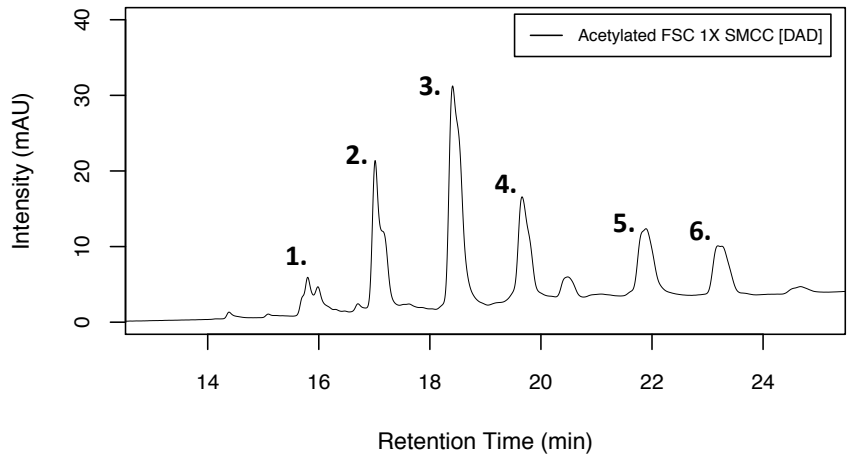

B.

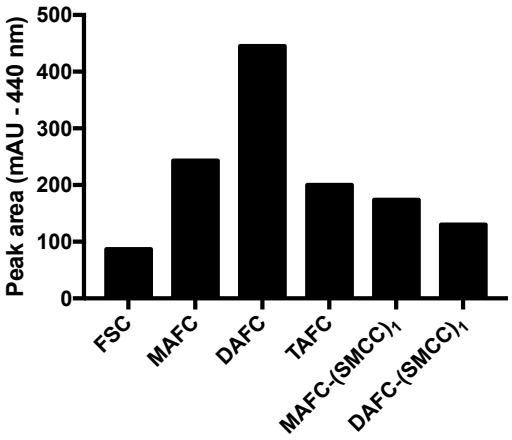

Figure 6.7 (A) RP-HPLC analysis with DAD detection (440 nm) shows the formation of MAFC-$(SMCC)_1$ and DAFC-$(SMCC)_1$ for conjugation to SATA-KLH (**1.** FSC, **2.** MAFC, **3.** DAFC, **4.** TAFC, **5.** MAFC-$(SMCC)_1$, and **6.** DAFC-$(SMCC)_1$). (B) Graphical representation of the peak area (mAU – 440 nm) associated with FSC, MAFC, DAFC, TAFC, FSC-$(SMCC)_1$, MAFC-$(SMCC)_1$ and DAFC-$(SMCC)_1$.

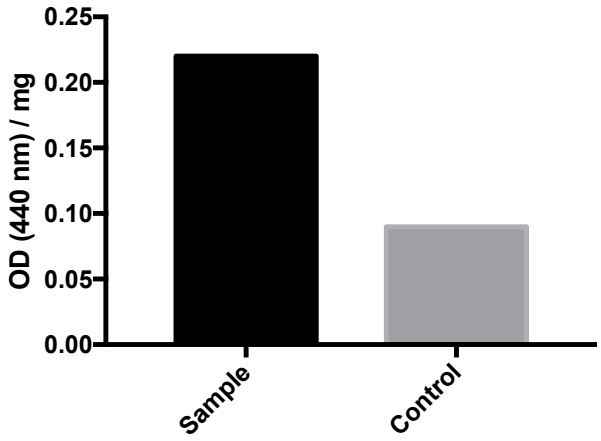

Figure 6.8 A small-scale sample and negative control (omitting Sulfo-SMCC) were also conducted in parallel for comparative analysis to confirm conjugation *via* measurement of the λ_{max} of ferri-siderophores (440 nm). After PD10 separation, the OD/ mg of protein was determined and showed an average OD of 0.22/ mg protein in the small-scale sample and an OD of 0.09/ mg of protein in the control.

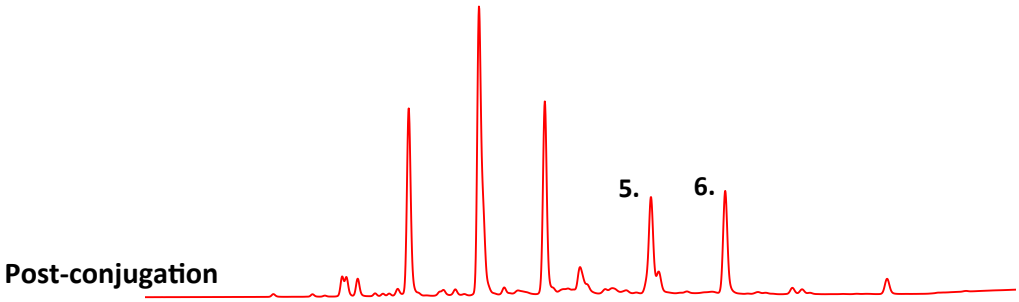

B.

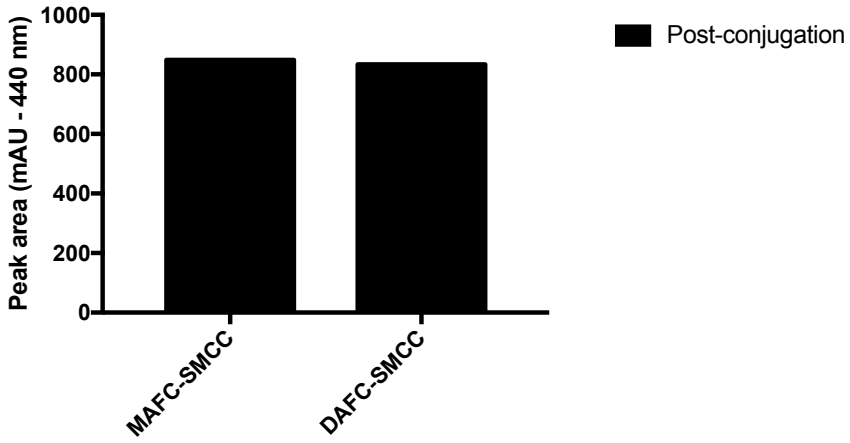

Figure 6.9 (A) RP-HPLC analysis with DAD detection (440 nm) shows the levels of MAFC-$(SMCC)_1$ (Peak **5.**) and DAFC-$(SMCC)_1$ (Peak **6.**) at the end of the conjugation. (B) Graphical representation of the peak areas (mAU – 440 nm) associated with MAFC-$(SMCC)_1$ and DAFC-$(SMCC)_1$ at the end of the conjugation.

6.2.2 Immunisation of mice

The acetylated FSC-KLH immunogen (50 μg soluble and insoluble fractions) (Section 6.2.1.2) was mixed with adjuvant, Pam3Cys in a final volume of 100 μl and intraperitoneally administered to BALB/c mice (n = 3; 6 – 8 weeks old). Mice received three additional boosters of the same composition over 3 week intervals. After the third booster, tail bleeds were taken and sera isolated for polyclonal antibody analysis. A fourth and final booster was administered 3 days prior to the fusion.

6.2.3 Development of an ELISA for the detection of anti-TAFC antibodies

6.2.3.1 Assay principle

The primary basis for screening anti-TAFC antibodies was by either (i) indirect ELISA, or (ii) competitive ELISA using plates coated with acetylated FSC^{+Fe} conjugated to BSA and free competing TAFC. The principle of these assays is described in Figure 6.10.

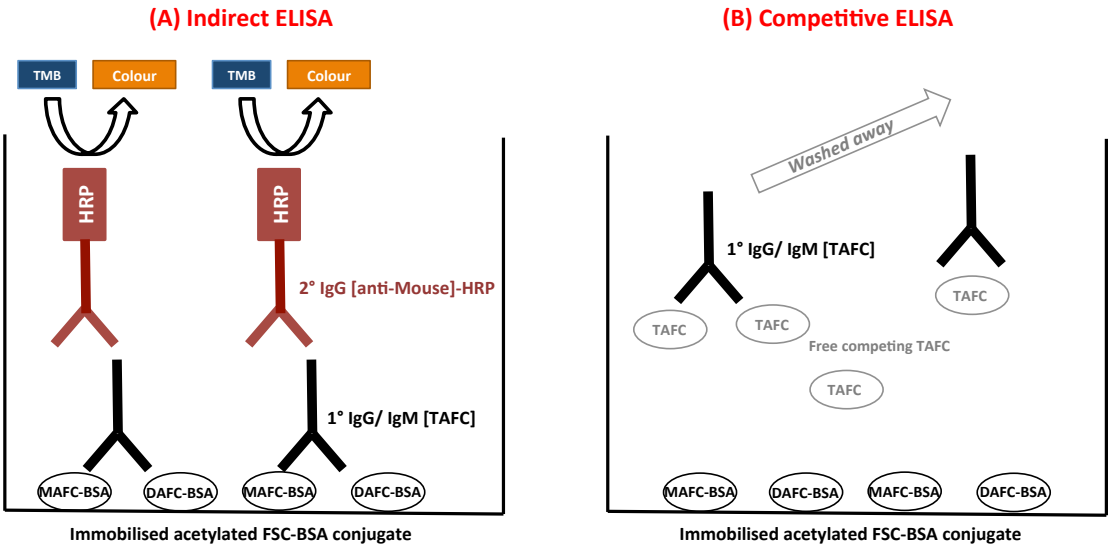

Figure 6.10 ELISA principle. In an indirect ELISA, anti-TAFC antibodies (1°) bind acetylated FSC-BSA (MAFC-BSA and DAFC-BSA) coated onto the wells of an ELISA plate. (A) Binding to the plate immobilises the antibody so that it resists removal upon washing. The 1° antibody is then bound by an anti-mouse antibody conjugated to HRP (2°) which similarly immobilises on the plate. After substrate (TMB) addition, HRP forms a coloured product generating a signal output readable at 450 nm. (B) In contrast, when competing TAFC is added before the 1° antibody, it competes with MAFC- or DAFC-BSA on the plate for 1° anti-TAFC antibody binding. Upon binding the competitor, the anti-TAFC antibody is no longer immobilised on the plate and is washed away. Subsequently, the 2° antibody has no

site for immobilisation and is also washed away. Consequently, there is less/ no colour development upon substrate and a lower signal output.

6.2.3.2 Conjugation of acetylated FSC-SMCC to SATA-BSA

Acetylated FSC^{+Fe} was conjugated to BSA for ELISA plate coating. Similar to the acetylated FSC-KLH immunogen preparation, FSC^{+Fe} was RP-HPLC purified and acetylated *via* sequential addition of SNA. This was analysed by RP-HPLC to estimate relative levels of FSC, MAFC, DAFC, and TAFC. Subsequently, the acetylated FSC was derivatised by the addition of Sulfo-SMCC equimolar to the moles of FSC, MAFC, and DAFC. This was immediately added to demasked SATA-KLH and the reaction was allowed to proceed at room temperature for 2 h followed by overnight at 4 °C (Section 2.2.5.2.3). SDS-PAGE analysis of the resultant conjugate indicated an increased molecular mass in comparison to BSA or SATA-BSA (Figure 6.11). Using the λ_{max} of ferri-siderophores (440 nm), spectrophotometry was primarily used as a measure of successful conjugation. Following the reaction, the sample was dialysed against PBS. The OD (440 nm) and Bradford assay were used to determine the siderophore and protein content to be 156 µM and 1 mg/ ml respectively, indicating conjugation of 156 nmol siderophore per mg BSA.

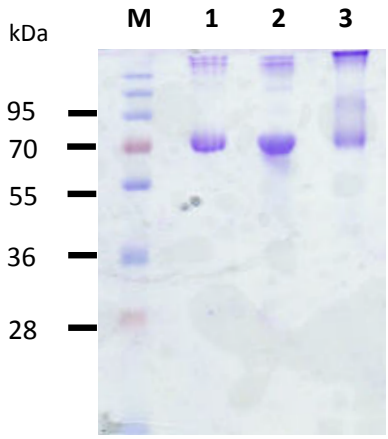

Figure 6.11 SDS-PAGE analysis of acetylated FSC^{+Fe}-BSA. M: Molecular mass marker. 1: Unmodified BSA. 2: SATA-BSA (masked). 3. Acetylated FSC^{+Fe}-BSA.

6.2.4 Screening strategy

The strategy for screening for anti-TAFC antibodies is summarised in Figure 6.12. After immunisations, a tail bleed was taken to screen for anti-TAFC polyclonal antibodies by competitive ELISA. By screening the mice at this stage it was possible to select the best mouse with which to proceed to hybridoma generation. After assay optimisation and screening (Section 6.2.5), mouse F was selected for spleen removal and hybridoma generation as described in Section 2.2.9. Hybridoma supernatant was screened directly by competitive TAFC ELISA as optimised for tail bleed screening. Any hybridomas positively selected were sub-cultured and screened again by competitive ELISA. From these, the best antibody producers were selected for cloning.

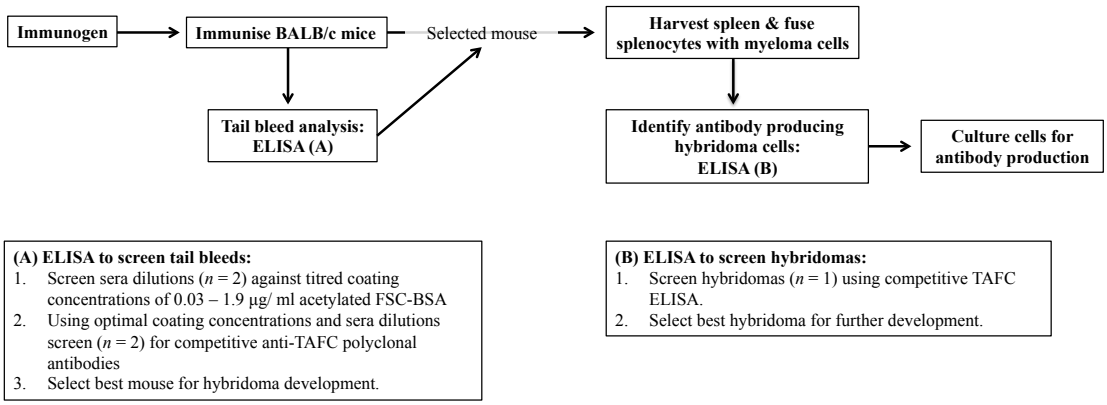

Figure 6.12 Schematic of overall screening strategy for screening for (i) anti-TAFC antibodies in tail bleeds, and (ii) anti-TAFC hybridomas.

6.2.5 Screening of murine sera

6.2.5.1 Optimisation of ELISA coating concentration

To establish a suitable concentration, murine tail bleed sera from mice F, G, and H were analysed on ELISA plates (n = 2) coated with a titred range of acetylated FSC-BSA concentrations (0.03 – 1.9 µg/ ml) (Section 6.2.3.2). Sera were diluted 1 in 102,400, 1 in 140,000, or 1 in 180,000 and an indirect ELISA carried out as per Section 2.2.8. A coating concentration of 0.12 µg/ ml paired with a sera dilution of 1 in 102,400 showed a mean OD (450/ 620 nm) of 1.2, 0.82, and 1.08 for mice F, G, and H, respectively (Figure 6.13) (Appendices, Supplementary Table 23). Thus, a coating concentration of 0.12 µg/ ml was selected for all further ELISA analysis.

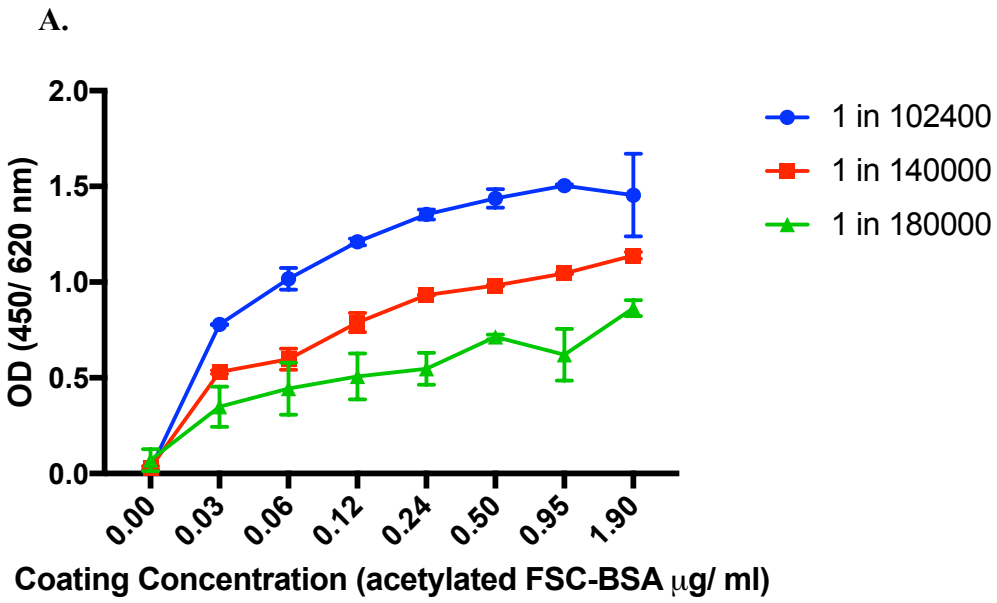

B.

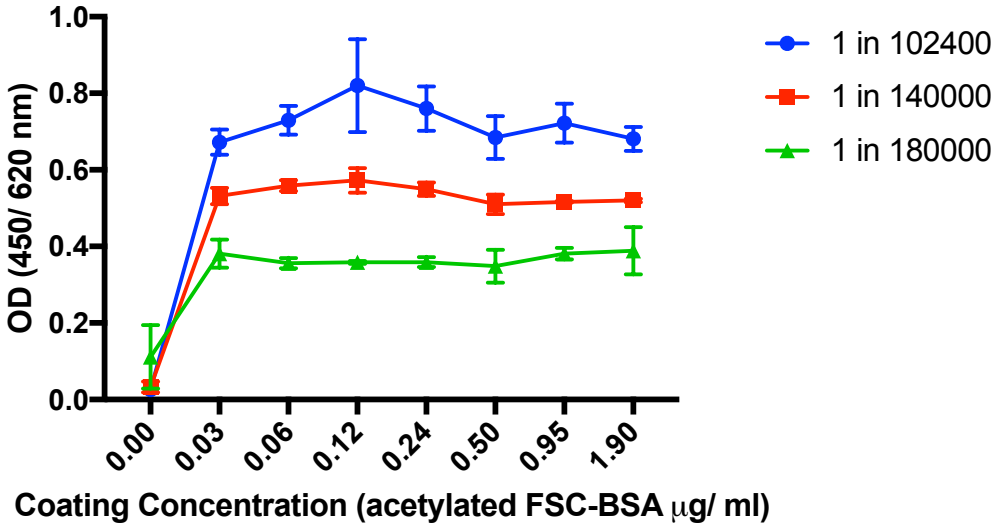

C.

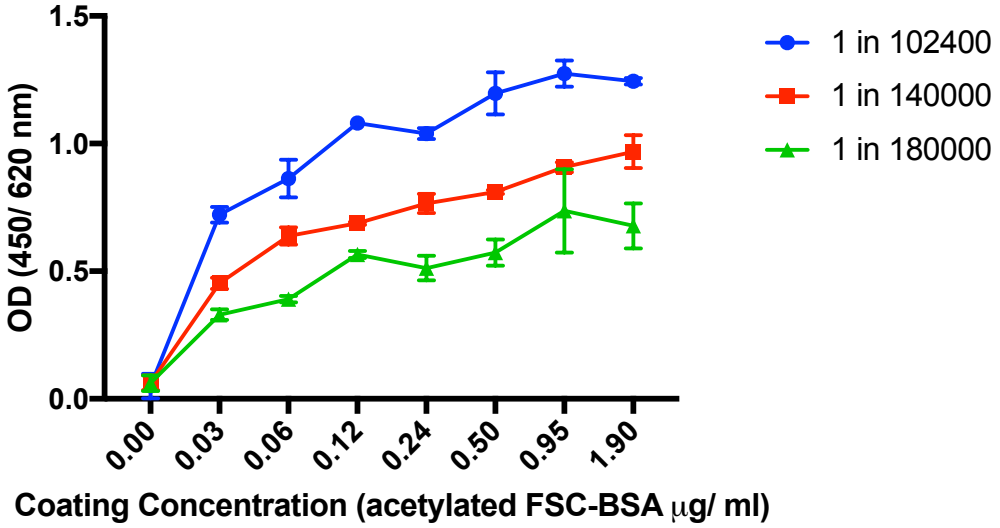

Figure 6.13 Indirect acetylated FSC ELISA analysis of murine tail bleeds. Murine tail bleeds from (A) mouse F, (B) mouse G, and (C) mouse H were analysed on ELISA plates coated with a titre of acetylated FSC-BSA concentrations to establish a suitable coating concentration at several sera dilutions (1 in 102,400, 1 in 140,000, and 1 in 180,000). A coating concentration of 0.12 μg/ ml was selected for further analysis.

6.2.5.2 Mouse F, G, and H produce competitive anti-TAFC polyclonal antibodies

Murine tail bleed sera were analysed by competitive TAFC ELISA to establish if mice F, G, and H possessed competitive TAFC antibodies. Sera was diluted 1 in 80,000 and analysed by competitive TAFC ELISA (n = 2) with a coating concentration of 0.12 µg/ ml. Mouse F, G, and H all showed decreasing OD (450/ 620 nm) with increasing competing TAFC concentration indicative of the presence of competitive anti-TAFC antibodies (Figure 6.14) (Appendices, Supplementary Table 24). Mouse F showed the largest $\Delta OD_{450/620}$ (1.25 at 0 µM TAFC and 0.59 at 100 µM TAFC) and thus, was prioritised for further analysis.

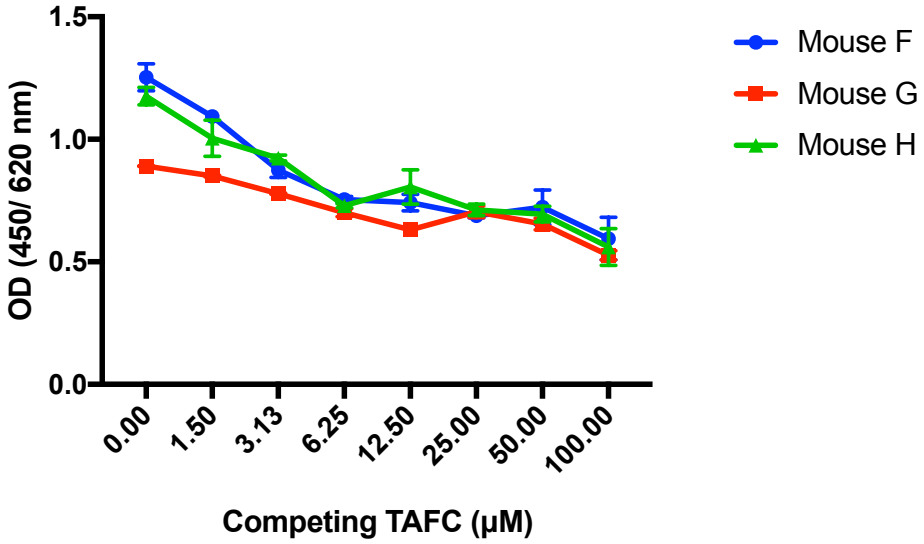

Figure 6.14 Competitive TAFC ELISA analysis of murine tail bleeds. Tail bleeds from mice F, G, and H were analysed by competitive TAFC ELISA. Serum from all mice showed decreasing OD (450/ 620 nm) with increasing competing TAFC concentration indicative of the presence of competitive anti-TAFC antibodies.

6.2.5.3 Mouse F produces competitive and specific anti-TAFC polyclonal antibodies

The polyclonal antibodies present in sera from mouse F were next tested for specificity for TAFC compared with other competitors including free iron, and BmGT. Tail bleed serum was diluted 1 in 80,000 and analysed by competitive ELISA (n = 2) with a coating concentration of 0.12 µg/ ml. Serum analysis indicated the presence of competitive anti-TAFC antibodies that showed no competition against free iron or BmGT at the same concentration (Figure 6.15). This indicates that the polyclonal antibodies are highly specific for TAFC. A pre-bleed taken from one of the three mice prior to acetylated FSC-BSA immunisation was also diluted 1 in 100,000 and analysed which showed no binding to ELISA plates (Figure 6.15) (Appendices, Supplementary Table 25).

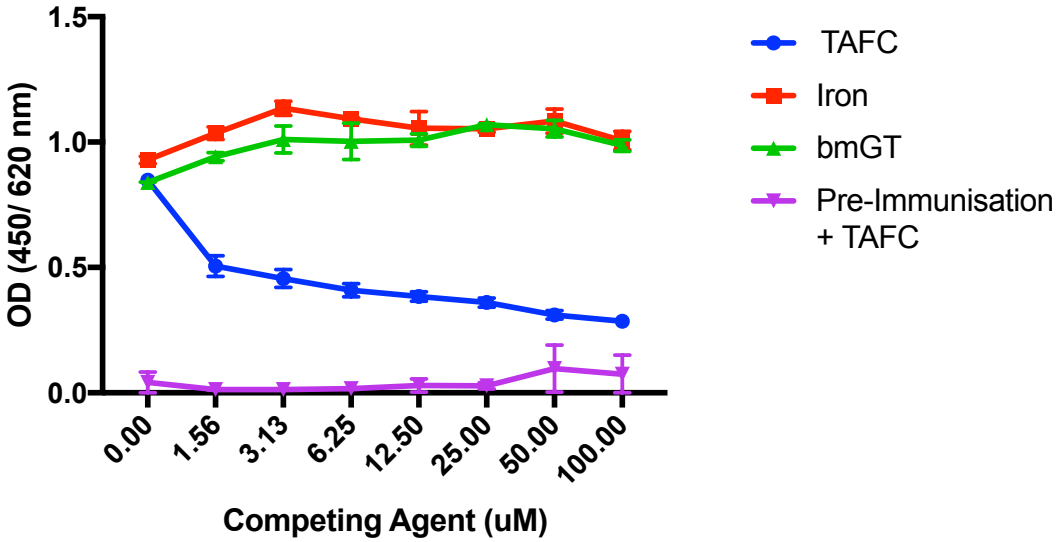

Figure 6.15 Competitive ELISA analysis to establish specificity of anti-TAFC polyclonal antibodies. Tail bleeds from mouse F were analysed by competitive ELISA with competitors: TAFC, iron, and BmGT. Only addition of competing TAFC resulted in a decreased OD (450/ 620 nm) with increasing competitor concentration.

Pre-immunisation control sera was also analysed and showed no affinity for acetylated FSC-BSA coated ELISA plates.

6.2.6 Generation of hybridomas producing anti-TAFC antibodies

After immunisations as per Section 6.2.2 and tail bleed analysis, mouse F was selected for the development of anti-TAFC producing hybridomas. A fourth and final booster of the acetylated FSC-KLH immunogen (50 μg) (Section 6.2.1.2) was mixed with adjuvant, Pam3Cys in a final volume of 100 μl and intraperitoneally administered to BALB/c mice 3 days prior to the fusion. The mouse was sacrificed, spleen removed and fusion was then carried out as per Section 2.2.9.2 (Köhler and Milstein, 1975).

6.2.6.1 Fusion efficiency

Following the fusion of the spleen from mouse F with SP/2/O-Ag 14 myeloma cells, as per Section 2.2.8.2, a 66.2% fusion efficiency was observed with 247 out of 342 wells of 48 well plates showing hybridoma generation.

6.2.6.2 Screening of hybridomas following fusion

Screening of hybridomas was carried out using a competitive TAFC ELISA (Section 6.2.4). The hybridoma supernatant was screened directly by competitive TAFC ELISA (n = 1) using the coating conditions optimised for antisera screening (Section 6.2.5.1) with or without free competing TAFC (at 100 μM only). Hybridoma supernatant with affinity for plate coated acetylated FSC-BSA that showed inhibition upon the addition of competing TAFC were regarded as positive. In total, 74 hybridoma supernatants were screened this way and 26 hybridomas were transferred to 6 well plates for further subculturing and screening (Appendices, Supplementary Table 26). Figure 6.16 shows the OD (450/ 620 nm) readings obtained from this screen for hybridomas that were ultimately selected and carried forward; 1D1, 3B6, 3C7, and 6C6.

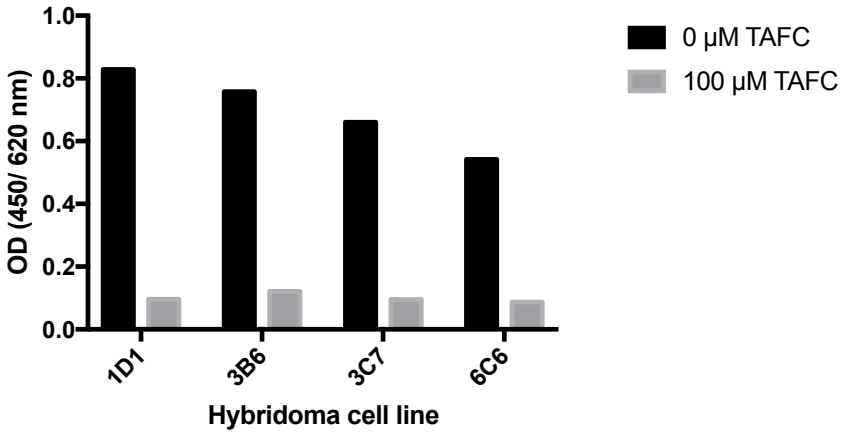

Figure 6.16 Competitive ELISA screening of supernatant from hybridomas 1D1, 3B6, 3C7, and 6C6. Hybridoma supernatant was screened using competitive TAFC ELISA, by adding supernatant directly to ELISA plate wells with and without competing TAFC (100 µM). Supernatant with affinity for plate-coated acetylated FSC-BSA that showed inhibition upon the addition of competing TAFC were regarded as positive and hybridomas moved to 6 well plates. All four hybridomas selected showed some degree of competition for free TAFC.

Any hybridomas positively identified from first screening stage were sub-cultured according to Section 2.2.9.4. Subsequently, hybridoma supernatants were again screened by competitive ELISA (n = 1). Figure 6.17 shows the OD (450/ 620 nm) readings obtained from this screen for hybridomas; 1D1, 3B6, 3C7, and 6C6 (Appendices, Supplementary Table 27). All hybridoma supernatants exhibited some degree of competition for free TAFC whereby signal (OD 450/ 620 nm) was reduced upon the addition of TAFC (100 µM). All hybridomas were subjected to cloning by limiting dilution (Section 2.2.9.5). Despite repeated efforts, we were unable to isolate a monoclonal anti-TAFC antibody producing hybridoma. However, the 6C6 hybridoma exhibited sustained high level antibody production of anti-TAFC antibody

over a period of several months and thus was selected for anti-TAFC antibody production.

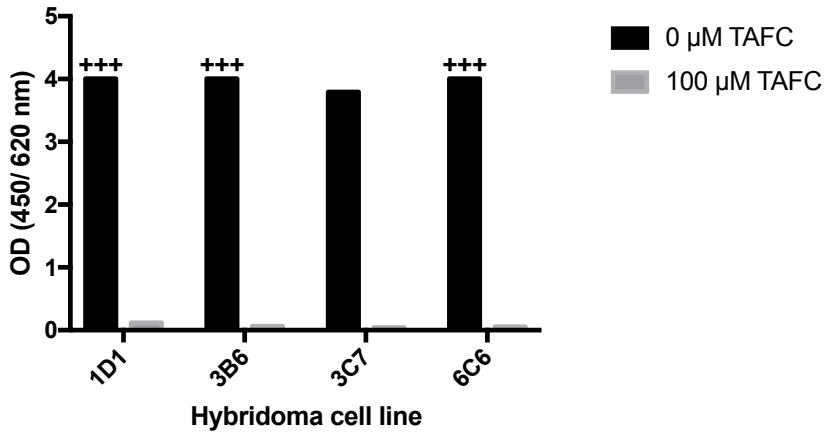

Figure 6.17 Competitive ELISA screening of supernatant from hybridomas 1D1, 3B6, 3C7, and 6C6 following subculture. Hybridoma supernatant was screened by competitive TAFC ELISA, by addition to ELISA plates wells with and without 100 µM TAFC. All hybridoma supernatants showed some degree of competition for free TAFC. The OD (450/ 620 nm) for supernatant collected from hybridomas, 1D1, 3B6, and 6C6 were too high for the spectrophotometer to read and is instead represented by the maximum OD of 4 with "+++".

6.2.7 The 6C6 hybridoma produces anti-TAFC IgG

The 6C6 hybridoma was maintained as described in Section 2.2.2 with growth in Hybridoma Culture Medium (Section 2.1.2.4). Any supernatant from growth was retained for characterisation or antibody purification. Antibody isotyping analysis was carried out using the Isostrip^{TM} Mouse Monoclonal Antibody Isotyping Kit (Roche) (Section 2.2.9.6) and indicated 6C6 hybridoma to be producing predominantly IgG_3 antibodies with a κ light chain (Figure 6.18). Analysis of culture supernatant by competitive TAFC ELISA also indicated the hybridoma produced competitive anti-TAFC antibodies whereby supernatant showed decreasing OD (450/ 620 nm) with increasing competing TAFC concentration (Figure 6.19) (Appendices, Supplementary Table 28). This analysis indicated the anti-TAFC antibody was highly sensitive, as clear competition for TAFC was observed at 1.56 μM.

The 6C6 hybridoma was subsequently sent for large-scale culture and IgG purification *via* commercial arrangement. However, when the antibody collected from this culture supernatant was analysed by competitive TAFC ELISA there was no anti-TAFC activity whatsoever (data not shown). Together with the inability to establish a monoclonal hybridoma from 6C6, this suggested that 6C6 was comprised of a mixed population of hybridomas. Moreover, it suggested these hybridomas were producing other antibodies without specificity for TAFC. Therefore, the anti-TAFC antibody likely represented only a sub-set of the antibodies produced by 6C6 and therefore may even be of a different isotype other than IgG_3.

Figure 6.18 Isostrip analysis of 6C6 hybridoma supernatant indicated it predominantly produces an IgG_3 heavy chain and κ light chain.

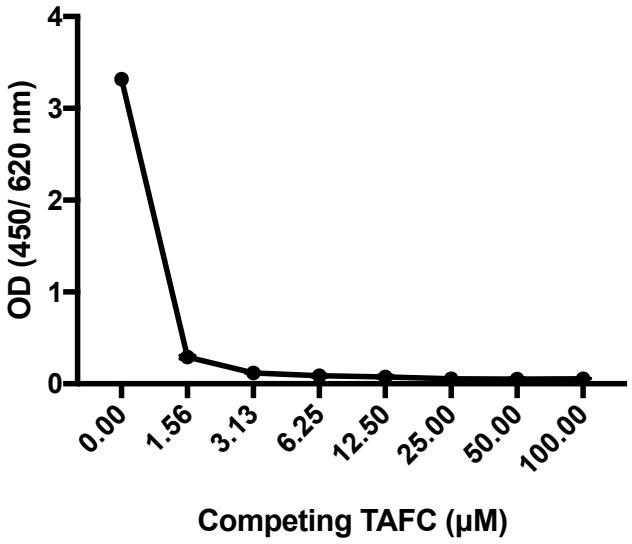

Figure 6.19 Competitive TAFC ELISA analysis of 6C6 hybridoma supernatant. Hybridoma supernatant from 6C6 was analysed by competitive TAFC ELISA. Supernatant showed decreasing OD (450/ 620 nm) with increasing competing TAFC concentration (mean $OD_{450/\ 620}$ 3.32 at 0 μM TAFC and 0.06 at 100 μM TAFC). Clear competition was apparent at low concentrations of TAFC (mean $OD_{450/\ 620}$ 0.29 at 1.56 μM).

6.2.8 Protein A affinity purification of anti-TAFC IgG

Supernatant was collected from the culture of 6C6 hybridoma and IgG was purified by Protein A affinity chromatography as per Section 2.2.11.2 (Figure 6.20). Supernatant before and after purification were analysed by competitive ELISA (n = 3). This indicated the successful complete collection of anti-TAFC antibody, whereby there was anti-TAFC activity in the supernatant before purification, but not in the flow-through (Figure 6.21) (Appendices, Supplementary Table 29). Purified IgG was also analysed by reducing SDS-PAGE in which heavy, and light chains were visible (Figure 6.22).

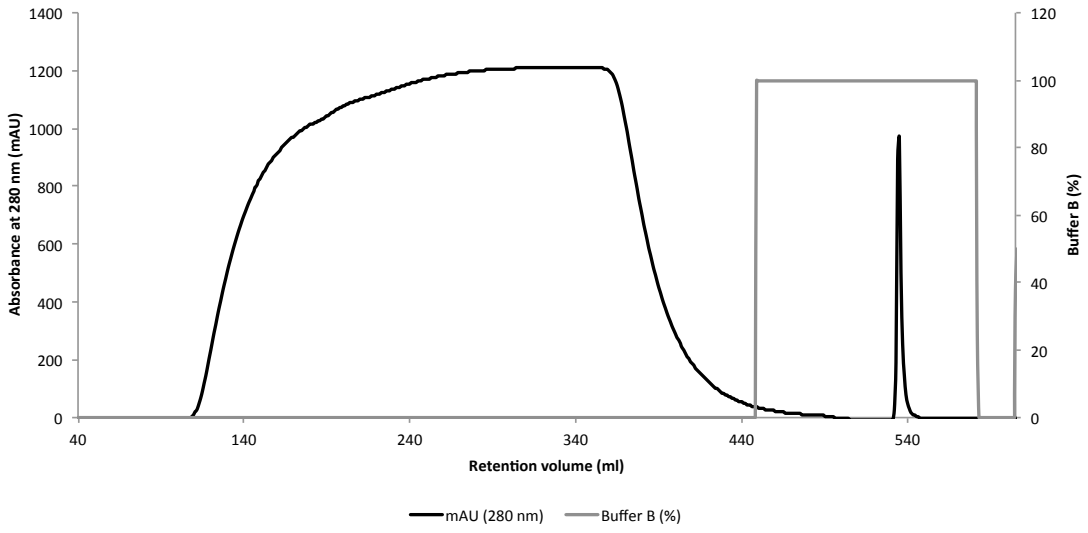

Figure 6.20 ÄKTA purification of IgG by Protein A chromatography. Culture supernatant from the 6C6 hybridoma was collected and applied to equilibrated pre-packed Protein A Sepharose columns (GE Healthcare) as described in Section 2.2.11.2. Flow-through was retained for later ELISA analysis to confirm successful purification of anti-TAFC IgG. After application, the column was washed with Equilibration buffer (Buffer B) and any bound IgG was eluted in Elution Buffer.

Purified IgG was collected in fractions, pooled, and dialysed against sodium phosphate buffer for later analysis by SDS-PAGE and ELISA.

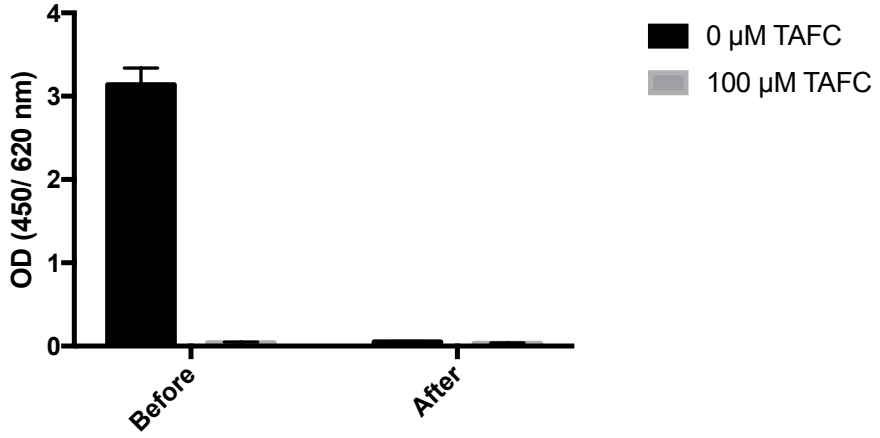

Figure 6.21 Competitive ELISA analysis of 6C6 hybridoma supernatant before and after Protein A purification shows anti-TAFC activity before but not after purification. This indicates the successful complete collection of the anti-TAFC IgG from culture supernatant.

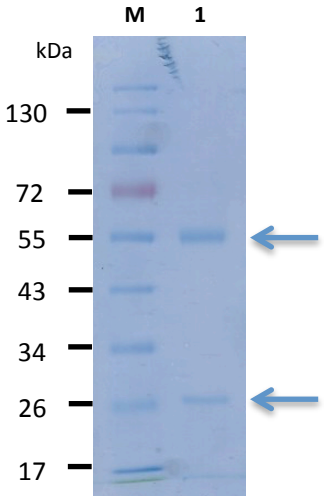

Figure 6.22 IgG was analysed by SDS-PAGE after Protein A purification from hybridoma supernatant. M: Molecular mass ladder. 1: Anti-TAFC IgG. Arrows indicate positions of heavy and light chains respectively.

6.2.9 Development of a competitive TAFC ELISA with Protein A purified IgG

IgG purified by Protein A chromatography from 6C6 supernatant was analysed to determine the optimal IgG concentration for ELISA analysis. IgG (0.16 – 10 μg/ ml) (n = 2) was added to ELISA plates coated with 0.12 μg/ ml acetylated FSC-BSA (as previously used in hybridoma and tail bleed screening for competitive ELISA) (Figure 6.23) (Appendices, Supplementary Table 30). An IgG concentration of 2.5 μg/ ml was selected for all further ELISA analysis.

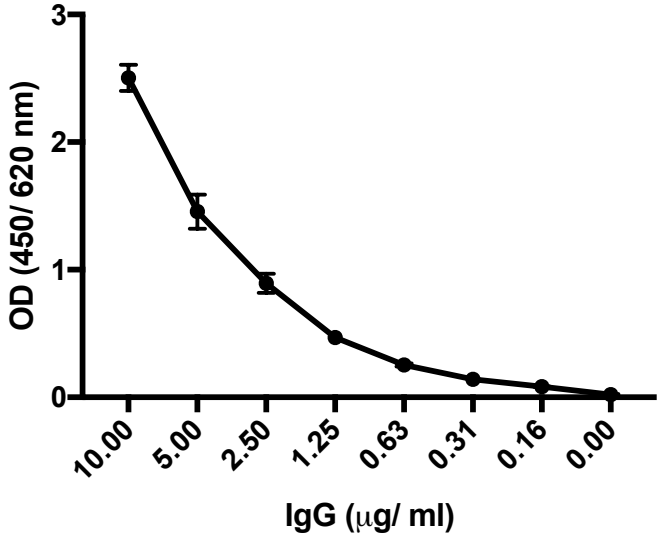

Figure 6.23 Optimisation of IgG concentration (μg/ ml) for ELISA analysis. IgG was titred (0.16 – 10 μg/ ml) and added to acetylated FSC-BSA coated ELISA plates to determine the optimal concentration of IgG to use for further ELISA analysis. A concentration of 2.5 μg/ ml was selected for all further ELISA analysis.

Using the optimised IgG concentration (2.5 µg/ ml) along with the previously optimised coating conditions, anti-TAFC IgG was subjected to further characterisation. To establish the extent of its specificity for TAFC, the IgG was screened by competitive TAFC ELISA using TAFC along with several other competitors (FSC, BmGT, ferrichrome, and ferri-ornibactin). The IgG exhibited high specificity for TAFC, showing competition for TAFC, but not the other metabolites (Figure 6.24) (Appendices, Supplementary Table 31).

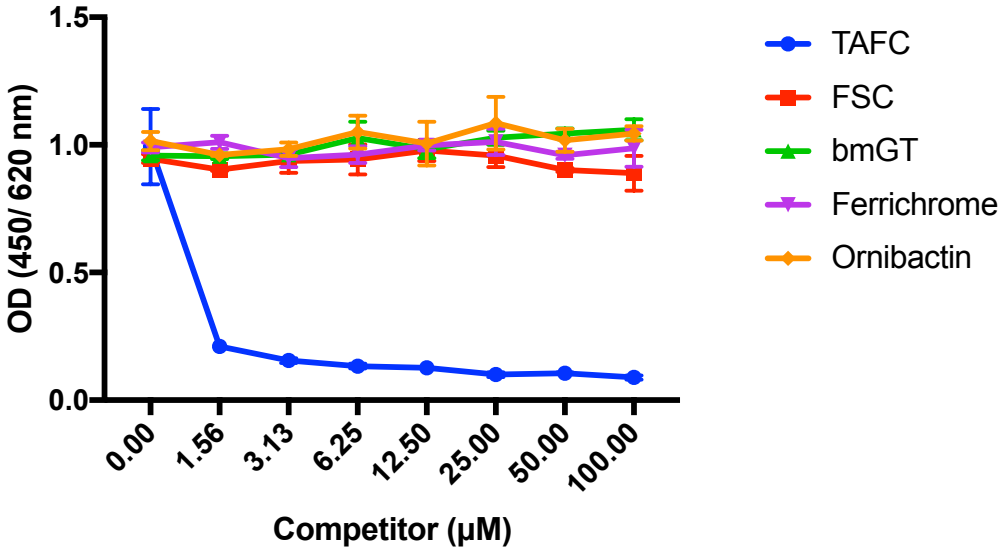

Figure 6.24 Competitive ELISA analysis of anti-TAFC IgG indicates high specificity for TAFC. Purified IgG was analysed by competitive ELISA with a titre (1.56 – 100 µM) of several competitors: ferri-triacetylfusarinine C (TAFC), ferri-fusarinine C (FSC), BmGT, ferrichrome, and ferri-ornibactin on acetylated FSC-BSA coated ELISA plates. IgG shows competition with TAFC (mean $OD_{450/620}$ 0.99 at 0 µM TAFC and 0.09 at 100 µM TAFC), but not other metabolites.

Following assessment of the specificity of anti-TAFC IgG (Figure 6.24), it was apparent that the antibody was capable of detecting competing TAFC concentrations lower than previously tested. To assess this, a revised competitive TAFC ELISA was carried out with competing TAFC titred from 0.1 – 6.25 µM. This analysis indicated the antibody was capable of detecting concentrations of TAFC as low as 0.1 µM (Figures 6.25). The assay was also used to detect TAFC in supernatant from *A. fumigatus* wild-type grown for 72 h in iron-replete MM as a competitor. The fungal supernatant was ferrated in excess (similar to Section 2.2.4.2), quantified as per Section 2.2.3.1 and added to the ELISA as a competitor alongside TAFC. Anti-TAFC IgG showed similar competition for TAFC as ferrated wild-type supernatant at equivalent concentrations (Figure 6.25) (Appendices, Supplementary Table 32).

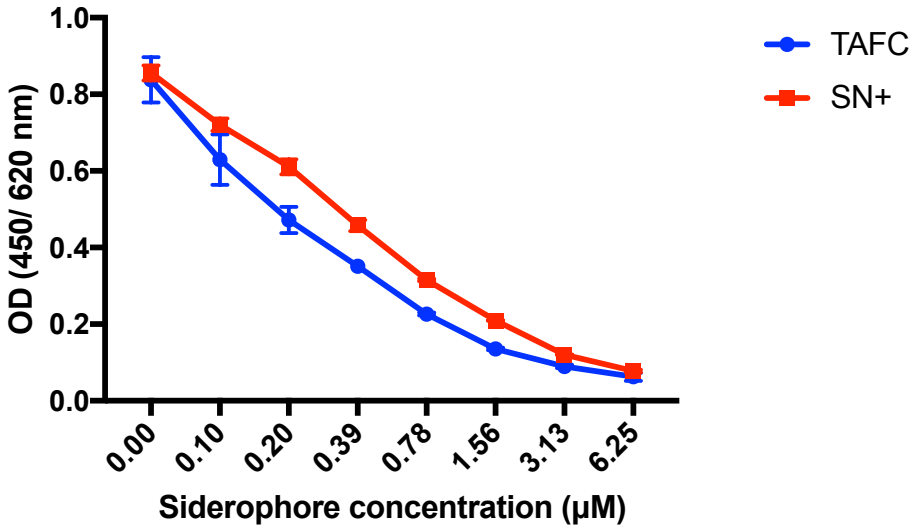

Figure 6.25 Competitive TAFC ELISA is a sensitive assay for the detection of TAFC. After establishing the competitive TAFC ELISA it was used to detect purified TAFC (TAFC) and TAFC in ferrated *A. fumigatus* wild-type supernatant (SN+). IgG showed decreasing OD (450/ 620 nm) with increasing competing TAFC concentration from (i) TAFC (mean $OD_{450/\ 620}$ 0.84 at 0 µM TAFC and 0.06 at 100

μM TAFC) and (ii) SN+ (mean $OD_{450/620}$ 0.86 at 0 μM TAFC and 0.08 at 100 μM TAFC).

6.2.10 Strategy for sequencing the anti-TAFC antibody

In order to obtain the sequence of the anti-TAFC antibody Fab region, a proteogenomic strategy was implemented. This comprised of MS-based peptide sequencing to identify residues associated with the N-terminus of the heavy and light chains and the CH_1 rand C-terminus residues for the heavy and light chain, respectively (Figure 6.26). These residues then allow for the design of primers for the specific amplification of the anti-TAFC antibody Fab region from hybridoma cDNA. Importantly, there was evidence to indicate the 6C6 hybridoma was a heterogenous population of hybridomas producing other antibodies in addition to anti-TAFC IgG (Section 6.2.8). Hence, to characterise the peptides of anti-TAFC IgG, it was first necessary to immunoaffinity purify the antibody to ensure that only peptides associated with anti-TAFC IgG would be analysed.

To immunoaffinity purify the anti-TAFC antibody, acetylated FSC was conjugated onto NHS-activated magnetic beads. The beads were prepared as described in Section 2.2.5.5. Briefly, FSC^{+Fe} was sequentially acetylated to yield maximal DAFC levels. This was then conjugated to the beads *via* an amine group as per the manufacturer's instructions. These beads were then used to immunoaffinity purify the anti-TAFC antibody from Protein A purified IgG (total IgG) produced by the 6C6 hybridoma.

First, the functionality of the beads was validated using an analytical small-scale immunoaffinity pull-down (Section 6.2.11). The presence of anti-TAFC IgG in the Protein A purified IgG was previously confirmed using the competitive TAFC

ELISA (Section 6.2.9). Protein A purified IgG was incubated with the acetylated FSC magnetic beads. Subsequently, beads were probed with an anti-mouse antibody to detect antibody binding. As the beads contained the same antigenic mixture as on the competitive TAFC ELISA plates, any bound antibodies were inferred to be similarly against TAFC. Once the functionality of the beads was confirmed, a large-scale immunoaffinity pull-down was carried out (Section 6.2.12). Protein A purified IgG was incubated with the acetylated FSC beads and any bound antibody was eluted. Eluted antibody was analysed by competitive TAFC ELISA, Isostrip^{TM}, and SDS-PAGE. SDS-PAGE analysis permitted the separation of the heavy and light chains allowing for separate analysis (Section 6.2.13). Bands were excised and digested with three different enzymes (trypsin, Glu-C, or Asp-N) to generate three different antibody peptide maps. Trypsin cleaves at the carboxyl side of arginine or lysine residues, Glu-C cleaves at the carboxyl side of glutamic acid, and Asp-N cleaves at the amino side of aspartic acid. Peptides were analysed by Q-Exactive LC-MS/MS and mass spectra were interpreted using PEAKS protein bioinformatic software. Peptides were exported and those with overlapping residues were assembled both manually and using the ALPS assembly system (Tran *et al.*, 2016). Using this information the putative N- and C-terminal residues for the anti-TAFC antibody Fab region were identified (Section 6.2.14 – 6.2.15). Subsequently, primers were designed for the specific amplification of the anti-TAFC antibody Fab region using cDNA from the 6C6 hybridoma (Section 6.2.16). The workflow for this strategy is summarised in Figure 6.27.

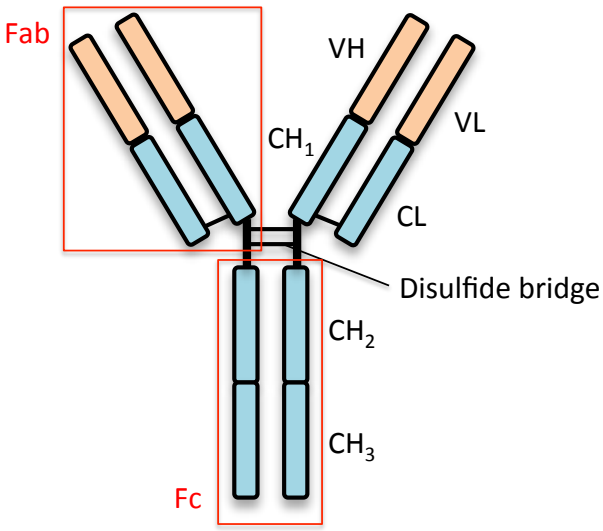

Figure 6.26 Schematic of the basic IgG structure. IgG is a heterotetrameric protein comprised of two heavy and light chains linked by disulfide bonds. The heavy chain is comprised of a variable region (VH), and three conserved regions (CH_{1-3}), with the N-terminus at the start of the VH and C-terminus at the end of the CH_3. While the light chain is comprised of a variable region (VL) and a conserved region (CL), with the N-terminus at the start of the VL and C-terminus at the end of the CL. The Fab region (fragment antibody binding) is comprised of the VL, CL, VH, and CH_1 linked by disulfide bridges. The variable regions (VL and VH) are primarily responsible for antigen binding. The fragment crystallisable (Fc) region is comprised of the CH_2 and CH_3 domains. It contains no antigen binding domains, but is important for effector functions (Janeway, 2001).

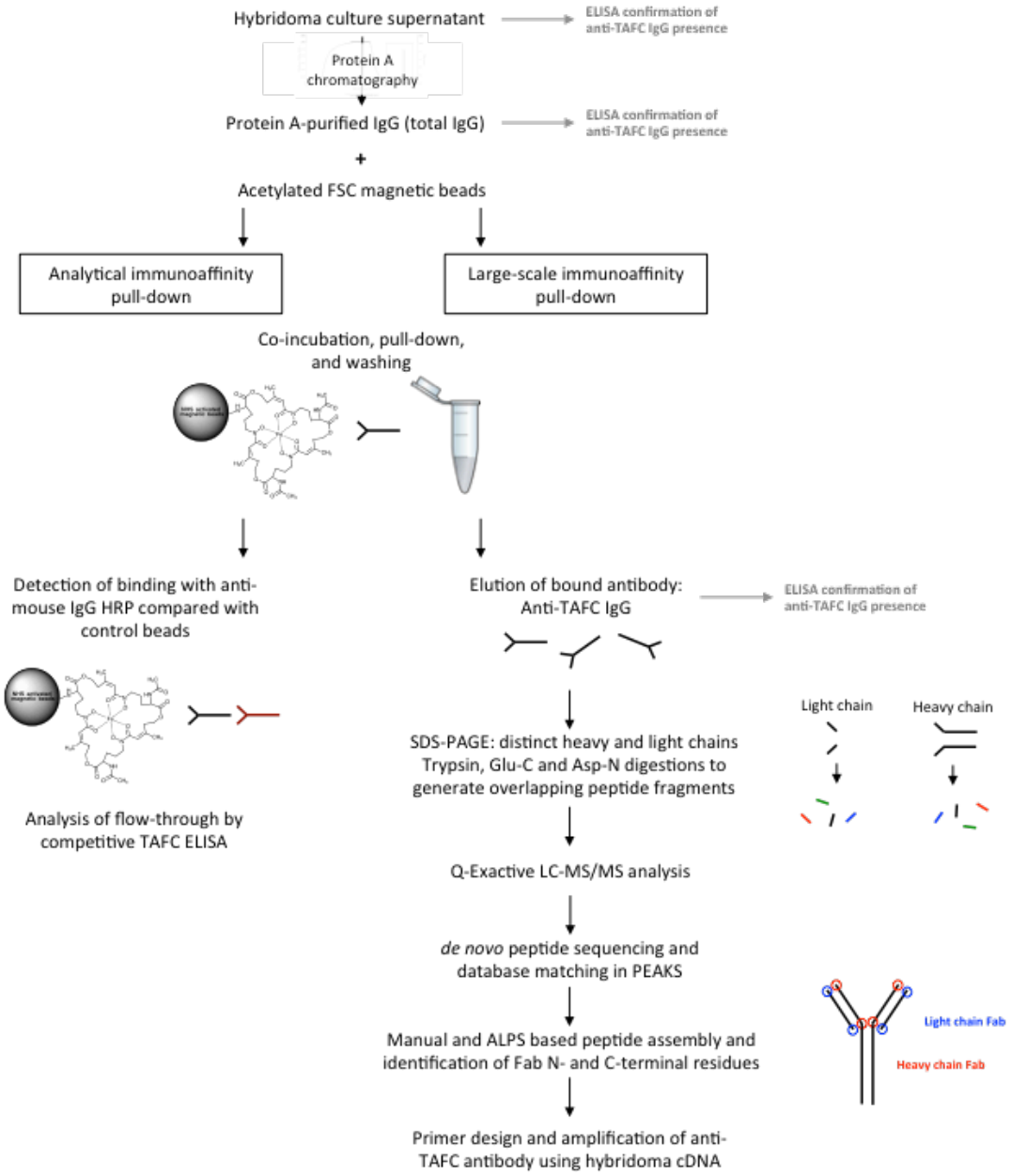

Figure 6.27 Strategy for sequencing the TAFC antibody. Total IgG was purified from hybridoma culture supernatant using Protein A affinity chromatography. Protein A purified IgG was incubated with acetylated FSC coated magnetic beads. Binding of antibodies to the beads was confirmed in a small-scale analytical pull-down using an anti-mouse IgG HRP and a competitive ELISA analysis of flow-through to detect binding. After functionality was confirmed, a large-scale pull-down was performed with bound antibody eluted instead. Immunoaffinity purified antibody was analysed

by competitive TAFC ELISA to confirm the presence of anti-TAFC antibodies. Heavy and light chains were separated by SDS-PAGE and associated bands excised and digested with trypsin, Glu-C, or Asp-N to generate differential but overlapping peptide maps. Peptides were analysed by LC-MS/MS and interpreted using PEAKS. Peptides were exported manually and using the ALPS system according to Tran *et al*. (2016). Peptide sequences of the N- and C-terminus of the Fab region were used to generate primers for the specific amplification of the TAFC antibody Fab region using hybridoma cDNA.

6.2.11 Analytical scale immunoaffinity pull-down of anti-TAFC IgG

To confirm functionality of acetylated FSC coated magnetic beads in binding to anti-TAFC antibodies, a small-scale analytical pull-down was performed as per Section 2.2.11.3.1. Protein A purified IgG (total IgG) or diluent alone (TBST) were incubated with magnetic beads coated with and without acetylated FSC (Section 2.2.5.5). The reaction conditions are summarised in Table 6.1. Beads were subsequently probed with anti-mouse IgG HRP and developed using TMB substrate solution. The reaction was stopped and the OD (450/ 620 nm) measured. Antibodies were detected which bound to acetylated FSC coated beads only (Figure 6.28) (Appendices, Supplementary Table 33). The flow-through from this pull-down was retained and analysed by competitive TAFC ELISA. Similarly, this indicated that anti-TAFC antibodies were only bound to beads activated with acetylated FSC (Figure 6.29) (Appendices, Supplementary Table 34). Flow-through of IgG incubated with acetylated FSC beads had no anti-TAFC activity after incubation. In contrast, flow-through of IgG incubated with control beads had anti-TAFC activity after incubation.

Table 6.1 Summary of components of the analytical immunoaffinity pull-down of anti-TAFC antibodies using acetylated FSC coated magnetic beads.

Sample	Acetylated FSC beads	Control beads	Protein A purified IgG	TBST	Anti-mouse IgG-HRP
Sample composition	+	-	+	-	+
Control A composition	+	-	-	+	+
Control B composition	-	+	+	-	+

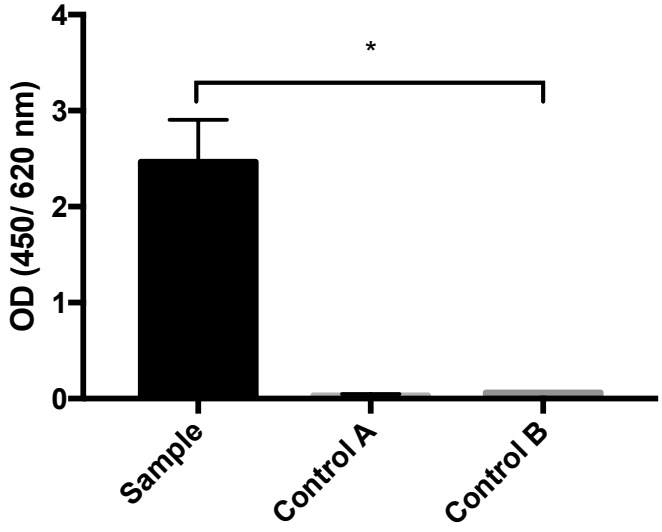

Figure 6.28 Analytical immunoaffinity pull-down (n = 2) of anti-TAFC antibody using acetylated FSC coated magnetic beads. Protein A purified IgG was incubated with magnetic beads coated with (Sample) or without (Control B) acetylated FSC. In addition, a control using TBST instead of Protein A purified IgG was included and incubated acetylated FSC coated beads (Control A). All beads were subsequently probed with anti-mouse IgG HRP and colour development read at OD 450/ 620 nm. This indicated antibodies bound only to beads coated with acetylated FSC.

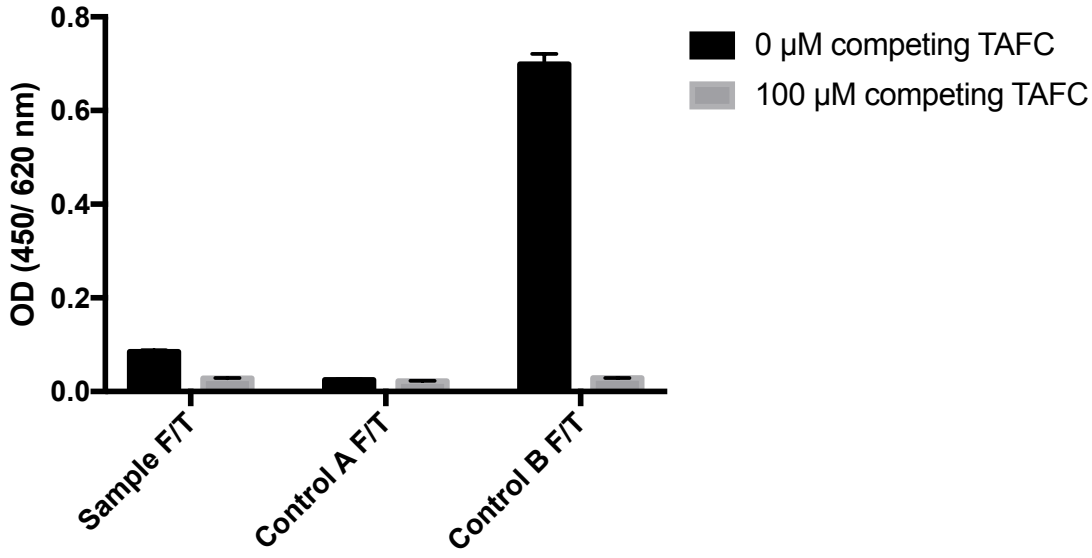

Figure 6.29 Competitive ELISA analysis of flow-through from the analytical immunoaffinity pull-down (n = 2). Analysis of flow-through (F/T) demonstrated the presence of anti-TAFC antibodies only following incubation of Protein A purified IgG with control beads (Control B F/T). Flow-through from Protein A purified IgG incubated acetylated FSC beads (Sample F/T) showed no anti-TAFC activity confirming successful removal of anti-TAFC IgG. Flow-through of TBST incubated with acetylated FSC beads also showed no anti-TAFC activity (Control A F/T).

6.2.12 Large-scale immunoaffinity pull-down of anti-TAFC IgG

Following confirmation of the functionality of the magnetic beads in extracting anti-TAFC antibodies in Section 6.2.11, a large-scale immunoaffinity pull-down was carried out. Anti-TAFC antibodies were immunoaffinity purified from Protein A purified IgG using acetylated FSC coated magnetic beads on a large-scale as per Section 2.2.11.3.2. Briefly, Protein A purified IgG was incubated with acetylated FSC coated magnetic beads, beads were washed and any bound antibody was eluted. Eluted antibody content was measured by A_{280} (Table 6.2) and an aliquot was analysed by competitive ELISA (Figure 6.30) (Appendices, Supplementary Table 35). In total, 1.2 mg of Protein A purified IgG from 6C6 hybridoma culture supernatant was used for immunoaffinity purification. This yielded 18 µg of anti-TAFC antibody (Table 6.2). The relatively low amount of eluted antibody from the total IgG (1.5%) suggested the anti-TAFC antibody only comprised a sub-set of the total IgG produced by the 6C6 hybridoma. This supported the observation in Section 6.2.7 and indicated that the 6C6 hybridoma was in fact a heterogeneous population, producing more than one IgG.

Table 6.2 Protein yields from large scale beads pull-down (according to A_{280}). Each elution was in a 200 µl volume.

	Input	Elution 1.	Elution 2.	Elution 3.	Elution 4.
Total protein (µg)	1200	9.5	0	2.75	5.4

Protein A purified IgG (total IgG) (2.5 µg/ ml), immunoaffinity purified antibody (1 µg/ ml), and immunoaffinity beads flow-through (diluted to 2.5 µg/ ml based on input) were analysed by competitive TAFC ELISA (Figure 6.30). The flow-through from immunoaffinity purification retained no anti-TAFC antibody activity indicating complete binding of anti-TAFC antibody to the beads. The immunoaffinity purified antibody, though at a lower concentration than Protein A purified IgG, showed a significantly higher OD than the Protein A purified IgG ($p < 0.0005$; unpaired t-test). When converted to OD (450/ 620 nm)/ µg protein input, Protein A purified IgG had an activity of 0.23 OD/ µg and immunoaffinity purified IgG has an activity of 3.6 OD/ µg.

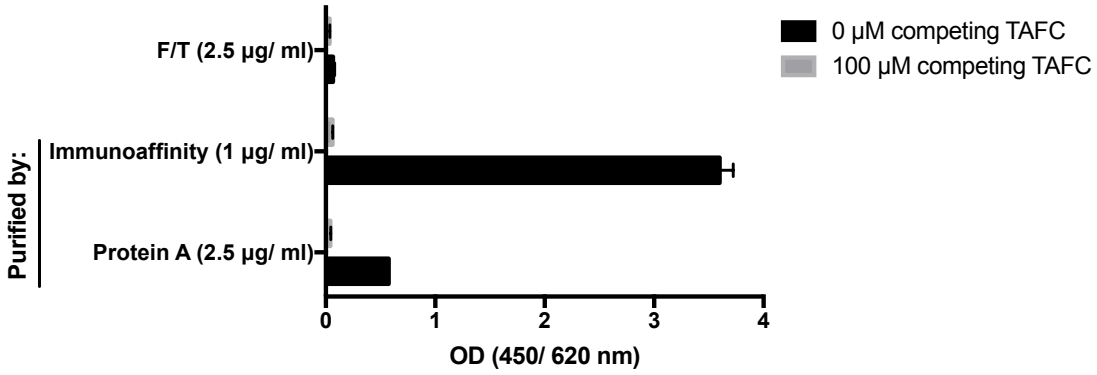

Figure 6.30 Comparative competitive TAFC ELISA analysis of Protein A purified (2.5 µg/ ml) and immunoaffinity purified (1 µg/ ml) anti-TAFC IgG. Despite a lower concentration, the eluted antibody showed a significantly higher OD ($p < 0.0005$; unpaired t-test) than the Protein A purified IgG. Flow-through from the immunoaffinity pull-down (F/T) showed no anti-TAFC activity confirming successful removal of anti-TAFC IgG.

6.2.13 SDS-PAGE and isotype analysis of immunoaffinity purified anti-TAFC IgG

Protein A purified IgG and immunoaffinity purified IgG from Section 6.2.12 will henceforth be referred to as before and after immunoaffinity purification, respectively. Both IgG samples were analysed by SDS-PAGE (Figure 6.31). The bands associated with the heavy and light chains were excised in three pieces each. Each piece was then digested with trypsin, Asp-N, or Glu-C and resultant peptides were analysed by LC-MS/MS (Section 2.2.13.2 and 2.2.13.7).

Antibody isotype analysis was carried out using the Isostrip^{TM} Mouse Monoclonal Antibody Isotyping Kit (Roche) (Section 2.2.9.6) and indicated the immunoaffinity purified anti-TAFC IgG to be an IgG_{2a} with a κ light chain (Figure 6.32). This was in contrast to isostrip analysis of the 6C6 hybridoma culture supernatant directly, which indicated IgG_3 isotype. This further supported the observation that the anti-TAFC antibody only comprised a sub-set of the total IgG produced by 6C6 and that this hybridoma was in fact a heterogeneous population (Section 6.2.7). Only immunoaffinity-purified antibody left over following SDS-PAGE analysis was used for the isotyping, hence, the amount used was quite low and IgG_{2a} band is quite faint.

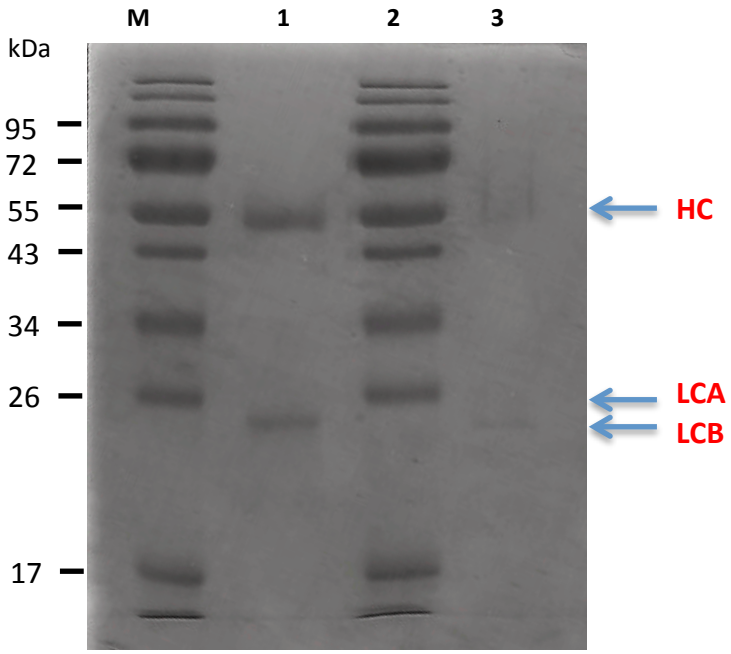

Figure 6.31 SDS-PAGE analysis of anti-TAFC IgG before and after immunoaffinity purification. M: Molecular mass marker. 1: Protein A purified IgG. 2: Molecular weight marker. 3. TAFC immunoaffinity purified IgG. Arrows indicated position of heavy (HC) and light chains A (LCA) and B (LCB) for immunoaffinity purified IgG. The higher band (light chain A) was not visible after scanning, however, arrow marks where the band was located.

Figure 6.32 Isostrip analysis of the immunoaffinity-purified anti-TAFC IgG indicated it to be an IgG_{2a} heavy chain and κ light chain. Because only immunoaffinity-purified antibody remaining following SDS-PAGE analysis was used, the amount was quite low and IgG_{2a} band is quite faint.

6.2.14 MS-based characterisation of the immunoaffinity purified anti-TAFC IgG heavy chain

A single heavy chain was observed in SDS-PAGE analysis of immunoaffinity purified IgG with one band at approximately 55 kDa (Figure 6.31). Along with the heavy chain from before immunoaffinity purification, both SDS-PAGE bands were excised in three pieces, digested with trypsin, Asp-N, or Glu-C and analysed by Q-Exactive LC-MS/MS (Section 2.2.13.2 and 2.2.13.7). Mass spectra were subsequently analysed using PEAKS for peptide identification and protein alignment as per Section 2.2.14.3 based on the ALPS system outlined by Tran *et al.* (2016). Peptides were identified by *de novo* sequencing and initially searched against a database containing murine antibodies and common contaminant proteins (from Tran *et al.,* (2016)). Following isotype identification, *de novo* sequences were searched again against a modified database also including additional IgG_{2a} κ antibody sequences from the online database, abYsis (www.abysis.org) (Swindells *et al.*, 2017).

6.2.14.1 Peptides show alignment to IgG_3 before immunoaffinity purification and IgG_{2A} after immunoaffinity purification

Peptides from the IgG heavy chains before and after immunoaffinity purification (digested with trypsin, Asp-N, or Glu-C) were analysed by LC-MS/MS. Mass spectra were subsequently analysed using PEAKS for peptide identification and protein alignment as per Section 2.2.14.3. Mass spectra were initially subjected to complete *de novo* sequencing for peptide identification. *De novo* sequences were then searched against a database containing murine antibodies and common contaminant proteins from Tran *et al.* (2016).

The protein with the highest sequence coverage before immunoaffinity purification is shown in Figure 6.33. BLAST sequence analysis of this template protein indicated it was an IgG_3 with 100% identity (IgG_3 heavy chain precursor [*Mus musculus*]; Accession: BAA03476.1). Furthermore, this protein possesses an LIKR sequence at residues 233 – 237 which has previously been reported in the CH_1 domain for IgG_3 but not other IgG isotypes (Sheriff *et al.*, 1996).

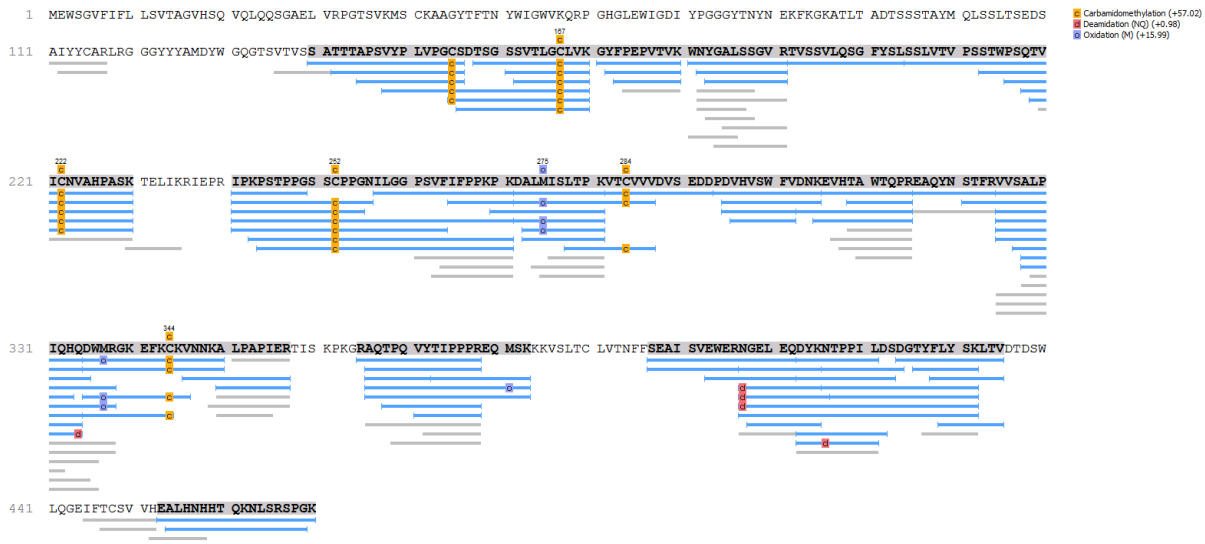

Figure 6.33 Peptides isolated from the IgG heavy chain before immunoaffinity purification show alignment to an IgG_3 (60% sequence coverage; -log10P score = 433; 83 peptides identified (49 unique)). At residues 233 – 237 this protein possesses an LIKR sequence previously found in IgG_3 but not other IgG isotypes (Sheriff *et al.*, 1996). Peptides derived from MS analysis are shown in blue or grey aligning to template protein sequence.

The protein with the highest sequence coverage after immunoaffinity purification is shown in Figure 6.34. BLAST sequence analysis indicated that this template protein was an IgG with 100% identity (chain B, structure of immunoglobulin; Accession: 1IGT_B); however the isotype of the BLAST hit was not reported. The isotype of another BLAST hit for this template protein with 87%

identity was reported as an IgG_{2a} (IgG_{2a} (mAb735) – mouse; Accession: S40295). Both proteins possess a VDKK sequence at the end of the CH_1 domain which has been reported in all IgG isotypes except IgG_3 (Sheriff *et al.*, 1996).

Figure 6.34 Peptides isolated from the IgG heavy chain after immunoaffinity purification show alignment to an IgG (52% sequence coverage; -log10P score = 368; 38 peptides identified (0 unique)). Peptides derived from MS analysis are shown in blue or grey aligning to template protein sequence.

A Clustal Omega alignment (generated using the 'msa' package in R, Section 2.2.15) of the conserved domains (CH_1, CH_2, and CH_3) from all murine IgG isotypes (IgG_1, IgG_{2a}, IgG_{2b}, and IgG_3) was carried out using sequences derived from UniProt (Figure 6.35). This alignment also shows the presence of residues, VDKK at the end of the CH_1 domain in all IgG isotypes except IgG_3 supporting the observation by Sheriff *et al.* (1996). Following this observation, it was hypothesized that the anti-TAFC antibody was not an IgG_3 but an IgG_{2a} while the total IgG (before immunoaffinity purification) was hypothesized to largely comprise of IgG_3. This was supported by isotype analysis in Section 6.2.7 and 6.2.13. With this in mind, an additional PEAKS database search was carried out, using the *de novo* sequences searched against a modified database including that of Tran *et al.* (2016)

supplemented with additional IgG_{2a} sequences from the online antibody sequence database, abYsis (www.abysis.org) (Swindells *et al.*, 2017).

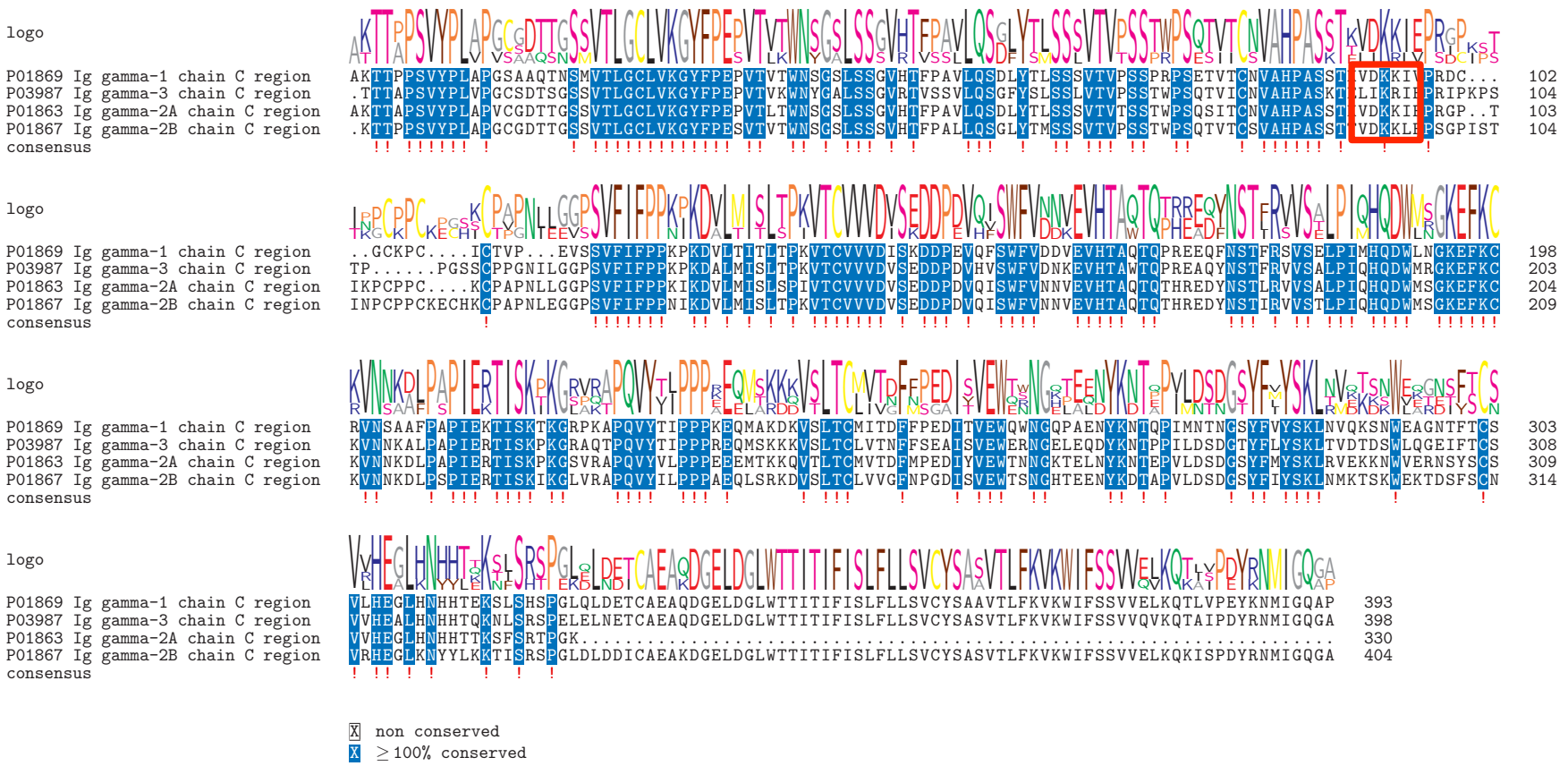

Figure 6.35 Clustal Omega alignment of the conserved domains (CH_1, CH_2, and CH_3) of all murine IgG isotypes (IgG_1, IgG_{2a}, IgG_{2b}, and IgG_3) (UniProt) show VDKK residues present in all IgG isotypes except IgG_3 in which a LIKR sequence is located (highlighted in red box).

6.2.14.2 Assembly of peptides for putative heavy chain peptide sequence

Peptides were exported from PEAKS and assembled manually and using the ALPS program from Tran *et al.* (2016) as described in Section 2.2.14.3.2. Peptide lists were refined to reduce redundancy. Any peptides matching conserved IgG_3 domains were removed as they likely represent contaminating IgG_3 carried over from the total IgG during immunoaffinity pull-down. Figure 6.36 shows the final assembled peptides for the putative heavy chain sequence. In several instances, two peptides were identified aligning to the same regions of the antibody. Specifically peptide conflicts were identified at residues 4-23, 63-65, and 89-90. As it was not possible to unequivocally determine which was truly associated with the anti-TAFC IgG all peptides were listed. This resulted in a total of 8 putative anti-TAFC IgG heavy chain sequences using the different combinations (Figure 6.36). Given they were to be used for primer design, the peptides aligning to the N-terminus were considered to be the most important in this workflow. Consequently, the assemblies were named for these two conflicting N-terminus peptides, heavy chain 1 (HC1) and heavy chain 2 (HC2). All peptide lists exported from PEAKS, output from ALPS, collectively gathered peptides, and manually assembled sequences are found in the Appendices in the folder, 'Data for antibody sequences'.

HC_1.1
QIQLVQSGPELKKPGETVKLSCKASGYTFTNYGMNWVK--------WMGWINTNTGEPTYAEEFKGRFTISR--------ASLNNLKNEDTALYYCARHDG---------DYWGQG
TTLTVSSAKTTAPSVYPLAPVCGDTTGSSVTLGCLVK----------NSGSLSSGVHTFPAVLQS--------------------------------VDKKIEPRGPTIKPCPPC
KCPAPNLLGGPSVFIFPPK--------------------------------VNNVEVHTAQTQTHREDYNSTLRVVSALPIQHQDWMSGKEFKCKVNNKDLPAPIERTISKPKGSV
RAPQVYVLPPPEEEMTKKQVTLTCMVT-----DIYVEWTNNGKTELNYKNTEPVLDSDGSYFMYSKLRVEKKNWVERNSYSCSVV HEGRHNHHTTKSFSR----

HC_1.2
QIQLVQSGPELKKPGETVKLSCKASGYTFTNYGMNWVK--------WMGWINTNTGEPTYAEEFKGRFTISR--------ASLNNLKSEDTALYYCARHDG---------DYWGQG
TTLTVSSAKTTAPSVYPLAPVCGDTTGSSVTLGCLVK----------NSGSLSSGVHTFPAVLQS--------------------------------VDKKIEPRGPTIKPCPPC
KCPAPNLLGGPSVFIFPPK--------------------------------VNNVEVHTAQTQTHREDYNSTLRVVSALPIQHQDWMSGKEFKCKVNNKDLPAPIERTISKPKGSV
RAPQVYVLPPPEEEMTKKQVTLTCMVT-----DIYVEWTNNGKTELNYKNTEPVLDSDGSYFMYSKLRVEKKNWVERNSYSCSVV HEGRHNHHTTKSFSR----

HC_1.3
QIQLVQSGPELKKPGETVKLSCKASGYTFTNYGMNWVK--------WMGWINTNTGEPTYADTVKGRFTISR--------ASLNNLKNEDTALYYCARHDG---------DYWGQG
TTLTVSSAKTTAPSVYPLAPVCGDTTGSSVTLGCLVK----------NSGSLSSGVHTFPAVLQS--------------------------------VDKKIEPRGPTIKPCPPC
KCPAPNLLGGPSVFIFPPK--------------------------------VNNVEVHTAQTQTHREDYNSTLRVVSALPIQHQDWMSGKEFKCKVNNKDLPAPIERTISKPKGSV
RAPQVYVLPPPEEEMTKKQVTLTCMVT-----DIYVEWTNNGKTELNYKNTEPVLDSDGSYFMYSKLRVEKKNWVERNS YSCSVV HEGRHNHHTTKSFSR----

HC_1.4
QIQLVQSGPELKKPGETVKLSCKASGYTFTNYGMNWVK--------WMGWINTNTGEPTYADTVKGRFTISR--------ASLNNLKSEDTALYYCARHDG---------DYWGQG
TTLTVSSAKTTAPSVYPLAPVCGDTTGSSVTLGCLVK----------NSGSLSSGVHTFPAVLQS--------------------------------VDKKIEPRGPTIKPCPPC
KCPAPNLLGGPSVFIFPPK--------------------------------VNNVEVHTAQTQTHREDYNSTLRVVSALPIQHQDWMSGKEFKCKVNNKDLPAPIERTISKPKGSV
RAPQVYVLPPPEEEMTKKQVTLTCMVT-----DIYVEWTNNGKTELNYKNTEPVLDSDGSYFMYSKLRVEKKNWVERNSYSCSVVH EGRHNHHTTKSFSR----

Figure 6.36 Putative light chain sequences for heavy chain 1 (HC1) and heavy chain 2 (HC2) assembled from exported peptides.

Figure legend: Tryptic peptide; Glu-C peptide; Asp-N peptide; overlapping tryptic and Asp-N peptide residues. Peptides derived from: a standard database match are not in bold/ underlined; ***de novo* sequencing are bold;** SPIDER database matches with a given PTM are underlined; **SPIDER database match using de novo sequences and PTMs are in bold and underlined**.

6.2.14.3 Identification of two putative N-terminal sequences for the anti-TAFC IgG heavy chain

Two conflicting peptides aligning to the N-terminus were derived from the assembly; LVESGGGLVK and QIQLVQSGPELK were both identified as putative N-terminal sequences (Figure 6.36). QIQLVQSGPELK was originally identified by *de novo* sequencing as QLQLVQSGPELK with an isoleucine-leucine mismatch at position 2. However, upon database interrogation this peptide was aligned to several proteins including that shown in Figure 6.37 and the leucine was corrected to isoleucine. Isoleucine and leucine share an identical mass (113.084064) and are therefore virtually impossible to differentiate using their *m/z* alone in *de novo* sequencing. Thus, database alignment to an IgG sequence containing isoleucine provides stronger support for the presence of an isoleucine residue and that identification, as leucine was a *de novo* sequencing error. BLAST sequence analysis indicated that the template protein used to correct this mismatch was an IgG Fab with 100% identity (Accession: 2ADF_H). Though the isotype was not reported, the protein contained the VDKK sequence reported in all IgG isotypes except IgG_3. Interestingly, the QIQLVQSGPELK peptide was uniquely detected in the *de novo* sequencing results after immunoaffinity purification (area = 3.6 X 10^6; ALC = 84%). A search for peptides matching 'QIQL' or 'QLQL' yielded no results in the *de novo* sequences from the heavy chain before immunoaffinity purification. Importantly, this suggests an enrichment of the QIQLVQSGPELK peptide upon immunoaffinity purification. Hence, this more likely represents the N-terminus of the anti-TAFC IgG.

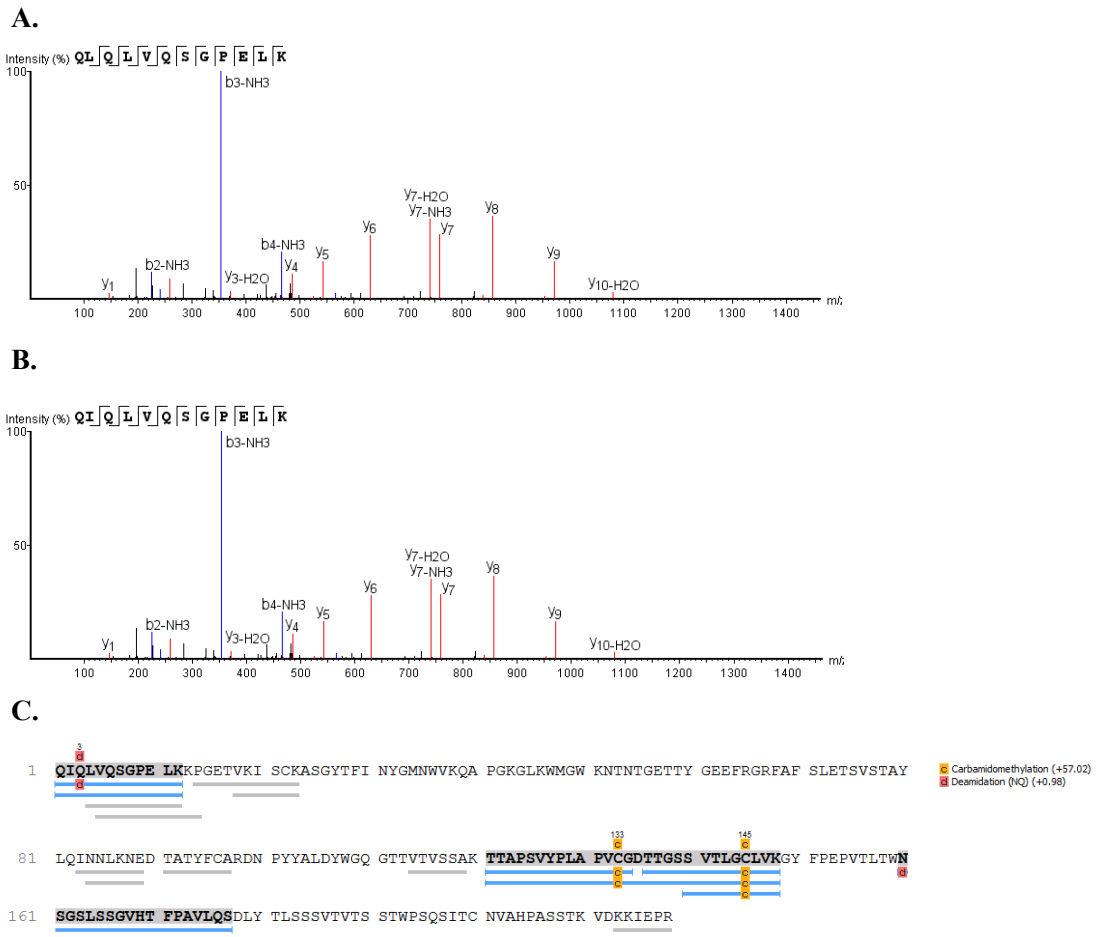

Figure 6.37 Detection of the putative N-terminal QIQLVQSGPELK sequence in IgG after immunoaffinity purification. (A) *De novo* sequencing originally identified this peptide with an isoleucine-leucine mismatch at position 2 (area = 3.6 X 10^6; ALC = 84%). (B) Database interrogation using the *de novo* sequences results corrected this mismatch (area = 3.6 X 10^6; -10logP = 62) following (C) alignment to an IgG Fab domain (27% sequence coverage; -log10P score = 186; 6 peptides identified (0 unique)). Peptides derived from MS analysis are shown in blue or grey aligning to template protein sequence.

The other putative N-terminal sequence, LVESGGGLVK, was found in several peptides identified by *de novo* sequencing of IgG both before (6 peptides) and after (3 peptides) immunoaffinity purification. The spectra used for the *de novo* sequencing of the most abundant of these peptides is shown in Figure 6.38. This peptide was subsequently matched to several proteins including that shown in Figure 6.39. BLAST sequence analysis indicated that the template protein was an IgG_{2a} Fab with 100% identity (IgG_{2a} heavy chain, partial [*Mus musculus*]; Accession: AAC98952.1).

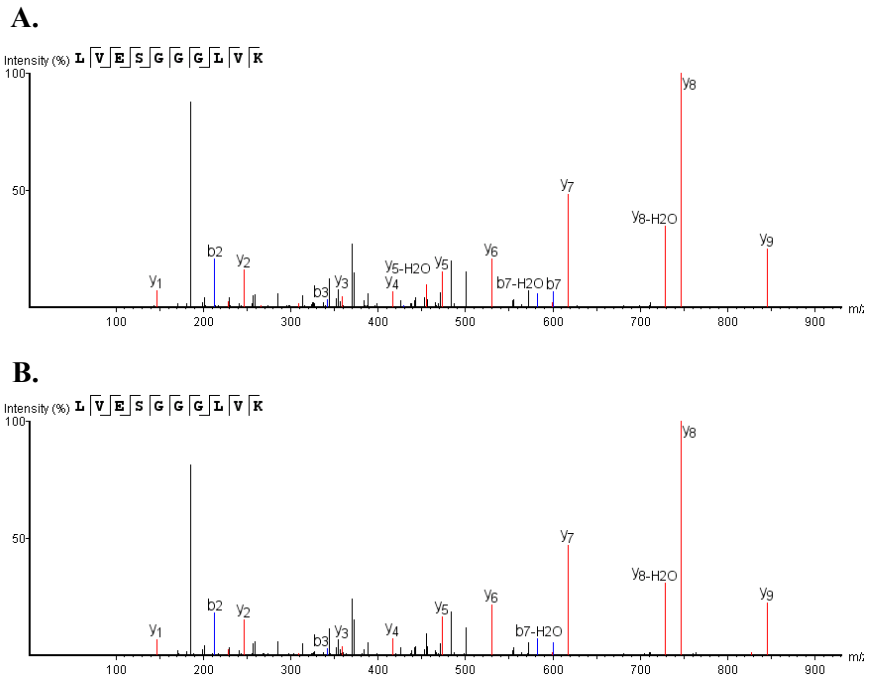

Figure 6.38 Detection of the putative N-terminal LVESGGGLVK sequence. *De novo* sequencing identified this peptide in IgG (A) before (area = 8.9 X 10^8; ALC = 94%) and (B) after (area = 9.9 X 10^6; ALC = 93%) immunoaffinity purification.

Figure 6.39 Alignment of the putative N-terminal LVESGGGLVK sequence to an IgG_{2a} (A) before (18% sequence coverage; -log10P score = 155; 7 peptides identified (0 unique)) and (B) after (29% sequence coverage; -log10P score = 207; 7 peptides identified (0 unique)) immunoaffinity purification. Peptides derived from MS analysis are shown in blue or grey aligning to template protein sequence.

6.2.14.4 Identification of conserved heavy chain domain sequences for the anti-TAFC IgG

Several sequences covering the end of the conserved heavy chain domains (CH_1) were derived from the assembly (Figure 6.36). One peptide was selected from these for reverse primer design to amplify the heavy chain Fab region; VDKKIEPR. The VDKKIEPR sequence was identified during a SPIDER database search after immunoaffinity purification when aligning to several proteins including that shown in Figure 6.40. BLAST sequence analysis indicated that this template protein was an IgG with 100% identity (immunoglobulin heavy chain, partial [*Mus musculus*]; Accession: AAN86780.1). The peptide contained a post-translational modification with the carbamylation of the N-terminal valine residue. This may account for its

lack of identification during *de novo* sequencing or standard database matching, as only carbamidomethylation, oxidation (methionine) and deamidation (asparagine or glutamine) were considered for modifications during these searches. Given the absence of VDKK in IgG_3 sequences, as discussed earlier, amplification of cDNA using this sequence is highly suitable for this project as it further reduces the likelihood of amplifying cDNA from the IgG_3 which appears to be predominant in the total IgG. A search for peptides matching 'VDKK' yielded no results in the SPIDER search for the heavy chain before immunoaffinity purification. Importantly, this suggests an enrichment of the VDKKIEPR peptide upon immunoaffinity purification.

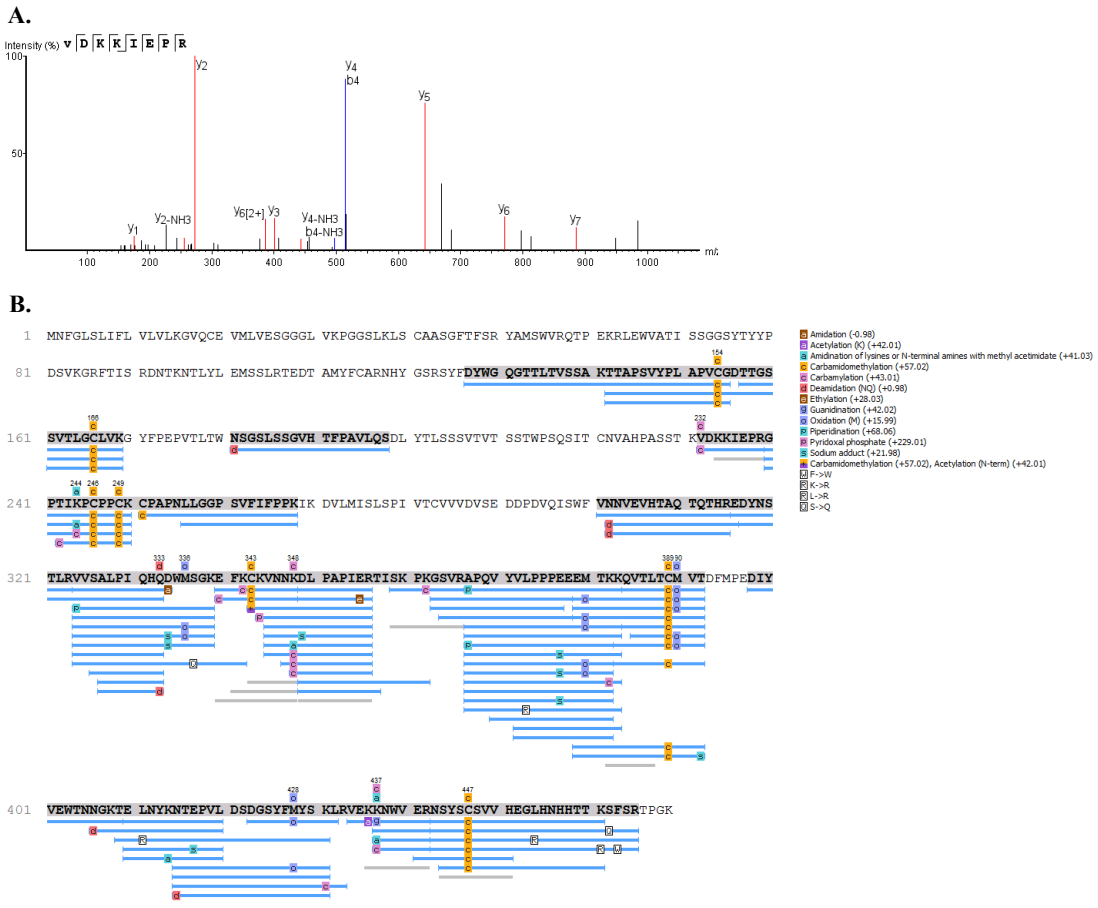

Figure 6.40 Detection of the CH_1 domain sequence, VDKKIEPR, in IgG after immunoaffinity purification. (A) This peptide was initially identified in a SPIDER database search (area = 1.7 X 10^5; -10logP = 58) following (B) alignment to an IgG

(55% sequence coverage; -log10P score = 392; 60 peptides identified (0 unique)) with inclusion of various PTMs. Peptides derived from MS analysis are shown in blue or grey aligning to template protein sequence.

6.2.15 MS-based characterisation of the immunoaffinity purified anti-TAFC IgG light chain

Two bands were observed following SDS-PAGE analysis of immunoaffinity purified IgG; a faint band at approximately 26 kDa (band A; light chain A (LCA)) and a band at approx. 25 kDa (band B; light chain B (LCB)) (Figure 6.31). Along with the single light chain observed in SDS-PAGE analysis of IgG before immunoaffinity purification, all bands were excised, digested with trypsin, Asp-N, or Glu-C and analysed by Q-Exactive LC-MS/MS (Section 2.2.13.2 and 2.2.13.7). Mass spectra were subsequently analysed using PEAKS for peptide identification and protein alignment as per Section 2.2.14.3 based on the ALPS system outlined by Tran *et al.* (2016). Peptides were identified by *de novo* sequencing and initially searched against a database containing murine antibodies and common contaminant proteins (from Tran *et al.,* (2016)). Following isotype identification, *de novo* sequences were searched again against a modified database also including additional IgG_{2a} κ antibody sequences from the online database, abYsis (www.abysis.org) (Swindells *et al.*, 2017).

6.2.15.1 Peptides show alignment to κ before and after immunoaffinity purification

Peptides from the IgG light chains before and after immunoaffinity purification (digested with trypsin, Asp-N, or Glu-C) were analysed by LC-MS/MS. Mass spectra were subsequently analysed using PEAKS for peptide identification and protein

alignment as per Section 2.2.14.3. Spectra were initially subjected to complete *de novo* sequencing for peptide identification. *De novo* sequences were then searched against a database containing murine antibodies and common contaminant proteins from Tran *et al.* (2016). The proteins with the highest score for all light chains are shown in Figure 6.41. The same protein was identified with the highest score before and after immunoaffinity purification in the case of light chain A only. The protein identified with the highest score for light chain B differed to that identified before immunoaffinity purification. All three proteins contained the conserved domain found in κ light chains. This is illustrated in a Clustal Omega alignment of the template proteins to the conserved κ domain of a murine light chain (UniProt) (Figure 6.42). Following this observation, it was therefore hypothesized that the anti-TAFC antibody had a κ light chain. With this in mind, an additional PEAKS database search was carried out for all further analysis, using the *de novo* sequences to interrogate a modified database including that of Tran *et al.* (2016) supplemented with additional IgG_{2a} and κ light chain sequences from the online antibody sequence database, abYsis (www.abysis.org) (Swindells *et al.*, 2017).

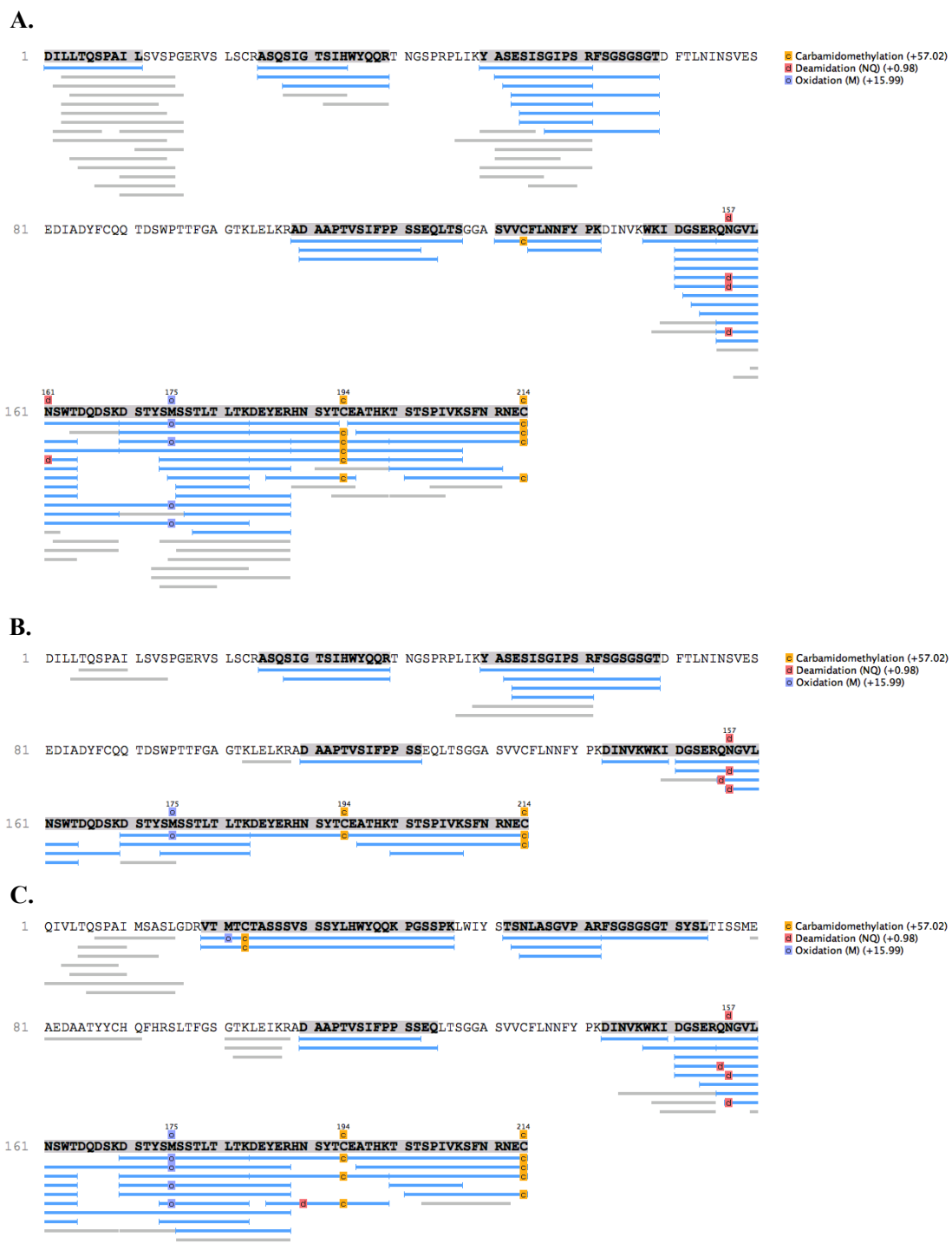

Figure 6.41 Peptides from the IgG light chain before and after immunoaffinity purification show alignment to immunoglobulin κ light chains. (A) Before immunoaffinity purification (67% sequence coverage; -log10P score = 396; 48 peptides identified (0 unique)). (B) After immunoaffinity purification (band A; light chain A) (56% sequence coverage; -log10P score = 308; 18 peptides identified (0

unique)). (C) After immunoaffinity purification (band B; light chain B) (65% sequence coverage; -log10P score = 327; 26 peptides identified (0 unique)). The same protein was identified with the highest score before and after immunoaffinity purification for light chain A and not light chain B. Peptides derived from MS analysis are shown in blue or grey aligning to template protein sequence.

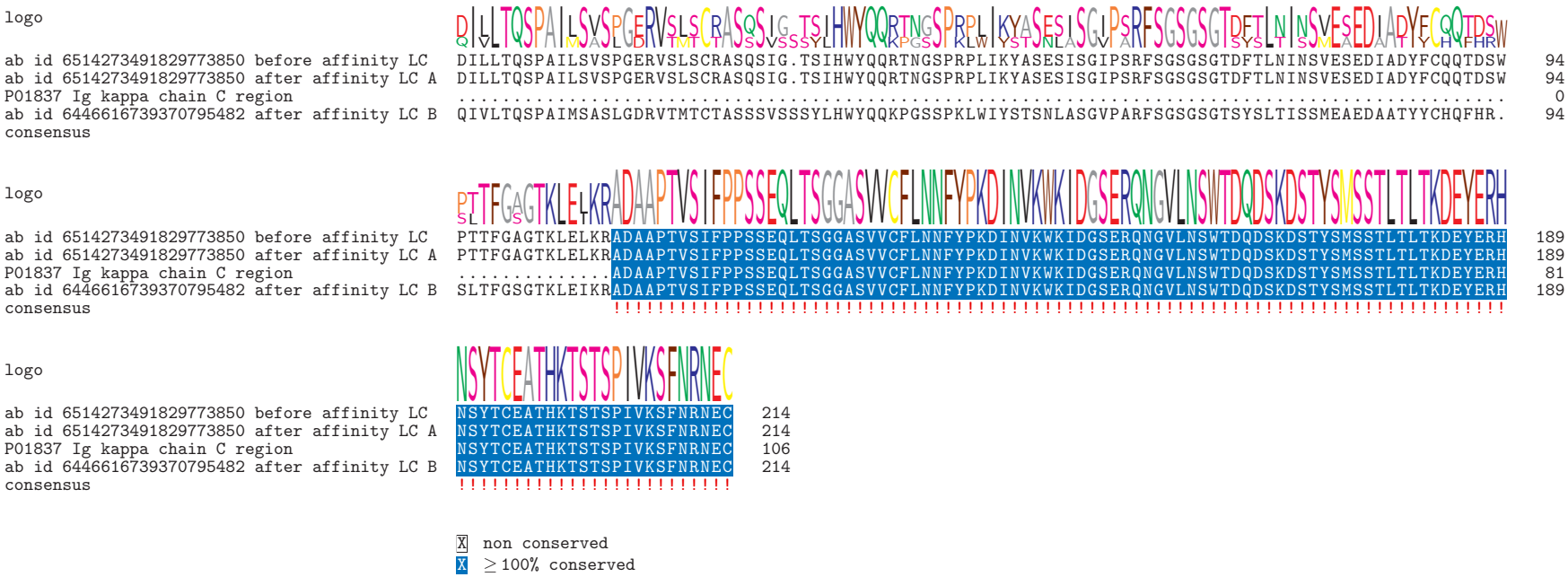

Figure 6.42 Clustal Omega alignment of the template proteins with the highest scores for all light chains with the murine κ light chain conserved domain, “Ig kappa chain C region” (UniProt). All proteins show complete alignment to the κ light chain conserved domain. Template protein names include the following terms in their identifiers; LC: Light chain from before immunoaffinity purification. LC A: Light chain A from after immunoaffinity purification. LC B: Light chain B from after immunoaffinity purification.

6.2.15.2 Assembly of peptides for putative light chain peptide sequences

Peptides were exported from PEAKS and assembled manually and using the ALPS program from Tran *et al.* (2016) as described in Section 2.2.14.3 for light chains after immunoaffinity purification (bands A and B independently). Peptide lists were refined to reduce redundancy. Figure 6.43 and 6.44 show the final assembled peptides for the putative sequence of light chain A and B, respectively. As with the heavy chain, in several instances, two peptides were identified aligning to the same regions of the antibody. Specifically, peptide conflicts were identified at residues 46-94 and 105-123 for light chain A, and residues 20-40 for light chain B. As it was not possible to unequivocally determine which was truly associated with the anti-TAFC IgG all peptides were listed. This resulted in a total of 4 putative anti-TAFC light chain sequences using the different combinations for light chain A and 2 possible sequences for light chain B. All peptide lists exported from PEAKS, output from ALPS, collectively gathered peptides, and manually assembled sequences are found in the Appendices in the folder, 'Data for antibody sequences'.

LCA_1.1
DILLTQSPAILSVSPGER------ASQSIGTSIHWYQQR------LWIYTTSNLASGVPAR--------------------------------SPPTFGGGTK-ELNYKNTEPVL-
-------------------------DIN VKWKIDGSERQNGVLNSWTDQDSKDSTYSMSSTLTLTKDEYERHNSYTCEATHKTSTSPIVKSFNRNEC

LCA_1.2
DILLTQSPAILSVSPGER------ASQSIGTSIHWYQQR------LWIYTTSNLASGVPAR--------------------------------SPPTFGGGTK------DAAPTVS
IFPPSS--------------------DIN VKWKIDGSERQNGVLNSWTDQDSKDSTYSMSSTLTLTKDEYERHNSYTCEATHKTSTSPIVKSFNRNEC

LCA_1.3
DILLTQSPAILSVSPGER------ASQSIGTSIHWYQQR------**LLLKYA**SESLSGLPSRFSGSGSGT**SYSLTLSSLEAEDAATYYCHQYHR**SPPTFGGGTK-ELNYKNTEPVL-
-------------------------DIN VKWKIDGSERQNGVLNSWTDQDSKDSTYSMSSTLTLTKDEYERHNSYTCEATHKTSTSPIVKSFNRNEC

LCA_1.4
DILLTQSPAILSVSPGER------ASQSIGTSIHWYQQR------**LLLKYA**SESLSGLPSRFSGSGSGT**SYSLTLSSLEAEDAATYYCHQYHR**SPPTFGGGTK------DAAPTVS
IFPPSS--------------------DIN VKWKIDGSERQNGVLNSWTDQDSKDSTYSMSSTLTLTKDEYERHNSYTCEATHKTSTSPIVKSFNRNEC

Figure 6.43 Putative light chain sequences for light chain A (band A; LCA) assembled from exported peptides.

Figure legend: Tryptic peptide; Glu-C peptide; Asp-N peptide; overlapping tryptic and Asp-N peptide residues; overlapping Glu-C and Asp-N peptide residues; overlapping tryptic Asp-N, and Glu-C peptide residues. Peptides derived from a: standard database match are not in bold/ underlined; ***de novo*** **sequencing are bold;** SPIDER database match with a given PTM are underlined; **SPIDER database match using de novo sequences and PTMs are in bold and underlined.**

LCB_1.1
QIVLTQSPAIMSAG—ERVTMTCTASSSVSSSYLHWYQQKPGSSPKLWIYTTSNLASGVPAR**FSGSGSGTSYSLTLSSMEAEDAATYYCHQYHRPPSGFGGGTKLELK**—DAAPTVSI
FPPSS------------------**KDANVAWKI**DGSERQNGVLNSWTDQDSKDSTYSMSSTLTLTKDEYERHNSYTCEATHKTSTSPIVKSFNRNEC

LCB_1.2
QIVLTQSPAIMSAG—ERVT----ASQSLGT-SLHWYQ--PGSSPKLWIYTTSNLASGVPAR**FSGSGSGTSYSLTLSSMEAEDAATYYCHQYHRPPSGFGGGTKLELK**—DAAPTVSI
FPPSS------------------**KDANVAWKI**DGSERQNGVLNSWTDQDSKDSTYSMSSTLTLTKDEYERHNSYTCEATHKTSTSPIVKSFNRNEC

Figure 6.44 Putative light chain sequences for light chain B (band B; LCB) assembled from exported peptides.

Figure legend: Tryptic peptide; Glu-C peptide; Asp-N peptide; overlapping tryptic and Asp-N peptide residues; overlapping Glu-C and Asp-N peptide residues; overlapping tryptic Asp-N, and Glu-C peptide residues. Peptides derived from a: standard database match are not in bold/ underlined; ***de novo* sequencing are bold;** SPIDER database match with a given PTM are underlined; **SPIDER database match using de novo sequences and PTMs are in bold and underlined.**

6.2.15.3 Identification of a putative N-terminal sequence for light chain A

A putative light chain A N-terminal sequence was derived from the assembly; DILLTQSPAILSVSPGER (Figure 6.43). DILLTQSPAILSVSPGER was identified during a SPIDER database search after immunoaffinity purification when aligning to several proteins including that shown in Figure 6.45. It was identified with a glutamine substitution for glutamic acid at position 17. This was corrected upon alignment to a light chain, which was also associated with aligning peptides LTQSPAILSVSPGER and ILSVSPGER, both with amidations at position 14 and 8 respectively. The presence of post-translational modifications in these peptides may account for their lack of identification during *de novo* sequencing or standard database matching, as only carbamidomethylation, oxidation (methionine) and deamidation (asparagine or glutamine) were considered as modifications during these searches. Interestingly, the template protein associated with these peptides was also observed to have the highest sequence coverage before immunoaffinity purification. Thus, it is possible that the presence of this protein represents carry-over of non-specifically binding antibodies following immunoaffinity purification.

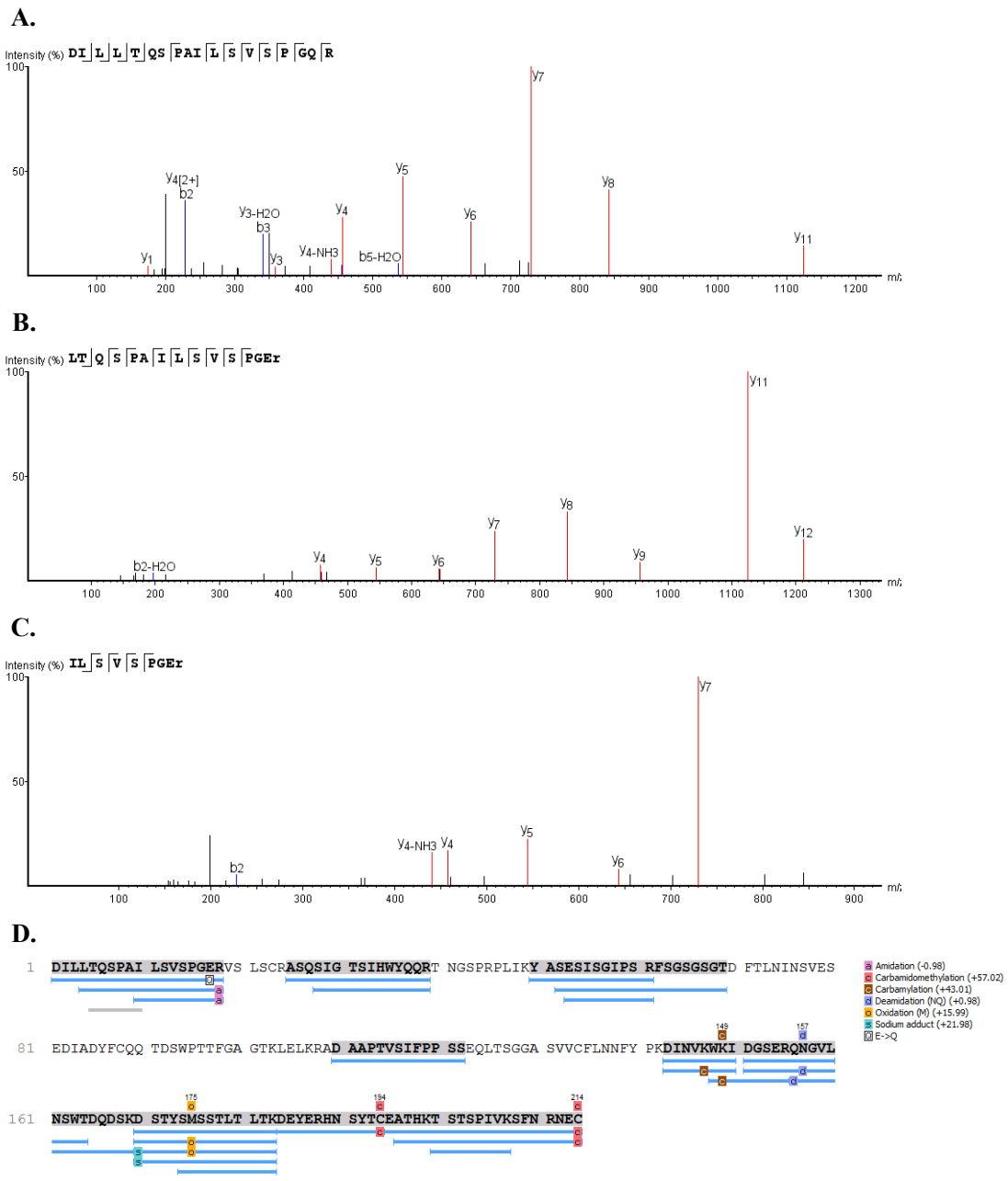

Figure 6.45 Detection of the putative N-terminal DILLTQSPAILSVSPGER sequence in IgG light chain A after immunoaffinity purification. (A) This peptide was identified in a SPIDER database search (area = 5.4 X 10^4; -10logP = 67) with a glutamine substitution for glutamic acid at position 17. This was corrected with detection of peptides (B) LTQSPAILSVSPGER (area = 8.4 X 10^4; -10logP = 65) and (C) ILSVSPGER (area = 2.8 X 10^4; -10logP = 44) and (D) alignment of all peptides to a light chain with a conserved κ domain (65% sequence coverage; -log10P score =

301; 20 peptides identified (0 unique)) with inclusion of various PTMs. Peptides derived from MS analysis are shown in blue or grey aligning to template protein sequence.

6.2.15.4 Identification of putative N-terminal sequence for light chain B

A putative light chain B N-terminal sequence was derived from the assembly; QIVLTQSPAIMSAGERVT (Figure 6.44). QIVLTQSPAIMSAGERVT was originally identified by *de novo* sequencing as QLVLTQSPALMSASLGER with several mismatches at positions 2, 10, and 14. However, upon database interrogation this peptide was aligned to a light chain κ variable region (abYsis accession: 006454) and several residues were corrected (Figure 6.46). A search for peptides matching QIVLTQ or QLVLTQ yielded no results in the *de novo* sequences from the light chain before immunoaffinity purification. Importantly, this suggests an enrichment of the QIVLTQSPAIMSAGERVT peptide upon immunoaffinity purification.

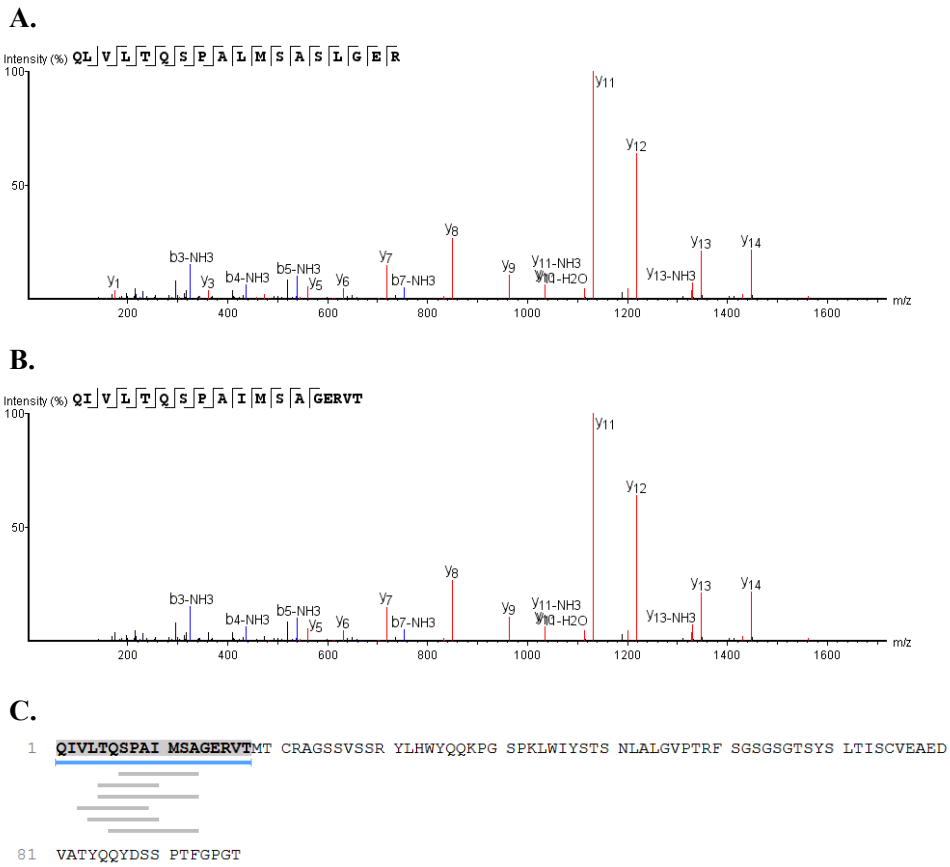

Figure 6.46 Detection of the putative N-terminal QIVLTQSPAIMSAGERVT sequence in IgG after immunoaffinity purification. (A) *De novo* sequencing originally identified this peptide with several mismatches (area = 7.2 X 10^6; ALC = 84%). (B) Database interrogation with the *de novo* sequence results corrected these mismatches (area = 7.2 X 10^6; -10logP = 53) by (C) alignment to a light chain κ variable region (19% sequence coverage; -log10P score = 61; 1 peptide identified (1 unique)).

6.2.15.5 Identification of conserved κ light chain C-terminal sequence

A putative light chain C-terminal sequence was derived from the assembly; EATHKTSTSPIVKSFNRNEC (Figure 6.43 and 6.44). This peptide was detected in a standard database search in all light chain peptide analysed (including before and after immunoaffinity purification) (Figure 6.47). It was found associated with several different antibodies for all analyses. Alignment of this peptide to the conserved

domain of a murine κ light chain (UniProt) indicates this is conserved for the κ isotype (Figure 6.48).

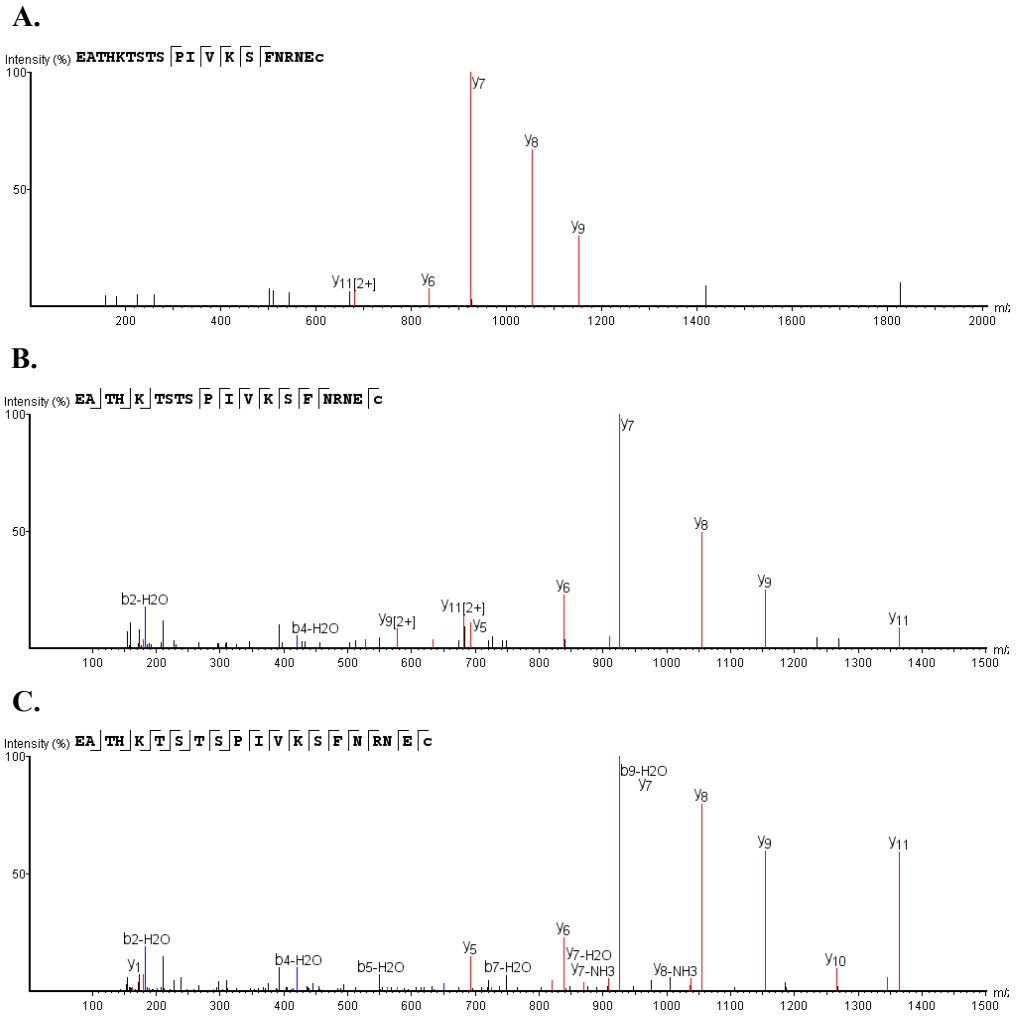

Figure 6.47 Detection of the putative C-terminal sequence, EATHKTSTSPIVKSFNRNEC, in all IgG light chains (before and after immunoaffinity purification). This peptide was identified in a standard database search of (A) the light chain from before immunoaffinity purification (area = 2.4 X 10^6; -10logP = 50), (B) light chain A from after immunoaffinity purification (area = 8.0 X 10^5; -10logP = 62), and (C) light chain B from after immunoaffinity purification (area = 5.9 X 10^6; -10logP = 78).

Figure 6.48 Clustal Omega alignment of the putative κ light chain C-terminal sequence, EATHKTSTSPIVKSFNRNEC, ('Ig kappa chain C terminal') to the murine conserved κ light chain domain, 'Ig kappa chain C region (UniProt).

6.2.16 Primer design using putative anti-TAFC IgG Fab N- and C-terminal sequences

The putative N- and C-terminal sequences obtained from Section 6.2.14 and 6.2.15 are summarised in Table 6.3. These were subsequently used by Dr Linan Xu to design degenerate primers for the specific amplification of anti-TAFC Fab from hybridoma cDNA (Table 6.4).

Table 6.3 Summary of the putative N- and C-terminal sequences for the anti-TAFC IgG_{2a} obtained from Section 6.2.14 and 6.2.15.

Sequence type:	Chain:	Name:	Peptide:	Primer type:
N-terminus	Heavy	HC1N	QIQLVQSGPELK	FWD
N-terminus	Heavy	HC2N	LVESGGGLVKGGSLK	FWD
C-terminus	Heavy	HCXC	VDKKIEPR	REV
N-terminus	Light	LCAN	DILLTQSPAILSVSPGER	FWD
N-terminus	Light	LCBN	QIVLTQSPAIMSAGERVT	FWD
C-terminus	Light	LCC	EATHKTSTSPIVKSFNRNEC	REV

Table 6.4 Primers designed for the heavy chain based on N- and C-terminal sequences obtained in Section 6.2.14 and 6.2.15. Restriction sites are depicted in lower case.

Name:	**Final primer with restriction site:**
HC1N-1	gcgaattcCARATHCARTTRGTNCAA
HC1N-2	gcgaattcCARATHCARCTNGTNCAA
HC1N-3	gcgaattcCARATHCARTTRGTNCAG
HC1N-4	gcgaattcCARATHCARCTNGTNCAG
HC2N-1	gcgaattcGGCGGNGGNTTRGTNAAA
HC2N-2	gcgaattcGGCGGNGGNCTNGTNAAA
HC2N-3	gcgaattcGGCGGNGGNTTRGTNAAG
HC2N-4	gcgaattcGGCGGNGGNCTNGTNAAG
HCXC-R	gcgtcgacGGYTCDATYTTYTTRTCNAC

Table 6.5 Primers designed for light chains A and B based on N- and C-terminal sequences obtained in Section 6.2.14 and 6.2.15. Restriction sites are depicted in lower case.

Name:	Final primer with restriction site:
LCAN-1	gcgaattcGAYATHTTRTTRACNCA
LCAN-2	gcgaattcGAYATHTTRCTNACNCA
LCAN-3	gcgaattcGAYATHCTNTTRACNCA
LCAN-4	gcgaattcGAYATHCTNCTNACNCA
LCBN-1	gcgaattcCARTCNCCNGCNATHATG
LCBN-2	gcgaattcCARAGYCCNGCNATHATG
LCC-R	gcgtcgacGTYTTRTGNGTNGCYTC

6.3 Discussion

Siderophore detection or deactivation represents a promising basis for the development of novel diagnostic and therapeutic strategies against *A. fumigatus* infection. To this end antibodies against TAFC were raised. In Chapter 4, DAFC was generated as a TAFC analogue by acetylating two of the three free amines in FSC. Fluorescently derivatised DAFC was taken up by *A. fumigatus* during iron-deplete growth despite amine modification. Using a similar strategy, a TAFC immunogen was synthesized using acetylated FSC. RP-HPLC purified FSC^{+Fe} was acetylated by SNA resulting in a heterogeneous mixture of FSC, MAFC, DAFC, and TAFC (collectively termed acetylated FSC) with enrichment for MAFC and DAFC. Acetylated FSC was then conjugated to KLH *via* heterobifunctional crosslinkers, Sulfo-SMCC and SATA, respectively, similar to FSC conjugation to KLH in Chapter 5 (Section 6.2.1). Utilising such a heterogeneous immunogen left potential for the same mouse to raise both FSC and TAFC antibodies, both of which could be isolated at the hybridoma screening stage. By using this strategy, there was further opportunity for developing an anti-FSC antibody, should immunisations with the FSC immunogen from Chapter 5 prove unsuccessful. Ultimately, generation of FSC antibodies from the immunogen synthesized in Chapter 5 was successful and additional attempts to generate anti-FSC antibodies were not necessary.

Generation of MAFC-$(SMCC)_1$ and DAFC-$(SMCC)_1$ were confirmed by RP-HPLC analysis. The peak associated with MAFC-$(SMCC)_1$ was identified by LC-MS/MS with detection of a doubly charged ion (M: 1040.4, $[M+2H]^{2+}$: observed *m/z* 521.1; expected *m/z* 521.2) (Figure 6.4). The peak associated with DAFC-$(SMCC)_1$ was identified by LC-MS/MS with detection of a singly charged ion (M: 1082.4, $[M+H]^{+}$: observed *m/z* 1083.4; expected *m/z* 1083.4) (Figure 6.5). After deprotection,

thiol incorporation in SATA-KLH was estimated to be 88 μmoles per μmole KLH (Section 6.2.1.3). After combination, the successful conjugation of MAFC-/ DAFC-SMCC to SATA-KLH was measured by quantifying siderophore incorporation using the λ_{max} of ferri-siderophores (440 nm), with an estimated 129 nmol siderophore per mg KLH. The acetylated FSC-KLH immunogen was then used to immunise BALB/c mice (n = 3).

As per Chapter 5, a competitive TAFC ELISA was developed for screening tail bleeds taken from the immunised mice (n =3) (Section 6.2.3). The principle of this ELISA is illustrated in Figure 6.10. Acetylated FSC^{+Fe} was conjugated to BSA *via* Sulfo-SMCC and SATA modification, respectively, for coating ELISA plates (Section 6.2.3.2). As with the competitive FSC ELISA in Chapter 5, the same crosslinkers used for the immunogen were used to generate this conjugate. By using the competitive ELISA format only antibodies against TAFC were selected and not antibodies against the crosslinkers. Moreover, despite use of a heterogeneous mixture of conjugation (MAFC-/ DAFC-BSA) for coating the ELISA plates, the use of competing TAFC allowed for exclusive detection of anti-TAFC antibodies. Only anti-TAFC antibodies would bind the acetylated FSC-BSA on the plate and show competition for TAFC. Successful conjugation of acetylated FSC-SMCC to SATA-BSA was measured by quantifying the siderophore incorporation using the λ_{max} of ferri-siderophores (440 nm), with an estimated 156 nmol siderophore per mg BSA. Acetylated FSC-BSA was then coated onto wells of an ELISA plate in a titre of concentrations (0.03 – 1.9 μg/ ml) and probed with murine antisera to identify optimal assay conditions (Section 6.2.5.1). A coating concentration of 0.12 μg/ ml was selected for further analysis. This was used in the competitive TAFC ELISA along with a titre of competing TAFC (100 μM – 1.56 μM). Using this format, sera from all

three mice showed competitive anti-TAFC activity (Section 6.2.5.2). Mouse F was selected for further analysis as it exhibited the highest $\Delta OD_{450/620}$ of all the mice upon the addition of competing TAFC (OD 1.25 at 0 μM TAFC and 0.59 at 100 μM TAFC). When mouse F was subsequently screened with the competing TAFC exchanged for free iron or BmGT, no competition was observed. This indicated that the polyclonal antibodies in mouse F were not non-specifically competing with TAFC. Furthermore, tail bleeds taken from an acetylated FSC-KLH immunised mouse prior to immunisation showed no anti-TAFC activity.

Mouse F was selected for sacrifice and splenectomy to develop hybridomas. A fusion efficiency of 66.2% was observed and resultant hybridomas were screened for anti-TAFC antibody production. The hybridoma supernatant was screened using the competitive TAFC ELISA only. In total, 74 hybridoma supernatants were screened and four hybridomas were ultimately carried forward; 1D1, 3B6, 3C7, and 6C6 (Section 6.2.6). Despite repeated efforts, we were unable to isolate a monoclonal anti-TAFC antibody producing hybridoma. However, following repeated subculture and screening, the 6C6 hybridoma was determined to be relatively stable, producing high amounts of antibody and was carried forward for anti-TAFC antibody production.

The 6C6 hybridoma was further sub-cultured and any supernatant collected. Isostrip™ (Roche) analysis initially indicated the 6C6 hybridoma produced predominantly IgG_3 with a κ light chain (Section 6.2.7). Further competitive ELISA analysis of the supernatant indicated the presence of an antibody that could detect TAFC at as low as 1.56 μM (Figure 6.19). IgG was subsequently purified from culture supernatant by Protein A affinity chromatography and analysed by SDS-PAGE (Section 6.2.8). The use of this IgG in a competitive TAFC ELISA was

established. After assay optimisation, ELISA analysis indicated high specificity for TAFC. Exchange of the competing TAFC for other microbial siderophores (ferrichrome or ornibactin) or BmGT resulted in no competition (Figure 6.24). Similar to the activity of anti-FSC IgM in Chapter 5, the anti-TAFC IgG showed no competition for FSC. This suggests that this antibody is also not directed against iron-binding region of these hydroxamate siderophores and that the acetyl groups are important to the molecule's antigenicity.

After further optimisation, competitive ELISA analysis indicated the anti-TAFC antibody was highly sensitive and could detect TAFC at as low as 0.1 μM (Figure 6.25). To validate the use of the ELISA for detecting TAFC in biological samples, ferrated supernatant from iron-deplete culture of *A. fumigatus* wild-type was added to the assay in parallel with purified competitive TAFC at an equivalent concentration. The assay was able to detect TAFC in *A. fumigatus* wild-type culture supernatant at comparable levels to purified TAFC (Figure 6.24).

The ability of the anti-TAFC IgG to detect TAFC at concentrations as low as 100 nM after only limited optimisation is very promising. Early stage sample analysis by Carroll *et al*. (2016) of the levels of TAFC in the sera of patients with suspected or probable/ proven Aspergillosis detected mean values of 11.6 ng/ ml (13 nM) and 9.7 ng/ ml (11 nM), respectively (Carroll *et al.*, 2016). Furthermore, analysis by Luptáková *et al.* (2017) of TAFC levels in urine from a rat model of Aspergillosis indicated a mean value of 370 ng/ ml (408.5 nM) (Luptáková *et al.*, 2017). Hence, the anti-TAFC IgG is within the range of clinically relevant levels for the detection of Aspergillosis. Further ELISA optimisation would likely yield a more sensitive ELISA system or a lateral flow device capable of detecting lower levels. However, significantly more analysis of TAFC levels in the sera and urine of patients and the

general population is required. Unfortunately, there was insufficient anti-TAFC IgG to fully explore the ability of anti-TAFC IgG to impede the uptake of TAFC, as was carried out for anti-FSC IgM in Chapter 5. The remainder of anti-TAFC IgG was instead dedicated to an MS-based peptide-sequencing project to obtain N- and C-terminal residues suitable for specific primer design to amplify the cDNA for the anti-TAFC IgG.

Given the sensitive detection capability of the anti-TAFC IgG this antibody shows significant promise for use in a point-of-care diagnostic assay for the detection of TAFC. Hybridomas are often inherently unstable; hence, if possible it is best to obtain the sequences of antibodies to permit large-scale production and long-term access to the antibody. Antibody sequencing can be facilitated by the amplification of hybridoma cDNA using isotype-specific primers. However, despite repeated efforts, it was not possible to obtain a monoclonal hybridoma producing anti-TAFC antibodies using 6C6. Therefore, there may have been multiple hybridomas present in 6C6 producing antibodies against multiple antigens including TAFC. For this reason, the amplification of antibody sequences from cDNA using isotype-specific primers was unsuitable. Such amplification could potentially amplify the cDNA of an antibody without TAFC activity.

In order to obtain the sequence of the anti-TAFC antibody Fab region, a proteogenomic strategy was implemented as described in Section 6.2.10. The anti-TAFC antibody was immunoaffinity purified using magnetic beads coated with acetylated FSC. The use of these beads in purifying anti-TAFC IgG was first functionally validated on an analytical scale (Section 6.2.11). Beads coated with and without acetylated FSC were incubated with Protein A purified IgG or TBST, flow-through was retained and after a wash step, beads were probed with an anti-mouse

IgG HRP to detect binding. Firstly, only incubation of the total IgG with beads coated in acetylated FSC resulted in antibody binding (Figure 6.28). In addition, the control using only TBST followed by the anti-mouse IgG HRP indicated limited non-specific binding by the secondary antibody. Secondly, when analysed by competitive TAFC ELISA, the flow-through of the total IgG incubated with control beads (without acetylated FSC) still showed the presence of anti-TAFC IgG (Figure 6.29). However, the flow-through of the total IgG incubated with acetylated FSC beads showed minimal anti-TAFC antibody activity. This suggests that the activation of the beads with acetylated FSC allowed them to bind the majority of the anti-TAFC antibodies in solution. Moreover, it indicates limited non-specific binding of antibodies to beads coated without acetylated FSC.

After the functionality of the beads in pulling down anti-TAFC IgG was determined, large-scale immunoaffinity purification was carried out. Protein A purified IgG was incubated with the acetylated FSC beads and any bound antibody eluted. In total, 1.2 mg of Protein A purified IgG from 6C6 culture supernatant was used and yielded 18 μg anti-TAFC antibody in total (Table 6.2). This was a surprisingly low yield representing only 1.5% of the total input IgG. Despite the relatively low yields of eluted antibody, the flow-through retained no anti-TAFC activity in the competitive TAFC ELISA indicating complete total binding of the anti-TAFC antibody. The eluted antibody was also analysed by competitive ELISA. Though used at a lower concentration (1 μg/ ml) than the Protein A purified antibody (2.5 μg/ ml), the eluted antibody showed a significantly higher OD ($p < 0.0005$; unpaired t-test) on the ELISA. When converted to OD (450/ 620 nm)/ μg protein input, Protein A purified IgG had an activity of 0.23 OD/ μg and immunoaffinity purified IgG has an activity of 3.6 OD/ μg. This indicates 94% less OD/ μg in the

Protein A purified IgG compared with the immunoaffinity purified IgG. Together this data clearly indicates that the anti-TAFC antibody comprises relatively little of the total IgG content produced by the 6C6 hybridoma. This again highlights the necessity of a MS-based sequencing strategy using immunoaffinity-purified antibody to obtain the antibody sequence.

The immunoaffinity purified anti-TAFC IgG was analysed by SDS-PAGE. Interestingly, in addition to a heavy and light chain at the expected sizes (55 and 25 kDa, respectively) another band, slightly higher than the predominant light chain was visible at 26 kDa. This band was quite faint and is not visible in the scanned image, however an arrow marking its location is denoted on Figure 6.31. Both light chain bands were subjected to further analysis with the 26 kDa band termed 'light chain A' and the 25 kDa band termed 'light chain B'. The Protein A purified IgG (henceforth considered 'before immunoaffinity purification') was also analysed by SDS-PAGE and showed heavy and light chain bands at the expected sizes. All heavy and light chain bands were excised in three pieces each and independently digested with three different enzymes (trypsin, Glu-C, or Asp-N) to generate three different antibody peptide maps. Peptides were analysed by Q-Exactive LC-MS/MS and mass spectra were interpreted using PEAKS protein bioinformatic software. The analysis method used was based on that outlined by Tran *et al*. (2016) using the ALPS workflow and is described in Section 2.2.14.3. Mass spectra of the same protein digested with the three enzymes (i.e. 3 raw MS files) were imported into PEAKS and analysed together. Peptides were identified using *de novo* sequencing in PEAKS, which were then searched against a database containing murine antibodies and common contaminant proteins (from Tran *et al.* (2016)). For the heavy chain analysis, database interrogation indicated the protein with the highest score before immunoaffinity

purification was an IgG_3 while after immunoaffinity purification the highest scoring protein was not an IgG_3 (Section 6.2.14.1). This was supported by isostrip analysis showing an IgG_3 in the culture supernatant but and an IgG_{2a} after immunoaffinity purification (Section 6.2.7 and 6.2.13). For the light chain analysis, database interrogation indicated all antibodies were of the κ isotype. This was expected as the majority of murine light chain antibodies are of the κ isotype (Janeway, 2001).

Following isotype identification, *de novo* sequences were searched again against a modified database supplemented with IgG_{2a} κ antibody sequences from the online database, abYsis (www.abysis.org) (Swindells *et al.*, 2017) using the parameters defined in Section 2.2.14.3.1. As per Tran *et al.* (2016), three lists of peptides were exported for each sample from this analysis representing (i) *de novo* sequences results on total mass spectra, (ii) results from the matching of *de novo* sequences to a database (using standard search parameters) in addition to any left over unmatched *de novo* sequences, and (iii) results from the matching of *de novo* sequences to a database (using modified search parameters allowing for errors in the *de novo* sequences or database sequences and for additional peptide modifications) in addition to any left over unmatched *de novo* sequences. These lists were processed using the ALPS.jar tool from Tran *et al.* (2016) to identify overlapping peptides. Sequence outputs were subjected to a BLAST search and any peptides matching a contaminant were removed. For the heavy chain, peptides found matching IgG_3 antibodies were also removed. Peptides generated from the ALPS assembly along with peptides manually extracted from database hits in PEAKS were collected. These were assembled into putative heavy and light chain sequences using overlapping regions and known template antibody sequences as a scaffold (Figure 6.36 6.43, and 6.44).

The generated N- and C-terminal sequences of the assembled antibody sequences were then further analysed. Two putative N-terminal sequences were identified corresponding to the same position in the immunoaffinity purified heavy chain, LVESGGGLVK and QIQLVQSGPELK (Figure 6.36). Interestingly, while the LVESGGGLVK was detected before and after immunoaffinity purification, the QIQLVQSGPELK peptide showed enrichment upon immunoaffinity purification. The QIQLVQSGPELK sequence therefore represents a more likely candidate for the anti-TAFC IgG N-terminus. However, it was decided to design forward primers based on both putative N-terminal sequences to attempt to amplify two sequences from cDNA and verify this *in vitro* in the future. Similarly, the putative CH_1 domain sequence VDKKIEPR showed enrichment upon immunoaffinity purification. This sequence has been identified in all IgG isotypes expect IgG_3 (Sheriff *et al.*, 1996). An observation that was supported upon aligning the sequences of all murine IgG isotype conserved domains using sequences from UniProt (Figure 6.42). Because the anti-TAFC antibody appears to be an IgG_{2a}, whereas the predominant antibody produced by the 6C6 hybridoma appears to be an IgG_3, VDKKIEPR represents an ideal sequence for reverse primer design.

A single putative N-terminal sequence was identified for light chain A, DILLTQSPAILSVSPGER (Figure 6.43). In addition, a single putative N-terminal sequence was identified for light chain B, QIVLTQSPAIMSAGERVT (Figure 6.44). Interestingly, the QIVLTQSPAIMSAGERVT sequence showed enrichment upon immunoaffinity purification (Section 6.2.15.4). However, like with the heavy chain N-terminal sequences, it was decided to design primers for both light chains to attempt to amplify two sequences from cDNA and verify this *in vitro* in the future. A putative light chain C-terminal sequence was also identified in all light chains

analysed, EATHKTSTSPIVKSFNRNEC. This sequence is conserved in all kappa light chains and is therefore suitable for reverse primer design for both light chain A and B.

The putative N- and C-terminal sequences derived from this work are summarised in Table 6.3. They were subsequently used to design degenerate primers. These will be used for the specific amplification of the anti-TAFC Fab sequence using cDNA synthesised from RNA isolated from the 6C6 hybridoma.

This work has demonstrated the generation of anti-siderophore antibodies against *A. fumigatus* extracellular siderophore, TAFC. Following Protein A purification, antibody characterisation indicated the antibody was a highly specific and sensitive anti-TAFC IgG capable of detecting TAFC at concentrations as low as 0.1 μM. This sensitivity places the detection capability of the anti-TAFC IgG within clinically relevant levels according to recent work showing the MS detection of TAFC in sera from patients with suspected or probable/ proven Aspergillosis as well as urine from a rat model of Aspergillosis (Carroll *et al.*, 2016; Luptáková *et al.*, 2017). Hence, this anti-TAFC antibody shows promise for incorporation into a point-of-care based diagnostic assay for *A. fumigatus* infection. Due to the potential of this antibody and the inherent instability of hybridomas, a proteogenomic strategy to sequence the anti-TAFC antibody was implemented. Using immunoaffinity purified anti-TAFC IgG, the putative N- and C-terminal residues of the anti-TAFC IgG Fab were identified by LC-MS/MS. These have been used to generate primers for the specific amplification of the anti-TAFC antibody Fab from hybridoma cDNA to obtain the full Fab sequence.

Chapter 7

Discussion

Chapter 7 Discussion

Iron is essential to all eukaryotes and almost all prokaryotes. Although one of the most abundant metals on earth, its bioavailability to living organisms is quite low due to formation of ferric hydroxides in aerobic environments. As a result, many iron-requiring microorganisms have developed sophisticated systems for the procurement of iron in starved environments (Caza and Kronstad, 2013; Crawford and Wilson, 2015; Haas, 2014). In *A. fumigatus* these mechanisms translate into virulence factors during colonisation of susceptible hosts (Haas, 2012; Moore, 2013). This is because human innate immune defences restrict the bioavailability of iron to invading pathogens (Cassat and Skaar, 2013; Caza and Kronstad, 2013). Exploiting this information to direct the development of new tools for diagnosing and treating *A. fumigatus* infection has been the premise of the work presented in this thesis. This was achieved in several respects, which will be further discussed throughout this Section and are summarised in Figure 7.1.

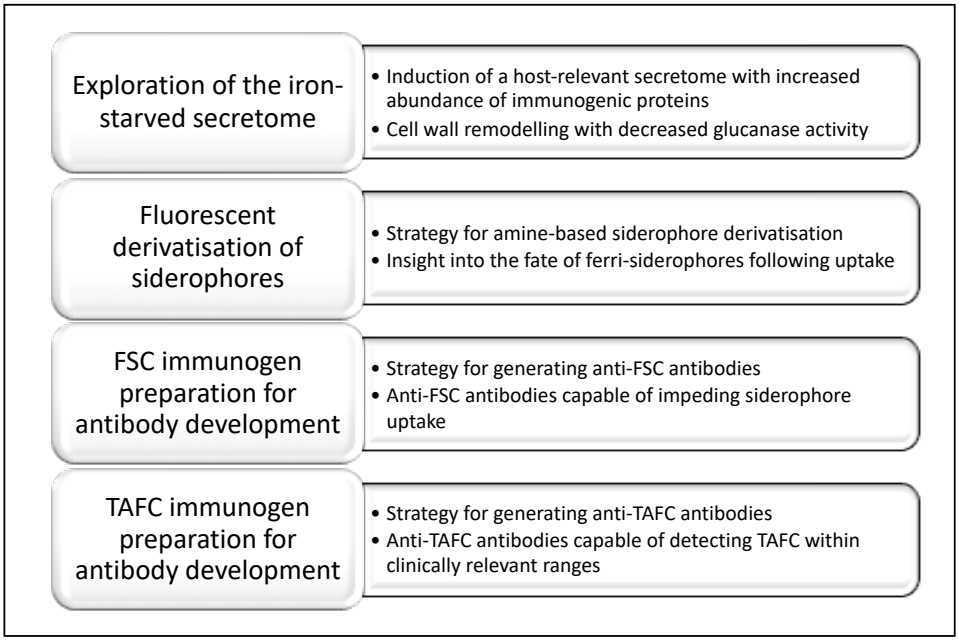

Figure 7.1 Summary of the key results for each research objective in this thesis.

Iron is embedded within biological systems; hence survival in an iron-starved environment prompts extensive remodelling of an organism's transcriptome, proteome, and metabolome. While significant efforts using transcriptomic and reverse genetic studies have informed on the magnitude and consequence of iron starvation in *A. fumigatus* (Haas, 2012, 2014, Schrettl *et al.*, 2008, 2010), only limited proteomic studies have been similarly conducted (Moloney *et al.*, 2016a; Mulvihill *et al.*, 2017). Proteome studies can provide a different and additive insight to transcriptional studies. While transcriptomic analysis can reveal the regulatory mechanisms governing iron metabolism, proteome analysis can determine protein abundances also incorporating post-translational regulatory mechanisms. Furthermore, proteomics can also inform on protein localisation through analysis of subcellular fractions and secreted proteins (Moloney *et al.*, 2016). The application of proteomics in this context was demonstrated in Chapter 3, whereby iron starvation was shown to induce significant remodelling of the *A. fumigatus* secretome.

Along with the cell wall, the secretome is pertinent to immune recognition, given its position at the host-pathogen interface. Detailed analysis in Chapter 3 indicated that iron starvation drastically altered the secretome of *A. fumigatus* and, consequently, the antigens it presents to the host. Many of the proteins with increased abundance under iron starvation had previously been defined as immunoreactive, either as allergens or through IgG reactivity with sera from patients with IA/ ABPA (Abad *et al.*, 2010; Asif *et al.*, 2010; Singh *et al.*, 2010a, 2010; Teutschbein *et al.*, 2016; Upadhyay *et al.*, 2012; Virginio *et al.*, 2014). Following development of an indirect ELISA, analysis of secreted proteins with human sera indicated significantly ($p < 0.0001$; paired t-test) greater immunoreactivity against proteins isolated from iron-deplete growth. This demonstrates that the collection of antigenic proteins

displayed to the host is influenced by iron bioavailability. Furthermore, it raises an important consideration for *in vitro* analysis of biomarkers in *A. fumigatus,* as such studies should aim to analyse proteins that are most relevant to host recognition.

Analysis of the iron-deplete secretome also indicated a differential abundance of enzymes involved in remodelling cell wall polysaccharide constituents. Interestingly, there was a directed differential abundance of enzymes acting on the cell wall component, glucan (Mouyna *et al.*, 2013). Glucan-directed enzymes with increased abundance were predominantly involved in glucan chain branching, elongation, or crosslinking. In contrast, enzymes with decreased abundance were predominantly involved in hydrolysing β-1,3-glucan chains as glucanases. This was supported by analysis of glucanase activity of the secreted proteome obtained from iron-limiting conditions. Proteins isolated from iron-deplete growth showed significantly ($p < 0.0001$; unpaired t-test) lower glucanase activity (mU/ mg) than those from iron-replete growth. Interestingly, many of these enzymes showed a similar reshuffling during the fungal response to azole exposure (Amarsaikhan *et al.*, 2017; Gautam *et al.*, 2016; Sorgo *et al.*, 2011). Azoles are a class of antifungals that target the integral cell membrane component, ergosterol (Valiante *et al.*, 2015). During iron starvation ergosterol levels in *A. fumigatus* are decreased due to the diversion of an ergosterol biosynthetic intermediate (mevalonate) to the production of siderophores for iron uptake (Figure 1.4) (Yasmin *et al.*, 2012). There appear to be similarities in stress responses to iron starvation and azole exposure, including the activation of a MAPK pathway known as the cell wall integrity pathway (Dichtl *et al.*, 2012, 2016; Jain *et al.*, 2011; Valiante *et al.*, 2015). A mutual activation of this pathway under both of these stressors suggests a compensatory cell wall remodelling in response to impaired cell membrane integrity, which was similarly observed in *C.*

albicans in response to azole exposure (Sorgo *et al.*, 2011). This phenotype indicates further implications for the *in vitro* study of *A. fumigatus,* as iron starvation can impact antifungal tolerance. *A. fumigatus* is more susceptible to membrane targeting antifungals, voriconazole and AMB, during iron-deplete growth (Yasmin *et al.*, 2012). Furthermore, a synergistic inhibition of growth is observed upon combinatorial use of iron chelators and antifungals; including lactoferrin with AMB, and deferiprone with ketoconazole (Zarember *et al.*, 2009).

Information on the response of microbial pathogens to iron starvation has already guided novel approaches for antimicrobial therapies. The production of iron-chelating siderophores by microorganisms can be hijacked in a Trojan horse strategy, whereby siderophores are conjugated to an antimicrobial to improve drug delivery (Ghosh *et al.*, 2017; Möllmann *et al.*, 2009; Schalk and Mislin, 2017). Though this has yet to be demonstrated in *A. fumigatus,* the uptake of fluorescent siderophores, revealed in Chapter 4, indicates a practical validity to the uptake of modified siderophores. In this work, FSC was used to generate a semi-synthetic TAFC analogue, DAFC, by acetylating two – as opposed to three – of the free amines in FSC. Both FSC and DAFC were then fluorescently derivatised with the fluorophore, NBD-X-SE. Uptake studies with both FSC- and DAFC-NBD showed a localisation of fluorescence to vacuoles within hyphae exclusively during iron-starved growth. This strongly suggests that the transporters expressed during iron-deplete growth mediated fluorescent siderophore uptake (Moloney *et al.*, 2016a). Moreover, preservation of uptake despite conjugation to NBD shows that, in this instance, siderophore uptake was preserved in *A. fumigatus* despite significant structural modification. Hence, in future, a similar workflow to that utilised in Chapter 4 could be implemented for the development of antifungal-siderophore conjugates. Whereby, FSC or DAFC are

conjugated to antifungal compounds containing functional groups amenable to cross-linker modification. Furthermore, fluorescently derivatised siderophores could also be implemented to screen for inhibitors of siderophore-mediated iron uptake.

Siderophore functionality can also be exploited as a therapeutic target by directly interfering with their uptake. This strategy is actually utilised by the mammalian innate immune system, whereby siderocalins (Lcn1 and Lcn2) bind microbial siderophores to prevent their uptake (Aznar and Dellagi, 2015; Clifton *et al.*, 2009; Dartt, 2011). Lcn1 can bind TAFC in addition to other bacterial and fungal siderophores and inhibits growth of *A. fumigatus in vivo* (Fluckinger *et al.*, 2004; Leal *et al.*, 2013). By raising antibodies against siderophores, a similar proteinaceous sequestration could be achieved with potentially much higher specificity. In addition, antibodies against siderophores could also be deployed in a diagnostic assay, whereby antibody-based siderophore detection in patient samples acts as a biomarker of *A. fumigatus* infection.

The presence of three free amine groups means FSC is particularly amenable to modification with the amine-reactive compounds. This is demonstrated in work by others (Knetsch *et al.*, 2015; Petrik *et al.*, 2017; Zhai *et al.*, 2015) and with the generation of several compounds in Chapter 4, including FSC-$(NBD)_1$ and DAFC-$(NBD)_1$. In a similar strategy to that used for NBD-X-SE derivatisation, immunogens consisting of FSC and acetylated FSC (predominantly MAFC and DAFC) conjugated to KLH, were generated by work presented in Chapters 5 and 6. Of note, across this and the fluorescent siderophore work was that FSC acetylation or conjugation to a protein appeared to stabilise FSC. The ester linkages of FSC are particularly susceptible to hydrolysis as a result of the neighbouring amine groups (Renshaw *et*

al., 2002). Hence, acetylation of these amines, as in MAFC, DAFC, or TAFC, or their conjugation to a fluorophore or protein likely reduces this instability.

In the preparation of the siderophore-protein immunogen, conjugation was mediated by introducing mutually reactive groups, maleimide and thiol, *via* crosslinkers, Sulfo-SMCC and SATA, respectively. Generation of maleimide-activated siderophores (FSC-$(SMCC)_1$, MAFC-$(SMCC)_1$, and DAFC-$(SMCC)_1$) was confirmed by LC-MS/MS and RP-HPLC analysis. Thiol incorporation in SATA-KLH was confirmed using an Aldrithiol™-4 assay following thiol deprotection. Mixing of maleimide-activated siderophores with deprotected SATA-KLH resulted in a stable thioether bond between the maleimide and thiol groups (Hermanson, 2008). Subsequently, following a size exclusion separation (e.g. dialysis) free unconjugated siderophore and crosslinker were removed leaving only siderophore-activated KLH. Following dialysis, siderophore incorporation in KLH was measured using the λ_{max} of ferri-siderophores (440 nm) (Schrettl *et al.*, 2010). This was primarily used to determine the successful conjugation of maleimide-activated siderophores to SATA-KLH for both immunogens.

Several strategies could be implemented to further improve the formulation of these immunogens. For example, the nature of the maleimide-activated siderophore reaction mixture before addition to SATA-KLH meant the NHS ester of any unreacted Sulfo-SMCC was likely still active during conjugation. This could be quenched prior to addition to SATA-KLH so that no unnecessary maleimide-activation of KLH amines occurred. Alternatively, maleimide-activated siderophore could be separated from free Sulfo-SMCC prior to conjugation, for example *via* Sep-Pak C18 extraction. However, the maleimide group stability would need to be monitored through this process to validate this method (Hermanson, 2008).

Ultimately the siderophore immunogens were successful in raising antibodies against their cognate haptens. Hence, this work has demonstrated that the principle of using FSC and acetylated FSC conjugated to KLH *via* Sulfo-SMCC and SATA for raising anti-FSC and anti-TAFC antibodies, respectively, is valid. The successful generation of anti-FSC and anti-TAFC antibodies was demonstrated at several stages using competitive ELISA systems. Mice were immunised with FSC-KLH or acetylated FSC-KLH and tail bleeds were taken for polyclonal antibody analysis. Analysis indicated that all mice possessed polyclonal antibodies with affinity for their immunised siderophore conjugated to BSA as opposed to KLH. Moreover, one FSC-KLH immunised mice possessed competitive anti-FSC antibodies. While all three of the acetylated FSC-KLH immunised mice possessed competitive anti-TAFC antibodies. Following tail bleed analysis, the best mice were selected for sacrifice, spleen removal, and hybridoma generation. A fusion efficiency of 78.6% and 66.2% was observed for hybridoma generation from the FSC-KLH and acetylated FSC-KLH immunised mice, respectively.

Following hybridoma generation, a monoclonal hybridoma (7D8-C) was established which produced anti-FSC IgM. Culture supernatant was collected from this hybridoma and anti-FSC IgM was purified by ammonium sulphate precipitation. This antibody was then implemented in a competitive FSC ELISA. The competitive FSC ELISA exhibited high specificity for FSC, showing competition for FSC, but not the other metabolites (BmGT, ferrichrome, or ornibactin). Furthermore, the ELISA was capable of detecting FSC directly in culture supernatant from *A. fumigatus* Δ*sidG* (Schrettl *et al.*, 2007), which is unable to produce TAFC and predominantly produces FSC instead. A bioassay was then implemented to establish if anti-FSC IgM could impede the uptake of FSC in *A. fumigatus*. To achieve this, a strain deficient in

extracellular siderophore biosynthesis (Δ*sidD*) was used (Schrettl *et al.*, 2007). Supplementation with FSC restored growth of *A. fumigatus* Δ*sidD* during iron-deplete growth. However, when FSC was pre-incubated with anti-FSC IgM this growth restoration was inhibited. This indicated that antibody-based immobilisation of siderophores can impede siderophore-mediated iron uptake by *A. fumigatus.* The siderocalin, Lcn1, has also been demonstrated to impede siderophore-mediated iron uptake using a bioassay (Fluckinger *et al.*, 2004). Pre-incubation of TAFC with Lcn1 inhibited TAFC-mediated growth restoration in a strain of *A. nidulans* completely deficient in siderophore biosynthesis (Δ*sidA*). Lcn1 can actually bind a range of compounds (Dartt, 2011). Hence, the highly specific binding of FSC by anti-FSC IgM offers direct evidence for proteinaceous siderophore sequestration as a means of impeding siderophore-mediated iron uptake, by a pathogen with intact intracellular siderophore (FC) functionality, as an antifungal strategy.

Following hybridoma generation, a hybridoma (6C6) was established which produced anti-TAFC IgG. Culture supernatant was collected and IgG purified by Protein A chromatography. Protein A purified IgG was then implemented in a competitive TAFC ELISA. The competitive TAFC ELISA exhibited high specificity for TAFC, showing competition for TAFC, but not the other metabolites (BmGT, ferrichrome, or ornibactin). Furthermore, this ELISA was capable of detecting TAFC directly in culture supernatant from *A. fumigatus* wild-type. Interestingly, the competitive TAFC ELISA showed no specificity for FSC. This was similarly observed for the competitive FSC ELISA, in which no competition was observed upon exchange of FSC for TAFC. Lack of cross-competition between FSC and TAFC suggests that the epitope recognised by each antibody does not encompass the iron-binding region. This is in contrast to the mechanism of ligand recognition by the

siderophore transporter, MirB, in which the iron-binding region is believed to be important (Raymond-Bouchard *et al.*, 2012). Both FSC and TAFC possess three N^5-anhydromevalonyl-N^5-hydroxyornithine groups linked by ester bonds (Haas, 2014). As TAFC is the acetylated derivative of FSC, the main difference between the molecules is the three outward facing acetyl groups in TAFC where there are three amines in FSC (Figure 1.3). Together, this suggests that the epitope recognised by both antibodies is towards the outer region of the siderophores and not the iron-binding region.

After optimisation, the competitive TAFC ELISA was capable of detecting TAFC at concentrations as low as 100 nM. Recent analysis by Carroll *et al*. (2016) showed TAFC in the sera of patients with suspected or probable/ proven Aspergillosis detected mean values of 11.6 ng/ ml (13 nM) and 9.7 ng/ ml (11 nM), respectively. Furthermore, analysis by Luptáková *et al.* (2017) showed TAFC in urine from a rat model of Aspergillosis at a mean value of 370 ng/ ml (408.5 nM). Hence, the anti-TAFC IgG is capable of detecting TAFC concentrations within clinically relevant levels. As only limited ELISA optimisation yielded this sensitivity, further optimisation would likely yield a system capable of detecting lower levels. TAFC represents a more promising biomarker compared with FSC as it is produced at higher levels, is more stable and its uptake has been demonstrated *in vivo* (Haas *et al.*, 2015; Moloney *et al.*, 2016a; Petrik *et al.*, 2010b, 2012, 2017; Renshaw *et al.*, 2002; Schrettl *et al.*, 2007). However, significantly more analysis of the levels of TAFC in sera and urine from patients and the general population is required to validate its use in diagnosing infection.

Given the sensitive detection capability of the anti-TAFC IgG and the inherent instability of hybridoma cells, it was decided to obtain the antibody sequence. In

doing so, the antibody can be recombinantly expressed in a suitable vector system in high amounts and long-term access preserved (Frenzel *et al.*, 2013) (Figure 6.27). The use of isotype-specific primers for the amplification of the antibody sequence from hybridoma cDNA was unsuitable for this work for several reasons. It was not possible to establish a monoclonal hybridoma from 6C6 and large-scale culture of it by commercial arrangement resulted in purification of an IgG without anti-TAFC activity (data not shown). This suggested that the 6C6 hybridoma was actually comprised of a heterogeneous population producing more than one antibody, not all of which were TAFC-specific. Though isotype analysis of the 6C6 cell culture supernatant indicated that the predominant antibody was an IgG_3, the proportion of this population represented by the anti-TAFC IgG was unknown. Hence, it was possible that the anti-TAFC IgG was of a different IgG subtype (IgG_1, IgG_{2a}, or IgG_{2b}). Therefore, isotype-specific amplification of hybridoma cDNA could result in amplification of a different antibody without anti-TAFC activity. Instead, a proteogenomic strategy was implemented whereby MS-based peptide sequencing of immunoaffinity purified anti-TAFC IgG was used to identify N- and C-terminal sequences. Using this approach, the N- and C-terminal sequences for two immunoaffinity purified light chains (light chains A and B) were obtained. In addition, two conflicting sequences were identified corresponding to the N-terminus of the IgG_{2a} heavy chain. It was not possible to confidently verify which sequences comprised the anti-TAFC Fab at this point. It was, therefore, decided to design primers based on all N- and C-terminal sequences for Fab amplification from hybridoma cDNA. If all sets of primers amplify Fab cDNA, recombinant expression of four possible combinations of the heavy and light chains will be carried out.

Subsequent *in vitro* assessment of their activity in a competitive TAFC ELISA can then be used to determine which sequences comprise the anti-TAFC Fab.

Antibody fragments, as opposed to full-length antibodies, are generally more amenable to recombinant expression as there are less folding requirements (Frenzel *et al.*, 2013). Though lacking the isotype-specific effector functions of the Fc region, the Fab retains the antigen binding capacity of the original antibody (Janeway, 2001). Hence, an anti-TAFC Fab can be implemented in a TAFC detection system and TAFC sequestering system. Ultimately, expression of the anti-TAFC Fab in a suitable vector system for high-level production can yield sufficient Fab for further *in vitro* application development, *in vitro* characterisation, and *in vivo* characterisation. First, implementation of the anti-TAFC Fab in an assay for the detection of TAFC in patient samples represents the most promising application thus far. It is likely that the anti-TAFC Fab could be used to establish a highly sensitive point-of-care assay. Second, as all of the anti-TAFC IgG was dedicated to the MS-based peptide-sequencing project, unfortunately, there was insufficient anti-TAFC IgG to explore its ability to impede TAFC uptake, as carried out for anti-FSC IgM. However, given the use of an antibody to impede siderophore uptake in *A. fumigatus* was demonstrated with the anti-FSC IgM in Chapter 5, it is possible that the anti-TAFC Fab could possess similar activity. Investigation of both the anti-FSC IgM and anti-TAFC Fab in inhibiting fungal growth *in vivo* using a model organism, such as *G. mellonella* is therefore warranted. Targeting TAFC in this way is of more clinical relevance than FSC, given its higher abundance and demonstrated utilisation *in vivo* (Haas *et al.*, 2015; Moloney *et al.*, 2016a; Petrik *et al.*, 2010b, 2012, 2017; Renshaw *et al.*, 2002; Schrettl *et al.*, 2007). The use of mAbs in a form of passive immunotherapy is increasingly appealing for the treatment of microbial infection in light of the

emerging resistance against current antimicrobial drugs. There are several examples of the use of mAbs in treating bacterial infection through the neutralisation of excreted toxins (Saylor *et al.*, 2009).

Siderophore immunogens also have potential to act as vaccines for the prophylactic treatment of microbial infection. Importantly, recent studies have demonstrated the use of siderophore-based immunogens to be feasible. Mike *et al.* (2016) showed that intranasal immunisation with siderophore immunogens protected against a urinary tract infection caused by uropathogenic *E. coli* in mice. Siderophores, yersinibactin (YBT) or aerobactin (AER) were conjugated to cationised BSA (cBSA) *via* 1-ethyl- 3-(3-dimethylaminopropyl) carbodiimide (EDC). Interestingly, co-administration of YBT or AER with cBSA without EDC conjugation also induced a protective effect. This indicates that only co-administration, and not conjugation, with a carrier protein was necessary in this case, which suggests that siderophores could be readily implemented multicomponent vaccines (Mike *et al.*, 2016). Sassone-Corsi *et al.* (2016) demonstrated that intranasal immunisation with siderophore immunogens reduced gut colonisation with pathogen *Salmonella* in mice. Siderophore, enterobactin (ENT) was conjugated to cholera toxin subunit B (CTB) *via* polyethylene glycol (PEG_3). Immunisation with ENT-CTB resulted in IgA production against ENT and its C-glucosylated derivative (GlcENT) in mucosae. Importantly, this work demonstrated targeted antimicrobial activity, whereby the *Salmonella* burden was reduced, but levels of beneficial *Lactobaccilli* species increased (Sassone-Corsi *et al.*, 2016). Highly specific targeting of pathogenic microbes such as this represents a significant advantage of siderophore-based therapeutic approaches, particularly when compared to broad-spectrum antimicrobials. Given the production of anti-siderophore antibodies, the FSC and

TAFC immunogens presented in this thesis were effective at raising an adaptive immune response. Hence, a similar formulation strategy to that reported here could be implemented in a siderophore-based vaccination strategy against *A. fumigatus* infection. The prospect of a vaccine against *A. fumigatus* is enticing, due to the aforementioned challenges associated with antifungal therapy (Section 1.1.3 and 1.2.7) (Ito *et al.*, 2009; Stevens *et al.*, 2011). There is also evidence for the efficacy of a vaccination against *A. fumigatus* infection. For example, immunisation of mice with crude hyphal extracts prior to immune suppression provided protection against invasive pulmonary Aspergillosis (Ito and Lyons, 2002).

To conclude, this thesis has demonstrated that iron starvation induces significant secretomic remodelling in *A. fumigatus* that is important to host recognition. Fluorescent derivatisation of *A. fumigatus* siderophores demonstrated that uptake was preserved despite significant chemical modification. Using a similar derivatisation strategy, siderophore immunogens were synthesised and used to generate hybridomas, which produced anti-siderophore antibodies. An anti-FSC IgM was characterised from this work, which demonstrated inhibition of siderophore-mediated iron uptake in *A. fumigatus* Δ*sidD in vitro*. Furthermore, an anti-TAFC IgG was generated capable of the highly sensitive detection of TAFC concentrations within clinically relevant ranges. A proteogenomic strategy was also devised and implemented to sequence this antibody so that it may be preserved for long-term access and high-level production. In conclusion, the data presented in this thesis will underpin future developments directed towards diagnosis of, and therapy against, *A. fumigatus* infection.

Bibliography

References

Abad, A., Fernández-Molina, J. V., Bikandi, J., Ramírez, A., Margareto, J., Sendino, J., *et al.* (2010) What makes Aspergillus fumigatus a successful pathogen? Genes and molecules involved in invasive aspergillosis., *Revista iberoamericana de micología*, 27 (4), pp. 155–82. DOI:10.1016/j.riam.2010.10.003.

Adav, S. S., Ravindran, A. and Sze, S. K. (2013) Proteomic analysis of temperature dependent extracellular proteins from Aspergillus fumigatus grown under solid-state culture condition., *Journal of Proteome Research*, 12 (6), pp. 2715–31. DOI:10.1021/pr4000762.

Adav, S. S., Ravindran, A. and Sze, S. K. (2015) Quantitative Proteomic Study of Aspergillus Fumigatus Secretome Revealed Deamidation of Secretory Enzymes., *Journal of Proteomics*, 119, pp. 154–168. DOI:10.1016/j.jprot.2015.02.007.

Aimanianda, V., Bayry, J., Bozza, S., Kniemeyer, O., Perruccio, K., Elluru, S. R., *et al.* (2009) Surface hydrophobin prevents immune recognition of airborne fungal spores., *Nature*, 460 (7259), pp. 1117–21. DOI:10.1038/nature08264.

Aisen, P., Enns, C. and Wessling-Resnick, M. (2001) Chemistry and biology of eukaryotic iron metabolism., *The International Journal of Biochemistry & Cell Biology*, 33 (10), pp. 940–59.

Albrecht, D., Guthke, R., Brakhage, A. A. and Kniemeyer, O. (2010) Integrative analysis of the heat shock response in Aspergillus fumigatus., *BMC Genomics*, 11 (1), pp. 32. DOI:10.1186/1471-2164-11-32.

Amarsaikhan, N., Albrecht-Eckardt, D., Sasse, C., Braus, G. H., Ogel, Z. B. and Kniemeyer, O. (2017) Proteomic profiling of the antifungal drug response of Aspergillus fumigatus to voriconazole, *International Journal of Medical Microbiology*. DOI:10.1016/j.ijmm.2017.07.011.

Ardon, O., Nudelman, R., Caris, C., Libman, J., Shanzer, A., Chen, Y. and Hadar, Y. (1998) Iron uptake in Ustilago maydis: tracking the iron path., *Journal of Bacteriology*, 180 (8), pp. 2021–6.

Ardon, O., Weizman, H., Libman, J., Shanzer, A., Chen, Y. and Hadar, Y. (1997) Iron uptake in Ustilago maydis: studies with fluorescent ferrichrome analogues, *Microbiology*, 143 (11), pp. 3625–3631. DOI:10.1099/00221287-143-11-3625.

Asif, A. R., Oellerich, M., Amstrong, V. W., Gross, U. and Reichard, U. (2010) Analysis of the cellular Aspergillus fumigatus proteome that reacts with sera from rabbits developing an acquired immunity after experimental aspergillosis., *Electrophoresis*, 31 (12), pp. 1947–58. DOI:10.1002/elps.201000015.

Asif, A. R., Oellerich, M., Amstrong, V. W., Riemenschneider, B., Monod, M. and Reichard, U. (2006) Proteome of conidial surface associated proteins of Aspergillus fumigatus reflecting potential vaccine candidates and allergens., *Journal of Proteome Research*, 5 (4), pp. 954–62. DOI:10.1021/pr0504586.

Aznar, A. and Dellagi, A. (2015) New insights into the role of siderophores as triggers of plant immunity: what can we learn from animals?, *Journal of Experimental Botany*, 66 (11), pp. 3001–3010. DOI:10.1093/jxb/erv155.

Bacher, P., Kniemeyer, O., Teutschbein, J., Thön, M., Vödisch, M., Wartenberg, D., *et al.* (2014) Identification of immunogenic antigens from Aspergillus fumigatus by direct multiparameter characterization of specific conventional and regulatory CD4+ T cells., *Journal of Immunology (Baltimore, Md. : 1950)*, 193 (7), pp. 3332–43. DOI:10.4049/jimmunol.1400776.

Baddley, J. W. (2011) Clinical risk factors for invasive aspergillosis., *Medical Mycology*, 49 Suppl 1, pp. S7–S12. DOI:10.3109/13693786.2010.505204.

Balenga, N. A., Klichinsky, M., Xie, Z., Chan, E. C., Zhao, M., Jude, J., Laviolette, M., Panettieri, R. A. and Druey, K. M. (2015) A fungal protease allergen provokes airway hyper-responsiveness in asthma., *Nature Communications*, 6, pp. 6763. DOI:10.1038/ncomms7763.

Barker, B. M., Kroll, K., Vödisch, M., Mazurie, A., Kniemeyer, O. and Cramer, R. A. (2012) Transcriptomic and proteomic analyses of the Aspergillus fumigatus hypoxia response using an oxygen-controlled fermenter., *BMC Genomics*, 13, pp. 62. DOI:10.1186/1471-2164-13-62.

Barton, R. C. (2013) Laboratory diagnosis of invasive aspergillosis: from diagnosis to prediction of outcome., *Scientifica*, 2013, pp. 459405. DOI:10.1155/2013/459405.

Beauvais, A., Bozza, S., Kniemeyer, O., Formosa, C., Formosa, C., Balloy, V., *et al.* (2013) Deletion of the α-(1,3)-glucan synthase genes induces a restructuring of the conidial cell wall responsible for the avirulence of Aspergillus fumigatus., *PLoS*

Pathogens, 9 (11), pp. e1003716. DOI:10.1371/journal.ppat.1003716.

Behnsen, J., Lessing, F., Schindler, S., Wartenberg, D., Jacobsen, I. D., Thoen, M., Zipfel, P. F. and Brakhage, A. A. (2010) Secreted Aspergillus fumigatus protease Alp1 degrades human complement proteins C3, C4, and C5., *Infection and Immunity*, 78 (8), pp. 3585–94. DOI:10.1128/IAI.01353-09.

Bergeron, R. J., Bharti, N., Singh, S., Mcmanis, J. S. and Green, L. G. (2010) Vibriobactin Antibodies: A Vaccine Strategy, *Journal of Medical Chemistry*, 52 (12), pp. 3801–3813. DOI:10.1021/jm900119q.Vibriobactin.

Bergmann, A., Hartmann, T., Cairns, T., Bignell, E. M. and Krappmann, S. (2009) A Regulator of Aspergillus fumigatus Extracellular Proteolytic Activity Is Dispensable for Virulence, *Infection and Immunity*, 77 (9), pp. 4041–4050. DOI:10.1128/IAI.00425-09.

Blatzer, M., Schrettl, M., Sarg, B., Lindner, H. H., Pfaller, K. and Haas, H. (2011) SidL, an Aspergillus fumigatus transacetylase involved in biosynthesis of the siderophores ferricrocin and hydroxyferricrocin., *Applied and Environmental Microbiology*, 77 (14), pp. 4959–66. DOI:10.1128/AEM.00182-11.

Brown, G. D., Denning, D. W., Gow, N. A. R., Levitz, S. M., Netea, M. G. and White, T. C. (2012) Hidden Killers: Human Fungal Infections, *Science Translational Medicine*, 4 (165), pp. 165rv13-165rv13. DOI:10.1126/scitranslmed.3004404.

Bruns, S., Seidler, M., Albrecht, D., Salvenmoser, S., Remme, N., Hertweck, C., Brakhage, A. A., Kniemeyer, O. and Müller, F.-M. C. (2010) Functional genomic profiling of Aspergillus fumigatus biofilm reveals enhanced production of the mycotoxin gliotoxin., *Proteomics*, 10 (17), pp. 3097–107. DOI:10.1002/pmic.201000129.

Buyer, J. S., Sikora, L. J. and Kratzke, M. G. (1990) Monoclonal Antibodies to Ferric Pseudobactin, the Siderophore of Plant Growth-Promoting Pseudomonas putida B10., *Applied and Environmental Microbiology*, 56 (2), pp. 419–24.

Cagas, S. E., Jain, M. R., Li, H. and Perlin, D. S. (2011a) Profiling the Aspergillus fumigatus proteome in response to caspofungin., *Antimicrobial Agents and Chemotherapy*, 55 (1), pp. 146–54. DOI:10.1128/AAC.00884-10.

Cagas, S. E., Jain, M. R., Li, H. and Perlin, D. S. (2011b) The proteomic signature of

Aspergillus fumigatus during early development., *Molecular & Cellular Proteomics : MCP*, 10 (11), pp. M111.010108. DOI:10.1074/mcp.M111.010108.

Carberry, S., Molloy, E., Hammel, S., O'Keeffe, G., Jones, G. W., Kavanagh, K. and Doyle, S. (2012) Gliotoxin effects on fungal growth: mechanisms and exploitation., *Fungal Genetics and Biology : FG & B*, 49 (4), pp. 302–12. DOI:10.1016/j.fgb.2012.02.003.

Carberry, S., Neville, C. M., Kavanagh, K. and Doyle, S. (2006) Analysis of major intracellular proteins of Aspergillus fumigatus by MALDI mass spectrometry: identification and characterisation of an elongation factor 1B protein with glutathione transferase activity., *Biochemical and Biophysical Research Communications*, 341 (4), pp. 1096–104. DOI:10.1016/j.bbrc.2006.01.078.

Carroll, C. S., Amankwa, L. N., Pinto, L. J., Fuller, J. D., Moore, M. M. and Larcher, G. (2016) Detection of a Serum Siderophore by LC-MS/MS as a Potential Biomarker of Invasive Aspergillosis, *PLOS ONE*, 11 (3), pp. e0151260. DOI:10.1371/journal.pone.0151260.

Cassat, J. E. and Skaar, E. P. (2013) Iron in infection and immunity., *Cell Host & Microbe*, 13 (5), pp. 509–19. DOI:10.1016/j.chom.2013.04.010.

Castellana, N. E., McCutcheon, K., Pham, V. C., Harden, K., Nguyen, A., Young, J., *et al.* (2011) Resurrection of a clinical antibody: Template proteogenomic de novo proteomic sequencing and reverse engineering of an anti-lymphotoxin-α antibody, *PROTEOMICS*, 11 (3), pp. 395–405. DOI:10.1002/pmic.201000487.

Caza, M. and Kronstad, J. W. (2013) Shared and distinct mechanisms of iron acquisition by bacterial and fungal pathogens of humans., *Frontiers in Cellular and Infection Microbiology*, 3, pp. 80. DOI:10.3389/fcimb.2013.00080.

Cerqueira, L. B., de Francisco, T. M. G., Gasparetto, J. C., Campos, F. R. and Pontarolo, R. (2014) Development and Validation of an HPLC-MS/MS Method for the Early Diagnosis of Aspergillosis, *PLoS ONE*, 9 (4), pp. e92851. DOI:10.1371/journal.pone.0092851.

Champer, J., Diaz-Arevalo, D., Champer, M., Hong, T. B., Wong, M., Shannahoff, M., *et al.* (2012) Protein targets for broad-spectrum mycosis vaccines: quantitative proteomic analysis of Aspergillus and Coccidioides and comparisons with other

fungal pathogens., *Annals of the New York Academy of Sciences*, 1273, pp. 44–51. DOI:10.1111/j.1749-6632.2012.06761.x.

Chanda, A., Roze, L. V, Kang, S., Artymovich, K. A., Hicks, G. R., Raikhel, N. V, Calvo, A. M. and Linz, J. E. (2009) A key role for vesicles in fungal secondary metabolism., *Proceedings of the National Academy of Sciences of the United States of America*, 106 (46), pp. 19533–8. DOI:10.1073/pnas.0907416106.

Chaudhuri, R., Ansari, F. A., Raghunandanan, M. V. and Ramachandran, S. (2011) FungalRV: adhesin prediction and immunoinformatics portal for human fungal pathogens., *BMC Genomics*, 12 (1), pp. 192. DOI:10.1186/1471-2164-12-192.

Clarke, S. C., Dumesic, P. A., Homer, C. M., O'Donoghue, A. J., La Greca, F., Pallova, L., Majer, P., Madhani, H. D. and Craik, C. S. (2016) Integrated Activity and Genetic Profiling of Secreted Peptidases in Cryptococcus neoformans Reveals an Aspartyl Peptidase Required for Low pH Survival and Virulence., *PLoS Pathogens*, 12 (12), pp. e1006051. DOI:10.1371/journal.ppat.1006051.

Clifton, M. C., Corrent, C. and Strong, R. K. (2009) Siderocalins: siderophore-binding proteins of the innate immune system., *Biometals : An International Journal on the Role of Metal Ions in Biology, Biochemistry, and Medicine*, 22 (4), pp. 557–64. DOI:10.1007/s10534-009-9207-6.

Crawford, A. and Wilson, D. (2015) Essential metals at the host-pathogen interface: nutritional immunity and micronutrient assimilation by human fungal pathogens, *FEMS Yeast Research*, 301 (7), pp. fov071. DOI:10.1093/femsyr/fov071.

Dagenais, T. R. T. and Keller, N. P. (2009) Pathogenesis of Aspergillus fumigatus in invasive aspergillosis, *Clinical Microbiology Reviews*, 22 (3), pp. 447–465. DOI:10.1128/CMR.00055-08.

Damron, F. H., Oglesby-Sherrouse, A. G., Wilks, A. and Barbier, M. (2016) Dual-seq transcriptomics reveals the battle for iron during Pseudomonas aeruginosa acute murine pneumonia., *Scientific Reports*, 6, pp. 39172. DOI:10.1038/srep39172.

Dartt, D. A. (2011) Tear Lipocalin: structure and Function, *The Ocular Surface*, 9 (3), pp. 126–138. DOI:10.1016/S1542-0124(11)70022-2.

Daven, S. (2009) Technical Guide for ELISA - Protocols - Troubleshooting. Available from: https://www.seracare.com/globalassets/resources/technical-

guides/technical-guide-kpl_elisa.pd.pdf

de Groot, P. W. J., Bader, O., de Boer, A. D., Weig, M. and Chauhan, N. (2013) Adhesins in human fungal pathogens: glue with plenty of stick., *Eukaryotic Cell*, 12 (4), pp. 470–81. DOI:10.1128/EC.00364-12.

De Pauw, B., Walsh, T. J., Donnelly, J. P., Stevens, D. A., Edwards, J. E., Calandra, T., *et al.* (2008) Revised definitions of invasive fungal disease from the European Organization for Research and Treatment of Cancer/Invasive Fungal Infections Cooperative Group and the National Institute of Allergy and Infectious Diseases Mycoses Study Group (EORTC/MSG) C, *Clinical Infectious Diseases : An Official Publication of the Infectious Diseases Society of America*, 46 (12), pp. 1813–21. DOI:10.1086/588660.

Denikus, N., Orfaniotou, F., Wulf, G., Lehmann, P. F., Monod, M. and Reichard, U. (2005) Fungal antigens expressed during invasive aspergillosis., *Infection and Immunity*, 73 (8), pp. 4704–13. DOI:10.1128/IAI.73.8.4704-4713.2005.

Dichtl, K., Helmschrott, C., Dirr, F. and Wagener, J. (2012) Deciphering cell wall integrity signalling in Aspergillus fumigatus: identification and functional characterization of cell wall stress sensors and relevant Rho GTPases., *Molecular Microbiology*, 83 (3), pp. 506–19. DOI:10.1111/j.1365-2958.2011.07946.x.

Dichtl, K., Samantaray, S. and Wagener, J. (2016) Cell wall integrity signaling in human pathogenic fungi., *Cellular Microbiology*. DOI:10.1111/cmi.12612.

Dolan, S. K., O'Keeffe, G., Jones, G. W. and Doyle, S. (2015) Resistance is not futile: gliotoxin biosynthesis, functionality and utility., *Trends in Microbiology*, 23 (7), pp. 419–28. DOI:10.1016/j.tim.2015.02.005.

Dolan, S. K., Owens, R. A., O'Keeffe, G., Hammel, S., Fitzpatrick, D. A., Jones, G. W. and Doyle, S. (2014) Regulation of nonribosomal peptide synthesis: bis-Thiomethylation attenuates gliotoxin biosynthesis in Aspergillus fumigatus., *Chemistry & Biology*, 21 (8), pp. 999–1012. DOI:10.1016/j.chembiol.2014.07.006.

Domingo, M. P., Colmenarejo, C., Martínez-Lostao, L., Müllbacher, A., Jarne, C., Revillo, M. J., *et al.* (2012) Bis(methyl)gliotoxin proves to be a more stable and reliable marker for invasive aspergillosis than gliotoxin and suitable for use in diagnosis., *Diagnostic Microbiology and Infectious Disease*, 73 (1), pp. 57–64.

DOI:10.1016/j.diagmicrobio.2012.01.012.

Doyle, J. M., Walshe, K., Gordon, N., Kavanagh, K. and Gallagher, L. (2012) Method for detecting infections. PCT/EP2012/0591.33.

Doyle, S. (2011) Fungal proteomics: from identification to function., *FEMS Microbiology Letters*, 321 (1), pp. 1–9. DOI:10.1111/j.1574-6968.2011.02292.x.

Eisendle, M., Oberegger, H., Zadra, I. and Haas, H. (2003) The siderophore system is essential for viability of Aspergillus nidulans: functional analysis of two genes encoding l-ornithine N 5-monooxygenase (sidA) and a non-ribosomal peptide synthetase (sidC)., *Molecular Microbiology*, 49 (2), pp. 359–75.

Ene, I. V., Heilmann, C. J., Sorgo, A. G., Walker, L. A., de Koster, C. G., Munro, C. A., Klis, F. M. and Brown, A. J. P. (2012) Carbon source-induced reprogramming of the cell wall proteome and secretome modulates the adherence and drug resistance of the fungal pathogen C andida albicans, *PROTEOMICS*, 12 (21), pp. 3164–3179. DOI:10.1002/pmic.201200228.

Farnell, E., Rousseau, K., Thornton, D. J., Bowyer, P. and Herrick, S. E. (2012) Expression and secretion of Aspergillus fumigatus proteases are regulated in response to different protein substrates., *Fungal Biology*, 116 (9), pp. 1003–12. DOI:10.1016/j.funbio.2012.07.004.

Fluckinger, M., Haas, H., Merschak, P., Glasgow, B. J. and Redl, B. (2004) Human tear lipocalin exhibits antimicrobial activity by scavenging microbial siderophores., *Antimicrobial Agents and Chemotherapy*, 48 (9), pp. 3367–72. DOI:10.1128/AAC.48.9.3367-3372.2004.

Fox, M., Gray, G., Kavanagh, K., Lewis, C. and Doyle, S. (2004) Detection of Aspergillus fumigatus mycotoxins: immunogen synthesis and immunoassay development, *Journal of Microbiological Methods*, 56 (2), pp. 221–230. DOI:10.1016/j.mimet.2003.10.009.

Free, S. J. (2013) Fungal cell wall organization and biosynthesis., *Advances in Genetics*, 81, pp. 33–82. DOI:10.1016/B978-0-12-407677-8.00002-6.

Frenzel, A., Hust, M. and Schirrmann, T. (2013) Expression of recombinant antibodies., *Frontiers in Immunology*, 4, pp. 217. DOI:10.3389/fimmu.2013.00217.

Froissard, M., Belgareh-Touzé, N., Dias, M., Buisson, N., Camadro, J.-M.,

Haguenauer-Tsapis, R. and Lesuisse, E. (2007) Trafficking of siderophore transporters in Saccharomyces cerevisiae and intracellular fate of ferrioxamine B conjugates., *Traffic (Copenhagen, Denmark)*, 8 (11), pp. 1601–16. DOI:10.1111/j.1600-0854.2007.00627.x.

Funk, J., Schaarschmidt, B., Slesiona, S., Hallström, T., Horn, U. and Brock, M. (2016) The glycolytic enzyme enolase represents a plasminogen-binding protein on the surface of a wide variety of medically important fungal species, *International Journal of Medical Microbiology*, 306 (1), pp. 59–68. DOI:10.1016/j.ijmm.2015.11.005.

Ganz, T. (2009) Iron in innate immunity: starve the invaders, *Current Opinion in Immunology*, 21 (1), pp. 63–67. DOI:10.1016/j.coi.2009.01.011.

Gardiner, D. M. and Howlett, B. J. (2005) Bioinformatic and expression analysis of the putative gliotoxin biosynthetic gene cluster of *Aspergillus fumigatus*, *FEMS Microbiology Letters*, 248 (2), pp. 241–248. DOI:10.1016/j.femsle.2005.05.046.

Gautam, P., Mushahary, D., Hassan, W., Upadhyay, S. K., Madan, T., Sirdeshmukh, R., Sundaram, C. S. and Sarma, P. U. (2016) In-depth 2-DE reference map of Aspergillus fumigatus and its proteomic profiling on exposure to itraconazole., *Medical Mycology*, pp. myv122. DOI:10.1093/mmy/myv122.

Gautam, P., Shankar, J., Madan, T., Sirdeshmukh, R., Sundaram, C. S., Gade, W. N., Basir, S. F. and Sarma, P. U. (2008) Proteomic and transcriptomic analysis of Aspergillus fumigatus on exposure to amphotericin B., *Antimicrobial Agents and Chemotherapy*, 52 (12), pp. 4220–7. DOI:10.1128/AAC.01431-07.

Gautam, P., Sundaram, C. S., Madan, T., Gade, W. N., Shah, A., Sirdeshmukh, R. and Sarma, P. U. (2007) Identification of novel allergens of Aspergillus fumigatus using immunoproteomics approach., *Clinical and Experimental Allergy : Journal of the British Society for Allergy and Clinical Immunology*, 37 (8), pp. 1239–49. DOI:10.1111/j.1365-2222.2007.02765.x.

Gautam, P., Upadhyay, S. K., Hassan, W., Madan, T., Sirdeshmukh, R., Sundaram, C. S., *et al.* (2011) Transcriptomic and proteomic profile of Aspergillus fumigatus on exposure to artemisinin., *Mycopathologia*, 172 (5), pp. 331–46. DOI:10.1007/s11046-011-9445-3.

Georgiou, G., Ippolito, G. C., Beausang, J., Busse, C. E., Wardemann, H. and Quake, S. R. (2014) The promise and challenge of high-throughput sequencing of the antibody repertoire, *Nature Biotechnology*, 32 (2), pp. 158–168. DOI:10.1038/nbt.2782.

Ghosh, M., Miller, P. A., Möllmann, U., Claypool, W. D., Schroeder, V. A., Wolter, W. R., *et al.* (2017) Targeted Antibiotic Delivery: Selective Siderophore Conjugation with Daptomycin Confers Potent Activity against Multidrug Resistant *Acinetobacter baumannii* Both in Vitro and in Vivo, *Journal of Medicinal Chemistry*, 60 (11), pp. 4577–4583. DOI:10.1021/acs.jmedchem.7b00102.

Gow, N. A. R., Latge, J.-P. and Munro, C. A. (2017) The Fungal Cell Wall: Structure, Biosynthesis, and Function, *Microbiology Spectrum*, 5 (3). DOI:10.1128/microbiolspec.FUNK-0035-2016.

Gozalbo, D., Gil-Navarro, I., Azorín, I., Renau-Piqueras, J., Martínez, J. P. and Gil, M. L. (1998) The cell wall-associated glyceraldehyde-3-phosphate dehydrogenase of Candida albicans is also a fibronectin and laminin binding protein., *Infection and Immunity*, 66 (5), pp. 2052–9.

Grahl, N., Puttikamonkul, S., Macdonald, J. M., Gamcsik, M. P., Ngo, L. Y., Hohl, T. M. and Cramer, R. A. (2011) In vivo hypoxia and a fungal alcohol dehydrogenase influence the pathogenesis of invasive pulmonary aspergillosis., *PLoS Pathogens*, 7 (7), pp. e1002145. DOI:10.1371/journal.ppat.1002145.

Grahl, N., Shepardson, K. M., Chung, D. and Cramer, R. A. (2012) Hypoxia and fungal pathogenesis: to air or not to air?, *Eukaryotic Cell*, 11 (5), pp. 560–70. DOI:10.1128/EC.00031-12.

Gründlinger, M., Gsaller, F., Schrettl, M., Lindner, H. and Haas, H. (2013a) Aspergillus fumigatus SidJ mediates intracellular siderophore hydrolysis., *Applied and Environmental Microbiology*, 79 (23), pp. 7534–6. DOI:10.1128/AEM.01285-13.

Gründlinger, M., Yasmin, S., Lechner, B. E., Geley, S., Schrettl, M., Hynes, M. and Haas, H. (2013b) Fungal siderophore biosynthesis is partially localized in peroxisomes., *Molecular Microbiology*, 88 (5), pp. 862–75. DOI:10.1111/mmi.12225.

Gsaller, F., Eisendle, M., Lechner, B. E., Schrettl, M., Lindner, H., Müller, D., Geley, S. and Haas, H. (2012) The interplay between vacuolar and siderophore-mediated iron

storage in Aspergillus fumigatus., *Metallomics : Integrated Biometal Science*, 4 (12), pp. 1262–70. DOI:10.1039/c2mt20179h.

Gupta, S., Singh, S., Kathuria, A., Kumar, M., Sharma, S., Kumar, R., *et al.* (2011) Ammonium derivatives of chromenones and quinolinones as lead antimicrobial agents, *Journal of Chemical Sciences*, 124 (2), pp. 437–449. DOI:10.1007/s12039-011-0147-7.

Guthals, A., Gan, Y., Murray, L., Chen, Y., Stinson, J., Nakamura, G., Lill, J. R., Sandoval, W. and Bandeira, N. (2017) De Novo MS/MS Sequencing of Native Human Antibodies, *Journal of Proteome Research*, 16 (1), pp. 45–54. DOI:10.1021/acs.jproteome.6b00608.

Haas, H. (2012) Iron - a key nexus in the virulence of Aspergillus fumigatus., *Frontiers in Microbiology*, 3 (February), pp. 28. DOI:10.3389/fmicb.2012.00028.

Haas, H. (2014) Fungal siderophore metabolism with a focus on Aspergillus fumigatus., *Natural Product Reports*, 31 (10), pp. 1266–1276. DOI:10.1039/c4np00071d.

Haas, H., Eisendle, M. and Turgeon, B. G. (2008) Siderophores in fungal physiology and virulence., *Annual Review of Phytopathology*, 46, pp. 149–87. DOI:10.1146/annurev.phyto.45.062806.094338.

Haas, H., Petrik, M. and Decristoforo, C. (2015) An iron-mimicking, trojan horse-entering fungi-has the time come for molecular imaging of fungal infections?, *PLoS Pathogens*, 11 (1), pp. e1004568. DOI:10.1371/journal.ppat.1004568.

Haas, H., Schoeser, M., Lesuisse, E., Ernst, J. F., Parson, W., Abt, B., Winkelmann, G. and Oberegger, H. (2003) Characterization of the Aspergillus nidulans transporters for the siderophores enterobactin and triacetylfusarinine C, *Biochemical Journal*, 371 (2), pp. 505–513. DOI:10.1042/bj20021685.

Hagag, S., Kubitschek-Barreira, P., Neves, G. W. P., Amar, D., Nierman, W., Shalit, I., Shamir, R., Lopes-Bezerra, L. and Osherov, N. (2012) Transcriptional and proteomic analysis of the Aspergillus fumigatus ΔprtT protease-deficient mutant., *PloS One*, 7 (4), pp. e33604. DOI:10.1371/journal.pone.0033604.

Halliwell, B. and Gutteridge, J. M. (1984) Oxygen toxicity, oxygen radicals, transition metals and disease., *The Biochemical Journal*, 219 (1), pp. 1–14.

Heilmann, C. J., Sorgo, A. G., Mohammadi, S., Sosinska, G. J., de Koster, C. G., Brul, S., de Koning, L. J. and Klis, F. M. (2013) Surface stress induces a conserved cell wall stress response in the pathogenic fungus Candida albicans., *Eukaryotic Cell*, 12 (2), pp. 254–64. DOI:10.1128/EC.00278-12.

Heinekamp, T., Thywißen, A., Macheleidt, J., Keller, S., Valiante, V. and Brakhage, A. A. (2013) Aspergillus fumigatus melanins: interference with the host endocytosis pathway and impact on virulence, *Frontiers in Microbiology*, 3, pp. 440. DOI:10.3389/fmicb.2012.00440.

Hermanson, G. T. (2008) *Bioconjugate Techniques*. Elsevier Inc.

Hissen, A. H. T., Chow, J. M. T., Pinto, L. J. and Moore, M. M. (2004) Survival of Aspergillus fumigatus in serum involves removal of iron from transferrin: the role of siderophores., *Infection and Immunity*, 72 (3), pp. 1402–8.

Hissen, A. H. T., Wan, A. N. C., Warwas, M. L., Pinto, L. J. and Moore, M. M. (2005) The Aspergillus fumigatus siderophore biosynthetic gene sidA, encoding L-ornithine N5-oxygenase, is required for virulence., *Infection and Immunity*, 73 (9), pp. 5493–503. DOI:10.1128/IAI.73.9.5493-5503.2005.

Houser, J., Komarek, J., Kostlanova, N., Cioci, G., Varrot, A., Kerr, S. C., *et al.* (2013) A soluble fucose-specific lectin from Aspergillus fumigatus conidia--structure, specificity and possible role in fungal pathogenicity., *PloS One*, 8 (12), pp. e83077. DOI:10.1371/journal.pone.0083077.

Howard, D. H., Rafie, R., Tiwari, A. and Faull, K. F. (2000) Hydroxamate Siderophores of Histoplasma capsulatum, *Infection and Immunity*, 68 (4), pp. 2338–2343. DOI:10.1128/IAI.68.4.2338-2343.2000.

Huang, N., Siegel, M. M., Kruppa, G. H. and Laukien, F. H. (1999) Automation of a Fourier transform ion cyclotron resonance mass spectrometer for acquisition, analysis, and e-mailing of high-resolution exact-mass electrospray ionization mass spectral data, *Journal of the American Society for Mass Spectrometry*, 10 (11), pp. 1166–1173. DOI:10.1016/S1044-0305(99)00089-6.

Huayhuaz, J. A. A., Vitorino, H. A., Campos, O. S., Serrano, S. H. P., Kaneko, T. M. and Espósito, B. P. (2017) Desferrioxamine and desferrioxamine-caffeine as carriers of aluminum and gallium to microbes via the Trojan Horse Effect, *Journal of Trace*

Elements in Medicine and Biology, 41, pp. 16–22. DOI:10.1016/j.jtemb.2017.01.006.

Ishikawa, M., Ninomiya, T., Akabane, H., Kushida, N., Tsujiuchi, G., Ohyama, M., Gomi, S., Shito, K. and Murata, T. (2009) Pseurotin A and its analogues as inhibitors of immunoglobulin E [correction of immunoglobuline E] production., *Bioorganic & Medicinal Chemistry Letters*, 19 (5), pp. 1457–60. DOI:10.1016/j.bmcl.2009.01.029.

Ito, J. I. and Lyons, J. M. (2002) Vaccination of corticosteroid immunosuppressed mice against invasive pulmonary aspergillosis., *The Journal of Infectious Diseases*, 186 (6), pp. 869–71. DOI:10.1086/342509.

Ito, J. I., Lyons, J. M., Diaz-Arevalo, D., Hong, T. B. and Kalkum, M. (2009) Vaccine progress., *Medical Mycology*, 47 Suppl 1 (Supplement 1), pp. S394-400. DOI:10.1080/13693780802552614.

Jain, R., Valiante, V., Remme, N., Docimo, T., Heinekamp, T., Hertweck, C., Gershenzon, J., Haas, H. and Brakhage, A. A. (2011) The MAP kinase MpkA controls cell wall integrity, oxidative stress response, gliotoxin production and iron adaptation in Aspergillus fumigatus., *Molecular Microbiology*, 82 (1), pp. 39–53. DOI:10.1111/j.1365-2958.2011.07778.x.

Janeway, C. (2001) *Immunobiology 5 : the immune system in health and disease*. Garland Pub.

Johnson, G., Ferrini, A., Dolan, S. K., Nolan, T., Agrawal, S., Doyle, S. and Bustin, S. A. (2014) Biomarkers for invasive aspergillosis: the challenges continue, *Biomarkers in Medicine*, 8 (3), pp. 429–451. DOI:10.2217/bmm.13.129.

Jones, C. M., Wells, R. M., Madduri, A. V. R., Renfrow, M. B., Ratledge, C., Moody, D. B. and Niederweis, M. (2014) Self-poisoning of Mycobacterium tuberculosis by interrupting siderophore recycling., *Proceedings of the National Academy of Sciences of the United States of America*, 111 (5), pp. 1945–50. DOI:10.1073/pnas.1311402111.

Kamath, K. S., Kumar, S. S., Kaur, J., Venkatakrishnan, V., Paulsen, I. T., Nevalainen, H. and Molloy, M. P. (2015) Proteomics of hosts and pathogens in cystic fibrosis., *Proteomics. Clinical Applications*, 9 (1–2), pp. 134–46. DOI:10.1002/prca.201400122.

Kaur, S. and Singh, S. (2014) Biofilm formation by Aspergillus fumigatus., *Medical*

Mycology, 52 (1), pp. 2–9. DOI:10.3109/13693786.2013.819592.

Kerr, S. C., Fischer, G. J., Sinha, M., McCabe, O., Palmer, J. M., Choera, T., *et al.* (2016) FleA Expression in Aspergillus fumigatus Is Recognized by Fucosylated Structures on Mucins and Macrophages to Prevent Lung Infection., *PLoS Pathogens*, 12 (4), pp. e1005555. DOI:10.1371/journal.ppat.1005555.

Kim, Y., Yun, C.-W. and Philpott, C. C. (2002) Ferrichrome induces endosome to plasma membrane cycling of the ferrichrome transporter, Arn1p, in Saccharomyces cerevisiae, *The EMBO Journal*, 21 (14), pp. 3632–3642. DOI:10.1093/emboj/cdf382.

Kinoshita, H., Wakahara, N., Watanabe, M., Kawasaki, T., Matsuo, H., Kawai, Y., *et al.* (2008) Cell surface glyceraldehyde-3-phosphate dehydrogenase (GAPDH) of Lactobacillus plantarum LA 318 recognizes human A and B blood group antigens., *Research in Microbiology*, 159 (9–10), pp. 685–91. DOI:10.1016/j.resmic.2008.07.005.

Knetsch, P. A., Zhai, C., Rangger, C., Blatzer, M., Haas, H., Kaeopookum, P., Haubner, R. and Decristoforo, C. (2015) [(68)Ga]FSC-(RGD)3 a trimeric RGD peptide for imaging αvβ3 integrin expression based on a novel siderophore derived chelating scaffold-synthesis and evaluation., *Nuclear Medicine and Biology*, 42 (2), pp. 115–22. DOI:10.1016/j.nucmedbio.2014.10.001.

Kniemeyer, O., Lessing, F., Scheibner, O., Hertweck, C. and Brakhage, A. A. (2006) Optimisation of a 2-D gel electrophoresis protocol for the human-pathogenic fungus Aspergillus fumigatus., *Current Genetics*, 49 (3), pp. 178–89. DOI:10.1007/s00294-005-0047-9.

Kniemeyer, O., Schmidt, A. D., Vödisch, M., Wartenberg, D. and Brakhage, A. A. (2011) Identification of virulence determinants of the human pathogenic fungi Aspergillus fumigatus and Candida albicans by proteomics., *International Journal of Medical Microbiology : IJMM*, 301 (5), pp. 368–77. DOI:10.1016/j.ijmm.2011.04.001.

Knutsen, A. P., Bush, R. K., Demain, J. G., Denning, D. W., Dixit, A., Fairs, A., *et al.* (2012) Fungi and allergic lower respiratory tract diseases., *The Journal of Allergy and Clinical Immunology*, 129 (2), pp. 280-91–3. DOI:10.1016/j.jaci.2011.12.970.

Köhler, G. and Milstein, C. (1975) Continuous cultures of fused cells secreting

antibody of predefined specificity., *Nature*, 256 (5517), pp. 495–7.

Kousha, M., Tadi, R. and Soubani, A. O. (2011) Pulmonary aspergillosis: a clinical review., *European Respiratory Review : An Official Journal of the European Respiratory Society*, 20 (121), pp. 156–74. DOI:10.1183/09059180.00001011.

Kragl, C., Schrettl, M., Abt, B., Sarg, B., Lindner, H. H. and Haas, H. (2007) EstB-mediated hydrolysis of the siderophore triacetylfusarinine C optimizes iron uptake of Aspergillus fumigatus., *Eukaryotic Cell*, 6 (8), pp. 1278–85. DOI:10.1128/EC.00066-07.

Kroll, K., Shekhova, E., Mattern, D. J., Thywissen, A., Jacobsen, I. D., Strassburger, M., *et al.* (2016) The hypoxia-induced dehydrogenase HorA is required for coenzyme Q10 biosynthesis, azole sensitivity and virulence of Aspergillus fumigatus., *Molecular Microbiology*. DOI:10.1111/mmi.13377.

Kubitschek-Barreira, P. H., Curty, N., Neves, G. W. P., Gil, C. and Lopes-Bezerra, L. M. (2013) Differential proteomic analysis of Aspergillus fumigatus morphotypes reveals putative drug targets., *Journal of Proteomics*, 78, pp. 522–34. DOI:10.1016/j.jprot.2012.10.022.

Kuboi, S., Ishimaru, T., Tamada, S., Bernard, E. M., Perlin, D. S. and Armstrong, D. (2013) Molecular characterization of AfuFleA, an L-fucose-specific lectin from Aspergillus fumigatus., *Journal of Infection and Chemotherapy : Official Journal of the Japan Society of Chemotherapy*, 19 (6), pp. 1021–8. DOI:10.1007/s10156-013-0614-9.

Kumar, A., Ahmed, R., Singh, P. K. and Shukla, P. K. (2011) Identification of virulence factors and diagnostic markers using immunosecretome of Aspergillus fumigatus., *Journal of Proteomics*, 74 (7), pp. 1104–12. DOI:10.1016/j.jprot.2011.04.004.

Kumar, A. and Shukla, P. K. (2015) A monoclonal antibody against glycoproteins of Aspergillus fumigatus shows anti-adhesive potential., *Microbial Pathogenesis*, 79, pp. 24–30. DOI:10.1016/j.micpath.2015.01.003.

Kwon-Chung, K. J. and Sugui, J. A. (2013) Aspergillus fumigatus--what makes the species a ubiquitous human fungal pathogen?, *PLoS Pathogens*, 9 (12), pp. e1003743. DOI:10.1371/journal.ppat.1003743.

Lamb, A. L. (2015) Breaking a pathogen's iron will: Inhibiting siderophore production as an antimicrobial strategy., *Biochimica et Biophysica Acta*, 1854 (8), pp. 1054–70. DOI:10.1016/j.bbapap.2015.05.001.

Larcher, G., Dias, M., Razafimandimby, B., Bomal, D. and Bouchara, J.-P. (2013) Siderophore Production by Pathogenic Mucorales and Uptake of Deferoxamine B, *Mycopathologia*, 176 (5–6), pp. 319–328. DOI:10.1007/s11046-013-9693-5.

Latgé, J.-P. (2010) Tasting the fungal cell wall., *Cellular Microbiology*, 12 (7), pp. 863–72. DOI:10.1111/j.1462-5822.2010.01474.x.

Latgé, J. P. (1999) Aspergillus fumigatus and aspergillosis., *Clinical Microbiology Reviews*, 12 (2), pp. 310–50.

Leal, S. M., Roy, S., Vareechon, C., Carrion, S. deJesus, Clark, H., Lopez-Berges, M. S., *et al.* (2013) Targeting iron acquisition blocks infection with the fungal pathogens Aspergillus fumigatus and Fusarium oxysporum., *PLoS Pathogens*, 9 (7), pp. e1003436. DOI:10.1371/journal.ppat.1003436.

Lee, M. J. and Sheppard, D. C. (2016) Recent advances in the understanding of the Aspergillus fumigatus cell wall., *Journal of Microbiology (Seoul, Korea)*, 54 (3), pp. 232–42. DOI:10.1007/s12275-016-6045-4.

Lesuisse, E., Blaiseau, P. L., Dancis, A. and Camadro, J. M. (2001) Siderophore uptake and use by the yeast Saccharomyces cerevisiae., *Microbiology (Reading, England)*, 147 (Pt 2), pp. 289–98. DOI:10.1099/00221287-147-2-289.

Lewis, R. E., Wiederhold, N. P., Chi, J., Han, X. Y., Komanduri, K. V, Kontoyiannis, D. P. and Prince, R. A. (2005) Detection of gliotoxin in experimental and human aspergillosis., *Infection and Immunity*, 73 (1), pp. 635–7. DOI:10.1128/IAI.73.1.635-637.2005.

Liu, D., Li, J., Zhao, S., Zhang, R., Wang, M., Miao, Y., Shen, Y. and Shen, Q. (2013) Secretome diversity and quantitative analysis of cellulolytic Aspergillus fumigatus Z5 in the presence of different carbon sources., *Biotechnology for Biofuels*, 6 (1), pp. 149. DOI:10.1186/1754-6834-6-149.

Liu, M. and Gelli, A. (2008) Elongation factor 3, EF3, associates with the calcium channel Cch1 and targets Cch1 to the plasma membrane in Cryptococcus neoformans., *Eukaryotic Cell*, 7 (7), pp. 1118–26. DOI:10.1128/EC.00116-08.

Lodish, H. F. (2000) *Molecular cell biology*. W.H. Freeman.

Lowe, R. G. T., Howlett, B. J., Murat, C., Balestrini, R. and Coutinho, P. (2012) Indifferent, Affectionate, or Deceitful: Lifestyles and Secretomes of Fungi, *PLoS Pathogens*, 8 (3), pp. e1002515. DOI:10.1371/journal.ppat.1002515.

Luptáková, D., Pluháček, T., Petřík, M., Novák, J., Palyzová, A., Sokolová, L., *et al.* (2017) Non-invasive and invasive diagnoses of aspergillosis in a rat model by mass spectrometry, *Scientific Reports*, 7 (1), pp. 16523. DOI:10.1038/s41598-017-16648-z.

Lytton, S. D., Cabantchik, Z. I., Libman, J. and Shanzer, A. (1991) Reversed siderophores as antimalarial agents. II. Selective scavenging of Fe(III) from parasitized erythrocytes by a fluorescent derivative of desferal., *Molecular Pharmacology*, 40 (4), pp. 584–90.

Margalit, A. and Kavanagh, K. (2015) The innate immune response to Aspergillus fumigatus at the alveolar surface., *FEMS Microbiology Reviews*, 39 (5), pp. 670–87. DOI:10.1093/femsre/fuv018.

Martín del Campo, J. S., Vogelaar, N., Tolani, K., Kizjakina, K., Harich, K. and Sobrado, P. (2016) Inhibition of the Flavin-Dependent Monooxygenase Siderophore A (SidA) Blocks Siderophore Biosynthesis and Aspergillus fumigatus Growth, *ACS Chemical Biology*, pp. acschembio.6b00666. DOI:10.1021/acschembio.6b00666.

McCotter, S. W., Horianopoulos, L. C. and Kronstad, J. W. (2016) Regulation of the fungal secretome, *Current Genetics*, 62 (3), pp. 533–545. DOI:10.1007/s00294-016-0578-2.

McDonagh, A., Fedorova, N. D., Crabtree, J., Yu, Y., Kim, S., Chen, D., *et al.* (2008) Sub-telomere directed gene expression during initiation of invasive aspergillosis., *PLoS Pathogens*, 4 (9), pp. e1000154. DOI:10.1371/journal.ppat.1000154.

Miethke, M. and Marahiel, M. A. (2007) Siderophore-based iron acquisition and pathogen control., *Microbiology and Molecular Biology Reviews : MMBR*, 71 (3), pp. 413–51. DOI:10.1128/MMBR.00012-07.

Mike, L. A., Smith, S. N., Sumner, C. A., Eaton, K. A. and Mobley, H. L. T. (2016) Siderophore vaccine conjugates protect against uropathogenic Escherichia coli urinary tract infection., *Proceedings of the National Academy of Sciences of the United States of America*, pp. 201606324. DOI:10.1073/pnas.1606324113.

Möllmann, U., Heinisch, L., Bauernfeind, A., Köhler, T. and Ankel-Fuchs, D. (2009) Siderophores as drug delivery agents: application of the 'Trojan Horse' strategy., *Biometals : An International Journal on the Role of Metal Ions in Biology, Biochemistry, and Medicine*, 22 (4), pp. 615–24. DOI:10.1007/s10534-009-9219-2.

Moloney, N. M. N. M., Owens, R. A. R. A., Meleady, P., Henry, M., Dolan, S. K. S. K., Mulvihill, E., Clynes, M. and Doyle, S. (2016a) The iron-responsive microsomal proteome of Aspergillus fumigatus, *Journal of Proteomics*, 136, pp. 99–111. DOI:10.1016/j.jprot.2015.12.025.

Moloney, N. M., Owens, R. A. and Doyle, S. (2016) Proteomic analysis of Aspergillus fumigatus – clinical implications, *Expert Review of Proteomics*, 13 (7), pp. 635–649. DOI:10.1080/14789450.2016.1203783.

Moore, M. M. (2013) The crucial role of iron uptake in Aspergillus fumigatus virulence., *Current Opinion in Microbiology*, 16 (6), pp. 692–9. DOI:10.1016/j.mib.2013.07.012.

Mouyna, I., Hartl, L. and Latgé, J.-P. (2013) β-1,3-glucan modifying enzymes in Aspergillus fumigatus., *Frontiers in Microbiology*, 4, pp. 81. DOI:10.3389/fmicb.2013.00081.

Mulvihill, E. D. E. D., Moloney, N. M. N. M., Owens, R. A. R. A., Dolan, S. K. S. K., Russell, L. and Doyle, S. (2017) Functional Investigation of Iron-Responsive Microsomal Proteins, including MirC, in Aspergillus fumigatus, *Frontiers in Microbiology*, 8 (MAR), pp. 418. DOI:10.3389/fmicb.2017.00418.

Muszkieta, L., Beauvais, A., Pähtz, V., Gibbons, J. G., Anton Leberre, V., Beau, R., *et al.* (2013) Investigation of Aspergillus fumigatus biofilm formation by various 'omics' approaches., *Frontiers in Microbiology*, 4, pp. 13. DOI:10.3389/fmicb.2013.00013.

Namvar, S., Warn, P., Farnell, E., Bromley, M., Fraczek, M., Bowyer, P. and Herrick, S. (2015) Aspergillus fumigatus proteases, Asp f 5 and Asp f 13, are essential for airway inflammation and remodelling in a murine inhalation model., *Clinical and Experimental Allergy : Journal of the British Society for Allergy and Clinical Immunology*, 45 (5), pp. 982–93. DOI:10.1111/cea.12426.

Nierman, W. C., Pain, A., Anderson, M. J., Wortman, J. R., Kim, H. S., Arroyo, J., *et*

al. (2005) Genomic sequence of the pathogenic and allergenic filamentous fungus Aspergillus fumigatus., *Nature*, 438 (7071), pp. 1151–6. DOI:10.1038/nature04332.

Noël, S., Guillon, L., Schalk, I. J. and Mislin, G. L. A. (2011) Synthesis of Fluorescent Probes Based on the Pyochelin Siderophore Scaffold, *Organic Letters*, 13 (5), pp. 844–847. DOI:10.1021/ol1028173.

O'Gorman, C. M., Fuller, H. T. and Dyer, P. S. (2009) Discovery of a sexual cycle in the opportunistic fungal pathogen Aspergillus fumigatus., *Nature*, 457 (7228), pp. 471–4. DOI:10.1038/nature07528.

O'Keeffe, G., Hammel, S., Owens, R. A., Keane, T. M., Fitzpatrick, D. A., Jones, G. W. and Doyle, S. (2014) RNA-seq reveals the pan-transcriptomic impact of attenuating the gliotoxin self-protection mechanism in Aspergillus fumigatus., *BMC Genomics*, 15 (1), pp. 894. DOI:10.1186/1471-2164-15-894.

Osherov, N. (2007) *The virulence of Aspergillus fumigatus*, Kavanagh, K. (ed.) . Dordrecht: Springer Netherlands. DOI:10.1007/978-1-4020-6397-8.

Ouchetto, H., Dias, M., Mornet, R., Lesuisse, E. and Camadro, J.-M. (2005) A new route to trihydroxamate-containing artificial siderophores and synthesis of a new fluorescent probe., *Bioorganic & Medicinal Chemistry*, 13 (5), pp. 1799–803. DOI:10.1016/j.bmc.2004.11.053.

Ouyang, H., Luo, Y., Zhang, L., Li, Y. and Jin, C. (2010) Proteome analysis of Aspergillus fumigatus total membrane proteins identifies proteins associated with the glycoconjugates and cell wall biosynthesis using 2D LC-MS/MS., *Molecular Biotechnology*, 44 (3), pp. 177–89. DOI:10.1007/s12033-009-9224-2.

Owens, R. A., O'Keeffe, G., O'Hanlon, K. A., Gallagher, L. and Doyle, S. (2014) Virulence Characteristics of Aspergillus fumigatus, in: Sullivan, D. J. and Moran, G. P. (eds.) *Human Pathogenic Fungi: Molecular Biology and Pathogenic Mechanisms*. Norfolk, UK: Caister Academic Press, pp. 163–194.

Pan, S.-J., Tapley, A., Adamson, J., Little, T., Urbanowski, M., Cohen, K., *et al.* (2015) Biomarkers for Tuberculosis Based on Secreted, Species-Specific, Bacterial Small Molecules, *Journal of Infectious Diseases*, 212 (11), pp. 1827–1834. DOI:10.1093/infdis/jiv312.

Pao, S. S., Paulsen, I. T. and Saier, Milton H., J. (1998) Major Facilitator

Superfamily, *Microbiol. Mol. Biol. Rev.*, 62 (1), pp. 1–34.

Park, Y.-S., Kim, J.-Y. and Yun, C.-W. (2016) Identification of ferrichrome- and ferrioxamine B-mediated iron uptake by Aspergillus fumigatus., *The Biochemical Journal*, 473 (9), pp. 1203–13. DOI:10.1042/BCJ20160066.

Paulick, M. G. and Bertozzi, C. R. (2008) The glycosylphosphatidylinositol anchor: a complex membrane-anchoring structure for proteins., *Biochemistry*, 47 (27), pp. 6991–7000. DOI:10.1021/bi8006324.

Petrik, M., Franssen, G. M., Haas, H., Laverman, P., Hörtnagl, C., Schrettl, M., Helbok, A., Lass-Flörl, C. and Decristoforo, C. (2012) Preclinical evaluation of two 68Ga-siderophores as potential radiopharmaceuticals for Aspergillus fumigatus infection imaging., *European Journal of Nuclear Medicine and Molecular Imaging*, 39 (7), pp. 1175–83. DOI:10.1007/s00259-012-2110-3.

Petrik, M., Haas, H., Dobrozemsky, G., Lass-Flörl, C., Helbok, A., Blatzer, M., Dietrich, H. and Decristoforo, C. (2010a) 68Ga-siderophores for PET imaging of invasive pulmonary aspergillosis: proof of principle., *Journal of Nuclear Medicine : Official Publication, Society of Nuclear Medicine*, 51 (4), pp. 639–45. DOI:10.2967/jnumed.109.072462.

Petrik, M., Haas, H., Helbok, A., Blatzer, M., Schrettl, M., Lass-Floerl, C. and Decristoforo, C. (2010b) Comparison of 68Ga-siderophores for imaging Aspergillus fumigatus infections with PET, *Nuclear Medicine and Biology*, 37 (6), pp. 726. DOI:10.1016/j.nucmedbio.2010.04.116.

Petrik, M., Zhai, C., Haas, H. and Decristoforo, C. (2017) Siderophores for molecular imaging applications., *Clinical and Translational Imaging*, 5 (1), pp. 15–27. DOI:10.1007/s40336-016-0211-x.

Pfaller, M. and Riley, J. (1992) Effects of fluconazole on the sterol and carbohydrate composition of four species of Candida, *European Journal of Clinical Microbiology & Infectious Diseases*, 11 (2), pp. 152–156. DOI:10.1007/BF01967067.

Philpott, C. C. and Protchenko, O. (2008) Response to iron deprivation in Saccharomyces cerevisiae., *Eukaryotic Cell*, 7 (1), pp. 20–7. DOI:10.1128/EC.00354-07.

Pianalto, K. and Alspaugh, J. (2016) New Horizons in Antifungal Therapy, *Journal of*

Fungi, 2 (4), pp. 26. DOI:10.3390/jof2040026.

Priebe, S., Kreisel, C., Horn, F., Guthke, R. and Linde, J. (2015) FungiFun2: a comprehensive online resource for systematic analysis of gene lists from fungal species., *Bioinformatics (Oxford, England)*, 31 (3), pp. 445–6. DOI:10.1093/bioinformatics/btu627.

Qi, J., Kizjakina, K., Robinson, R., Tolani, K. and Sobrado, P. (2012) A fluorescence polarization binding assay to identify inhibitors of flavin-dependent monooxygenases., *Analytical Biochemistry*, 425 (1), pp. 80–7. DOI:10.1016/j.ab.2012.03.002.

Raymond-Bouchard, I., Carroll, C. S., Nesbitt, J. R., Henry, K. a, Pinto, L. J., Moinzadeh, M., Scott, J. K. and Moore, M. M. (2012) Structural requirements for the activity of the MirB ferrisiderophore transporter of Aspergillus fumigatus., *Eukaryotic Cell*, 11 (11), pp. 1333–44. DOI:10.1128/EC.00159-12.

Reiber, K., Reeves, E. P., Neville, C. M., Winkler, R., Gebhardt, P., Kavanagh, K. and Doyle, S. (2005) The expression of selected non-ribosomal peptide synthetases in Aspergillus fumigatus is controlled by the availability of free iron., *FEMS Microbiology Letters*, 248 (1), pp. 83–91. DOI:10.1016/j.femsle.2005.05.028.

Renshaw, J. C., Robson, G. D., Trinci, A. P. J., Wiebe, M. G., Livens, F. R., Collison, D. and Taylor, R. J. (2002) Fungal siderophores: structures, functions and applications, *Mycological Research*, 106 (10), pp. 1123–1142. DOI:10.1017/S0953756202006548.

Robinson, M.-P., Ke, N., Lobstein, J., Peterson, C., Szkodny, A., Mansell, T. J., *et al.* (2015) Efficient expression of full-length antibodies in the cytoplasm of engineered bacteria, *Nature Communications*, 6, pp. 8072. DOI:10.1038/ncomms9072.

Romano, J., Nimrod, G., Ben-Tal, N., Shadkchan, Y., Baruch, K., Sharon, H. and Osherov, N. (2006) Disruption of the Aspergillus fumigatus ECM33 homologue results in rapid conidial germination, antifungal resistance and hypervirulence., *Microbiology (Reading, England)*, 152 (Pt 7), pp. 1919–28. DOI:10.1099/mic.0.28936-0.

Roze, L. V, Chanda, A. and Linz, J. E. (2011) Compartmentalization and molecular traffic in secondary metabolism: a new understanding of established cellular

processes., *Fungal Genetics and Biology : FG & B*, 48 (1), pp. 35–48. DOI:10.1016/j.fgb.2010.05.006.

Saier, M. H., Beatty, J. T., Goffeau, A., Harley, K. T., Heijne, W. H., Huang, S. C., *et al.* (1999) The major facilitator superfamily., *Journal of Molecular Microbiology and Biotechnology*, 1 (2), pp. 257–79.

Sasikumar, A. N. and Kinzy, T. G. (2014) Mutations in the chromodomain-like insertion of translation elongation factor 3 compromise protein synthesis through reduced ATPase activity., *The Journal of Biological Chemistry*, 289 (8), pp. 4853–60. DOI:10.1074/jbc.M113.536201.

Sassone-Corsi, M., Chairatana, P., Zheng, T., Perez-Lopez, A., Edwards, R. A., George, M. D., Nolan, E. M. and Raffatellu, M. (2016) Siderophore-based immunization strategy to inhibit growth of enteric pathogens., *Proceedings of the National Academy of Sciences of the United States of America*, 113 (47), pp. 13462–13467. DOI:10.1073/pnas.1606290113.

Savelieff, M. G. and Pappalardo, L. (2017) Novel cutting-edge metabolite-based diagnostic tools for aspergillosis., *PLoS Pathogens*, 13 (9), pp. e1006486. DOI:10.1371/journal.ppat.1006486.

Saylor, C., Dadachova, E. and Casadevall, A. (2009) Monoclonal antibody-based therapies for microbial diseases., *Vaccine*, 27 Suppl 6, pp. G38-46. DOI:10.1016/j.vaccine.2009.09.105.

Schalk, I. J. and Mislin, G. L. A. (2017) Bacterial Iron Uptake Pathways: Gates for the Import of Bactericide Compounds, *Journal of Medicinal Chemistry*, 60 (11), pp. 4573–4576. DOI:10.1021/acs.jmedchem.7b00554.

Scharf, D. H., Heinekamp, T. and Brakhage, A. A. (2014) Human and plant fungal pathogens: the role of secondary metabolites., *PLoS Pathogens*, 10 (1), pp. e1003859. DOI:10.1371/journal.ppat.1003859.

Schmeda-Hirschmann, G., Hormazabal, E., Rodriguez, J. A. and Theoduloz, C. (2008) Cycloaspeptide A and Pseurotin A from the Endophytic Fungus Penicillium janczewskii, *Zeitschrift Für Naturforschung C*, 63 (5–6), pp. 383–388. DOI:10.1515/znc-2008-5-612.

Schrettl, M., Beckmann, N., Varga, J., Heinekamp, T., Jacobsen, I. D., Jöchl, C., *et al.*

(2010) HapX-mediated adaption to iron starvation is crucial for virulence of Aspergillus fumigatus., *PLoS Pathogens*, 6 (9), pp. e1001124. DOI:10.1371/journal.ppat.1001124.

Schrettl, M., Bignell, E., Kragl, C., Joechl, C., Rogers, T., Arst, H. N., Haynes, K. and Haas, H. (2004) Siderophore biosynthesis but not reductive iron assimilation is essential for Aspergillus fumigatus virulence., *The Journal of Experimental Medicine*, 200 (9), pp. 1213–9. DOI:10.1084/jem.20041242.

Schrettl, M., Bignell, E., Kragl, C., Sabiha, Y., Loss, O., Eisendle, M., *et al.* (2007) Distinct roles for intra- and extracellular siderophores during Aspergillus fumigatus infection., *PLoS Pathogens*, 3 (9), pp. 1195–207. DOI:10.1371/journal.ppat.0030128.

Schrettl, M., Carberry, S., Kavanagh, K., Haas, H., Jones, G. W., Brien, O., *et al.* (2010b) Self-Protection against Gliotoxin — A Component of the Gliotoxin Biosynthetic Cluster , GliT , Completely Protects Aspergillus fumigatus Against Exogenous Gliotoxin, 6 (6). DOI:10.1371/journal.ppat.1000952.

Schrettl, M., Kim, H. S., Eisendle, M., Kragl, C., Nierman, W. C., Heinekamp, T., *et al.* (2008) SreA-mediated iron regulation in Aspergillus fumigatus., *Molecular Microbiology*, 70 (1), pp. 27–43. DOI:10.1111/j.1365-2958.2008.06376.x.

Shakoury-Elizeh, M., Protchenko, O., Berger, A., Cox, J., Gable, K., Dunn, T. M., Prinz, W. A., Bard, M. and Philpott, C. C. (2010) Metabolic response to iron deficiency in Saccharomyces cerevisiae., *The Journal of Biological Chemistry*, 285 (19), pp. 14823–33. DOI:10.1074/jbc.M109.091710.

Sharon, H., Hagag, S. and Osherov, N. (2009) Transcription factor PrtT controls expression of multiple secreted proteases in the human pathogenic mold Aspergillus fumigatus., *Infection and Immunity*, 77 (9), pp. 4051–60. DOI:10.1128/IAI.00426-09.

Sheppard, D. C. (2011) Molecular mechanism of Aspergillus fumigatus adherence to host constituents., *Current Opinion in Microbiology*, 14 (4), pp. 375–9. DOI:10.1016/j.mib.2011.07.006.

Sheridan, K. J., Dolan, S. K. and Doyle, S. (2014) Endogenous cross-talk of fungal metabolites., *Frontiers in Microbiology*, 5, pp. 732. DOI:10.3389/fmicb.2014.00732.

Sheriff, S., Jeffrey, P. D. and Bajorath, J. (1996) Comparison of CH1 Domains in Different Classes of Murine Antibodies, *Journal of Molecular Biology*, 263 (3), pp.

385–389. DOI:10.1006/jmbi.1996.0582.

Shevchenko, A., Tomas, H., Havlis, J., Olsen, J. V and Mann, M. (2007) In-gel digestion for mass spectrometric characterization of proteins and proteomes, *Nat. Protocols*, 1 (6), pp. 2856–2860.

Shi, L., Li, F., Huang, M., Lu, J., Kong, X., Wang, S. and Shao, H. (2012a) Immunoproteomics based identification of thioredoxin reductase GliT and novel Aspergillus fumigatus antigens for serologic diagnosis of invasive aspergillosis., *BMC Microbiology*, 12 (1), pp. 11. DOI:10.1186/1471-2180-12-11.

Shi, L., Li, F., Lu, J., Kong, X., Wang, S., Huang, M., Shao, H. and Shao, S. (2012b) Antibody specific to thioredoxin reductase as a new biomarker for serodiagnosis of invasive aspergillosis in non-neutropenic patients., *Clinica Chimica Acta; International Journal of Clinical Chemistry*, 413 (9–10), pp. 938–43. DOI:10.1016/j.cca.2012.02.011.

Singh, B., Oellerich, M., Kumar, R., Kumar, M., Bhadoria, D. P., Reichard, U., Gupta, V. K., Sharma, G. L. and Asif, A. R. (2010a) Immuno-reactive molecules identified from the secreted proteome of Aspergillus fumigatus., *Journal of Proteome Research*, 9 (11), pp. 5517–29. DOI:10.1021/pr100604x.

Singh, B., Sharma, G. L., Oellerich, M., Kumar, R., Singh, S., Bhadoria, D. P., Katyal, A., Reichard, U. and Asif, A. R. (2010) Novel cytosolic allergens of Aspergillus fumigatus identified from germinating conidia., *Journal of Proteome Research*, 9 (11), pp. 5530–41. DOI:10.1021/pr100605c.

Singh, S., Gupta, S., Singh, B., Sharma, S. K., Gupta, V. K. and Sharma, G. L. (2012) Proteomic characterization of Aspergillus fumigatus treated with an antifungal coumarin for identification of novel target molecules of key pathways., *Journal of Proteome Research*, 11 (6), pp. 3259–68. DOI:10.1021/pr300006j.

Sorgo, A. G., Brul, S., de Koster, C. G., de Koning, L. J. and Klis, F. M. (2013) Iron restriction-induced adaptations in the wall proteome of Candida albicans., *Microbiology (Reading, England)*, 159 (Pt 8), pp. 1673–82. DOI:10.1099/mic.0.065599-0.

Sorgo, A. G., Heilmann, C. J., Dekker, H. L., Bekker, M., Brul, S., de Koster, C. G., de Koning, L. J. and Klis, F. M. (2011) Effects of fluconazole on the secretome, the

wall proteome, and wall integrity of the clinical fungus Candida albicans., *Eukaryotic Cell*, 10 (8), pp. 1071–81. DOI:10.1128/EC.05011-11.

Stevens, D. a, Clemons, K. V and Liu, M. (2011) Developing a vaccine against aspergillosis., *Medical Mycology*, 49 Suppl 1 (April), pp. S170-6. DOI:10.3109/13693786.2010.497775.

Sugui, J. A., Kim, H. S., Zarember, K. A., Chang, Y. C., Gallin, J. I., Nierman, W. C. and Kwon-Chung, K. J. (2008) Genes differentially expressed in conidia and hyphae of Aspergillus fumigatus upon exposure to human neutrophils., *PloS One*, 3 (7), pp. e2655. DOI:10.1371/journal.pone.0002655.

Sugui, J. A., Rose, S. R., Nardone, G., Swamydas, M., Lee, C.-C. R., Kwon-Chung, K. J. and Lionakis, M. S. (2017) Host immune status-specific production of gliotoxin and bis-methyl-gliotoxin during invasive aspergillosis in mice, *Scientific Reports*, 7 (1), pp. 10977. DOI:10.1038/s41598-017-10888-9.

Suh, M.-J., Fedorova, N. D., Cagas, S. E., Hastings, S., Fleischmann, R. D., Peterson, S. N., *et al.* (2012) Development stage-specific proteomic profiling uncovers small, lineage specific proteins most abundant in the Aspergillus Fumigatus conidial proteome., *Proteome Science*, 10 (1), pp. 30. DOI:10.1186/1477-5956-10-30.

Suzuki, S., Sarikaya Bayram, Ö., Bayram, Ö. and Braus, G. H. (2013) conF and conJ contribute to conidia germination and stress response in the filamentous fungus Aspergillus nidulans., *Fungal Genetics and Biology : FG & B*, 56, pp. 42–53. DOI:10.1016/j.fgb.2013.04.008.

Swindells, M. B., Porter, C. T., Couch, M., Hurst, J., Abhinandan, K. R., Nielsen, J. H., Macindoe, G., Hetherington, J. and Martin, A. C. R. (2017) abYsis: Integrated Antibody Sequence and Structure—Management, Analysis, and Prediction, *Journal of Molecular Biology*, 429 (3), pp. 356–364. DOI:10.1016/j.jmb.2016.08.019.

Tekaia, F. and Latgé, J.-P. (2005) Aspergillus fumigatus: saprophyte or pathogen?, *Current Opinion in Microbiology*, 8 (4), pp. 385–92. DOI:10.1016/j.mib.2005.06.017.

Teutschbein, J., Albrecht, D., Pötsch, M., Guthke, R., Aimanianda, V., Clavaud, C., Latgé, J.-P., Brakhage, A. A. and Kniemeyer, O. (2010) Proteome profiling and functional classification of intracellular proteins from conidia of the human-pathogenic mold Aspergillus fumigatus., *Journal of Proteome Research*, 9 (7), pp.

3427–42. DOI:10.1021/pr9010684.

Teutschbein, J., Simon, S., Lother, J., Springer, J., Hortschansky, P., Morton, C. O., *et al.* (2016) Proteomic profiling of serological responses to Aspergillus fumigatus antigens in patients with invasive aspergillosis., *Journal of Proteome Research*. DOI:10.1021/acs.jproteome.6b00042.

Tran, N. H., Rahman, M. Z., He, L., Xin, L., Shan, B. and Li, M. (2016) Complete De Novo Assembly of Monoclonal Antibody Sequences., *Scientific Reports*, 6, pp. 31730. DOI:10.1038/srep31730.

Tuder, R. M., Yun, J. H., Bhunia, A. and Fijalkowska, I. (2007) Hypoxia and chronic lung disease., *Journal of Molecular Medicine (Berlin, Germany)*, 85 (12), pp. 1317–24. DOI:10.1007/s00109-007-0280-4.

Tyanova, S., Temu, T., Carlson, A., Sinitcyn, P., Mann, M. and Cox, J. (2015) Visualization of LC-MS/MS proteomics data in MaxQuant, *PROTEOMICS*, 15 (8), pp. 1453–1456. DOI:10.1002/pmic.201400449.

Tyanova, S., Temu, T. and Cox, J. (2016a) The MaxQuant computational platform for mass spectrometry-based shotgun proteomics, *Nature Protocols*, 11 (12), pp. 2301–2319. DOI:10.1038/nprot.2016.136.

Tyanova, S., Temu, T., Sinitcyn, P., Carlson, A., Hein, M. Y., Geiger, T., Mann, M. and Cox, J. (2016b) The Perseus computational platform for comprehensive analysis of (prote)omics data, *Nature Methods*, 13 (9), pp. 731–740. DOI:10.1038/nmeth.3901.

Upadhyay, S. K., Gautam, P., Pandit, H., Singh, Y., Basir, S. F. and Madan, T. (2012) Identification of fibrinogen-binding proteins of Aspergillus fumigatus using proteomic approach., *Mycopathologia*, 173 (2–3), pp. 73–82. DOI:10.1007/s11046-011-9465-z.

Upadhyay, S. K., Mahajan, L., Ramjee, S., Singh, Y., Basir, S. F. and Madan, T. (2009) Identification and characterization of a laminin-binding protein of Aspergillus fumigatus: extracellular thaumatin domain protein (AfCalAp)., *Journal of Medical Microbiology*, 58 (Pt 6), pp. 714–22. DOI:10.1099/jmm.0.005991-0.

Vaknin, Y., Shadkchan, Y., Levdansky, E., Morozov, M., Romano, J. and Osherov, N. (2014) The three Aspergillus fumigatus CFEM-domain GPI-anchored proteins (CfmA-C) affect cell-wall stability but do not play a role in fungal virulence., *Fungal*

Genetics and Biology : FG & B, 63, pp. 55–64. DOI:10.1016/j.fgb.2013.12.005.

Valiante, V., Macheleidt, J., Föge, M. and Brakhage, A. A. (2015) The Aspergillus fumigatus cell wall integrity signaling pathway: drug target, compensatory pathways, and virulence., *Frontiers in Microbiology*, 6, pp. 325. DOI:10.3389/fmicb.2015.00325.

Verwer, P. E. B., van Duijn, M. L., Tavakol, M., Bakker-Woudenberg, I. A. J. M. and van de Sande, W. W. J. (2012) Reshuffling of Aspergillus fumigatus cell wall components chitin and β-glucan under the influence of caspofungin or nikkomycin Z alone or in combination., *Antimicrobial Agents and Chemotherapy*, 56 (3), pp. 1595–8. DOI:10.1128/AAC.05323-11.

Vickers, I., Reeves, E. P., Kavanagh, K. A. and Doyle, S. (2007) Isolation, activity and immunological characterisation of a secreted aspartic protease, CtsD, from Aspergillus fumigatus., *Protein Expression and Purification*, 53 (1), pp. 216–24. DOI:10.1016/j.pep.2006.12.012.

Vidal-García, M., Domingo, M. P., De Rueda, B., Roc, L., Delgado, M. P., Revillo, M. J., Pardo, J., Gálvez, E. M. and Rezusta, A. (2016) Clinical validity of bis(methylthio)gliotoxin for the diagnosis of invasive aspergillosis, *Applied Microbiology and Biotechnology*, 100 (5), pp. 2327–2334. DOI:10.1007/s00253-015-7209-6.

Virginio, E. D., Kubitschek-Barreira, P. H., Batista, M. V., Schirmer, M. R., Abdelhay, E., Shikanai-Yasuda, M. A. and Lopes-Bezerra, L. M. (2014) Immunoproteome of Aspergillus fumigatus using sera of patients with invasive aspergillosis., *International Journal of Molecular Sciences*, 15 (8), pp. 14505–30. DOI:10.3390/ijms150814505.

Vödisch, M., Albrecht, D., Lessing, F., Schmidt, A. D., Winkler, R., Guthke, R., Brakhage, A. A. and Kniemeyer, O. (2009) Two-dimensional proteome reference maps for the human pathogenic filamentous fungus Aspergillus fumigatus., *Proteomics*, 9 (5), pp. 1407–15. DOI:10.1002/pmic.200800394.

Vödisch, M., Scherlach, K., Winkler, R., Hertweck, C., Braun, H.-P., Roth, M., *et al.* (2011) Analysis of the Aspergillus fumigatus proteome reveals metabolic changes and the activation of the pseurotin A biosynthesis gene cluster in response to hypoxia.,

Journal of Proteome Research, 10 (5), pp. 2508–24. DOI:10.1021/pr1012812.

Walsh, T. J., Anaissie, E. J., Denning, D. W., Herbrecht, R., Kontoyiannis, D. P., Marr, K. A., *et al.* (2008) Treatment of aspergillosis: clinical practice guidelines of the Infectious Diseases Society of America., *Clinical Infectious Diseases : An Official Publication of the Infectious Diseases Society of America*, 46 (3), pp. 327–60. DOI:10.1086/525258.

Ward, O. P., Qin, W. M., Dhanjoon, J., Ye, J. and Singh, A. (2005) Physiology and Biotechnology of Aspergillus, in: *Advances in applied microbiology*.58C, pp. 1–75.

Warris, A. (2015) Azole-resistant aspergillosis., *The Journal of Infection*, 71 Suppl 1, pp. S121-5. DOI:10.1016/j.jinf.2015.04.023.

Wartenberg, D., Lapp, K., Jacobsen, I. D., Dahse, H.-M., Kniemeyer, O., Heinekamp, T. and Brakhage, A. A. (2011) Secretome analysis of Aspergillus fumigatus reveals Asp-hemolysin as a major secreted protein., *International Journal of Medical Microbiology : IJMM*, 301 (7), pp. 602–11. DOI:10.1016/j.ijmm.2011.04.016.

Washburn, M. P., Wolters, D. and Yates, J. R. (2001) Large-scale analysis of the yeast proteome by multidimensional protein identification technology., *Nature Biotechnology*, 19 (3), pp. 242–7. DOI:10.1038/85686.

Wiemann, P., Lechner, B. E., Baccile, J. A., Velk, T. A., Yin, W.-B., Bok, J. W., *et al.* (2014) Perturbations in small molecule synthesis uncovers an iron-responsive secondary metabolite network in Aspergillus fumigatus., *Frontiers in Microbiology*, 5, pp. 530. DOI:10.3389/fmicb.2014.00530.

Wiśniewski, J. R., Hein, M. Y., Cox, J. and Mann, M. (2014) A 'Proteomic ruler' for Protein Copy Number and Concentration Estimation without Spike-in Standards., *Molecular & Cellular Proteomics : MCP*, 13 (12), pp. 3497–506. DOI:10.1074/mcp.M113.037309.

Wiśniewski, J. R., Ostasiewicz, P., Duś, K., Zielińska, D. F., Gnad, F. and Mann, M. (2012) Extensive quantitative remodeling of the proteome between normal colon tissue and adenocarcinoma., *Molecular Systems Biology*, 8 (1), pp. 611. DOI:10.1038/msb.2012.44.

Yasmin, S., Alcazar-Fuoli, L., Gründlinger, M., Puempel, T., Cairns, T., Blatzer, M., *et al.* (2012) Mevalonate governs interdependency of ergosterol and siderophore

biosyntheses in the fungal pathogen Aspergillus fumigatus., *Proceedings of the National Academy of Sciences of the United States of America*, 109 (8), pp. E497-504. DOI:10.1073/pnas.1106399108.

Yates, J. R., Ruse, C. I. and Nakorchevsky, A. (2009) Proteomics by mass spectrometry: approaches, advances, and applications., *Annual Review of Biomedical Engineering*, 11, pp. 49–79. DOI:10.1146/annurev-bioeng-061008-124934.

Yike, I. (2011) Fungal proteases and their pathophysiological effects., *Mycopathologia*, 171 (5), pp. 299–323. DOI:10.1007/s11046-010-9386-2.

Zarember, K. A., Cruz, A. R., Huang, C.-Y. and Gallin, J. I. (2009) Antifungal activities of natural and synthetic iron chelators alone and in combination with azole and polyene antibiotics against Aspergillus fumigatus., *Antimicrobial Agents and Chemotherapy*, 53 (6), pp. 2654–6. DOI:10.1128/AAC.01547-08.

Zhai, C., Summer, D., Rangger, C., Haas, H., Haubner, R. and Decristoforo, C. (2015) Fusarinine C, a novel siderophore-based bifunctional chelator for radiolabeling with Gallium-68., *Journal of Labelled Compounds & Radiopharmaceuticals*. DOI:10.1002/jlcr.3286.

Zhang, Y., Fonslow, B. R., Shan, B., Baek, M.-C. and Yates, J. R. (2013) Protein analysis by shotgun/bottom-up proteomics., *Chemical Reviews*, 113 (4), pp. 2343–94. DOI:10.1021/cr3003533.

Appendices

Appendices

See electronic resource.